UNIVERSITÉ DE STRASBOURG

ÉCOLE DOCTORALE Mathématiques, Sciences de l'information et de l'ingénieur

Laboratoire des sciences de l'ingénieur, de l'informatique et de l'imagerie

THÈSE présentée par :

Jiang JING

soutenue le : **16 March 2022**

pour obtenir le grade de : **Docteur de l'université de Strasbourg**

Discipline/ Spécialité : Physique et technologie des composants

---

Exciton dynamics and charge transport in ordered thin films based on triazatruxene derivatives

---

THÈSE dirigée par :
M. HEISER Thomas   Professeur, Université de Strasbourg

RAPPORTEURS :
M. CHÉNAIS Sébastien   Professeur, Université Sorbonne Paris Nord
Mme. LUDWIGS Sabine   Professeur, Universität Stuttgart

AUTRES MEMBRES DU JURY :
M. SIMON Laurent   Professeur, Mulhouse Materials Science Institute
M. REITER Günter   Professeur, University of Freiburg
Mme. STEVELER Emilie   Associate Professor, INSA Strasbourg

Contents

List of variables and abbreviations

A	Electron acceptor
Abs	Absorption
A/D	Acceptor/Donor Interface
A:D	Donor: Acceptor mixture
AFM	Atomic Force Microscopy
Ag	Silver
Al	Aluminum
Au	Gold
AM1.5G	The global standard spectrum
BHJ	Bulk heterojunction
C_{60}	Fullerene-60
C-AFM	Conductive-Atomic Force Microscopy
Ci	Capacitance of gate dielectric in OFET
CV	Cyclic Voltammetry
CW-PL	Continuous-wave photoluminescence
3D	Three dimensional
D	Electron donor
D	Diffusion coefficient

D_{col}	Lateral spacing of TAT columns
DBP	Tetraphenyldibenzoperiflanthen
DIO	1,8-diiodooctane
DSC	Differential Scanning Calorimetry
DOS	Density of states
E_a	Activation energy
EA	Electron affinity
EEA	Exciton-exciton annihilation
E_g	Band gap energy
E_{ox}	Potential of oxidation
E_{red}	Potential of reduction
ETL	Electron Transport Layer
Ep	Excitation pulse energies
EQE	External quantum efficiency
FF	Fill Factor
FRET	Förster energy transfer
FWHM	Full width half maximum
GIWAXS	Grazing Incidence Wide-angle X-ray Scattering
G	Exciton generation rate
HTL	Hole Transport Layer
HMDS	Hexamethyldisilazane
HOMO	Highest Occupied Molecular Orbital
I_{ds}	Drain current
L_D	Exciton diffusion length
IP	Ionization potential
ITO	Indium Tin Oxide
IRF	Instrument response function
J	Current density
J_m	Current density of point of maximum power
J_{sc}	Short circuit current density
k	Boltzmann constant
L	Thickness of active layer
LUMO	Lowest Unoccupied Molecular Orbital

M_D/P_A	Molecular donor/polymer acceptor
MoO_3	Molybdenum trioxide
NFAs	Non-fullerene acceptors
$N(0)$	Initial population of excitons
oDCB	Orth-dichlorobenzene
OFET	Organic Field Effect Transistor
OSC	Organic semiconductor
p_0	Charge density
P3HT	Poly(3-hexylthiophene)
PCBM	[6,6]-phenyl-C61-butyric acid methyl ester
PCE	Power Conversion Efficiency
PEDOT: PSS	Poly(3,4-ethylenedioxythiophene) polystyrene sulfonate
PL	Photoluminescence
PLQY	Photoluminescence quantum yield
P_{in}	Power of incident light
P_m	Point of maximum power
P/M	Polymer/molecular
R_a	Annihilation radius
R_C	Contact resistance
R_{ch}	Channel resistance
R_{total}	Total resistance
R_0	Förster radius
SAXS	Small-Angle X-ray Scattering
SCLC	Space-Charge-Limited-Current
Si	Silicon
SiO_2	Silicon oxide
SVA	Solvent vapor annealing
S_0	Ground state
S_1	Singlet
T	Temperature
TAT	Triazatruxene
T_{iso}	Temperature of isotropic state
TR-PL	Time-resolved photoluminescence

UV	Ultra-Violet
V_{ds}	Drain voltage
V_{gs}	Gate voltage
V_m	Voltage of point of maximum power
V_{th}	Threshold voltage
V_{oc}	Open circuit voltage
W	Channel width
ZnO	Zinc oxide
E_0	Vacuum permittivity
E_r	Relative permittivity
η	Power Conversion Efficiency
λ	Wavelength
μ	Charge carrier mobility
μ_0	Mobility at infinite temperature
μ_{lin}	Linear mobility of OFET
μ_{sat}	Saturation mobility of OFET
ϕ_{PL}	Quantum yield
κ^2	Dipole orientation
$\varepsilon(\lambda)$	Molar extinction coefficient
γ	Annihilation rate
τ	Exciton lifetime

Chapter 1
Introduction

1 General introduction

Human civilization could not have well developed without an energy revolution. After the 18th century, the widely use of coal, petroleum and electricity has promoted the first and second industrial revolutions, enabling human society to transform into an industrial civilization[1-3]. Since then, energy has become an important driving force for the development of the world economy. The massive use of fossil energy has brought a series of global problems, such as environmental impact and global climate change, which pushed most countries in the world to a conscious action to change their energy supply model. In addition, major investments in the so-called energy transition may boost the development of the world economy and push human society towards an ecologically responsible civilization. In this context, the development of clean energy supply has become a major goal. The Paris Agreement on climate change set up new requirements, balancing global greenhouse gas emissions and absorption to achieve a climate neutral world by mid-century[4, 5]. It will drive the energy supply systems to integrate new renewable energy sources as early as possible.

In principle, nuclear energy does not emit greenhouse gases directly and can therefore help to counter global climate change. However, the safety of nuclear power plants is a major concern, as in recent years, several nuclear accidents threatened the safety of humanity[6, 7]. It is therefore essential to develop renewable, clean, safe and reliable energy sources such as solar, wind and geothermal energy. Solar energy as an alternative energy source has made remarkable progress thanks to the developments of solar cells[8, 9].

Solar cells, also named photovoltaic cells, can directly transform sunlight into electrical energy. The most important parameter for evaluating a solar cell performance is the photovoltaic power conversion efficiency. So far, more and more researchers are

devoting their efforts to photovoltaic technology and many types of solar cells are available, such as silicon, perovskite, dye-sensitized, and organic solar cells[10-12].

Organic solar cells have many potential advantages such as easy manufacturing of thin-film devices by solution processing, flexibility, light-weight and eventually semi-transparent solar modules[13, 14]. The organic semiconductor materials that are used in organic solar cells can be divided into mono-disperse conjugated molecules (or "small molecules") and conjugated polymers. To date, state-of-the-art organic solar cells based on polymer/molecular blends, have already reached a power conversion efficiency up to 18%[14-16]. The performance of organic solar cells is strongly depending on the molecular properties of the materials, which are continuously being improved. In comparison to polymers, small semiconducting molecules are mono-disperse, easier to purify and often lead to crystalline thin-films with reduced structural disorder and enhanced electronic performance. They are therefore of particular interest to organic solar cell community.

Exciton dynamics and charge carrier transport are central properties that determine the performances of organic optoelectronic devices and have been shown to be highly dependent on molecular structure and the related solid-state molecular packing[17, 18]. Long exciton lifetimes and high diffusion lengths are crucially important for organic solar cell devices as they increase the probability that photon absorption leads to the generation of free charge carriers. However, organic semiconductors whose solid-state molecular organization allows efficient exciton transport over large distances (above 10 nm) are still rare[19, 20]. Moreover, efficient free charge carrier transport relies necessarily on strong intermolecular interactions. Many planar molecules have therefore been designed since it may be expected that planarity enhances intermolecular interactions and facilitate charge transport along the molecular stacking directions. Yet, planar molecules often lead to highly anisotropic properties, with poor charge transport

occurring along directions other than the stacking direction. This is particularly the case for molecules that are functionalized with alkyl chains, which are necessary to ensure good processability in solution but introduce detrimental insulating regions[21-23]. While this may have considerable impact on the performances of optoelectronic devices, and in particular organic solar cells, reports addressing anisotropy of charge transport in molecular thin-films or molecular design systems capable of efficient 3D transport are still rare. In this context, my work has been motivated by the recent development of a particular family of dumbbell shaped small molecules, which have been designed for photovoltaic applications, and for which first studies have revealed promising results in terms of 3D transport. Also, preliminary structural analyses suggested the existence of unusual liquid crystal and crystalline solid states that may confer efficient charge hopping pathways along the three dimensions of space. Moreover, beyond charge transport, studying the exciton transport in these systems appears also of interest, as the relationship between molecular structure and exciton dynamics is still far from being fully understood. This thesis has therefore been dedicated to the studies of charge transport and exciton dynamics in thin films composed of planar dumbbell shaped donor-acceptor-donor molecules including highly planar triazatruxene (TAT) units, with the aim to better understand the impact of the molecular structure of this particular family on molecular assembly, 3D charge transport and exciton diffusion.

The thesis is organized as follows:

Chapter 2 introduces the scientific background of organic semiconductors, charge transport, exciton dynamics and organic semiconductor applications.

Chapter 3 presents the state-of-the-art of charge transport and exciton dynamics in thin films of small molecules.

Chapter 4 describes the chemical and solid state properties of TAT-based molecules.

Chapter 5 is dedicated to the investigations of the exciton dynamics as a function of molecular structure and solid state. In particular, the exciton diffusion length of investigated molecular thin-films will be explored.

Chapter 6 presents the studies of charge carrier transport anisotropy as a function of the molecular self-assembly.

Chapter 7 describes first investigations of the photovoltaic properties of organic solar cells using TAT-based molecules as electron donor blended with an electron acceptor polymer.

Chapter 8 gives the conclusion and perspectives of my work.

References:

[1]   X. Du, *Chinese Journal of Population Resources and Environment*, 2015, **13**, 115-118.

[2]   D. Boyer, in *The promise of infrastructure*, Duke University Press, 2018, pp. 223-244.

[3]   B. Gong, *Shale Energy Revolution*, Springer, 2020.

[4]   P. Agreement, 2015.

[5]   J. Rogelj, M. Den Elzen, N. Höhne, T. Fransen, H. Fekete, H. Winkler, R. Schaeffer, F. Sha, K. Riahi and M. Meinshausen, *Nature*, 2016, **534**, 631-639.

[6]   S. J. Zinkle and G. Was, *Acta Materialia*, 2013, **61**, 735-758.

[7]   L. Darby, A. Hansson and C. Tisdell, *Case Studies in the Environment*, 2020, **4**.

[8]   V. Devabhaktuni, M. Alam, S. S. S. R. Depuru, R. C. Green II, D. Nims and C. Near, *Renewable and Sustainable Energy Reviews*, 2013, **19**, 555-564.

[9]   S. P. Sukhatme and J. Nayak, *Solar energy*, McGraw-Hill Education, 2017.

[10]   M. A. Green, *Englewood Cliffs*, 1982.

[11]   A. M. Bagher, M. M. A. Vahid and M. Mohsen, *American Journal of optics and Photonics*, 2015, **3**, 94-113.

[12]   A. Fahrenbruch and R. Bube, *Fundamentals of solar cells: photovoltaic solar energy conversion*, Elsevier, 2012.

[13]   Y. Li, G. Xu, C. Cui and Y. Li, *Advanced Energy Materials*, 2018, **8**, 1701791.

[14]   Y. Tong, Z. Xiao, X. Du, C. Zuo, Y. Li, M. Lv, Y. Yuan, C. Yi, F. Hao and Y.

Hua, *Sci China Chem*, 2020, **63**, 758-765.

[15]   T. Liu, T. Yang, R. Ma, L. Zhan, Z. Luo, G. Zhang, Y. Li, K. Gao, Y. Xiao and J. Yu, *Joule*, 2021, **5**, 914-930.

[16]   T. Yan, J. Ge, T. Lei, W. Zhang, W. Song, B. Fanady, D. Zhang, S. Chen, R. Peng and Z. Ge, *Journal of Materials Chemistry A*, 2019, **7**, 25894-25899.

[17]   C. Schnedermann, J. Sung, R. Pandya, S. D. Verma, R. Y. Chen, N. Gauriot, H. M. Bretscher, P. Kukura and A. Rao, *The journal of physical chemistry letters*, 2019, **10**, 6727-6733.

[18]   A. Platt, M. Kendrick, M. Loth, J. Anthony and O. Ostroverkhova, *Physical Review B*, 2011, **84**, 235209.

[19]   O. V. Mikhnenko, P. W. Blom and T.-Q. Nguyen, *Energy & Environmental Science*, 2015, **8**, 1867-1888.

[20]   D. P. McMahon and A. Troisi, *ChemPhysChem*, 2010, **11**, 2067-2074.

[21]   B. T. O'Connor, O. G. Reid, X. Zhang, R. J. Kline, L. J. Richter, D. J. Gundlach, D. M. DeLongchamp, M. F. Toney, N. Kopidakis and G. Rumbles, *Advanced Functional Materials*, 2014, **24**, 3422-3431.

[22]   E. J. Crossland, K. Tremel, F. Fischer, K. Rahimi, G. Reiter, U. Steiner and S. Ludwigs, *Advanced Materials*, 2012, **24**, 839-844.

[23]   A. Saeki, Y. Koizumi, T. Aida and S. Seki, *Accounts of chemical research*, 2012, **45**, 1193-1202.

Chapter 2
Scientific research background

Organic semiconductor materials

This chapter will focus on the basic concepts of organic semiconductors. In the first section, the history, molecular physics, and categories of organic semiconductors will be briefly presented. Two important physical parameters (charge transport and exciton dynamics) that relate to the optoelectronic properties of organic semiconductor materials will be described in the second section. In the last section, the applications of organic semiconductor materials will be presented as well.

2.1 Organic semiconductor materials

2.1.1 History of organic semiconductor materials

In the 1970s, Hideki Shirakawa[1] first discovered that doped conjugated polymers of polyacetylene ($[C_2H_2]_n$) could achieve conductive properties, and since then, there has been a boom in research on conductive organic materials[2-4]. Compared to conventional inorganic materials, organic semiconductor (OSC) materials possess a lot of significant advantages, such as flexibility, solution-processed and easily manufacture of thin-film devices by vacuum evaporation, etc.[5, 6] OSC materials are particularly attractive in three main applications: organic light-emitting diode (OLED)[7], organic field-effect transistor (OFET)[8] and organic photovoltaic cell (OPV)[6].

2.1.2 π-conjugated materials

OSCs are carbon-based materials and are also called π-conjugated materials. The term "conjugated" was created in 1899 by Johannes Thiele[9]. Electronic and optical properties of conjugated materials are caused by the π-orbitals of sp^2-hybridized carbon atoms[10]. One carbon atom has six electrons, the electronic configuration of carbon is $1s^2 2s^2 2p_x^1 2p_y^1$. The theory of orbital hybridization in bonding can explain the molecule geometry and atomic bonding properties. As an example, for ethylene ($CH_2=CH_2$) (shown in **Figure 2.1**), the 2s orbital of C mixes with the two 2p orbitals ($2p_x$, $2p_y$) to form three equal energy hybridized sp^2 orbitals. The energy of the remaining single $2p_z$

orbital is slightly higher than the hybridized orbitals (**Figure 2.1b**). Each sp^2 hybridized carbon uses three sp^2 hybridized orbitals to form three σ bonds, as shown in **Figure 2.1a**. The remaining $2p_z$ orbitals overlap with the adjacent $2p_z$ orbital, forming a π orbital and a π* orbital (**Figure 2.1b**). In particular, three sp^2 orbitals form a triangle within a plane and the p_z orbitals are in the plane perpendicular to it. In addition, the connected p_z orbitals with delocalized electrons will decrease the overall energy of the molecule and increase stability of conjugated system. In this system, the π electrons do not belong to a single atom but rather to a group of atoms, so they can support intramolecular charge carrier transport and result in high electronic polarizability in OSC materials. In OSC materials, the π-π bond structure is extended to many adjacent atoms, based on the repetition of the molecular structure units and the compounds may be cyclic, acyclic, linear or mixed.

According to the frontier orbital theory, in π-conjugated systems, the (π) orbital is referred to as the "Highest Occupied Molecular Orbital" (HOMO) and the (π*) orbital is referred to as the "Lowest Unoccupied Molecular Orbital" (LUMO) (as shown in **Figure 2.1c**). In OSC materials, these two discrete HOMO/LUMO levels can be likened to the valence and conduction bands in inorganic semiconductor materials. When an electron of the HOMO energy level is excited to the LUMO energy level, a pair of hole-electron bound together is formed, called exciton (see below). The optoelectronic properties of OSC materials are determined by the exciton dynamics but also by the free charge carriers generated from exciton dissociation.
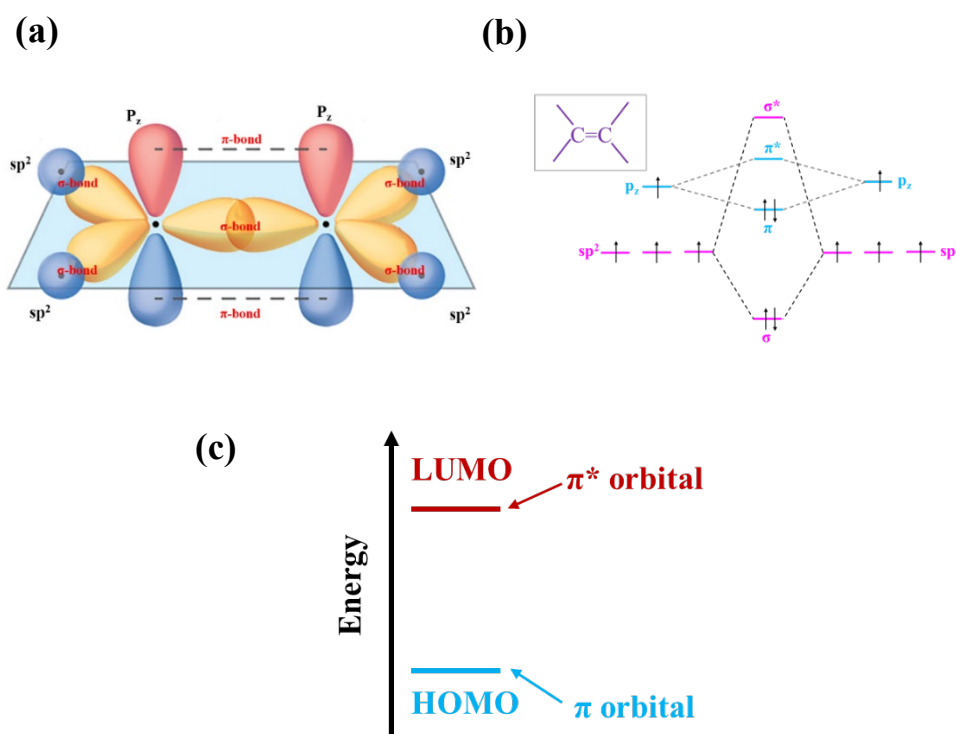
(a)

(b)

(c)

Figure 2.1 *(a) Hybridized atomic orbitals and chemical bonding in an ethylene C_2H_4 molecule. (Copyright from https://courses.lumenlearning.com/suny-chem-atoms-first/chapter/multiple-bonds-2/). (b) Energy diagram of the carbon-carbon bonding with the sp^2 hybridization. (c) Diagram of the molecular orbitals of a π-conjugated molecule.*

2.1.3 Categories of organic semiconductor materials

OSC materials can be divided into two main categories: small-molecules (or molecular OSCs) and polymers. In fact, due to the modifiability of organic molecules, there are thousands of OSCs with different chemical structures. For example, molecular OSCs include pentacene[11], triphenylamine[12], fullerene[13], phthalocyanine[14], perylene derivatives[15] etc., as shown in **Figure 2.2**. Polymeric OSCs include poly(p-phenylene)[16], polypyrrole[17], polythiophene[18] etc., as shown in **Figure 2.3**. Polymer OSCs are made up of repeating units, called "monomers" and form a long molecular chain. Molecular OSCs do not have repeating units as polymers in the molecular structure, and usually consist of a relatively large π-π conjugated system. Moreover, in comparison with polymers, molecular OSC materials are easier to purify, and the

corresponding thin-films are easily processed from vacuum evaporated technique[19]. In addition, small-molecules are monodisperse so that they possess more reproducible properties.
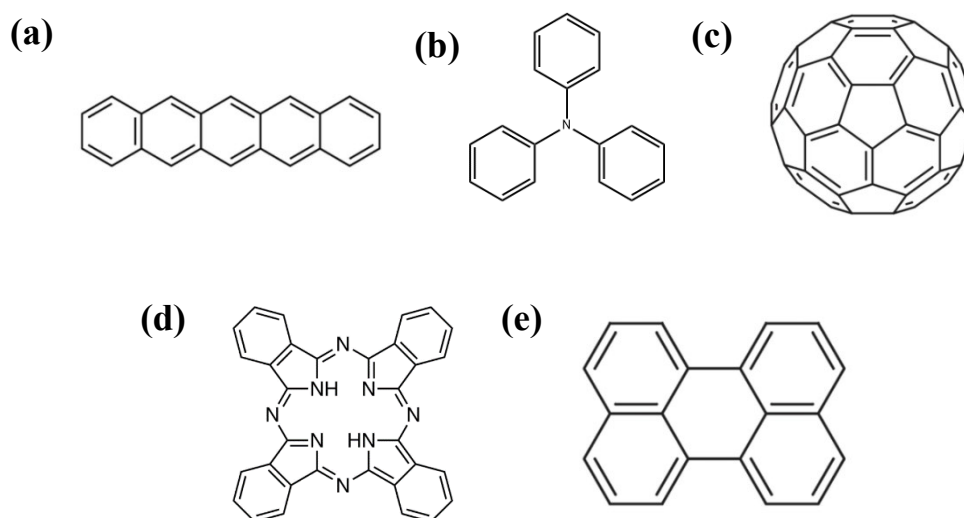

Figure 2.2 *Chemical structure of typical molecular materials: (a) pentacene, (b) triphenylamine, (c) fullerene, (d) phthalocyanine, (e) perylene.*
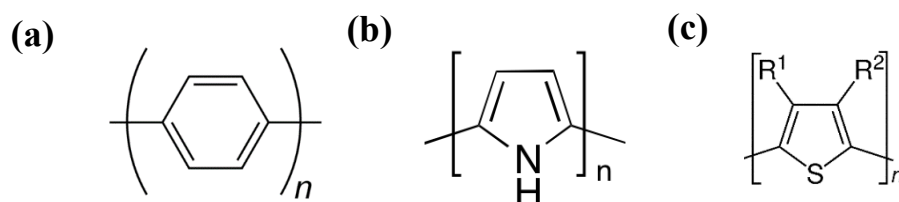

Figure 2.3 *Chemical structure of typical polymers: (a) poly(p-phenylene), (b) polypyrrole, (c) polythiophene.*

Furthermore, depending on the majority charge carriers in the OSCs (i.e., those who can be most easily injected from an electrode or generated by doping), the materials can be divided into three categories: p-type materials with holes as the majority charge carriers, n-type materials with electrons as the majority charge carriers and ambipolar materials showing both p- and n-type characteristics. P-type semiconductors are electron donor (D) materials and are characterized by relatively high lying LUMO and HOMO levels in comparison to n-type semiconductors. N-type semiconductors

correspond to electron acceptor materials (A). Moreover, p-type materials show higher air stability and generally higher charge carrier mobilities than n-type materials, and the development of ambipolar or n-type OSC materials is lagging behind the one of p-type materials [20-22].

2.2 Charge transport in organic semiconductor materials

In OSCs, charge transport requires charge carriers (holes or electrons) to be able to migrate within or between molecules. Charge carrier transport is an important factor that limits semi-conductive performance[23]. Since the weak van der Waals forces are dominating the intermolecular interactions in OSCs, charge carriers are localized onto conjugated parts of the molecule. Moreover, in OSCs, charge carriers are more localized than in inorganic semiconductors. Therefore, the charge carrier transport through the OSCs is determined by hopping between conjugated parts. Efficient charge transport requires that charge carriers are neither trapped nor recombined during their transport. Therefore, charge carrier transport could be influenced by many factors, including molecular structure, packing order, impurities or defects, temperature, electric field, and density of charge carriers, etc.

When an external electric field is applied, the charge carriers drift under the influence of the Coulomb force. The mobility (μ) can be expressed by the ratio of the drift velocity of the charge (v) to the magnitude of the applied electric field (F):[23]

$$\mu = v/F \quad (2.1)$$

According to the different degree of delocalization of charge carriers in the OSCs, three models have been developed to describe charge transport in OSCs: the band-like transport, the multi trap and release (MTR), and the variable-range-hopping (VRH)[24-

[26] models. The band-like transport model is usually expected to be applied to crystalline materials. In crystalline inorganic semiconductors, the strong coupling between neighboring atoms allows charge carriers to be delocalized and the corresponding charge carrier mobility is best described by band-like transport. In this model, mobilities increase with decreasing temperature following [27, 28]:

$$\mu \propto T^{-n} \quad n = 1, 2, 3 \quad (2.2)$$

For polycrystalline or semi-crystalline OSCs with a relatively low degree of structural disorder, charge carriers transport lead to MTR transport. The basic assumptions of this model are: charge carriers in the semiconductor are trapped in localized states and the release of trapped charges is a thermally activated process. Free charge carriers are in delocalized states (band-like transport). Such transport is dependent on the energy levels of the localized states, charge density and temperature.

In amorphous or highly disordered OSCs, charge transport mainly occurs by hopping among localized states, and the most commonly used model is VRH. In the VRH model, charge carriers may hop a short distance (nearest neighbors) or a longer distance provided the activation energy E_a is sufficiently low. Due to an energy barrier that must be overcome, the hopping transport shows temperature-dependent behavior. The mobility μ shows an thermally activated behavior following the Arrhenius law[23]:

$$\mu \propto \cdot exp\left(-\frac{E_a}{kT}\right) \quad (2.3)$$

where k is the Boltzmann constant and T is the temperature in Kelvin (K).

The energetic distribution of localized states in an OSCs is described by its density of states (DOS). Usually, a Gaussian DOS is used for bulk OSCs materials[29, 30] (**Figure**

2.4). The width at have maximum of the Gaussian is linked to structural disorder. According to the Gaussian disorder model, hopping is most efficient near the so-called "transport-level", which is located slightly below the DOS maximum. Hopping between energy tail states is hampered by large activation energies. As a consequence, the measured mobility is expected to be strongly dependent on charge carrier density (occupancy rate) which in turn depends on the device type used to estimate the mobility (see below).
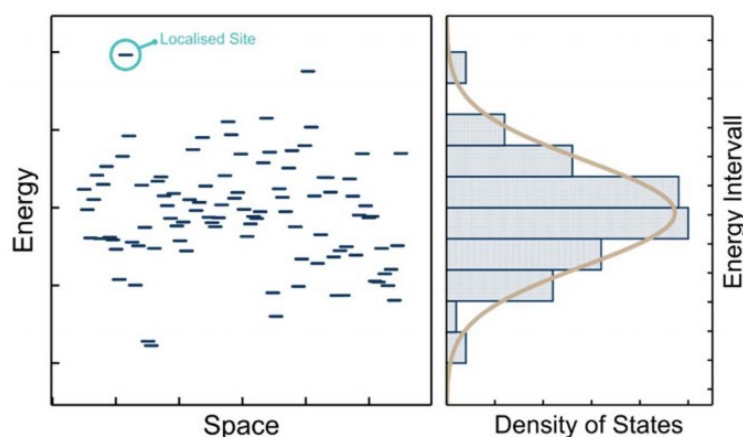

Figure 2.4 *Distribution of localized sites in space and energy according to a Gaussian distribution equation. (Copyright from H. Abdalla, Sweden, 2018)*

2.2.1 Charge carriers transport anisotropy

In many OSCs, the charge carrier hopping transport is anisotropic, due to molecular stacking structures that induce anisotropic intermolecular interactions. For example, the charge carriers transport within π-conjugated Poly(3-hexylthiophene-2,5-diyl) (P3HT)[31, 32] thin-films occurs along three directions: (1) intrachain transport (conjugation direction), (2) interchain transport along π-π stacking and (3) interchain transport along alkyl chain stacking direction (as shown in **Figure 2.5**). The intrachain charge carriers transport mainly depends on the effective π-conjugation length along the molecular backbone. High coplanarity along the backbone will lead to high π-conjugation and hence efficient intrachain transport. The interchain charge carriers transport occurs along π-π stacking and alkyl chain stacking directions. Generally, the

most beneficial intermolecular charge carrier hopping path is along the π-π stacking, which usually has the shortest interchain distance among all directions and most pronounced wavelength overlap, resulting in anisotropic charge transport.
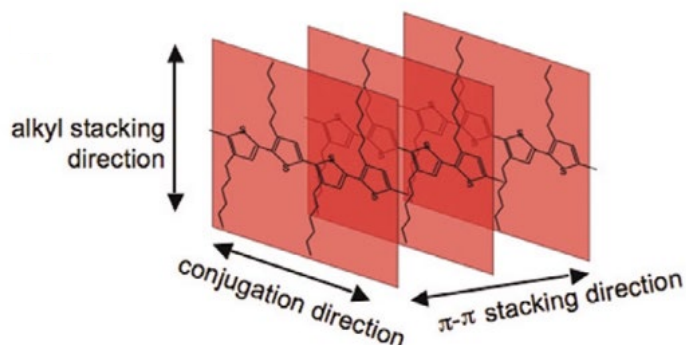

Figure 2.5 *Charge carriers transport directions in π-conjugated P3HT: intrachain transport (Conjugation direction) and interchain transports (alkyl stacking direction and π-π stacking direction). (Copyright from Alberto Salleo, Charge transport in polymeric transistors, materials today, 2007)*

In addition, the molecular shape or conformation impacts the molecular stacking structure, and therefore the charge carrier transport anisotropy. For example, discotic molecules tend to form nematic-columnar phases[33] (illustrated in **Figure 2.6a),** while calamitic molecules tend to form smectic phases[34], in which the molecules are organized in lamellar systems (as shown in **Figure 2.6b**). **Figure 2.6** illustrates charge carrier transport pathways in the discotic and calamitic liquid crystalline materials, where the conducting aromatic core is represented in green and the insulating alkyl chains are in blue. Obviously, for nematic-columnar phase (a), charge carriers transport is favored only along the column (one-dimensional transport), while for lamellar systems (b), two-dimensional charge carrier transport is favored within the layers. This shows that the molecular stacking structure has a significant impact on the charge carriers transport anisotropy.

As the anisotropy of the mobility in OSCs is a key factor for electronic device applications, the mobility has to be evaluated along different directions. In thin-film

devices, charge carrier transport measurements along a direction perpendicular to the substrate provides access to the "out-of-plane" mobility (**Figure 2.7**) and can be done by space-charge-limited-current (SCLC)[35], time-of-flight (TOF)[36]. On the contrary, the in-plane mobility (**Figure 2.7**) describes the charge carriers transport parallel to the device substrate and is generally determined by characterizing organic field-effect transistors (OFET).
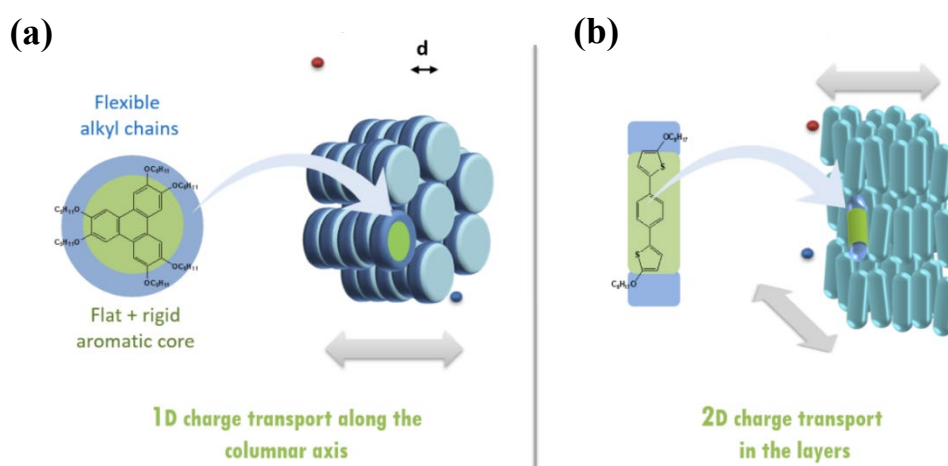
Figure 2.6 *Charge transport pathway in a (a) discotic and (b) calamitic liquid crystalline materials.*
(Copyright from https://www.moleculargardens.cnrs.fr/2018/11/08/liquid-crystals/)

Anisotropic charge transfer can maximize the efficiency of OSC materials for some applications. For instance, materials with high in-plane mobility are good candidates for high mobility field-effect transistors, while materials with high out-of-plane mobility are particularly suitable for light emitting diodes or solar cells.

Figure 2.7 *Charge carriers transport pathway in the out-of-plane and in-plane.*

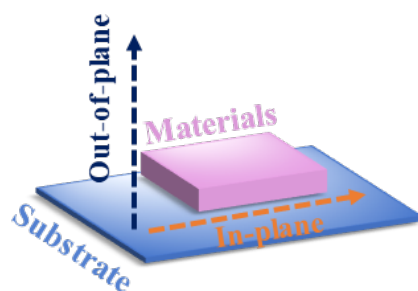In this thesis, the state-of-the-art on charge carrier transport will be presented in chapter 3 and the self-assembly structure of investigated molecules will be described in chapter 4. The results of carrier mobilities measurements using either SCLC or OFET devices, will be presented in chapter 6.

2.3 Exciton dynamics in organic semiconductor materials

Absorption of photons by OSCs leads to the generation of excitons firstly, rather than free charge carriers. The excitons can be considered as a bounded electron-hole pair. The performances of OSC devices therefore depend not only on the free charge carriers transport properties, but also on the exciton dynamics. Indeed, the exciton dynamics underlies the photocurrent in OPV devices and the electroluminescent properties in OLEDs (see below)[37, 38].

2.3.1 Exciton

As mentioned above, the absorption of photons in OSCs will generate excitons, which corresponds essentially to molecules in an excited state. **Figure 2.8a** shows the Jablonski energy diagram[39] that displays energy transitions that may result from the absorption of a photon by an isolated molecule. These states are positioned vertically by their energy and grouped horizontally by spin multiplicity[40, 41]. Excitons with total spin of zero or one are called singlet or triplet, respectively (as shown in **Figure 2.8b**). The route 1 shows a molecule excited from the ground state S_0 to the singlet excited state S_1 after absorption of a photon; Triplet excited state T_1 can be created by the intersystem crossing (route 4). The radiative transitions 2 and 6 to the ground state correspond to photoluminescence and phosphorescence, respectively. The nonradiative transitions 3 and 5 compete with 2 and 6. Moreover, transition 7 shows the absorption of a photon from state T_1 to a higher triplet excited state T_n.

Excitons are electrically neutral species. The singlet exciton binding energy (energy necessary to dissociate the exciton into an electron-hole pair) is usually around 0.3-0.5 eV, and its lifetime is generally of the order of nanoseconds (ns). The binding energy of triplet excitons (0.8-0.9 eV) is higher than the singlet due to the attractive exchange interaction of the same spin orientation[42]. In general, the triplet excited state is more stable than the singlet excited state. As a consequence, the triplet exciton has a longer exciton lifetime than the singlet, which is about a few microseconds (μs) [40, 41, 43, 44].
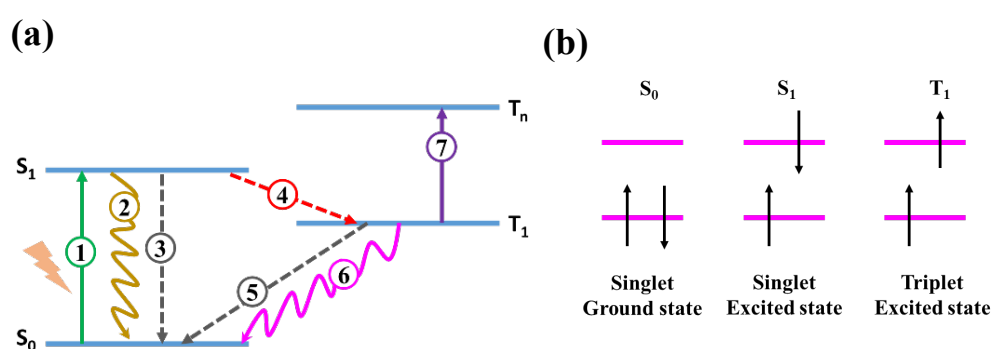

Figure 2.8 *(a) The Jablonski diagram of electronic transitions in organic semiconductors. The energies of singlet (S_0 and S_1) and triplet (T_1 and T_n) states are scaled vertically. Absorption (1), fluorescence (2), intersystem crossing (4), phosphorescence (6), nonradiative transitions (3 and 5) and photoinduced absorption (7) are presented as arrows. (b) Exciton spin states.*

2.3.2 Exciton diffusion

Excitons in OSC materials are mobile species and are characterized diffusion length (L_D) in the range of 1-10 nm[40, 41, 45, 46]. The latter is limited by the exciton lifetime and depends on the diffusion coefficient (D). Exciton diffusion corresponds to an energy transfer that occurs either by a Förster transfer or Dexter transfer.

The Förster mechanism (**Figure 2.9a**), also called Förster resonant energy transfer (FRET), is dominant in the case of singlet excitons[40, 41, 47]. It occurs when the emission spectrum of the "*donor*" singlet has a significant overlap with the absorption spectrum

of the "*acceptor*" singlet. Therefore, the efficiency of FRET decreases with increasing distance between *donor* and *acceptor*. The distance is described by the Förster radius (R_0), which is defined as the distance between "*donor*" and "*acceptor*" for 50% FRET efficiency[48]. R_0 is a critical parameter which is determined by several other factors such as dipole-dipole orientation, refractive index, photoluminescence quantum yield (PLQY), and spectral overlap between emission and absorption spectra[41, 49]. Usually, this type of energy transfer occurs for *donor-acceptor* separations in the range of 1-5 nm. Triplet excitons may also undergo FRET for phosphorescent donors[50].
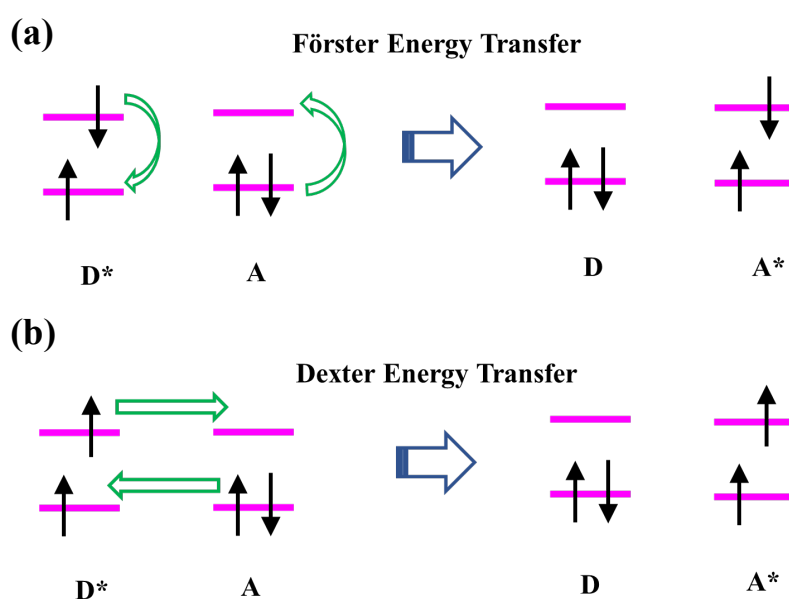
Figure 2.9 *(a) Scheme of Förster energy transfer represented for a singlet exciton and (b) scheme of Dexter energy transfer for a triplet exciton. The horizontal lines are HOMO and LUMO energy levels of "donor" (D) and "acceptor" (A) molecules. The asterisk denotes excited state. The arrows represent simultaneous rearrangement of the electronic configuration.*

Dexter energy transfer (**Figure 2.9b**) occurs when there is a significant overlap of molecular orbitals (corresponding to a distance of only about 0.1-1 nm) between "*donor*" and "*acceptor*". [41, 51] Both singlet and triplet excitons may be transferred via Dexter energy transfer. The FRET mechanism is usually more efficient than Dexter energy

transfer for singlet excitons, while the majority of triplet exciton migration occurs via Dexter energy transfer.

2.4 Application of organic semiconductor materials

The remarkable advantages of OSCs (i.e., solution-processed, flexible, thin and cost-efficient performance) have led to their significant development in the following three main application fields: organic light-emitting diodes (OLEDs)[52, 53], organic field-effect transistors (OFETs)[54, 55] and organic photovoltaic cells (OPVs)[56, 57].

2.4.1 Organic light-emitting diodes

Since the first report by Ching W. Tang and Steven Van Slyke in 1987[58], OLED have become promising optoelectronic devices in full-color display panels and eco-friendly lighting sources. OLED devices (whose structure is shown in **Figure 2.10**) use an OSC thin-film as the emissive electroluminescent layer, and emit light in response to an electric current. Electrons and holes are injected into the light-emitting layer from the two adjacent electrodes to form excitons, the latter recombining to release photons. Moreover, the color of the emitted light is determined by the emitter materials fluorescence.
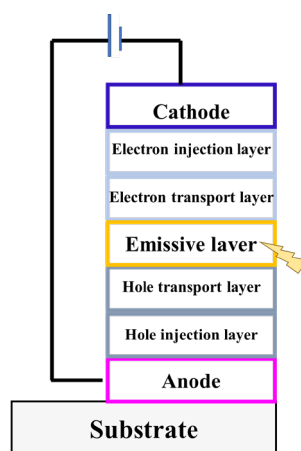

Figure 2.10 Structure of an OLED device.

Achieving OLEDs with high-performances requires OSC emitting materials with suitable photoelectric properties, such as high charge carrier mobilities, and stronger fluorescence, etc.[59] To date, three generations of OLED devices have been reported based on different mechanisms of electroluminescence. The first-generation emitters only use the singlet excitons. The simple spin-statistics predicts that when a hole and an electron recombine to form an exciton, only 25% of the excitons created are singlet excitons, and 75% are triplets, limiting the external quantum efficiency (EQE) of first-generation OLED to maximum 25% [60, 61]. In order to improve the performance of OLEDs, the use of triplet excitons has been consequently considered. Thus, the second generation is made of phosphorescent emitters which allow transitions from the excited triplet states (T1) to the singlet ground state (S0) (see **Figure 2.8**). The third generation of OLEDs is constituted of thermally activated delayed fluorescence (TADF) materials, for which the thermally activated transformation of triplet excitons into singlet excitons is followed by light emission. So far, a green OLED (third generation) with a record-high EQE of 37.8% was achieved by Cheng et al[62]. Emitter materials are essential to the performance of OLEDs, the latter depending on the chemical structure and organization in thin-films of the organic molecules. Fabrication and characterization of OLEDs are also one of the ways to evaluate the photoelectric performance of OSC materials, such as charge carrier density, out-of-plane transport property, exciton dynamics, and electroluminescence performance of OSCs, etc.[59]

2.4.2 Organic field-effect transistors

In 1986, H. Koezuka, A. Tsumura and Tsuneya Ando reported the first OFET based on a conjugated polymer of thiophene[63]. Since then, with the synthesis of new OSC materials and the optimization of the preparation of OFET devices, OFET have been used for various applications, such as biosensors[64], photodetectors[65] and flexible displays[66]. **Figure 2.11** shows a typical structure of a bottom gate bottom contact

OFET device, wherein the gate controls the current between the source and the drain electrodes, similar to a tap that controls the water flow. Between the gate and the electrode is an insulator layer. Charge carriers are injected into channel at the source electrode and collected by the drain electrode, while the gate terminal controls the charge accumulation in the channel. By controlling the gate voltage, the current from source to drain can be adjusted for the transistor to work like a switch. The OFET performances highly depend on thin-film morphology, structural order, and contact resistance (suitable match of energy level with electrodes/ dielectrics)[67-69].
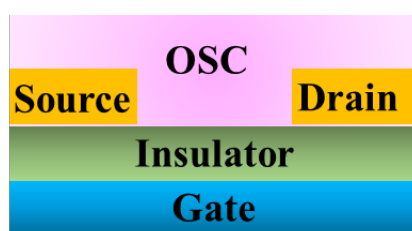

Figure 2.11 *Structure of a bottom gate bottom contact OFET device.*

It is worth mentioning that OFET are useful devices to characterize the in-plane charge carrier mobility for OSC materials (also called field-effect mobility). In this thesis, the experiments and results of in-plane mobility characterization of investigated OSCs will be presented in chapter 6.

OFET materials

OFETs can be prepared either by vacuum evaporation of small-molecules, or by solution-process of polymers or small-molecules. So far, more and more people are paying attention to solution processing of organic semiconductors for OFETs, as they can be suitable for large-area processing[70]. Currently, the highest field-effect hole mobility is based on a solution-processable p-type polymer, poly[4-(4,4-dihexadecyl-4H-cyclopenta[1,2-b:5,4-b′]dithiophen-2-yl)-alt[1,2,5] thiadiazolo [3,4-c]pyridine] (PCDTPT)[71], which shown hole mobility over 36 cm^2 V^{-1}s^{-1}. For n-type solution-

processable polymer, electron mobility of 8.5 cm^2 V^{-1}s^{-1} was found for naphthalenediimide benzothiadiazole (PNBS)-based polymer[72]. For ambipolar solution-processable polymer, the mobilities of hole and electron in the selenophene-diketopyrrolopyrrole with siloxane chains (PTDPPSe-Si)-based polymer reached the respective values of 8.84 cm^2 V^{-1}s^{-1} and 4.34 cm^2 V^{-1}s^{-1}[73].

State-of-the-art solution-processable small-molecules let to field-effect mobilities that are low compared to polymers. For instance, hole mobility 3.40 cm^2 V^{-1}s^{-1} was found for p-type solution-processable small molecule (triisopropylsilyl) pentacene (TIPS-Pentacene) [74]. Bogyu Lim[75] reported that diketopyrrolopyrrole (DPP)-based p-type solution-processable small-molecules with siloxane side-chains shown hole mobility as 3.04 cm^2 V^{-1}s^{-1}. For n-type solution-processable small-molecules, electron mobility of 0.77 cm^2 V^{-1}s^{-1} was found for quinoidal dithioalkylterthiophene (DSTQ-14)[76]. For ambipolar solution-processable small molecule, methyl 2-(4-methoxyphenyl)-6-((4-methoxyphenyl)ethynyl)quinoline-4-carboxylate with mobility up to 0.10 cm^2 V^{-1}s^{-1} for hole and 0.05 cm^{2}V^{-1}s^{-1} for electron is observed[77].

2.4.3 Organic photovoltaic cells

Organic solar cell devices are composed of OSC materials as active layer sandwiched between two electrodes with different work functions[78, 79]. In the OPV device, at least one electrode is transparent and lets sunlight spectrum pass through, allowing the active layer to harvest the sunlight. Generally, the active layer is formed of a blend of electron donor (D) and electron acceptor (A) materials. D and A of OSC materials differ by their frontier orbital energy positions: electron donor has a higher HOMO level and possesses the lowest ionization potential. On the contrary, the electron acceptor has the lowest LUMO level and therefore the highest electronic affinity[80, 81]. The dissociation of photogenerated excitons into free charge carriers takes place at the D/A interface. As shown in **Figure 2.12**, if the energy of the LUMO of the acceptor is significantly lower

than the LUMO of the excited donor molecule, and also if there is a significant wavefunctions overlap between wavefunctions of the donor and acceptor molecules, the electron may be transferred from donor to acceptor. The resulting charge-transfer state (CT) dissociates into free electron/hole pair (charge-separated state) which diffuse to the collecting electrodes and lead to the generation of a photocurrent. A similar process takes place for holes if the photon is absorbed by the A.

The whole operating process of an organic solar cell follows five steps (as shown in **Figure 2.12**): (1) Light absorption and exciton generation; (2) Exciton diffusion to D/A interface; (3) Exciton dissociation; (4) Free charge carriers transport; (5) Charge collection at the electrode. Each step in the process is critical to the power conversion efficiency; especially, exciton dynamics and charge carrier transport are crucial parameters for the performances of OPV devices. To create a photocurrent, photogenerated excitons in OPV devices need to be dissociated into free charge carriers at a D/A interface, as the exciton binding energy is larger than the thermal energy at room temperature[41]. Moreover, excitons have generally short lifetimes τ (<1 ns) and small diffusion lengths L_D (<10 nm) which limit the PCE of OPV devices[48, 82]. To avoid this restriction and allow high proportion of excitons to reach the D/A interface, it is necessary to use a bulk heterojunctions (BHJ) structure, whose morphology is determinant, but still difficult to control[83, 84]. Also, exciton dissociation results in energy loss (typically of the order of the exciton binding energy) and therefore lowers the maximum achievable PCE in comparison to other inorganic PV technologies.
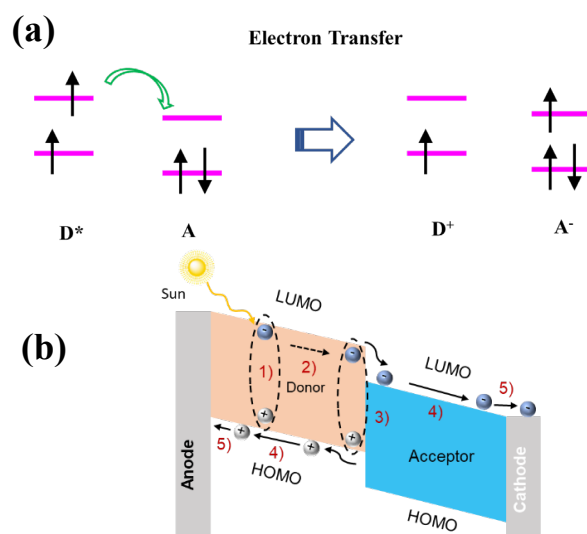
(a)

(b)

***Figure 2.12** (a) Electron transfer from an excited donor molecule (D*) to a neutral acceptor (A). The asterisk denotes excited state. The arrows represent simultaneous rearrangement of the electronic configuration. (b) Energy level diagram of donor and acceptor materials in an organic solar cell: the five steps of photovoltaic effect are represented by numbers and detailed above.*

Characterization of organic photovoltaic cells

Typical *J-V* (current density / voltage) curves of an organic solar cell device measured under the dark and illumination are shown in **Figure 2.13**. The photovoltaic parameters are the open-circuit voltage (V_{oc}) and the short circuit current density (J_{sc}). The *J-V* curves were measured under an AM 1.5G-100 mW/cm^2 solar simulator.
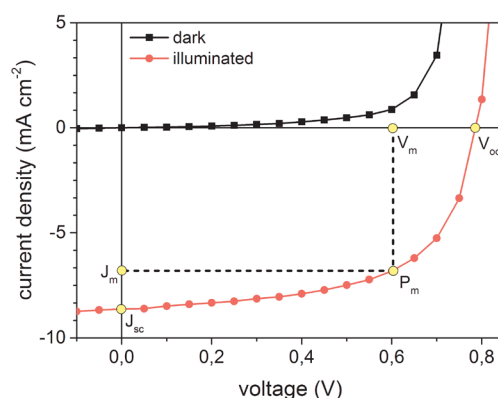

***Figure 2.13** Dark and illuminated J-V characteristics of an organic solar cell. The point of maximum power (P$_m$), as well as the two characteristic parameters, the short circuit current density J$_{sc}$ and the open circuit voltage V$_{oc}$ are marked in yellow. (Copyright from Tianyan Han.[85])*

The power conversion efficiency (PCE or η) is defined as the ratio between the maximum output power P_m and the incident light power P_{in}.

$$\eta\ (\%) = \frac{P_m}{P_{in}} \quad (2.4)$$

The parameters that influence the efficiency of organic solar cells during their operation are V_{oc}, J_{sc} and the fill factor (*FF)*.

a.) Influence of V_{oc}

V_{oc} represents the maximum voltage that a solar cell can provide to an external circuit (**Figure 2.13**). Numerous studies have demonstrated that the theoretical maximum value of V_{oc} is determined by the effective energy gap (E_g) between the HOMO of the donor and the LUMO of the acceptor of the BHJ.[86] The experimental values of V_{oc} are however always lower, due to various loss mechanisms:

$$e\ V_{oc} = E_g - E_{loss} \quad (2.5)$$

where E_{loss} is an empirical factor of losses in solar cells and e is the elementary charge.

Notably, Scharber et al.[87] found that the empirical E_{loss} in BHJ solar cell is generally around 0.3eV. Equation 2.5 is important for predicting V_{oc}, but, since losses are specific to each OPV system, research about E_{loss} is still ongoing[86].

b.) Influence of J_{sc}

J_{sc} represents the current density obtained by solar cells under short circuit condition (V=0V) (**Figure 2.13**). According to the organic solar cell working principle, J_{sc} is determined by the:

(1). number of photons absorbed in active layers;

(2). exciton diffusion efficiency (fraction of excitons reaching the D/A interface);

(3). exciton dissociation efficiency at the D/A interface;

(4). charge carriers transport towards the electrodes;

(5). charge carriers extraction efficiency.

Hence, J_{sc} depends strongly on the absorption spectrum and morphology of the active layers, the latter being critical to charge transport and exciton dissociation efficiency.

c.) Influence of FF

FF is a measure of how efficiently photo-generated charge carriers can be extracted under the maximum power point P_m operating conditions. It is defined as the ratio between the maximum power point ($P_m = V_m \cdot J_m$ -see **Figure 2.13**) and the product of the open circuit voltage and the short circuit current:

$$FF = \frac{V_m \cdot J_m}{V_{oc} \cdot J_{sc}} \quad (2.6)$$

According to equation 2.4 and 2.6, power conversion efficiency η can be expressed as:

$$\eta = \frac{V_{oc} \cdot J_{sc} \cdot FF}{P_{in}} \quad (2.7)$$

The parameters that impact the V_{oc}, J_{sc}, FF and therefore the PCE are: high absorption, long exciton diffusion length, efficient exciton dissociation, charge carriers mobilities, charge recombination rates and charge carrier extraction efficiency.

Development of organic photovoltaic cells

Along with the development of OSC materials and optimization of processing OPV devices, the efficiency records of OPV have reached up to 18.2% so far[88] (**Figure 2.14**). OPV devices have huge potential to become popular for solar energy harvesting due to

its continuous efficiency improvements. But there are still some key issues that need to be solved, such as long-term stability or the feasibility of large area printing [79, 89, 90], etc. In this thesis, the investigated OSCs aim to the fabrication of OPV devices. The experimental details and results will be presented in the chapter 7.
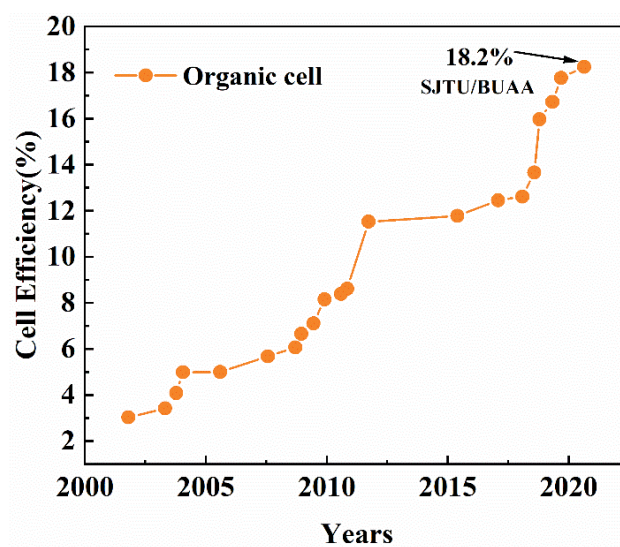

Figure 2.14 Record efficiencies of organic solar cells based on organic molecular materials from 2000 to 2020. Data copyright: National Renewable Energy Laboratory Research Cell Efficiency Records (https://www.nrel.gov/pv/cell-efficiency.html).

References:

[1]   H. Shirakawa, E. J. Louis, A. G. MacDiarmid, C. K. Chiang and A. J. Heeger, *Journal of the Chemical Society, Chemical Communications*, 1977, 578-580.

[2]   F.-C. Chen, in *Encyclopedia of Modern Optics (Second Edition)*, eds. B. D. Guenther and D. G. Steel, Elsevier, Oxford, 2018, pp. 220-231.

[3]   W. Brütting, in *Physics of Organic Semiconductors*, 2005, pp. 1-14.

[4]   G. Horowitz, *Advanced Materials*, 1990, **2**, 287-292.

[5]   S. Allard, M. Forster, B. Souharce, H. Thiem and U. Scherf, *Angewandte Chemie International Edition*, 2008, **47**, 4070-4098.

[6]   J. D. Myers and J. Xue, *Polymer Reviews*, 2012, **52**, 1-37.

[7]   A. Salehi, X. Fu, D.-H. Shin and F. So, *Advanced Functional Materials*, 2019, **29**, 1808803.

[8]   Y. Yamashita, *Science and Technology of Advanced Materials*, 2009, **10**, 024313.

[9]   J. Thiele, *Justus Liebigs Annalen der Chemie*, 1899, **306**, 87-142.

[10]   M.-L. Theye and V. Paret, *Carbon*, 2002, **40**, 1153-1166.

[11]   R. B. Campbell, J. M. Robertson and J. Trotter, *Acta Crystallographica*, 1961, **14**, 705-711.

[12]   S. Tokito, H. Tanaka, K. Noda, A. Okada and Y. Taga, *Applied Physics Letters*, 1997, **70**, 1929-1931.

[13]   F. Wudl, *Journal of Materials Chemistry*, 2002, **12**, 1959-1963.

[14]   A. B. P. Lever, M. R. Hempstead, C. C. Leznoff, W. Liu, M. Melnik, W. A. Nevin and P. Seymour, *Pure and Applied Chemistry*, 1986, **58**, 1467-1476.

[15]   A. G. Macedo, L. P. Christopholi, A. E. X. Gavim, J. F. de Deus, M. A. M. Teridi, A. R. b. M. Yusoff and W. J. da Silva, *Journal of Materials Science: Materials in Electronics*, 2019, **30**, 15803-15824.

[16]   J. K. Stille and Y. Gilliams, *Macromolecules*, 1971, **4**, 515-517.

[17]   A. F. Diaz, J. I. Castillo, J. A. Logan and W.-Y. Lee, *Journal of Electroanalytical Chemistry and Interfacial Electrochemistry*, 1981, **129**, 115-132.

[18]   R. J. Waltman, J. Bargon and A. F. Diaz, *The Journal of Physical Chemistry*, 1983, **87**, 1459-1463.

[19]   A. Mishra and P. Bäuerle, *Angewandte Chemie International Edition*, 2012, **51**, 2020-2067.

[20]   S. Griggs, A. Marks, H. Bristow and I. McCulloch, *Journal of Materials Chemistry C*, 2021.

[21]   A. Petritz, M. Krammer, E. Sauter, M. Gärtner, G. Nascimbeni, B. Schrode, A. Fian, H. Gold, A. Cojocaru and E. Karner-Petritz, *Advanced functional materials*, 2018, **28**, 1804462.

[22]   S. Z. Bisri, C. Piliego, J. Gao and M. A. Loi, *Advanced Materials*, 2014, **26**, 1176-1199.

[23]   V. Coropceanu, J. Cornil, D. A. da Silva Filho, Y. Olivier, R. Silbey and J.-L.

Brédas, *Chemical Reviews*, 2007, **107**, 926-952.

[24]   C. Liu, K. Huang, W.-T. Park, M. Li, T. Yang, X. Liu, L. Liang, T. Minari and Y.-Y. Noh, *Materials Horizons*, 2017, **4**, 608-618.

[25]   O. Marinov, M. Deen, J. A. Jiménez-Tejada and C. Chen, *Physics Reports*, 2020, **844**, 1-105.

[26]   N. Lu, L. Li, D. Geng and M. Liu, *Organic Electronics*, 2018, **61**, 223-234.

[27]   T. Sakanoue and H. Sirringhaus, *Nature Materials*, 2010, **9**, 736-740.

[28]   J. S. Lee, M. V. Kovalenko, J. Huang, D. S. Chung and D. V. Talapin, *Nat Nanotechnol*, 2011, **6**, 348-352.

[29]   S. D. Baranovskii, H. Cordes, F. Hensel and G. Leising, *Physical Review B*, 2000, **62**, 7934-7938.

[30]   R. A. Marcus, *Journal of Electroanalytical Chemistry*, 1997, **438**, 251-259.

[31]   A. Nawaz, A. Kumar and I. A. Hümmelgen, *Organic Electronics*, 2017, **51**, 94-102.

[32]   M. Brinkmann and P. Rannou, *Advanced Functional Materials*, 2007, **17**, 101-108.

[33]   S. Chandrasekhar and G. S. Ranganath, *Reports on Progress in Physics*, 1990, **53**, 57-84.

[34]   C. L. Radford, A. D. Hendsbee, M. Abdelsamie, N. M. Randell, Y. Li, M. F. Toney and T. L. Kelly, *ACS Applied Energy Materials*, 2018, **1**, 6513-6523.

[35]   R. Agrawal, P. Kumar, S. Ghosh and A. K. Mahapatro, *Applied Physics Letters*, 2008, **93**, 073311.

[36]   I. H. Campbell, D. L. Smith, C. J. Neef and J. P. Ferraris, *Applied Physics Letters*, 1999, **74**, 2809-2811.

[37]   J. M. Szarko, B. S. Rolczynski, S. J. Lou, T. Xu, J. Strzalka, T. J. Marks, L. Yu and L. X. Chen, *Advanced Functional Materials*, 2014, **24**, 10-26.

[38]   S. Reineke and M. A. Baldo, *physica status solidi (a)*, 2012, **209**, 2341-2353.

[39]   D. Frackowiak, *Journal of Photochemistry and Photobiology B: Biology*, 1988,

2, 399.

[40] S. M. Menke and R. J. Holmes, *Energy Environ. Sci.*, 2014, **7**, 499-512.

[41] O. V. Mikhnenko, P. W. M. Blom and T.-Q. Nguyen, *Energy & Environmental Science*, 2015, **8**, 1867-1888.

[42] C. Karunakaran and M. Balamurugan, in *Spin Resonance Spectroscopy*, ed. C. Karunakaran, Elsevier, 2018, pp. 169-228.

[43] R. C. Powell, *Journal of Luminescence*, 1975, **11**, 1-45.

[44] Z. Xu and B. Hu, *Advanced Functional Materials*, 2008, **18**, 2611-2617.

[45] P. E. Shaw, A. Ruseckas and I. D. W. Samuel, *Advanced Materials*, 2008, **20**, 3516-3520.

[46] T. Zhang, D. B. Dement, V. E. Ferry and R. J. Holmes, *Nature Communications*, 2019, **10**, 1156.

[47] S. Faure, C. Stern, R. Guilard and P. D. Harvey, *Journal of the American Chemical Society*, 2004, **126**, 1253-1261.

[48] M. T. Sajjad, A. Ruseckas and I. D. W. Samuel, *Matter*, 2020, **3**, 341-354.

[49] R. R. Lunt, J. B. Benziger and S. R. Forrest, *Advanced Materials*, 2010, **22**, 1233-1236.

[50] Y. Kawamura, J. Brooks, J. J. Brown, H. Sasabe and C. Adachi, *Physical review letters*, 2006, **96**, 017404.

[51] S. S. Skourtis, C. Liu, P. Antoniou, A. M. Virshup and D. N. Beratan, *Proceedings of the National Academy of Sciences*, 2016, **113**, 8115-8120.

[52] A. Buckley, *Organic light-emitting diodes (OLEDs): materials, devices and applications*, Elsevier, 2013.

[53] T.-T. Bui, F. Goubard, M. Ibrahim-Ouali, D. Gigmes and F. Dumur, *Beilstein journal of organic chemistry*, 2018, **14**, 282-308.

[54] G. Horowitz, *Advanced materials*, 1998, **10**, 365-377.

[55] C. a. Di, F. Zhang and D. Zhu, *Advanced Materials*, 2013, **25**, 313-330.

[56] A. W. Hains, Z. Liang, M. A. Woodhouse and B. A. Gregg, *Chemical reviews*,

2010, **110**, 6689-6735.

[57]   E. L. Ratcliff, B. Zacher and N. R. Armstrong, *The Journal of Physical Chemistry Letters*, 2011, **2**, 1337-1350.

[58]   C. W. Tang and S. A. VanSlyke, *Applied physics letters*, 1987, **51**, 913-915.

[59]   B. Geffroy, P. le Roy and C. Prat, *Polymer International*, 2006, **55**, 572-582.

[60]   G. Hong, X. Gan, C. Leonhardt, Z. Zhang, J. Seibert, J. M. Busch and S. Bräse, *Advanced Materials*, 2021, **33**, 2005630.

[61]   D. J. Gaspar and E. Polikarpov, *OLED fundamentals: materials, devices, and processing of organic light-emitting diodes*, CRC press, 2015.

[62]   T.-L. Wu, M.-J. Huang, C.-C. Lin, P.-Y. Huang, T.-Y. Chou, R.-W. Chen-Cheng, H.-W. Lin, R.-S. Liu and C.-H. Cheng, *Nature Photonics*, 2018, **12**, 235-240.

[63]   H. Koezuka, A. Tsumura and T. Ando, *Synthetic Metals*, 1987, **18**, 699-704.

[64]   A. Turner, I. Karube and G. S. Wilson, *Biosensors: fundamentals and applications*, Oxford university press, 1987.

[65]   D. Yang and D. Ma, *Advanced Optical Materials*, 2019, **7**, 1800522.

[66]   S. H. Ko, H. Pan, D. Lee, C. P. Grigoropoulos and H. K. Park, *Japanese Journal of Applied Physics*, 2010, **49**, 05EC03.

[67]   S. Liu, W. M. Wang, A. L. Briseno, S. C. B. Mannsfeld and Z. Bao, *Advanced Materials*, 2009, **21**, 1217-1232.

[68]   A. A. Virkar, S. Mannsfeld, Z. Bao and N. Stingelin, *Advanced Materials*, 2010, **22**, 3857-3875.

[69]   W. H. Lee, J. H. Cho and K. Cho, *Journal of Materials Chemistry*, 2010, **20**, 2549-2561.

[70]   M. Shao, S. Das, K. Xiao, J. Chen, J. K. Keum, I. N. Ivanov, G. Gu, W. Durant, D. Li and D. B. Geohegan, *Journal of Materials Chemistry C*, 2013, **1**, 4384-4390.

[71]   C. Luo, A. K. K. Kyaw, L. A. Perez, S. Patel, M. Wang, B. Grimm, G. C. Bazan, E. J. Kramer and A. J. Heeger, *Nano Letters*, 2014, **14**, 2764-2771.

[72]   Z. Zhao, Z. Yin, H. Chen, L. Zheng, C. Zhu, L. Zhang, S. Tan, H. Wang, Y. Guo, Q. Tang and Y. Liu, *Advanced Materials*, 2017, **29**, 1602410.

[73]   J. Lee, A. R. Han, H. Yu, T. J. Shin, C. Yang and J. H. Oh, *Journal of the American Chemical Society*, 2013, **135**, 9540-9547.

[74]   H. Yoo, H. H. Choi, T. J. Shin, T. Rim, K. Cho, S. Jung and J.-J. Kim, *Advanced Functional Materials*, 2015, **25**, 3658-3665.

[75]   B. Lim, H. Sun, J. Lee and Y.-Y. Noh, *Scientific reports*, 2017, **7**, 1-8.

[76]   S. Vegiraju, A. A. Amelenan Torimtubun, P.-S. Lin, H.-C. Tsai, W.-C. Lien, C.-S. Chen, G.-Y. He, C.-Y. Lin, D. Zheng, Y.-F. Huang, Y.-C. Wu, S.-L. Yau, G.-H. Lee, S.-H. Tung, C.-L. Wang, C.-L. Liu, M.-C. Chen and A. Facchetti, *ACS Applied Materials & Interfaces*, 2020, **12**, 25081-25091.

[77]   A. Anjali, R. Dheepika, P. M. Imran, N. S. P. Bhuvanesh and S. Nagarajan, *ACS Applied Electronic Materials*, 2020, **2**, 2651-2661.

[78]   Z. Hu, J. Wang, X. Ma, J. Gao, C. Xu, K. Yang, Z. Wang, J. Zhang and F. Zhang, *Nano Energy*, 2020, 105376.

[79]   O. A. Abdulrazzaq, V. Saini, S. Bourdo, E. Dervishi and A. S. Biris, *Particulate science and technology*, 2013, **31**, 427-442.

[80]   W. C. Choy, *Organic solar cells: Materials and device physics*, Springer, 2012.

[81]   P. Cheng and X. Zhan, *Chemical Society Reviews*, 2016, **45**, 2544-2582.

[82]   S. M. Menke, W. A. Luhman and R. J. Holmes, *nature materials*, 2013, **12**, 152-157.

[83]   W. A. Hammed, R. Yahya, A. Bola, #039, u. Lukman and H. N. M. E. Mahmud, *Energies*, 2013, **6**, 5847-5868.

[84]   Y. Zhang, K. Liu, J. Huang, X. Xia, J. Cao, G. Zhao, P. W. K. Fong, Y. Zhu, F. Yan, Y. Yang, X. Lu and G. Li, *Nature Communications*, 2021, **12**, 4815.

[85]   T. Han, Université de Strasbourg, 2017.

[86]   N. K. Elumalai and A. Uddin, *Energy & Environmental Science*, 2016, **9**, 391-410.

[87]   M. C. Scharber, D. Mühlbacher, M. Koppe, P. Denk, C. Waldauf, A. J. Heeger and C. J. Brabec, *Advanced Materials*, 2006, **18**, 789-794.

[88]   L. Wang, C. Guo, X. Zhang, S. Cheng, D. Li, J. Cai, C. Chen, Y. Fu, J. Zhou and H. Qin, *Chemistry of Materials*, 2021, **33**, 8854-8862.

[89]   S. Ganesan, S. Mehta and D. Gupta, *Opto-Electronics Review*, 2019, **27**, 298-320.

[90]   H. Cao, W. He, Y. Mao, X. Lin, K. Ishikawa, J. H. Dickerson and W. P. Hess, *Journal of Power Sources*, 2014, **264**, 168-183.

Chapter 3
State-of-the-art

Charge transport; Exciton dynamics

The development of solution-processed BHJ organic solar cells based on small molecules (or molecular-based organic solar cells) allowed to reach a PCE exceeding 17%[1]. This progress has been achieved mainly by modifying the chemical structure of the molecules and by optimizing the OPV devices. Moreover, as described in chapter 2, the performances of BHJ organic solar cells rely on both the exciton ability to reach the D/A interface and efficiently dissociate into free charge carriers, and on efficient charge transport. In this chapter, state-of-the-art of charge transport properties (section 3.1) and exciton dynamics (section 3.2) of small-molecules will be presented.

3.1 Charge transport

Charge transport properties are known to significantly influence the performance of organic optoelectronic devices. Much efforts have therefore been done to better understand the relationships between molecular chemical structure and charge transport properties to develop materials with high charge carrier mobilities[2-4]. Strong intermolecular coupling and high stacking order are necessary to achieve efficient charge carrier transport. Therefore, planar conjugated molecules are expected to achieve high charge carrier mobilities along π-stacking directions due to their strong intermolecular coupling. However, coupling in the direction perpendicular to π-stacking is often weaker and responsible for anisotropic transport [5, 6]. For highly planar molecular semiconductors materials, the solubility is also important, as it relates to the solution-processability of organic photovoltaic devices. In this section, state-of-the-art of soluble planar molecular semiconductors that promote highly ordered molecular packing will be presented.

3.1.1 Planar molecules

Planar units (i.e., perylene, triphenylene) are expected to increase intermolecular coupling and allow a better molecular self-assembling leading to improved charge

carrier mobilities along π-stacking directions[7-9]. For example, in 1994 Adam, D.[10] synthesized a highly planar disk-like (or discotic) molecule 2,3,6,7,10,11-hexakis (hexylthio) triphenylene (HHTT) (**Figure 3.1**). HHTT was found to form an ordered columnar phase with intermolecular stacking distance of 3.63 Å exhibiting a time-of-flight (TOF) hole mobility of 0.1 cm^2 V^{-1}s^{-1}, a record value for molecular semiconductors at that time. This encouraging result gave rise to wide scientific and technological interests in discotic-planar molecules as potential candidates for optoelectronic materials. Several discotic-planar molecules have been investigated more recently,[11] such as perylene and triphenylene derivatives.
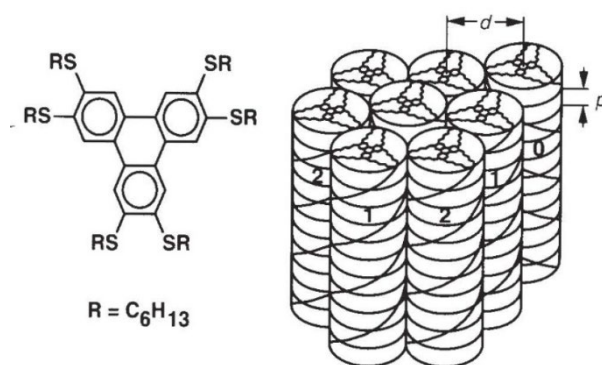

Figure 3.1 *Molecular 2,3,6,7,10,11-hexakis(hexylthio)triphenylene (HHTT) and structure of the corresponding columnar phase.(Copyright from Adam, D. [10])*

In order to enhance the charge transport property along the molecular packing direction, the intermolecular distance should be as short as possible[12]. The intermolecular distances for typical discotic-columnar mesogens range from 3.5 to 4.5 Å.[13] R.I. Gearba et al.[14] demonstrated that discotic hexaazatriphenylene derivatives (HAT-CONHR) (**Figure 3.2**), which form hydrogen bonds resulting in a smaller intermolecular distance of 3.18 Å, exhibited a higher charge carrier mobility (0.08 cm^2 V^{-1}s^{-1}) (measured by microwave conductivity (PR-TRMC)) than without hydrogen bonds (0.02 cm^2 V^{-1}s^{-1}).
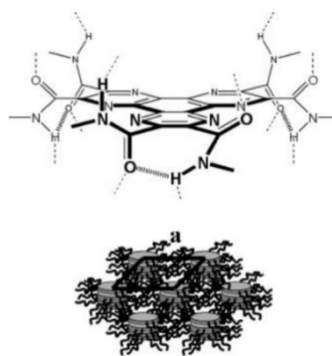
Figure 3.2 *Structure of HAT-CONHR molecule and model for the supramolecular disk assembly in the ordered hexagonal columnar phase.(Copyright from R.I. Gearba et al.* [14]*)*

Synthesizing planar molecules with high charge carrier mobility and good solubility in common solvents at the same time is challenging[15-17]. To achieve high solubility of molecular semiconductors, one strategy consists to introduce aliphatic side-chains along the molecular backbone. Functionalization with alkyl side-chains does indeed ensure good processability in solution, but may also introduce detrimental insulating regions and impact molecular stacking order[18-22]. As a consequence, the length and volume of the alkyl side-chains are important factors, that need to be optimized. As shown in **Figure 3.3a**, Asmita Shah et al.[23] have studied TOF hole mobility as a function of the length of alkyl chains attached to the discotic triphenylene core (HAT$_n$, *n* present the number of carbon). The HAT$_4$ compound exhibited higher mobility compared to the HAT$_5$, HAT$_6$ and HAT$_8$, attributed to a better packing order. The average hole mobilities for the HAT$_5$, HAT$_6$ and HAT$_8$ in the hexagonal columnar phase (**Figure 3.3b**) were found to be 2.27×10^{-3} cm^{2}V^{-1}s^{-1}, 4.86×10^{-4} cm^{2}V^{-1}s^{-1} and 1.7×10^{-4} cm^{2}V^{-1}s^{-1}, respectively. Whereas, for the HAT$_4$, the hole mobilities was found to be 1.216×10^{-2} cm^{2}V^{-1}s^{-1} and 0.6×10^{-2} cm^{2}V^{-1}s^{-1} in the columnar plastic and crystalline intermediate phases, respectively. The molecular ordering decreases with increasing the length of the alkyl chain attached to the discotic triphenylene core and leads to a lower hole mobility.
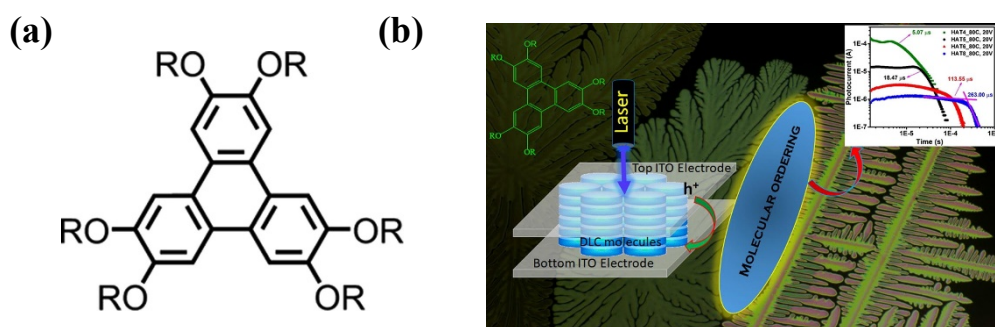
(a)   **(b)**

Figure 3.3 *(a) Chemical structure of hexaalkoxytriphenylene (HAT$_n$) discotic liquid crystal with R = C$_n$H$_{2n+1}$. (b) Columnar phase of HATn.(Copyright from Asmita Shah et al.* [23]*)*

3.1.2 D-A-D conjugated molecule

Thanks to their promising charge transport properties, molecular semiconductors are widely used in OPV devices. However, the optical energy gap of conventional OSCs are normally greater than 2 eV, which is larger than the optimum value determined by Shockly-Queisser (1.1-1.5 eV)[24]. Many efforts have therefore been devoted to design and synthesize new conjugated system with narrower energy gaps. The most common strategy is to design molecules composed of alternating electron-rich or donor ("D") moieties and electron-deficient or acceptor ("A") moieties along the conjugated backbone. Alternating D and A units is a well-known strategy used as well for the synthesis of low band-gap polymers to tune the frontier orbital energy levels (HOMO or LUMO). As illustrated in **Figure 3.4**, the HOMO level of a D-A segment is close to the HOMO of the donor unit, while the LUMO level is close to the acceptor LUMO[25].

Most reported low band-gap molecules do have either a A-D-A or a D-A-D structure[26, 27]. An additional advantage of these structures is that the end-groups can be used to promote the molecular self-assembly. Indeed, introducing planar units as D or A moieties to the backbone could be an efficient approach to improve the molecular self-assembly and correspondingly the charge transport properties.
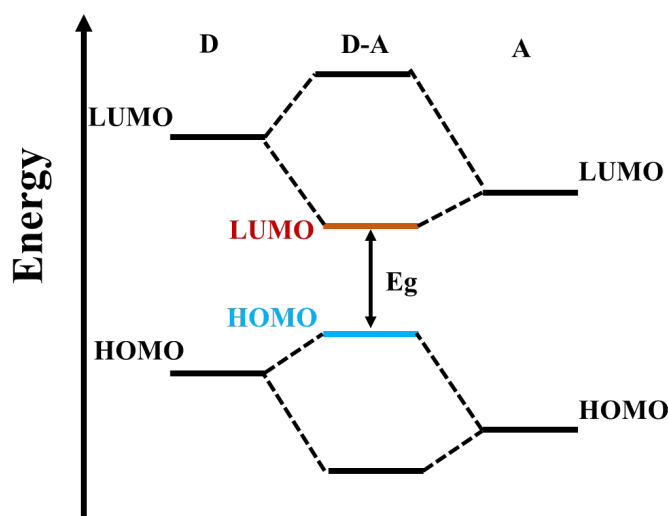
Figure 3.4*: Illustration of the hybridization of energy levels of a conjugated molecule alternating donor (D) and acceptor (A) units.*

O. P. Lee et al. have studied the influence of planar end units in conjugated D-A-D type molecules[28]. Here, different electron-rich units were attached onto an electron-withdrawing core diketopyrrolopyrrole (DPP). The functionalized DPP moiety allowed to control the molecular solution-processability and solid-states ordering by modulating the alkyl substituents. These electron-rich end-groups have different degrees of planarity (**Figure 3.5a**): **Molecule 1** possessed non-planar triphenylamine (TPA) end-groups, **Molecule 2** has a planar fused-ring benzo[1,2-b;4,5-b']dithiophene (BDT) unit but with no-coplanar alkoxy substituents, and **Molecules 3 and 4** have a highly planar pyrene end-groups, with different grafting positions. For each molecule, the hole mobilities in pure films and in blends with $PC_{71}BM$ (different weight ratios) have been investigated by Space-charge-limited current (SCLC) (**Figure 3.5b**). The results showed that **Molecule 4** with highly planar end-groups leads to the highest SCLC mobility of up to 2.5×10^{-3} $cm^2V^{-1}s^{-1}$. This result was attributed to the tighter interplanar distance (3.50 Å), promoted by the highly planar end-groups.
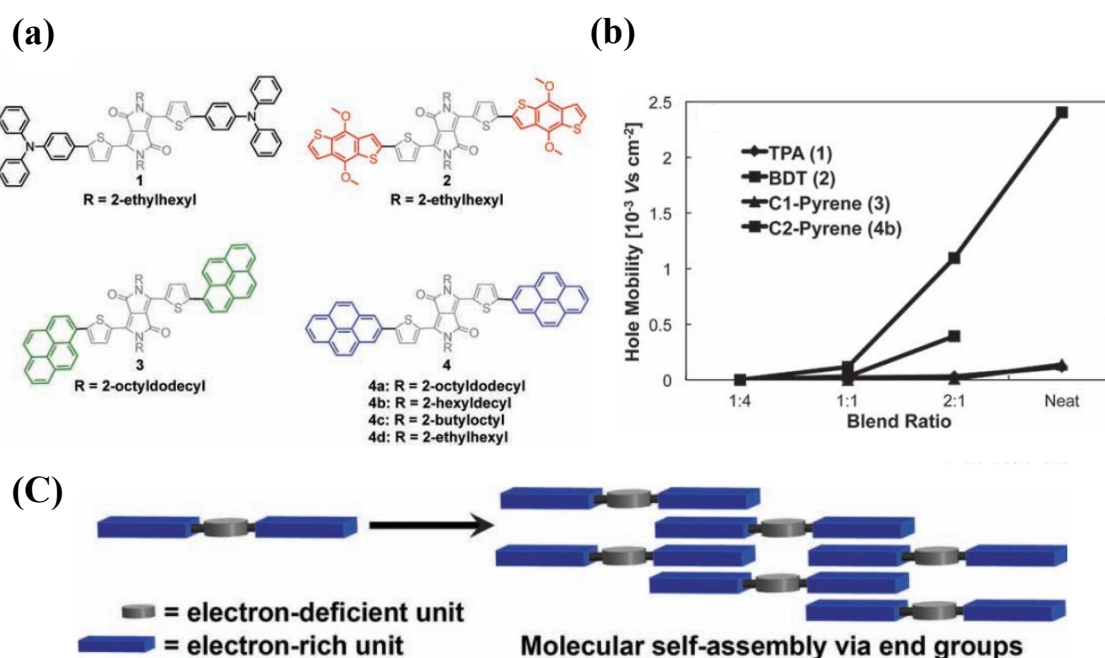
(a)

(b)

(C)

Figure 3.5 *(a) Chemical structures of molecules with DPP core moiety flanked by different electron-rich end-groups. (b) Effects of different blend ratios (small molecule: PC71BM) on SCLC hole mobility. (c) Illustration of molecular self-assembly through end-to-end π-π stacking. (Copyright from O. P. Lee, et al.[28])*

Similar to Asmita Shah et al.,[23] Yao Yang et al. [29] investigated impact of different side-chains on the molecular self-assembly and the corresponding charge transport properties in a different family of D-A-D conjugated molecules. Yao Yang et al. synthesized highly conjugated fluorene-bridged planar triphenylene (TP) functionalized with alkyl chains (**Figure 3.6a**). The length of the alkyl chains on the central fluorene unit was changed in order to modulate the molecular self-assembling. Charge carrier mobilities were measured by TOF. FTP-866 displays a hole mobility in the crystalline state of a maximum 4×10^{-3} $cm^2V^{-1}s^{-1}$ that the authors attributed to the molecular organization depicted in **Figure 3.6b**. The FTP-888 molecule, which has the same alkyl chains on the central fluorene unit as FTP-866 but a higher aliphatic volume fraction, displays a lower hole mobility (around 10^{-4} $cm^2V^{-1}s^{-1}$). The results highlight the fact that charge carrier mobility is not only governed by the chemical structure of the conjugated backbone, but also by the molecular solid-states.
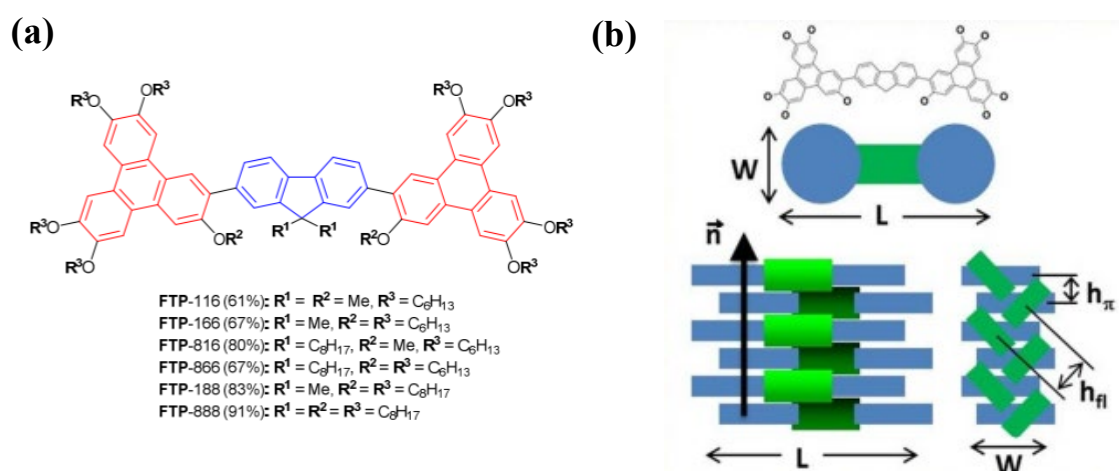
Figure 3.6 *(a) Chemical structure of fluorene-bridged triphenylene triads. Me: methyl. (b) Self-organization models of triad molecules in the various columnar phases. Frame: schematic representation of the mesogenic core of FTP-nom triads, composed of two triphenylene rings (TP, blue discs) connected by 9,9-dialkylfluorene cores (green rectangles).(Copyright from Yao Yang et al. [29])*

3.1.3 Triazatruxene

Triazatruxene (TAT) is a conjugated chemical unit that is highly planar and can be easily functionalized by solubilizing substituents. It is therefore of particular interest to organic electronics. TAT was first reported in 1980,[30, 31] and is considered as an extended π-system, in which three carbazole units (**Figure 3.7a**) share one aromatic ring (blue area in **Figure 3.7b**). Moreover, the high chemical stability and hole-transporting nature of carbazole-based oligomers, make TAT an attractive candidate for hole charge transporting materials in organic optoelectronic devices.
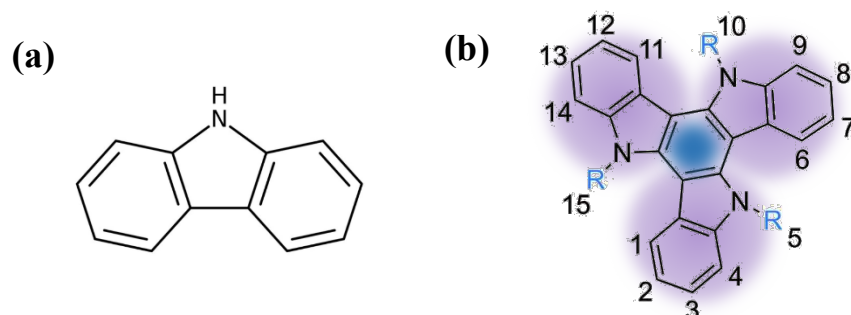

Figure 3.7 *(a) Chemical structure of carbazole. (b) Chemical structure of the triazatruxene (TAT).*

As mentioned previously, the alkyl side-chains of semiconducting molecules control their solubility and impact the stacking order. M. Talarico et al.[32] have investigated the effect of side-chains on the self-assembly of TAT derivatives and the corresponding charge transport properties. Three soluble TAT derivatives with different substituents on the N atoms were considered derivatives (compounds 1-3 in **Figure 3.8)**. The results showed that compounds 1, 2, and 3 in the liquid crystalline states lead to a SCLC hole mobility value of $0.01 cm^2V^{-1}s^{-1}$, $0.1 cm^2V^{-1}s^{-1}$, and $0.05 cm^2V^{-1}s^{-1}$, respectively. The compound with the shortest N-substituent (2) gave the highest mobility. This result was attributed to the lower degree of planarity of the central core for compounds 1 and 3, resulting in larger average intermolecular stacking distance. The more efficient intermolecular π-orbital overlap for compound 2 (expected by the authors) was considered to be responsible for the higher charge carrier mobility (although no quantitative information about the π-stacking distances was provided in Ref. [32])
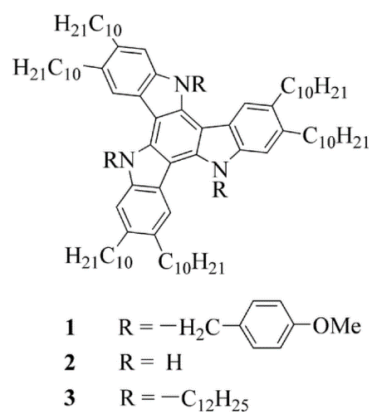
Figure 3.8 *Chemical structure of compounds 1-3.(Copyright from M. Talarico et al.* [32]*)*

Similarly to the work of M. Talarico et al., F. Gallego-Gómez et al.[33] synthesized and studied a TAT derivative (TAT$_{C8}$ in **Figure 3.9**), whose three amine groups (position 5, 10 and 15) carry $C_8 H_{17}$ linear alkyl chains to provide a good solubility. They observed the formation of ordered columnar nanostructures in solution-processed cast

films, with a face-to-face π-stacking distance as low as 3.27 Å. While this is a promising feature for charge transport, no mobility data was provided in Ref. [33].
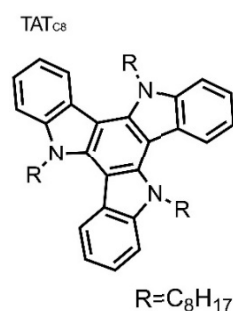
Figure 3.9 *Chemical structure of TAT$_{C8}$. (Copyright from F. Gallego-Gómez et al.[33])*

In a second article, E. M. García-Frutos et al.[34] report the study of three new TAT derivatives. As shown in **Figure 3.10**, each TAT derivative possessed the same alkyl side-chains (C$_{12}$H$_{25}$) on the amine groups, but differed in their substitution group at positions 2, 3, 7, 8, 12 and 13 (**Figure 3.7b**). The latter were expected to influence the molecular packing and π-stacking distances. The results revealed that the SCLC hole mobility of compound **4** can reach up to 0.02 cm^{2}V^{-1}s^{-1} in the columnar hexagonal mesophase, whereas the mobility of compound **5** is around 6×10^{-4} cm^{2}V^{-1}s^{-1}. The highest SCLC mobility (1.4 cm^{2}V^{-1}s^{-1}) was however observed for compound **6**, and could be associated to the smaller stacking distance of compound **6** (3.4 Å) in comparison to compound **5** (4.4 Å) and **4** (3.9 Å). The above results demonstrate that the molecular self-assembly and stacking distances highly depend on the nature (volume, lengths, …) of the alkyl side-chains, which correspondingly have a significant impact on the charge transport property.
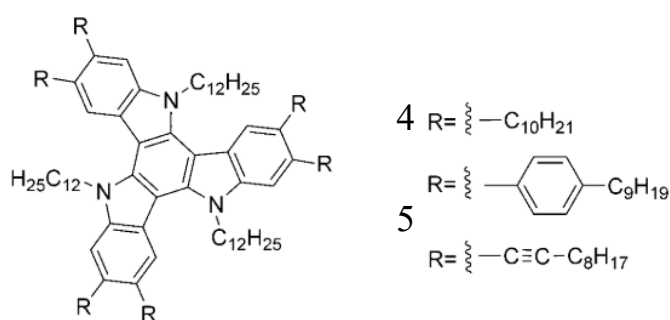
Figure 3.10 Chemical structures of compounds 4-6.(Copyright from E. M. García-Frutos et al. [34])

Expanding the π-system of TAT unit has been another way followed by some groups to improve the molecular self-assembly and charge transport. Qun Ye et al.[35] presented two large core-expanded TAT-based discotic molecules with different side-chains (**Figure 3.11**). The π-stacking distance of 3.76 Å and 3.75 Å were observed for derivative **TAT-1** and **TAT-2**, respectively. Charge transport properties have been measured by SCLC in the liquid crystalline state and the mobilities obtained for **TAT-1** and **TAT-2** are 0.14 cm^2 v^{-1}s^{-1} and 0.69 cm^2 v^{-1}s^{-1}, respectively. According to the views of Qun Ye et al., the higher mobility of TAT-2 is due to the stronger intermolecular interaction in comparison to TAT-1, even if the π-stacking distances were similar.

Figure 3.11 Molecular structure of TAT-1 and TAT-2.(Copyright from Qun Ye et al. [35])

The conjugated TAT derivatives **TAT-1** or **TAT-2**[35] are star-shaped. Our research consortium (including the teams of N. Leclerc at ICPEES, S. Mery at IPCMS and ICube), followed a strategy that combines both approaches of Yao Yang et al.[29] (D-A-D structure with planar D units) and Baomin Zhao et al.,[36] by designing D-A-D molecules based on TAT as end-groups (rather than perylene). For example, as shown in **Figure 3.12**, a series of "dumbbell-shaped" molecules, with benzo[2,1,3]-thiadiazole (Btz), pyridal[2,1,3]-thiadiazole (Pytz), or thieno[1,2,5]-thiadiazole (Ttz) as electron-withdrawing cores, respectively, and TAT as end-groups were investigated. Indeed, by varying the electron-attracting central moiety, the optoelectronic properties could be tuned[37-40].
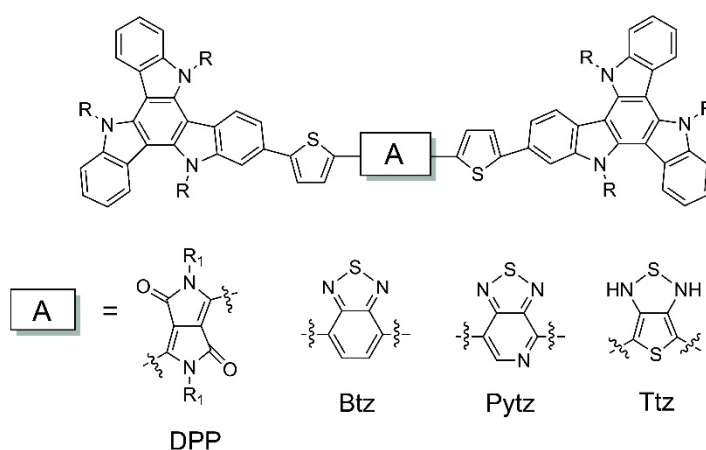
Figure 3.12 *Chemical structures of TAT-based dumbbell-shaped molecules with different central cores[37-40].*

The most recent one example of such "dumbbell-shaped" molecules is **TPD-TAT**, as shown in **Figure 3.13**. The TAT units are attached onto a central chromophore thiophene-thienopyrroledione-bithiophene (TPD) (electron acceptor). Different side-chains are attached on both TPD and TAT units to tune their solubility and thermal properties. Both, good planarity and solubility were achieved at the same time. T. Han et al.[41] showed that the charge transport properties of TPD-TAT derivative thin-films are impacted, as expected, by the nature (linear or branched) of the alkyl side-chains.

The in-plane (by OFET) and out-of-plane (by SCLC) charge carrier mobilities, measured in as-deposited thin films, are summarized in the **Table 3.1**. The highest OFET (2.8×10^{-4} cm^{2}V^{-1}s^{-1}) and SCLC (2.3×10^{-3} cm^{2}V^{-1}s^{-1}) charge carrier mobilities were found for linear side-chains on both units (TPD$_{C8}$-TAT$_{C8}$). These observations are in-line with X-ray scattering and differential scanning calorimetry results, which showed that the derivatives with linear chains on the TAT exhibit crystalline and liquid-crystalline phases, while branched chains on the TAT lead to amorphous materials. In addition, for the derivatives with linear side-chains on TAT, linear chains on TPD led to more pronounced structural order (as indicated by narrower scattering lines and a higher transition temperature).

TPD$_{C8}$-TAT$_{C8}$: R = C$_8$; R$_1$ = C$_8$
TPD$_{EH}$-TAT$_{C8}$: R = C$_8$; R$_1$ = EH
TPD$_{C8}$-TAT$_{EH}$: R = EH ; R$_1$ = C$_8$
TPD$_{EH}$-TAT$_{EH}$: R = EH ; R$_1$ = EH

EH =
C$_8$ =
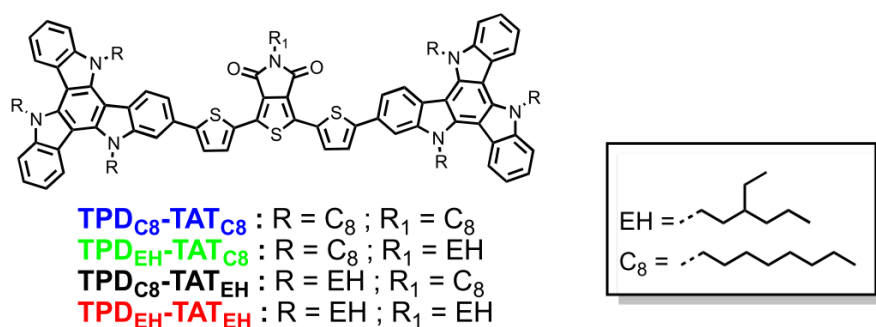
***Figure 3.13** Chemical structure of dumbbell-shaped molecules TPD-TAT. (Copyright from T. Han et al. [41])*

***Table 3.1** Hole mobilities values determined from OFETs and SCLC measurements. (Copyright from T. Han et al. [41])*

Molecule	OFET μ_h (cm^{2}v^{-1}s^{-1})	SCLC μ_h (cm^{2}v^{-1}s^{-1})
TPD$_{C8}$-TAT$_{C8}$	$(2.8 \pm 0.8) \times 10^{-4}$	$(2.3 \pm 0.8) \times 10^{-3}$
TPD$_{EH}$-TAT$_{C8}$	$(4.9 \pm 1.8) \times 10^{-5}$	$(1.8 \pm 0.7) \times 10^{-3}$
TPD$_{C8}$-TAT$_{EH}$	$(2.6 \pm 0.1) \times 10^{-5}$	$(4.7 \pm 2.9) \times 10^{-5}$
TPD$_{EH}$-TAT$_{EH}$	$(4.5 \pm 0.4) \times 10^{-5}$	$(3.8 \pm 0.9) \times 10^{-5}$

To sum up, charge carrier transport in OSCs is highly dependent on the chemical structure of the molecules. The molecular shape, the position or nature of side-chains,

and the planarity of the units do all have a strong impact on the stacking order of OSCs and on the related charge hopping process. As described above, perylene, TP, and TAT derivatives are all discotic-planar molecule. For TAT derivatives, the carbazole-based oligomers have a high chemical stability, a hole-transporting nature, and are easy to functionalize, making them particularly attractive for hole transporting materials. At the same time, the molecular shapes are directing the molecular assembly. Compared to star-shaped molecules, dumbbell-shaped molecules have two planar end-groups that promote end-to-end π-stacking and may therefore lead to unusual molecular assemblies. On the basis of this, the hole transporting dumbbell-shaped molecular TPD-TAT derivatives occurs as a highly interesting system and has therefore been chosen to be the main topic of my thesis.

In addition, as described in chapter 2, charge carrier transport is often anisotropic in ordered OSCs, as it is for instance the case for discotic planar molecules. In such cases, the high mobility axis is along the π-stacking direction, which needs to be controlled in view of their application in devices. However, studies on charge transport anisotropy in the discotic materials are still rare. Most researchers carried out SCLC and TOF measurements to investigate out-of-plane mobility. In comparison, Tian Han et al,[41] studied charge carrier transport by SCLC and OFET, allowing some insight into both out-of-plane and in-plane mobilities. To verify whether the measured charge transport is along the π-stacking direction, structural analysis by X-ray scattering is needed. In this thesis, we combined GIWAXS (for molecular stacking structure, see chapter 4), SCLC and OFET (for mobilities, see chapter 6) to provide a comprehensive understanding of charge transport anisotropy in the investigated molecular system.

3.2 Exciton dynamics

A longer exciton diffusion is necessary for achieving high-performance OPV devices. Yost et al.[42] showed that exciton diffusion length has a theoretical upper limit (i.e.,

exciton lifetime, energy transfer efficiency), which in the case of singlet excitons is roughly around 100-200 nm, but can reach 10 μm in the case of triplet excitons. Yet, most OPV devices rely on singlet excitons, with diffusion lengths estimated to be less than 10 nm. There have been multiple efforts to understand what factors limit the singlet exciton diffusion length and to figure out ways to enhance it, improving the performances of OPV devices. The common strategies to enhance exciton diffusion include optimizing the Förster energy transfer and controlling the degree of crystallinity in the solid-states[43-45]. In this section, state-of-the-art of singlet exciton diffusion in molecular semiconductors will be presented.

As previously described in chapter 2, exciton diffusion can be modeled as an intermolecular energy transfer. During this process, radiative and non-radiative recombination are competing. Non-radiative recombination increases heat losses and is hindering exciton diffusion[46-48]. Thus, one of the methods to improve exciton diffusion length is reducing the non-radiative decay rate k_{nr}. This route was followed by S. M. Menke et al.[49] who diluted subphthalocyanine (SubPc) into a high band gap matrix 1,4-phenylenebis(triphenylsilane) (UGH2) in order to separate SubPc molecules and reduce k_{nr}. By applying thickness-dependent photoluminescence (PL) quenching experiment, the results demonstrated that the exciton diffusion length increases from L_D=10.7 nm to L_D=15.3 nm when the concentration of SubPc decreases from 100 wt% to 25 wt% in SubPc: UGH2 blends. Intermolecular interactions between SubPc molecules are suppressed in such blends resulting in reduction of self-quenching. However, decreasing further the concentration of SubPc (< 25 wt%) increases the separation between SubPc molecules and lowers the energy transfer efficiency, and thus shorter the exciton diffusion length (**Figure 3.14**).
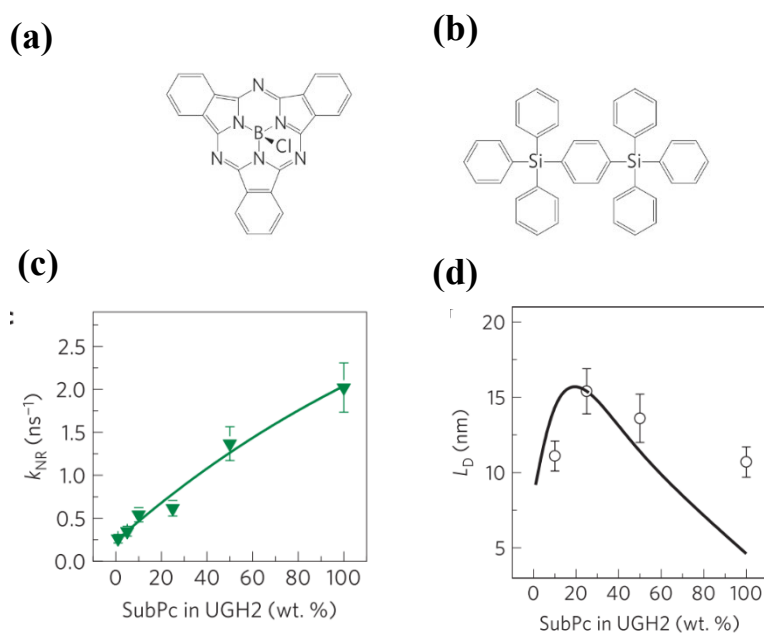
(a)

(b)

(c)

(d)

Figure 3.14 *Molecular structures of (a) SubPc, (b) UGH2. (c) Dependence of non-radiative decay rate of a subphthalocyanine (SubPc) in blends with high bandgap matrix UGH2. (d) Calculated (black line) and experimentally measured (open symbols) L_D as a function of composition. (Copyright from S. M. Menke et al.[49])*

Many examples have shown that molecular thin-films with higher stacking order exhibited longer singlet diffusion lengths[44, 50, 51]. Thermal annealing and solvent vapor annealing (SVA) are conventional ways to improve the degree of order or crystallinity in molecular solid-states[52, 53]. Yun Long et al.[54] reported that molecular packing order of DTS(FBTTh$_2$)$_2$ (**Figure 3.15**) is improved through thermal annealing, leading to an increase of the exciton lifetime from 0.36 ns to 0.52 ns and of the diffusion length L_D from 15 nm to 27 nm. They estimated L_D by exciton-exciton annihilation experiments, which is also one of the methods used in this thesis (details will be presented in chapter 5).
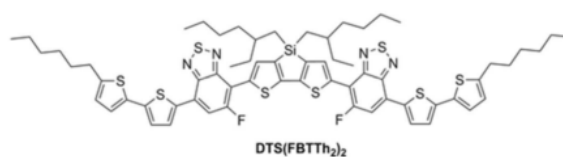

DTS(FBTTh$_2$)$_2$

Figure 3.15 *Chemical structure of the molecule DTS(FBTTh$_2$)$_2$. (Copyright from Yun Long et al.[54])*

Yiwei Zhang et al.[55] demonstrated that the exciton diffusion length in DR3TBDTT (**Figure 3.16**) thin-films is increased from L_D=16 nm to L_D=24 nm (measured by thickness-dependent PL quenching) by SVA and correlates with the average crystal size (**Figure 3.16b and c**). Moreover, they observed that the exciton lifetime (0.84 ns and 0.85 ns, with or without SVA) is not significantly affected by the size of crystals, indicating that exciton diffusion is limited by intra-grain structural order rather than by grain boundaries. On the opposite, the PL decay observed in DR3TBDTT:PC71BM blends by Muhammad T. Sajjad et al.[56] showed that exciton lifetime significantly increased from 0.04 ns to 0.15 ns with increasing crystal size of DR3TBDTT by SVA. They attributed this result to the diffusion-limited PL quenching at the D/A interface. However, the authors did not measure the exciton diffusion length in the blends.
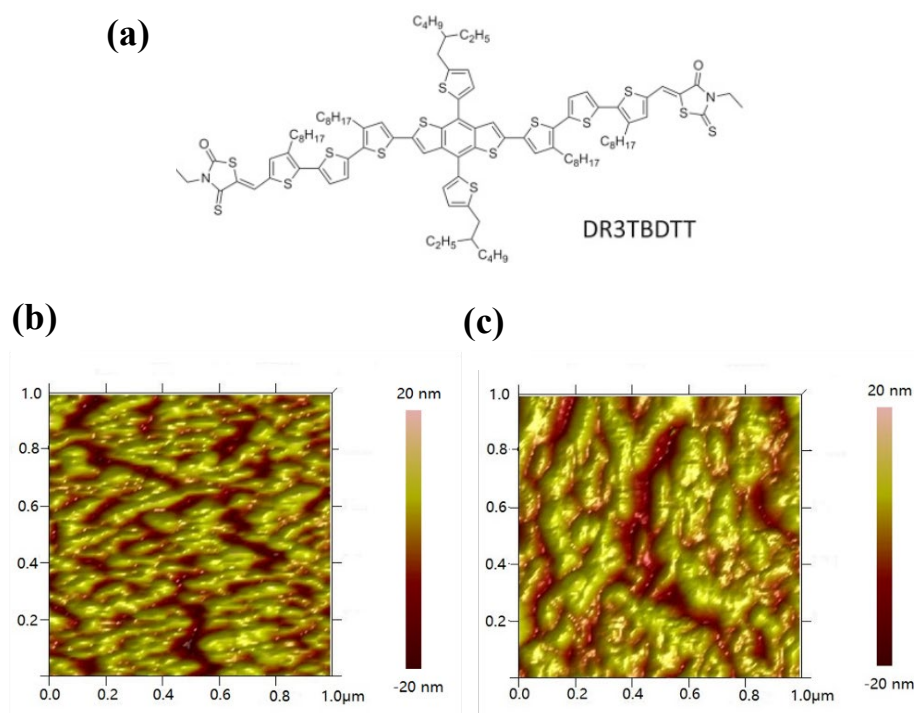

Figure 3.16 (a) Chemical structure of the molecule DR3TBDTT. AFM images of DR3TBDTT films (c) before and (d) after SVA. (Copyright from Muhammad T. Sajjad et al.[56])

Stacking ordered of thin films is not only dependent on the thermal treatment but also highly dependent on the chemical structure of the molecules. Muhammad T. Sajjad et al.[56] investigated DR3TBDTT and SMPV1 molecules with different length of alkyl side-chains (**Figure 3.17**). In this case, the exciton diffusion length was measured by using exciton-exciton annihilation. In the as-deposited state, thin-films of DR3TBDTT have a significantly longer diffusion length (L_D=25 nm) compared to SMPV1 (L_D=7 nm), presumably due to the higher crystallinity of DR3TBDTT. After SVA with different solvents (**Figure 3.17c**), the diffusion length increases with decreasing boiling point: from L_D=25 nm to L_D=45 nm for DR3TBDTT, and from L_D=7 nm to L_D=14 nm for SMPV1, presumably because of the higher vapor pressure and thus more efficient SVA.
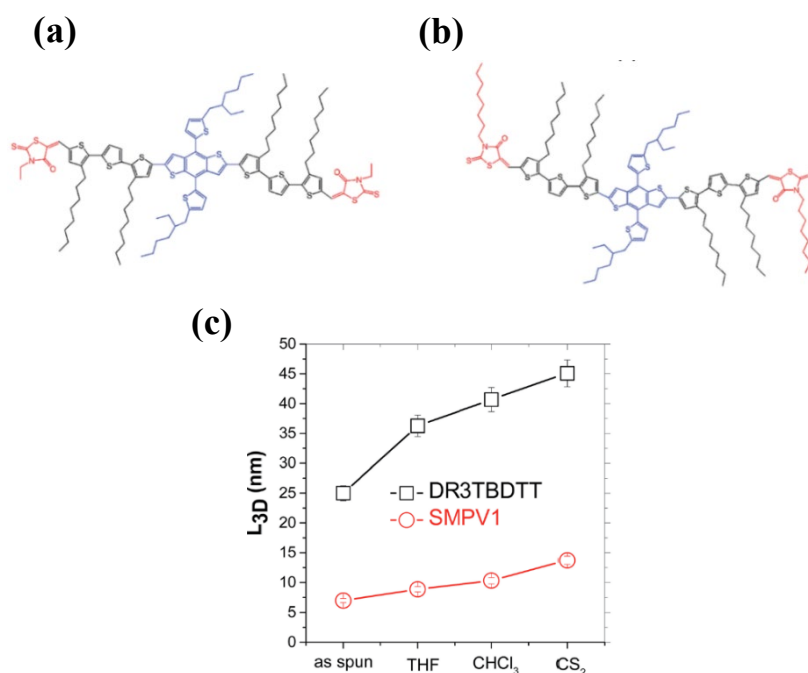
Figure 3.17 *Molecular structures of (a) DR3TBDTT and (b) SMPV1. (c) Exciton diffusion length for different solvents. (Copyright from Muhammad T. Sajjad et al. [56])*

Similarly, J. D. A. Lin et al. [57] investigated exciton diffusion in phenyl substituted diketopyrrolopyrrole (DPP) derivatives with different conjugation lengths and side-chains. As shown in **Figure 3.18a**, the conjugation length is increased by two thiophene units from compound A to B. Comparing compound B to C, the linear alkyl side-chains

on the lactam nitrogen unit is replaced by the ethyl-hexyl groups. These modifications in chemical structures have been shown to induce different molecular packing order and different crystallinity (A > B > C) (**Figure 3.18b**). The authors use six experimental methods to estimate the exciton diffusion length. More details about these methods are shown in reference [57]. Here, only the exciton diffusion length determined from the technique based on the FRET theory coupled with quantum yield (also used in this thesis) measurements is presented. The details of this technique will be presented in chapter 5.

The exciton diffusion lengths for compounds A, B, and C were found to be L_D=13.8 nm, L_D=8.5 nm and L_D=5.8 nm, respectively. The results show that decreasing conjugation length or increasing molecular order by adopting linear side-chains correlate well with an enhancement of exciton diffusion length. It is interesting to note that an increase in the conjugation length is unfavorable for the exciton diffusion but favorable for the charge carrier transport, a compromise is therefore to be found.
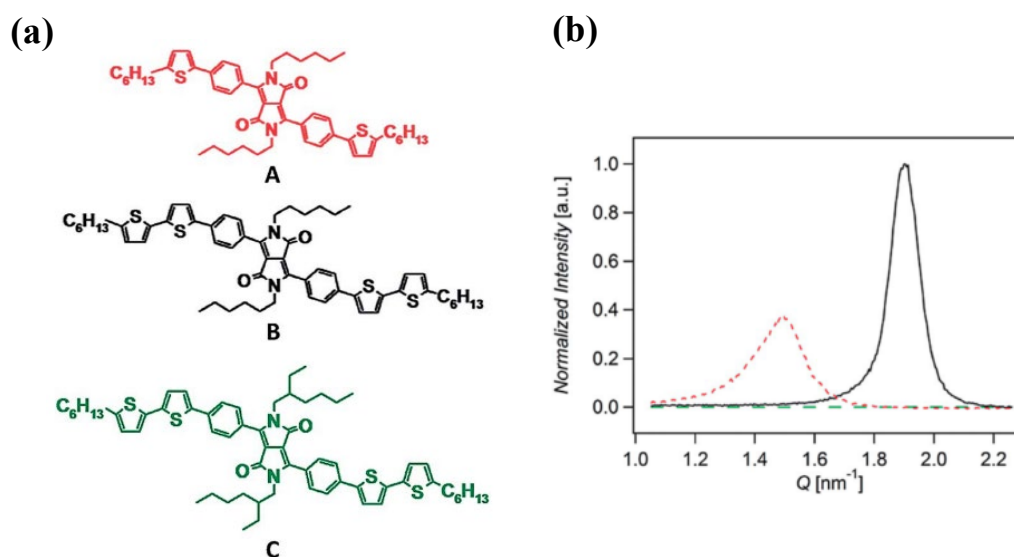

Figure 3.18 *(a) Chemical structures for compounds A, B, and C. (b) X-ray diffraction for films of A (solid black line), B (dotted red line), and C (dashed green line). Scattering intensity was normalized by film thickness, structure factor, multiplicity, unit cell volume, and the Lorenz-polarization. (Copyright from J. D. A. Lin et al.* [57]*)*

To sum up, exciton dynamics are an important factor that relate to the optoelectronic properties of molecular OSCs. The exciton diffusion length can be improved by using different routes, such as decreasing the non-radiative recombination or improving the molecular stacking. Post-deposition treatments by thermal annealing or solvent vapor annealing were also shown to capable to influence the molecular self-assembly and exciton diffusion. Finally, optimizing the chemical structure or end-groups of molecules to enhance structural order is another way to engineer the exciton diffusion length.

At the same time, the techniques to measure the exciton diffusion length turns out to be crucial. Indeed, different methods are often yielding different values for the same thin-film, as different diffusion models and related assumptions on physical parameters can induce errors in the calculation. Therefore, it is necessary to use a combination of methods to most accurately evaluate the exciton diffusion length and its correlation with the molecular structure and processing. In this thesis, two different approaches will be applied to evaluate the relationship between exciton dynamics and molecular self-assembly structure, which will be presented in chapter 5.

3.3 Thesis in context

Charge transport properties and exciton dynamics are known to critically influence the organic optoelectronic materials performance, which are highly dependent on the molecular chemical structure and solid-states. The previous investigations by Tianyan Han of the in-plane and out-of-plane mobilities in planar dumbbell-shaped TPD-TAT derivatives suggest that this molecular system is highly promising for hole-transporting materials in OPV applications. However, several issues need still to be clarified for these derivatives. For example, what is the solid-state structure or π-stacking orientation of TPD-TAT derivatives in the different solid-states (as-deposited, liquid crystalline,

crystalline)? How does the stacking order affect the anisotropy of charge transport? What is the relationship between exciton dynamics, molecular chemical structure, and self-assembly structure?

This thesis will focus on these issues. Firstly, the TPD-TAT derivatives and their molecular self-assembling properties will be presented in chapter 4. Secondly, exciton studies in TPD-TAT derivatives with different side-chains, which allow a better understanding of the effect of structural order on exciton dynamics, will be presented in chapter 5. Thirdly, the charge transport properties of these derivatives in different molecular solid-states will be described in chapter 6. Finally, chapter 7 presents the optoelectronic properties of molecular/polymer PNDIT2 blends as a possible bulk heterojunction for OPV devices.

References:

[1]   J. Qin, Z. Chen, P. Bi, Y. Yang, J. Zhang, Z. Huang, Z. Wei, C. An, H. Yao, X. Hao, T. Zhang, Y. Cui, L. Hong, C. Liu, Y. Zu, C. He and J. Hou, *Energy & Environmental Science*, 2021, **14**, 5903-5910.

[2]   V. Lemaur, D. A. da Silva Filho, V. Coropceanu, M. Lehmann, Y. Geerts, J. Piris, M. G. Debije, A. M. Van De Craats, K. Senthilkumar and L. D. A. Siebbeles, *Journal of the American Chemical Society*, 2004, **126**, 3271-3279.

[3]   S. Rudd, J. F. Franco-Gonzalez, S. Kumar Singh, Z. Ullah Khan, X. Crispin, J. W. Andreasen, I. Zozoulenko and D. Evans, *Journal of Polymer Science Part B: Polymer Physics*, 2018, **56**, 97-104.

[4]   M. C. R. Delgado, K. R. Pigg, D. A. da Silva Filho, N. E. Gruhn, Y. Sakamoto, T. Suzuki, R. M. Osuna, J. Casado, V. Hernández and J. T. L. Navarrete, *Journal of the American Chemical Society*, 2009, **131**, 1502-1512.

[5]   C. Janiak, *Journal of the Chemical Society, Dalton Transactions*, 2000, 3885-3896.

[6]   W. Hao, Y. Wang, H. Zhao, J. Zhu and S. Li, *Physical Chemistry Chemical Physics*, 2020, **22**, 13802-13807.

[7]   H. Zhang, Y. Liu, Y. Sun, M. Li, B. Kan, X. Ke, Q. Zhang, X. Wan and Y. Chen, *Chemical Communications*, 2017, **53**, 451-454.

[8]   K. Lim, M. J. Ju, J. Na, H. Choi, M. Y. Song, B. Kim, K. Song, J. S. Yu, E. Kim and J. Ko, *Chemistry–A European Journal*, 2013, **19**, 9442-9446.

[9]   X.-Y. Li, W.-J. Shi, X.-Q. Wang, L.-N. Ma, L. Hou and Y.-Y. Wang, *Crystal Growth & Design*, 2017, **17**, 4217-4224.

[10]   D. Adam, P. Schuhmacher, J. Simmerer, L. Häussling, K. Siemensmeyer, K. H. Etzbachi, H. Ringsdorf and D. Haarer, *Nature*, 1994, **371**, 141-143.

[11]   G. Kestemont, V. d. Halleux, M. Lehmann, D. A. Ivanov, M. Watson and Y. Henri Geerts, *Chemical Communications*, 2001, 2074-2075.

[12]   C.-y. Liu and A. J. Bard, *Nature*, 2002, **418**, 162-164.

[13]   K. Pieterse, A. Lauritsen, A. P. Schenning, J. A. Vekemans and E. W. Meijer, *Chemistry*, 2003, **9**, 5597-5604.

[14]   R. I. Gearba, M. Lehmann, J. Levin, D. A. Ivanov, M. H. J. Koch, J. Barberá, M. G. Debije, J. Piris and Y. H. Geerts, *Advanced Materials*, 2003, **15**, 1614-1618.

[15]   S. Allard, M. Forster, B. Souharce, H. Thiem and U. Scherf, *Angewandte Chemie International Edition*, 2008, **47**, 4070-4098.

[16]   T. Lee, C. E. Song, S. K. Lee, W. S. Shin and E. Lim, *ACS omega*, 2021, **6**, 4562-4573.

[17]   D. D. Günbaş, C. Xue, S. Patwardhan, M. C. Fravventura, H. Zhang, W. F. Jager, E. J. Sudhölter, L. D. Siebbeles, T. J. Savenije and S. Jin, *Chemical Communications*, 2014, **50**, 4955-4958.

[18]   P. M. Borsenberger, L. Pautmeier and H. Bässler, *The Journal of Chemical Physics*, 1991, **94**, 5447-5454.

[19]   V. Coropceanu, J. Cornil, D. A. da Silva Filho, Y. Olivier, R. Silbey and J.-L.

Brédas, *Chemical Reviews*, 2007, **107**, 926-952.

[20] I. I. Fishchuk, A. Kadashchuk, X. Li and J. Genoe, New York, NY, 2013.

[21] P. W. M. Blom, *Molecular and Polymer Semiconductors, Transport Properties of*, Elsevier, Oxford, 2001.

[22] B. Tu, Y. Wang, W. Chen, B. Liu, X. Feng, Y. Zhu, K. Yang, Z. Zhang, Y. Shi, X. Guo, H.-F. Li, Z. Tang, A. B. Djurišić and Z. He, *ACS Applied Materials & Interfaces*, 2019, **11**, 48556-48563.

[23] A. Shah, D. P. Singh, B. Duponchel, F. Krasisnski, A. Daoudi, S. Kumar and R. Douali, *Journal of Molecular Liquids*, 2021, **342**, 117353.

[24] M. C. Scharber and N. S. Sariciftci, *Progress in polymer science*, 2013, **38**, 1929-1940.

[25] Y. Wan, F. Ramirez, X. Zhang, T.-Q. Nguyen, G. C. Bazan and G. Lu, *npj Computational Materials*, 2021, **7**, 69.

[26] D. Gudeika, A. Miasojedovas, O. Bezvikonnyi, D. Volyniuk, A. Gruodis, S. Jursenas and J. V. Grazulevicius, *Dyes and Pigments*, 2019, **166**, 217-225.

[27] H. Y. Chung, J. Oh, J.-H. Park, I. Cho, W. S. Yoon, J. E. Kwon, D. Kim and S. Y. Park, *The Journal of Physical Chemistry C*, 2020, **124**, 18502-18512.

[28] O. P. Lee, A. T. Yiu, P. M. Beaujuge, C. H. Woo, T. W. Holcombe, J. E. Millstone, J. D. Douglas, M. S. Chen and J. M. J. Fréchet, *Advanced Materials*, 2011, **23**, 5359-5363.

[29] Y. Yang, H. Wang, H.-F. Wang, C.-X. Liu, K.-Q. Zhao, B.-Q. Wang, P. Hu, H. Monobe, B. Heinrich and B. Donnio, *Crystal Growth & Design*, 2018, **18**, 4296-4305.

[30] J. Bergman and N. Eklund, *Tetrahedron*, 1980, **36**, 1445-1450.

[31] J. Bergman and N. Eklund, *Tetrahedron*, 1980, **36**, 1439-1443.

[32] M. Talarico, R. Termine, E. M. García-Frutos, A. Omenat, J. L. Serrano, B. Gómez-Lor and A. Golemme, *Chemistry of Materials*, 2008, **20**, 6589-6591.

[33] F. Gallego-Gómez, E. M. García-Frutos, J. M. Villalvilla, J. A. Quintana, E.

Gutierrez-Puebla, A. Monge, M. A. Díaz-García and B. Gómez-Lor, *Advanced Functional Materials*, 2011, **21**, 738-745.

[34]   E. M. García-Frutos, U. K. Pandey, R. Termine, A. Omenat, J. Barberá, J. L. Serrano, A. Golemme and B. Gómez-Lor, *Angewandte Chemie International Edition*, 2011, **50**, 7399-7402.

[35]   Q. Ye, J. Chang, J. Shao and C. Chi, *Journal of Materials Chemistry*, 2012, **22**, 13180-13186.

[36]   B. Zhao, B. Liu, R. Q. Png, K. Zhang, K. A. Lim, J. Luo, J. Shao, P. K. H. Ho, C. Chi and J. Wu, *Chemistry of Materials*, 2010, **22**, 435-449.

[37]   T. Bura, N. Leclerc, S. Fall, P. Lévêque, T. Heiser, P. Retailleau, S. Rihn, A. Mirloup and R. Ziessel, *Journal of the American Chemical Society*, 2012, **134**, 17404-17407.

[38]   I. Bulut, P. Chávez, A. Mirloup, Q. Huaulmé, A. Hébraud, B. Heinrich, S. Fall, S. Méry, R. Ziessel, T. Heiser, P. Lévêque and N. Leclerc, *Journal of Materials Chemistry C*, 2016, **4**, 4296-4303.

[39]   T. Bura, N. Leclerc, S. Fall, P. Lévêque, T. Heiser and R. Ziessel, *Org Lett*, 2011, **13**, 6030-6033.

[40]   I. Bulut, P. Lévêque, B. Heinrich, T. Heiser, R. Bechara, N. Zimmermann, S. Méry, R. Ziessel and N. Leclerc, *Journal of Materials Chemistry A*, 2015, **3**, 6620-6628.

[41]   T. Han, I. Bulut, S. Méry, B. Heinrich, P. Lévêque, N. Leclerc and T. Heiser, *Journal of Materials Chemistry C*, 2017, **5**, 10794-10800.

[42]   S. R. Yost, E. Hontz, S. Yeganeh and T. Van Voorhis, *The Journal of Physical Chemistry C*, 2012, **116**, 17369-17377.

[43]   S. M. Menke, W. A. Luhman and R. J. Holmes, *Nature materials*, 2013, **12**, 152-157.

[44]   R. R. Lunt, N. C. Giebink, A. A. Belak, J. B. Benziger and S. R. Forrest, *Journal of Applied Physics*, 2009, **105**, 053711.

[45] X. Xie and H. Ma, *ChemistryOpen*, 2016, **5**, 201.

[46] S. Liu, J. Yuan, W. Deng, M. Luo, Y. Xie, Q. Liang, Y. Zou, Z. He, H. Wu and Y. Cao, *Nature Photonics*, 2020, **14**, 300-305.

[47] J. Benduhn, K. Tvingstedt, F. Piersimoni, S. Ullbrich, Y. Fan, M. Tropiano, K. A. McGarry, O. Zeika, M. K. Riede and C. J. Douglas, *Nature Energy*, 2017, **2**, 1-6.

[48] K. D. Rosenthal, M. P. Hughes, B. R. Luginbuhl, N. A. Ran, A. Karki, S. J. Ko, H. Hu, M. Wang, H. Ade and T. Q. Nguyen, *Advanced Energy Materials*, 2019, **9**, 1901077.

[49] S. M. Menke, W. A. Luhman and R. J. Holmes, *nature materials*, 2013, **12**, 152-157.

[50] L. D. Siebbeles, A. Huijser and T. J. Savenije, *Journal of Materials Chemistry*, 2009, **19**, 6067-6072.

[51] M. C. Fravventura, J. Hwang, J. W. Suijkerbuijk, P. Erk, L. D. Siebbeles and T. J. Savenije, *The journal of physical chemistry letters*, 2012, **3**, 2367-2373.

[52] X. Wang, Z. Du, K. Dou, H. Jiang, C. Gao, L. Han and R. Yang, *Advanced Energy Materials*, 2019, **9**, 1802530.

[53] S. Chen, Z. Li, Y. Qiao and Y. Song, *Journal of Materials Chemistry C*, 2021, **9**, 1126-1149.

[54] Y. Long, G. J. Hedley, A. Ruseckas, M. Chowdhury, T. Roland, L. A. Serrano, G. Cooke and I. D. W. Samuel, *ACS Applied Materials & Interfaces*, 2017, **9**, 14945-14952.

[55] Y. Zhang, M. T. Sajjad, O. Blaszczyk, A. Ruseckas, L. A. Serrano, G. Cooke and I. D. W. Samuel, *Organic Electronics*, 2019, **70**, 162-166.

[56] M. T. Sajjad, O. Blaszczyk, L. K. Jagadamma, T. J. Roland, M. Chowdhury, A. Ruseckas and I. D. W. Samuel, *Journal of Materials Chemistry A*, 2018, **6**, 9445-9450.

[57] J. D. A. Lin, O. V. Mikhnenko, J. Chen, Z. Masri, A. Ruseckas, A. Mikhailovsky,

R. P. Raab, J. Liu, P. W. M. Blom, M. A. Loi, C. J. García-Cervera, I. D. W. Samuel and T.-Q. Nguyen, *Materials Horizons*, 2014, **1**, 280-285.

Chapter 4
Materials: TPD-TAT derivatives

Chemical structure; Material properties

In this chapter, the material properties of TPD-TAT molecules as determined by differential scanning calorimetry (DSC), Polarized Optical Microscopy (POM) and X-ray diffraction will be presented. These measurements were done in collaboration with Benoit Heinrich at IPCMS and Dimitri Ivanov at IS2M. The chemical structure of investigated molecules will be presented in section 4.1. Section 4.2 is dedicated to the DSC measurements combined with POM that have been applied to study the thermal properties of the compounds. In section 4.3, Grazing Incidence Wide-Angle X-ray Scattering (GIWAXS) combined with Microfocus X-ray diffraction analyses, done to elucidate the microstructure of the bulk materials are presented. The experimental processes for the preparation of thin-films will be described in section 4.4. Please note that the results on molecular thermal properties, and structural properties are part of the article: "Efficient 3D charge transport in planar triazatruxene-based dumbbell-shaped molecules forming a bridged columnar phase, *J. Jing et al., J. Mater. Chem. A, 2021, 9.*"

4.1 Chemical structure

The investigated TPD-TAT molecules share the same conjugated "donor-acceptor-donor" backbone with a thienopyrroledione (or "TPD") unit as central core end-capped by two triazatruxene (or "TAT") units (**Figure 4.1**). The four investigated TPD-TAT molecules differ by the nature of the alkyl chains on TAT and TPD units, which are either linear or branched, as shown in **Figure 4.1**. The TAT unit has three amine groups able to carry alkyl chains. Also, TPD can be alkylated independently from the TAT unit. Thus, different side-chain combinations were explored, with either 2-ethylhexyl (EH) branched side chains, *n*-octyl (C_8) linear side chains or a combination of both 2-ethylhexyl and *n*-octyl side chains[1, 2]. For example, TPD_{EH}-TAT_{C8} corresponds to the derivative with a branched side-chain on the TPD unit and linear side-chains on both TAT units (**Figure 4.1**).
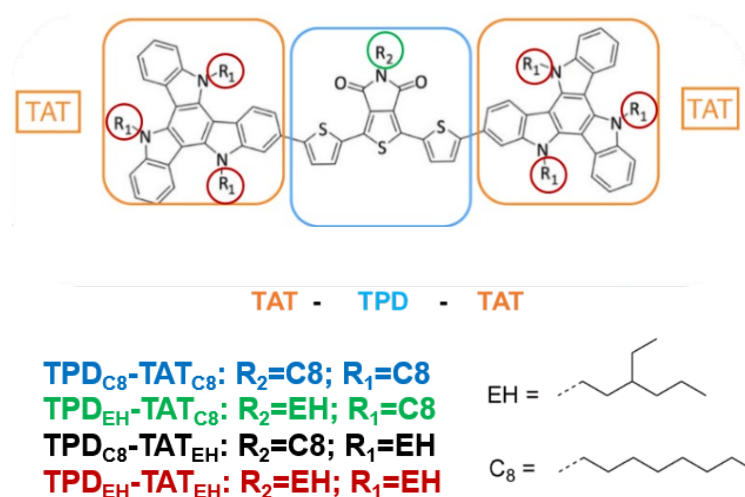
Figure 4.1 *Chemical structure of TPD-TAT derivatives. TPD-TAT derivatives were designed and synthesized by Dr. I. Bulut and Dr. Nicolas Leclerc from ICPEES.*

4.2 Thermal properties: Differential Scanning Calorimetry

Since the exciton dynamics and charge transport properties are highly dependent on structural order of the molecular thin-films [3-6], DSC associated to POM have been used to investigate the appropriate thermal treatments for TPD-TAT derivatives with different side-chains. As shown by DSC (**Figure 4.2a**), molecules with branched side-chains (EH) on the TAT units (TAT$_{EH}$) show only a glass transition (G) at 75-80°C and a melting into an isotropic liquid states (I_{so}) at 80 °C. When linear side-chains (C8) are grafted on the TAT (TAT$_{C8}$) units, significantly different thermal properties are observed. TDP-TAT$_{C8}$ derivatives undergo a glass transition at 80 °C, and a cold crystallization from the fluid nematic phase (N) into a crystalline state (C_r), and finally melting in isotropic liquid state at around 180 °C. The cold crystallization occurs at 145 °C and 120 °C for TPD$_{C8}$-TAT$_{C8}$ and TPD$_{EH}$-TAT$_{C8}$, respectively. Note that in the case of TPD-TAT molecules, the side-chains on the central chromophore TPD do not impact as much the thermal properties as do the side-chains on the TAT, pointing out that the molecular self-assembly is dominated by the planar TAT units[1].

Thanks to these DSC results, specific heating conditions in the range of the fluid nematic phase have been found to initiate a crystallization process of the bulk TPD_{C8}-TAT_{C8} material (details are shown in section 4.3). Accordingly, annealing as-deposited layers at 145 °C causes the molecules to crystallize in the form of micrometer-sized highly birefringent needle-like crystals (as shown in **Figures 4.2c and 4.2d**). The average size and density of crystalline needles depend on the spin-coated layer thickness and on the annealing process. In contrast, after 5 minutes annealing into the isotropic phase at 180 °C and rapid cooling to room temperature, smooth films in their nematic state are obtained (**Figure 4.2b**). Subsequent heating to 145 °C leads to an assembly of larger but fewer crystals (**Figure 4.2d**), compared to an annealing at 145 °C without going through the isotropic phase (**Figure 4.2c**). This indicates that annealing into the isotropic phase reduces the number of nucleation centers.

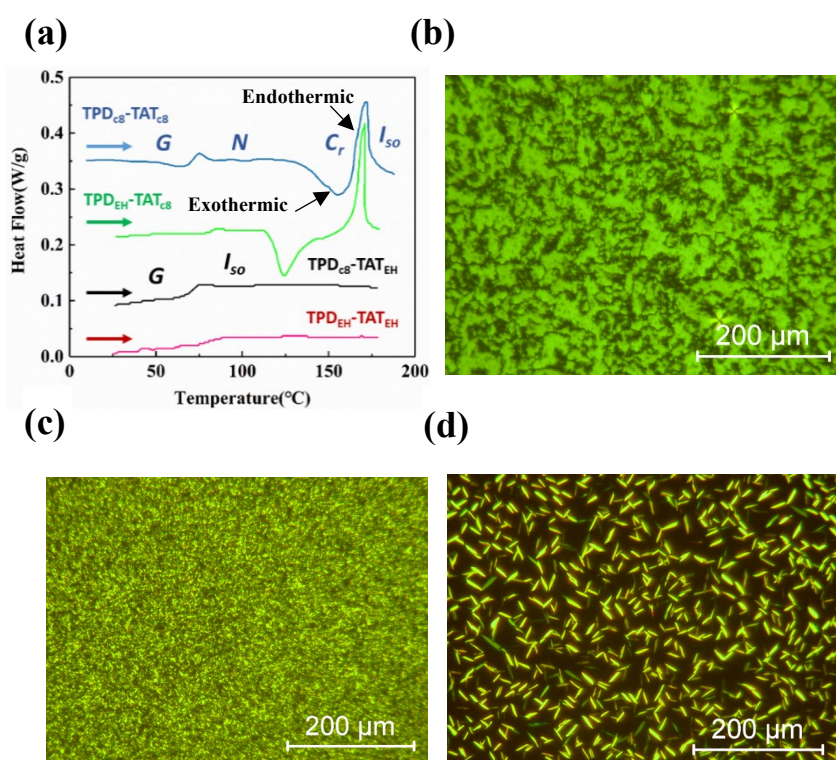***Figure 4.2*** *(a) DSC of TPD-TAT derivatives. First heating run from glass state (G) to isotropic liquid phase (Iso), through fluid nematic phase (N) and crystalline phase (Cr), obtained through cold crystallization and followed by melting. POM of a TPD$_{C8}$-TAT$_{C8}$ thin film: (b) nematic phase; (c) small crystals, the enlarged picture shows the smaller crystals clearly, as shown in Figure A4.1; (d) large crystals.*

Furthermore, different durations of the 180°C step induces different crystal sizes and densities, as shown in **Figure 4.2 a-e**. Finally, by measuring the average size of the longer crystal axis in each picture as a function of the annealing time at 145°C, we could estimate the crystal growth rate at 145°C to 25µm/h (slope of black dash line in **Figure 4.3f**).
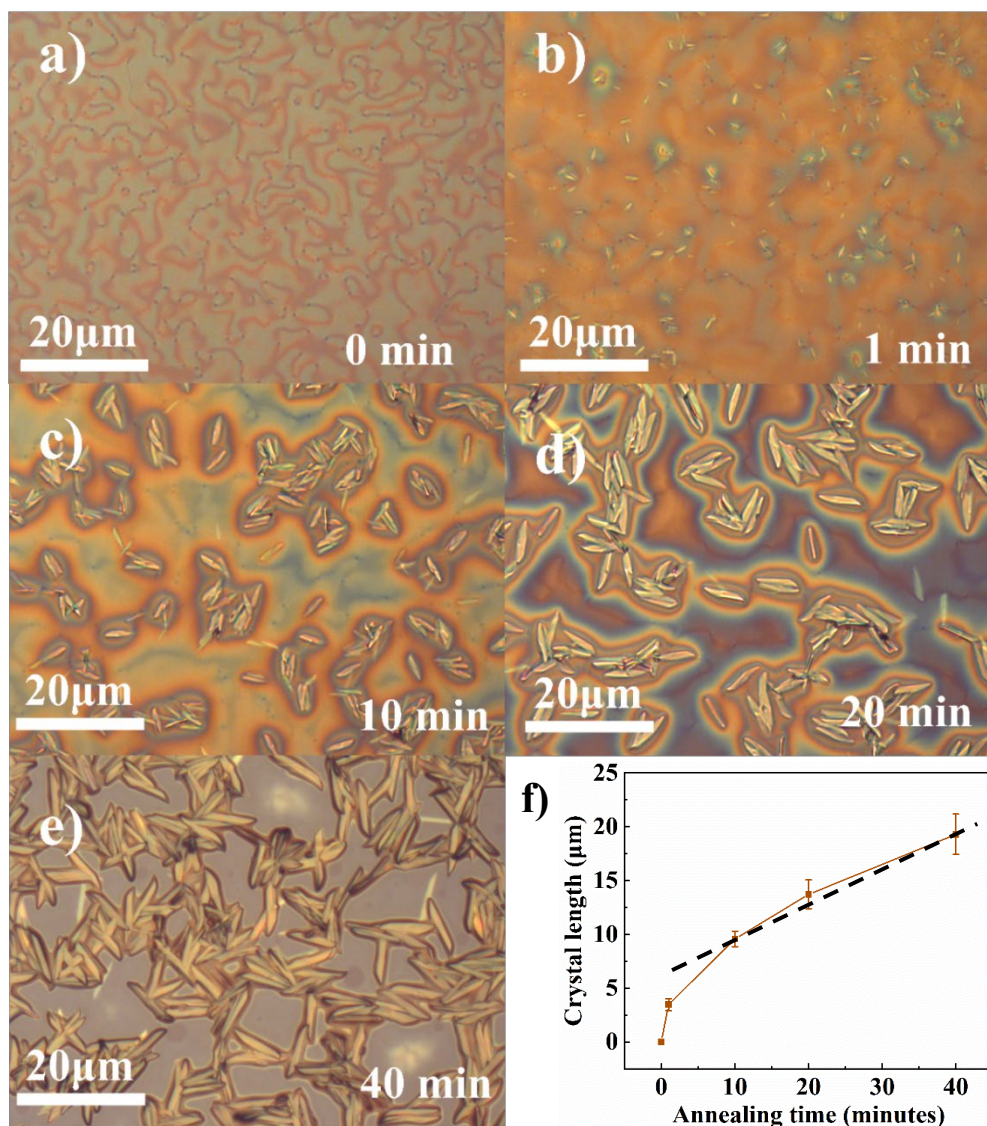

Figure 4.3 *Optical graphs of TPD$_{C8}$-TAT$_{C8}$ thin films that have undergone the 180°C annealing step, followed by rapid cooling and annealing at 145°C for various durations (a: no anneal, b: 1 min, c: 10 min, d: 20 min, e: 40 min). (f) Average size of the longer crystal axis as a function of annealing time.*

4.3 Structural properties

In this thesis, we will only focus on the molecular packing structure of the TPD_{C8}-TAT_{C8}, which was seen to adopt different solid-states (i.e., nematic, crystalline), depending on the thermal treatments. Here, GIWAXS and Microfocus X-ray diffraction results will be presented. Details of the corresponding experiments are described in the annex chapter A4.

4.3.1 Grazing Incidence Wide-Angle X-ray Scattering

The structure and morphology of TPD_{C8}-TAT_{C8} thin films, on either silicon or glass/ITO substrates, were investigated by GIWAXS. Details on thin-films deposition and thermal processing are given in section 4.4. For TPD_{C8}-TAT_{C8} thin-films, the GIWAXS pattern on as-deposited films displayed the characteristic broad scattering signals of the frozen nematic phase shown by bulk material (**Figure 4.4a**). Specifically, these signals originate from π-stacking distances within columns of TAT units (h_π = 3.8 Å), packing distances between molten alkyl chains (h_{ch} = 4.5 Å) and lateral spacing between columns (D_{col} = 18 Å). Correlation lengths calculated from peak widths using Scherrer equation[7] with shape factor K=0.9 are about 3 ~ 3.5 nm for h_π and 7 nm for D_{col}, representing 8 ~ 9 molecules in the piling direction and 4 columns in the lateral direction (**Figure 4.4b**). While h_{ch} and D_{col} formed continuous rings, h_π appeared as an arc centered on pattern equator, revealing that the direction of alignment of the columns (i.e., the nematic director) is parallel to the surface of the film and randomly switches between nematic domains while keeping its in-plane orientation. The close matching between D_{col} and the distance separating the center of both TAT units on a given molecule (22 Å) indicates that both TAT units are involved into two neighboring columnar stacks. This generates an original nematic self-assembly in which the columns of stacked TAT units spaced by molten chains are interconnected by TPD

bridges, as sketched in **Figure 4.4c**. Although, for clarity, this scheme exaggerates the regularity and persistence length of structural order, it emphasizes that each molecule is involved in two neighboring TAT-based columns, introducing potentially efficient hole conducting pathways through the insulating aliphatic periphery of the columns and giving rise to what might be termed a "*bridged columnar phase*"[8-10].
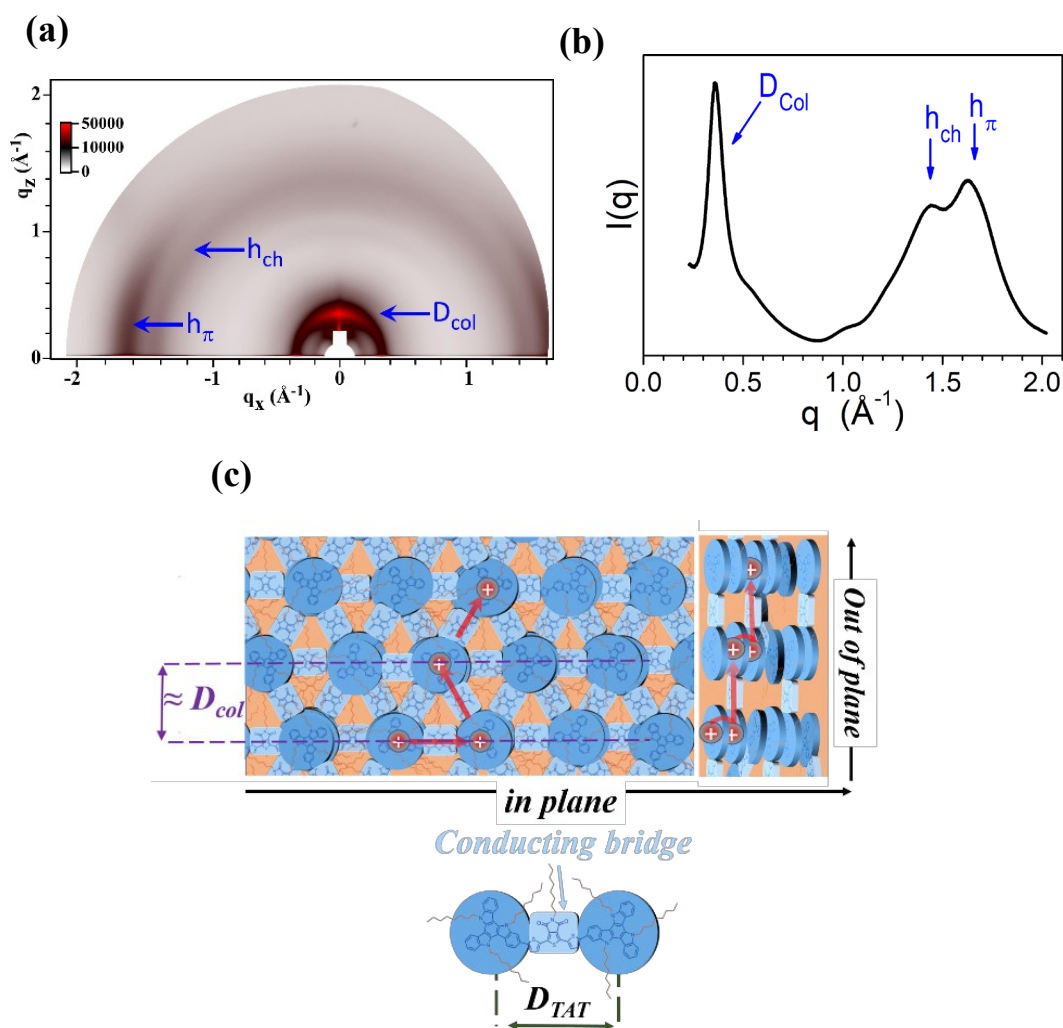
Figure 4.4 *(a) GIWAXS pattern of a nematic thin film on top of an oxidized silicon wafer. (b) Frozen mesophase (nematic state) displaying broad peaks originating from the π-stacking within columns of TAT units (hπ = 3.8 Å), packing between molten alkyl chains (hch = 4.5 Å) and lateral spacing between columns (Dcol = 18 Å). (c) Schematic view of the average local-range molecular packing of the columnar-nematic phase and illustration of charge transport pathways. The system is a fluid or frozen liquid crystal and involves a large amount of structural disorder which is illustrated in the right sketch.*

75

The GIWAXS pattern of a crystallized film is henceforth composed of spot-like reflections due to the spontaneous orientation of crystallites with respect to surface[11] (**Figure 4.5**). In the small-angle region, the (*hk0*) reflexes were sufficiently sharp for indexation according to an oblique lattice of parameters: a_{2D} = 25.2±0.1 Å, b_{2D} = 25.7±0.1 Å, γ_{2D} = 131±1°, which corresponds to the lateral arrangement of piled molecules. The fact that both parameters of the unit cell are close to each other and that the angle is not too far from 120°, it can be supposed that the observed crystalline phase stems from the parent hexagonal liquid-crystalline phase. Crystalline domains are predominantly oriented with the (*a*, *b*)-plane orthogonal and *b*-axis parallel to substrate, implying that the directions of molecular piling lie in the film plane as for the initial mesomorphic structure. The grouping of strong reflections at low q_x is consistent with this finding. Unfortunately, the diffraction peaks in the wide- and medium-angle range are broadened and cannot be resolved in individual reflections, which precludes the full determination of the three-dimensional structure at this stage. At the same time, all trials to grow crystals from solutions failed, presumably because a mesomorphic state was systematically obtained. It turned out that the crystalline state is currently only available through the above-described (section 4.1) thermal treatment in form of microcrystals, which are unsuitable for laboratory XRD. However, it was possible to conduct complementary microfocus X-ray experiments on individual microcrystals of a crystallized thin film using synchrotron radiation, the corresponding results are shown in the next paragraph[12-14].

(a)

(b)
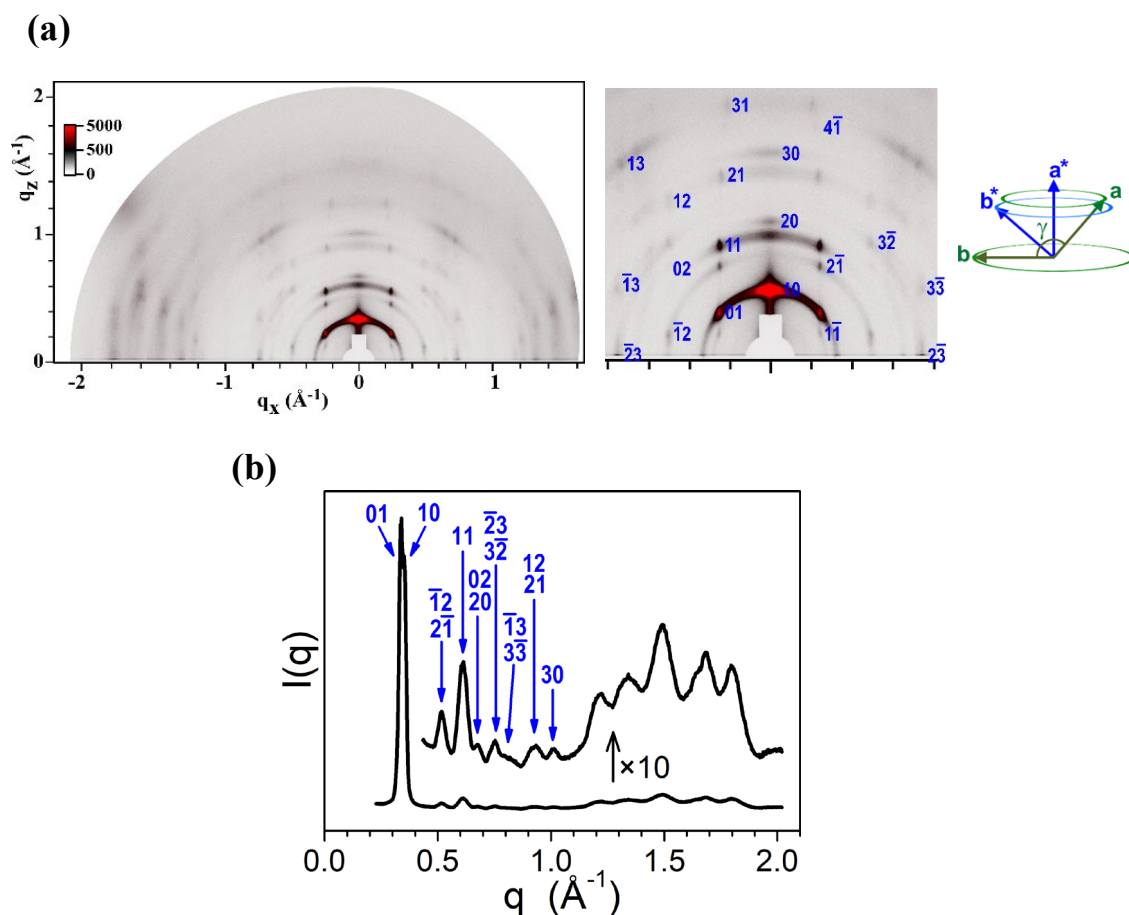
Figure 4.5 *(a) GIWAXS pattern of the crystalline thin film corresponding to Figure 4.1(c), indexation of reflection spots (blue labels), and orientations of sublattice axes in reciprocal space (blue) and direct space (green). (b) Crystal reflections of oblique sublattice in small-angle region. Reflections in wide-angle region are insufficiently resolved for the indexation of the 3D cell.*

4.3.2 Microfocus X-ray diffraction

Spatially resolved X-ray diffractograms were obtained by performing 2D scans of large crystals (around 10 μm long) with a step of 1μm. The aim of the measurements was to identify the crystallographic direction corresponding to the long axis of the needle-like crystals such as the ones observed with an on-axis optical microscope installed at the ID13 beamline of the European Synchrotron Radiation Facility (ESRF) (**Figure 4.6**). The micro-diffractogram acquired on a relatively isolated crystal shown in the magnified image in **Figure 4.6a and 4.6b**, displays sharp reflexes typical of a

crystalline phase (**Figure 4.6d**), which is in line with the data from GIWAXS measurements. Similarly, the *d*-spacings of the (*hkl*) reflexes can be extracted from the pseudo-powder 1D-reduced diffractogram and fitted to a 2D lattice with $a = 24.63 \pm 0.01$ Å, $b = 25.67 \pm 0.01$ Å and $\gamma = 129.55 \pm 0.01°$. Given that the sample-to-detector distance is precise within 20 μm and that the measurements are done on isolated crystallites, these values are very accurate and specific of the monocrystalline structure, while the ones obtained from GIWAXS provide an average set of parameters for the whole crystallized film. The crystallographic direction corresponding to the long axis of the crystal can be determined as follows. Firstly, the two strongest in-plane (*hk0*) reflections are indexed to $(\overline{3}50)$ and $(2\overline{3}0)$, the latter being also the strongest in-plane reflection in the GIWAXS pattern (**Figure 4.5a**). The line connecting the (*hk0*) reflections is called equator of the pattern[15, 16]. It is observed that the perpendicular direction (i.e., meridian) is very close to the long axis of the crystal as can be seen from the inclination angles σ_y and σ_x. Therefore, the long axis of the crystals corresponds to the direction of *c*-axis, which effectively lies in the film plane, as the direction of columns in the parent nematic phase.
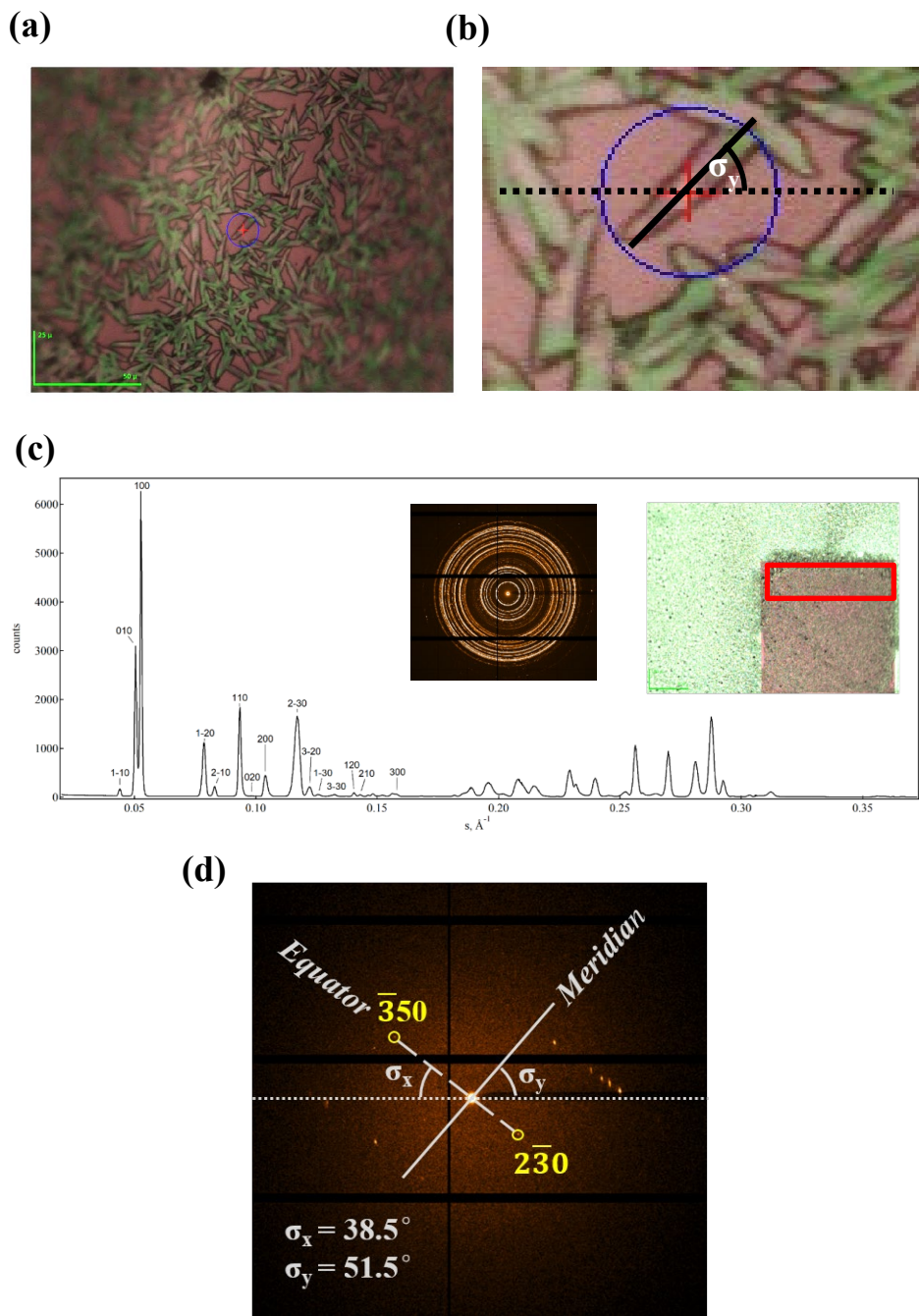
Figure 4.6 *(a) Layer of crystalline needles on Si₃N₄ membrane. (b) Isolated crystal on which the Microfocus X-ray diffraction measurement was done. (c) Radial profiles of Microfocus X-ray diffraction patterns. The figure insert shows the analysis of pseudo-powder data calculated for ~20'000 individual micro diffraction patterns using a maximum projection algorithm. (d) Microfocus X-ray diffraction on an isolated crystal of a thin film similar to (b); 350 and 230 are the Miller indices of reflections lying on the equator of the pattern; σ_x and σ_y are the inclination angles of the meridian in the image.*

4.4 Thin film elaboration

The material property investigations by POM and X-ray diffraction (GIWAXS) have been done on thin-films deposited on either quartz or oxidized silicon substrates from solution and submitted to various thermal treatments. The latter were selected to yield different solid-dates. Thin-film deposition conditions and thermal processes were as follows:

(1) Substrates (quartz, SiO_2): quartz cleaned with liquid dish soap and sonicated in a series of deionized water, acetone, and isopropanol for 15 minutes each.

(2) UV-Ozone treatment: the substrates were be treated in an UV-Ozone reactor for 30 minutes to eliminate any organic residues on the surface before spin-coating.

(3) Spin-coating thin-films: all solutions and thin-film preparation were done in a nitrogen filled glove box. Solutions were prepared at concentrations ranging from 1 to 20 mg/mL (for different thin-films thickness) with chloroform and left to stir overnight at room temperature. Solutions were spun onto the cleaned substrate with a deposition volume of 120 µL and a spin rate of 1500 rpm during 60 seconds.

(4) Thermal treatment: according to the DSC results shown in **Figure 4.2a** (experimental details on the DSC measurements are shown in the annex chapter A4), different annealing steps were applied to the TPD-TAT derivatives. For the TPD$_{C8}$-TAT$_{C8}$ thin-films, the following different annealing steps were applied under nitrogen ambient to achieve desired solid states:

i) Nematic state: annealing at 180 °C for 5 seconds (isotropic phase), followed by rapid cooling to room temperature.

ii) Crystalline state (small crystals): annealing at 100 °C for 5 minutes, followed by 120 °C for 5 minutes and 145 °C for 40 minutes (cold crystallization). The gradual increase in temperature is used to avoid film de-wetting.

iii) Crystalline state (large crystals): annealing at 180 °C for 5 minutes, followed by rapid cooling to room temperature and subsequent heating to 145 °C for 40 minutes.

4.5 Conclusion

DSC and POM results demonstrated that the molecular packing order can be tuned by side-chains engineering and thermal treatments. For TPD-TAT derivatives, strong intermolecular stacking interactions do not originate from TPD, but rather induced by the planar TAT units which dominate the molecular self-assembly. Thus, the side-chains on the TAT units play a leading role in the process of self-assembly of molecule, unlike the one on TPD. In addition, for TPD$_{C8}$-TAT$_{C8}$ thin-films, the crystal size can be controlled by the different thermal treatment parameters. As described in chapter 3, exciton dynamics are highly depending on thin-films packing structure. TPD-TAT derivatives are therefore good candidates for studying the impact of chemical structure and molecular packing on the exciton dynamics. The exciton dynamics of TPD-TAT derivatives will be presented in chapter 5.

Moreover, GIWAXS and Microfocus X-ray diffraction results on TPD$_{C8}$-TAT$_{C8}$ thin-films have revealed that, in both columnar-nematic and crystalline solid-states, the molecular piling direction is oriented parallel to the substrate and should favor in-plane charge transport. On the other hand, for out-of-plane charge transport, the pathways between adjacent molecular stacks must consist of inter-columnar hopping. In conventional molecular semiconductors that self-assemble into lamellar or columnar structures, the molecular stacks are generally separated by interlayers of insulating alkyl chains that hinder charge transport perpendicular to the stacking direction[17-20]. In contrast, for TPD$_{C8}$-TAT$_{C8}$ in the columnar-nematic phase, the molecules bridging neighboring columns may support such a transport (as illustrated in **Figure 4.4c**). The same is probably true for the crystalline films, with molecules bridging adjacent columns or layers through the insulating chain domains. However, since a full elucidation of the crystalline structure is not yet possible, measuring hole transport

perpendicular to the substrate is currently the only way to probe the existence of such conducting inter-columnar pathways. The charge transport properties of TPD$_{C8}$-TAT$_{C8}$ will be presented in chapter 6.

References:

[1]   T. Han, I. Bulut, S. Méry, B. Heinrich, P. Lévêque, N. Leclerc and T. Heiser, *Journal of Materials Chemistry C*, 2017, **5**, 10794-10800.

[2]   I. Bulut, P. Chávez, A. Mirloup, Q. Huaulmé, A. Hébraud, B. Heinrich, S. Fall, S. Méry, R. Ziessel, T. Heiser, P. Lévêque and N. Leclerc, *Journal of Materials Chemistry C*, 2016, **4**, 4296-4303.

[3]   V. Coropceanu, J. Cornil, D. A. da Silva Filho, Y. Olivier, R. Silbey and J.-L. Brédas, *Chemical Reviews*, 2007, **107**, 926-952.

[4]   F.-C. Chen, in *Encyclopedia of Modern Optics (Second Edition)*, eds. B. D. Guenther and D. G. Steel, Elsevier, Oxford, 2018, pp. 220-231.

[5]   S. M. Menke and R. J. Holmes, *Energy Environ. Sci.*, 2014, **7**, 499-512.

[6]   C. Y. Wong, B. L. Cotts, H. Wu and N. S. Ginsberg, *Nature communications*, 2015, **6**, 1-7.

[7]   V. Drits, J. Środoń and D. Eberl, *Clays and clay minerals*, 1997, **45**, 461-475.

[8]   H. Bengs, O. Karthaus, H. Ringsdorf, C. Baehr, M. Ebert and J. Wendorff, *Liquid Crystals*, 1991, **10**, 161-168.

[9]   M. A. Bates and D. Frenkel, *Physical Review E*, 1998, **57**, 4824.

[10]   S. Kohmoto, E. Mori and K. Kishikawa, *Journal of the American Chemical Society*, 2007, **129**, 13364-13365.

[11]   C. M. Sparks, U. E. Fittschen and G. J. Havrilla, *Spectrochimica Acta Part B: Atomic Spectroscopy*, 2010, **65**, 805-811.

[12]   A. J. Thompson, A. Worthy, A. Grosjean, J. R. Price, J. C. McMurtrie and J. K. Clegg, *CrystEngComm*, 2021.

[13]   A. Franks, *British Journal of Applied Physics*, 1958, **9**, 349.

[14]   S.-W. Kang, Q. Li, B. D. Chapman, R. Pindak, J. O. Cross, L. Li, M. Nakata and S. Kumar, *Chemistry of Materials*, 2007, **19**, 5657-5663.

[15]   D. J. Hulmes and A. Miller, *Nature*, 1979, **282**, 878-880.

[16]   G. Catalan, A. Janssens, G. Rispens, S. Csiszar, O. Seeck, G. Rijnders, D. H. Blank and B. Noheda, *Physical review letters*, 2006, **96**, 127602.

[17]   M. Funahashi, *Journal of Materials Chemistry C*, 2014, **2**, 7451-7459.

[18]   H. Tsao, H. J. Räder, W. Pisula, A. Rouhanipour and K. Müllen, *physica status solidi (a)*, 2008, **205**, 421-429.

[19]   B. Mu, J. Chen, K. Chen, C. Zhang and D. Chen, *Journal of Materials Chemistry C*, 2021.

[20]   H. Monobe, S. Mima and Y. Shimizu, *Chemistry Letters*, 2000, **29**, 1004-1005.

Chapter 5
Exciton dynamics

Exciton lifetime, Exciton diffusion length

As presented in chapter 3, exciton dynamics in OSCs are an important property for the operation of optoelectronic devices. In this chapter, methods for the determination of the exciton diffusion length and the corresponding experimental details will be described (section 5.1, and 5.2). The exciton lifetime of TPD-TAT derivatives as a function of chemical and self-assembly structures will be presented in section 5.3. In addition, exciton diffusion lengths of TPD$_{C8}$-TAT$_{C8}$ thin-films for different solid-states will be explored in section 5.3 as well.

5.1 Introduction

Exciton dynamics play an important role in the optoelectronic devices. However, accurate methodologies to measure the exciton diffusion length are crucial for the development of efficient OPV materials, but are not trivial to implement[1-3]. In this section, three different ways to estimate the exciton diffusion length will be described. Exciton diffusion can be modeled as Förster energy transfer (FRET)[3] and Dexter energy transfer for singlet and triplet exciton diffusion, respectively[4]. For the materials investigated in this thesis, the maximum exciton lifetime measured is lower than 1.5 ns, and can therefore be attributed singlet excitons following the FRET mechanism. The method used to determine the exciton diffusion length based on FRET requires the measurement of the photoluminescence quantum yield, and is therefore called the PLQY technique[5]. The details of the PLQY technique will be presented in section 5.3. The advantage of this method is that it requires only one sample to determine the exciton diffusion length. Nevertheless, it's validity relies on several assumptions discussed in section 5.3, whose accuracy may be limited.

The second method is based on the phenomenon of exciton-exciton annihilation (EEA). In case of a long enough exciton diffusion length, the probability that two excitons encounter each other during their intrinsic lifetime increases with the exciton density,

and results in a decrease in the measured exciton lifetime[6, 7]. Indeed, exciton-exciton annihilation occurs when two excitons interact and at least one of them recombines non-radiatively.[2] In the EEA theory method, the PL decay is measured at different initial excitation densities so that the annihilation rate and exciton diffusion coefficient are deduced by modeling these decays. Details of EEA theory method will be given in section 5.3. This technique also has the advantage of only requiring a single sample to determine the exciton diffusion length. However, the studied thin films require good photochemical stability, since the EEA requires very high laser energy densities, which can damage the samples.

The surface quenching of photoluminescence is the last technique presented here. In this case, a PL quencher is deposited on top of the OSC films and time-resolved PL is measured. If the thickness of the thin film is of the order of magnitude of the exciton diffusion length, a reduction in the exciton lifetime will be observed. The advantage of this technique is that it is straightforward to extract the exciton diffusion length. However, it requires the preparation of series of OSC films with different thicknesses. Moreover, the studied OSC films need to have ultra-flat surface and the quencher should not diffuse into the OSC[1, 2]. Such a "geometry" would be difficult to obtain in our crystalline films (high roughness) and the control of the film thickness at the nm scale (order of exciton diffusion length) is challenging. Thus, this method was not used in this thesis.

The two former exciton diffusion length measurement methods will therefore be used to determine the impact of the material properties (e.g., molecular and solid-state structures) on the exciton diffusion length. So far, the impact of side-chains on charge transport in molecular OSCs has been widely studied, but this is not yet the case for exciton dynamics[2, 8]. The molecular self-assembling structure has a significant impact on charge transport and should similarly influence exciton dynamics. In chapter 3, we

discussed some recent works which highlighted the relationship between exciton dynamics and molecular structure as well as solid-state order. The results on TPD-TAT derivatives described in chapter 4 demonstrated that different molecular packing order can be obtained by modifying the side-chains of the derivatives or the post-deposition treatment[9]. These TPD-TAT derivatives are therefore good candidates for studying the exciton dynamics.

In this chapter, the impact of side-chains and molecular self-assembly of TPD-TAT derivatives on the exciton dynamics will be described. Details of the thin-film preparation have been shown in chapter 4. Firstly, the exciton lifetime in different derivatives has been studied using time-resolved photoluminescence (TR-PL), continuous-wave photoluminescence (CW-PL) and time-resolved micro-PL measurements. Secondly, the exciton diffusion length in TPD_{C8}-TAT_{C8} thin-films has been determined through both methods (PLQY and EEA) as a function of molecular self-assembly. For the PLQY theory technique, UV-visible spectroscopy, CW-PL, ellipsometry and PLQY measurement have been used. Femtosecond time-resolved photoluminescence measurement was carried out for EEA theory technique.

5.2 Experimental details

5.2.1 Time-resolved photoluminescence

All TR-PL measurements were carried out in atmospheric environment at room temperature. **Scheme 5.1a** shows a diagram of the TR-PL measurement set up. The substrate (for thin-films) and the cuvette (for solutions) are made of quartz made to avoid background noise (signals from substrate or cuvette). In order to guide the laser beam and focus it on the sample, a tube and a lens have been inserted between the laser beam and sample. The radius of the focused laser beam is around 1.0±0.5 mm. In order to focus the photoluminescence into the streak camera and select the spectral region of

interest (PL from the sample: 650nm-700nm), a lens and a filter have been put between the sample and the streak camera.

The samples were excited using a laser from Spectra-Physics Mai Tai. The beam characteristics are the following: a pulse duration of 90 ps, an energy per pulse of 0.05 nJ, a wavelength of 511 nm and a repetition rate of 20 MHz. TR-PL was measured using a Hamamatsu C6860 streak camera with a S-20 photocathode in synchro-scan mode. The full width half maximum (FWHM) of the instrument response function (IRF) is 40 ps. Finally, a typical signal output is shown in **Scheme 5.1b**. The top image of **Scheme 5.1b** shows the picture registered through the slit of the streak camera as function of time (horizontally), the temporal resolution is of the order of a hundred ps. The bottom image of **Scheme 5.1b** shows the graph of the PL intensity as a function of time extracted from the top image by the software OptoAnalyse. In this graph, the x axis unit represents pixels and needs to be converted into time (in ns). A calibration procedure allowed to establish that one pixel is equivalent to 1.18×10^{-3} ns.
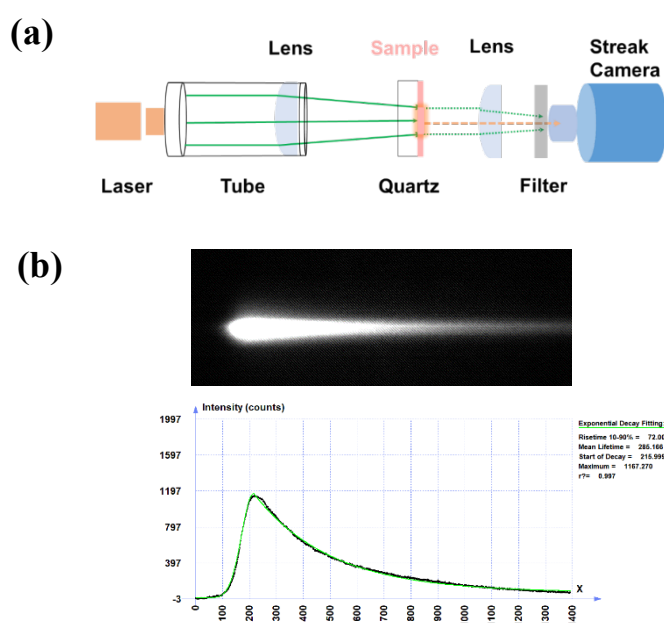
Scheme 5.1 (a) Scheme of Time-resolved photoluminescence set up. (b) Top side: image registered through the slit of the streak camera as function of time (horizontally); Bottom side: graph of the PL intensity as a function of time extracted from the top image.

5.2.2 Time-resolved photoluminescence for EEA measurements

The EEA measurements were done at ICPMS (J. Léonard's group) on a set-up shown in **Scheme 5.2**. The laser wavelength was 515 nm with ~60 fs pulses and a repetition rate ranging from 0.1 to 10 kHz. The excitation energy was 0.4 μJ per pulse. The TR-PL curves were measured using a Hamamatsu C10627 streak camera. The full width half maximum (FWHM) of the instrument response function (IRF) was 20 ps. For this study, because the laser energy density is high (0.01-3.0 J·cm^{-3}) samples were encapsulated to prevent laser damage. Encapsulated samples were prepared in a glove box fill with N_2, as explained below. Firstly, we cleaned the quartz substrate near the thin film edges and put four spacers (micrometer thickness) around the active layer with an appropriate amount of adhesive. Secondly, we covered the samples with another quartz substrate of the same size. Finally, we placed the samples under UV-light to cure the adhesive. It is important to cover the samples with a silicon wafer during curing time to prevent UV-light from damaging the thin-films. Moreover, we did also decrease the repetition rate of the laser while gradually increasing the excitation energy (per pulse), to avoid photobleaching of the samples. In order to ensure the reproducibility of the measurements, the TR-PL curve was measured again at low energy and superimposed with the previous low energy measurements after each excitation at high energy. This procedure aims to cross-check if there is no photobleaching occurred during the EEA measurements.
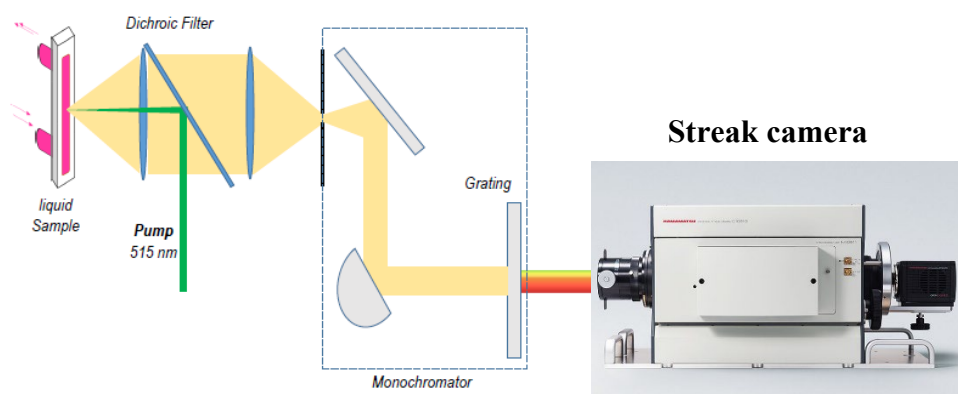
Scheme 5.2 *Scheme of time-resolved photoluminescene set up for EEA measurements. (Copyright from Amira Mounya Gharbi, Jérémie Léonard, IPCMS, Strasbourg)*

5.3 Results and discussion

5.3.1 CW- PL and TR-PL on TPD-TAT derivatives

CW-PL (experimental details of CW-PL are shown in chapter A5.4) were carried out to identify the PL transitions occurring in the TPD-TAT derivatives. TR-PL measurements were carried out to investigate the exciton lifetime in TPD-TAT derivatives as a function of chemical structure for solutions and solid-states and as a function of the self-assembled solid-state structures. **Figure 5.1** shows the CW-PL spectra and TR-PL transients measured for four TPD-TAT derivatives in solution and in different solid-states. The deconvolutions of these CW-PL spectra into three Gaussian peaks located at different wavelength (or energy) are shown in the annex (**Figures A5.1 to A5.4**). The peak positions after deconvolution are summarized in **Table 5.1** (in wavelength) and **Table 5.2** (in energy).

As shown in **Figure 5.1a and A5.1**, the four TPD-TAT derivatives in solution give rise to CW-PL spectra that are perfectly superimposed and split into mainly three vibronic peaks: a major emission band around 631 nm and two weak shoulders centered around 588nm and 650 nm (**Table 5.1**). The energy difference between the transitions being roughly constant (**Table 5.2**), we may attribute the emission bands to 0-0 (588nm), 0-1 (631 nm) and 0-2 (650 nm) transitions [10-12].

The TR-PL transients measured in solution (in the range from 650 to 700 nm) are also perfectly superimposed (**Figure 5.1b**). Fitting the PL decay by a decreasing mono-exponential function gives rise to a unique exciton lifetime of 0.7 ns in solution (**Table 5.3**), indicating that the side-chains do not alter the molecular conformation, in agreement with the behavior observed for the CW-PL measurements. The measured

exciton lifetime can thus be considered as an intrinsic property of photo-generated excitons in TPD-TAT derivatives, regardless of the nature of the side-chains.
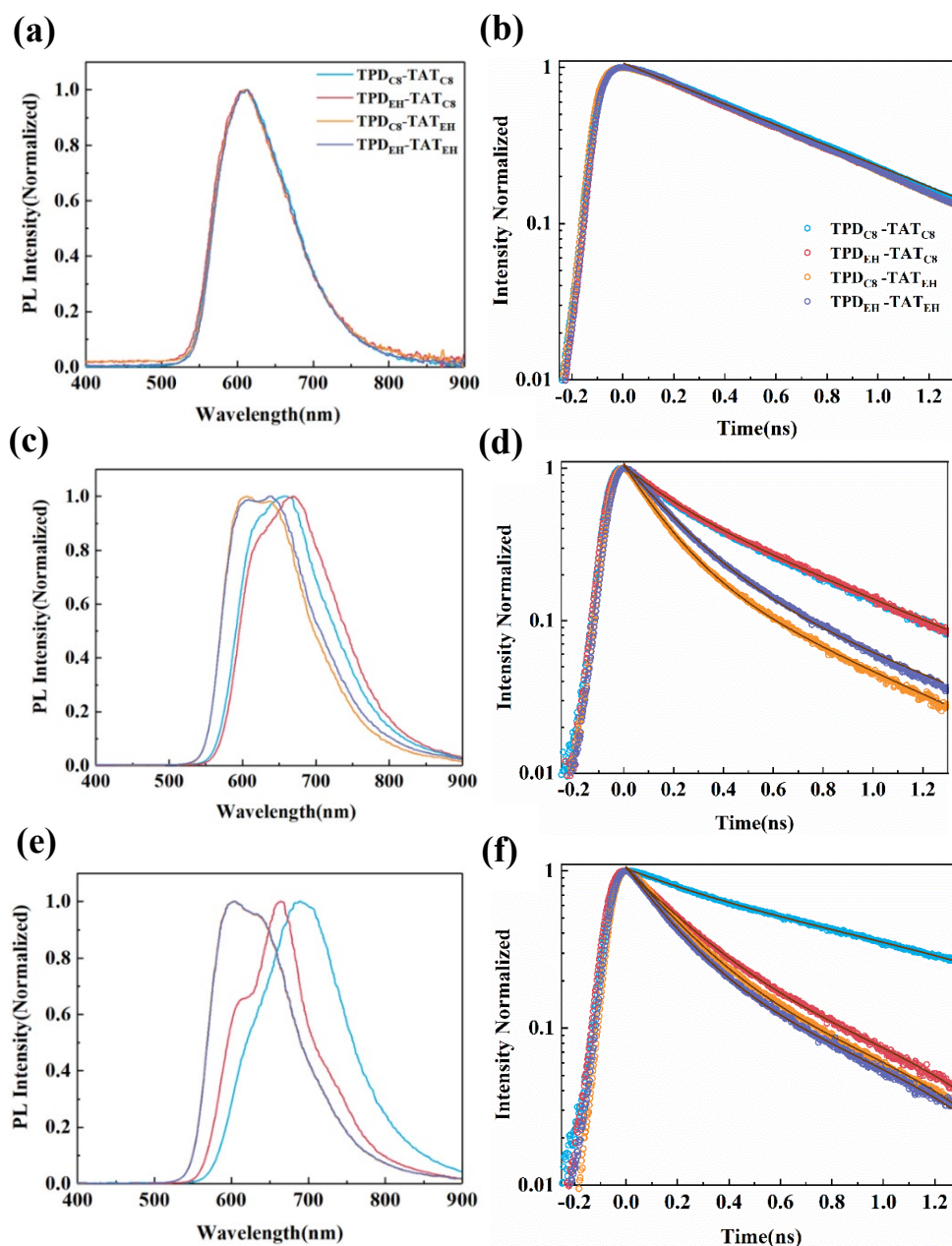

Figure 5.1 *CW- PL and TR-PL for different TPD-TAT derivatives in solution (a) and (b), in as-deposited thin films (c) and (d), and in annealed thin films (e) and (f), respectively. In solution, TR-PL transients are fitted by a mono-exponential decay, in solid-state, TR-PL transients are fitted by a bi-exponential decay.*

Table 5.1 *Positions of the PL peaks after deconvolution of the CW-PL spectra of TPD-TAT derivatives into three Gaussian peaks located at different wavelength (with error bar ±5nm).*

States	Molecules	0-0 (nm)	0-1 (nm)	0-2 (nm)
Solution	TPD_{C8}-TAT_{C8}			
	TPD_{EH}-TAT_{C8}	588	631	686
	TPD_{C8}-TAT_{EH}			
	TPD_{EH}-TAT_{EH}			
As-deposited	TPD_{C8}-TAT_{C8}	608	650	705
	TPD_{EH}-TAT_{C8}	608	660	712
	TPD_{C8}-TAT_{EH}	588	635	692
	TPD_{EH}-TAT_{EH}	588	635	692
Annealed	TPD_{C8}-TAT_{C8}	616	685	757
	TPD_{EH}-TAT_{C8}	605	660	695
	TPD_{C8}-TAT_{EH}	587	631	688
	TPD_{EH}-TAT_{EH}	587	631	688
Nematic	TPD_{C8}-TAT_{C8}	608	650	705

Table 5.2 *Positions of the PL peaks after deconvolution of the CW-PL spectrum of TPD-TAT derivatives into three Gaussian peaks located at different energy (with error bar ±0.01eV).*

States	Molecules	0-0 (eV)	*Gap*	0-1 (eV)	*Gap*	0-2 (eV)
Solution	TPD_{C8}-TAT_{C8}					
	TPD_{EH}-TAT_{C8}	2.11	0.15	1.96	0.16	1.80
	TPD_{C8}-TAT_{EH}					
	TPD_{EH}-TAT_{EH}					
As-deposited	TPD_{C8}-TAT_{C8}	2.04	0.13	1.91	0.15	1.76
	TPD_{EH}-TAT_{C8}	2.04	0.16	1.88	0.14	1.74
	TPD_{C8}-TAT_{EH}	2.11	0.16	1.95	0.16	1.79
	TPD_{EH}-TAT_{EH}	2.11	0.16	1.95	0.16	1.79
Annealed	TPD_{C8}-TAT_{C8}	2.01	0.20	1.81	0.17	1.64
	TPD_{EH}-TAT_{C8}	2.05	0.17	1.88	0.10	1.78
	TPD_{C8}-TAT_{EH}	2.11	0.15	1.96	0.16	1.80
	TPD_{EH}-TAT_{EH}	2.11	0.15	1.96	0.16	1.80
Nematic	TPD_{C8}-TAT_{C8}	2.04	0.15	1.89	0.16	1.73

Table 5.3 *Lifetime of TPD-TAT derivatives in solution (0.5mg/mL) and thin films (as-deposited and annealed). The lifetimes are obtained after a deconvolution of TR-PL transients with IRF and a fit with a mono-exponential function for solutions and with a bi-exponential function for thin films. For bi-exponential decays, the lifetime values are accompanied by that of their weight A_i in normalized spectra ($A_1+A_2 =1$). The values are given in ns and the error (noise, fit) is around ±0.05 ns.*

	Solution $(A\,e^{-t/\tau})$	Thin film $(A_1\,e^{-t/\tau_1} + A_2\,e^{-t/\tau_2})$			
		As-deposited		Annealed	
TPD$_{C8}$-TAT$_{C8}$		$\tau_1 = 0.15$	$A_1 = 0.4$	$\tau_1 = 0.20$	$A_1 = 0.1$
		$\tau_2 = 0.60$	$A_2 = 0.6$	$\tau_2 = 1.05$	$A_2 = 0.9$
TPD$_{EH}$-TAT$_{C8}$		$\tau_1 = 0.15$	$A_1 = 0.4$	$\tau_1 = 0.20$	$A_1 = 0.6$
	0.70	$\tau_2 = 0.60$	$A_2 = 0.6$	$\tau_2 = 0.50$	$A_2 = 0.4$
TPD$_{C8}$-TAT$_{EH}$		$\tau_1 = 0.10$	$A_1 = 0.7$	$\tau_1 = 0.15$	$A_1 = 0.7$
		$\tau_2 = 0.40$	$A_2 = 0.3$	$\tau_2 = 0.50$	$A_2 = 0.3$
TPD$_{EH}$-TAT$_{EH}$		$\tau_1 = 0.15$	$A_1 = 0.6$	$\tau_1 = 0.10$	$A_1 = 0.7$
		$\tau_2 = 0.45$	$A_2 = 0.4$	$\tau_2 = 0.40$	$A_2 = 0.3$

In order to evaluate the impact of intermolecular interactions on the exciton lifetime, CW-PL and TR-PL experiments were performed on thin films for the four TPD-TAT derivatives. The measurements were done on either as-deposited or annealed films and are shown on **Figure 5.1c and 5.1d**. The positions of the Gaussian peaks deconvoluted from the CW-PL spectra (**Figure A5.2**) for as-deposited thin-films are summarized in the **Table 5.1** and **Table 5.2**. As in solution, the shift in energy between the 0-1 and 0-0 transitions is approximately the same as that between the 0-1 and 0-2 transitions. In addition, the TPD-TAT$_{C8}$ derivatives clearly show a significant red-shift of the transition bands in comparison to TPD-TAT$_{EH}$. This red-shift indicates a stronger intermolecular coupling in the case of linear side-chains that should beneficial for to intermolecular charge and energy transfer[13, 14].

The TR-PL transients of as-deposited thin-films are shown in **Figure 5.1d**. Although they are no more mono-exponential (see below), the slower decrease in PL for TPD-

TAT$_{C8}$ points out a longer exciton lifetime (**Table 5.3**) for this derivative in comparison to TPD-TAT$_{EH}$, but shorter than in solution. The decrease in lifetime (in comparison to the reference value in solution) can be related to the intensity of intermolecular coupling in the solid-states. Strong π-stacking interactions do indeed often induce non-radiative recombination pathways that lead to a decrease in the exciton lifetime[15, 16]. On the other hand, the measured lifetimes indicate that TPD-TAT$_{C8}$ derivatives have a lower non-radiative recombination rate than TPD-TAT$_{EH}$ derivatives despite the stronger intermolecular coupling revealed by the CW-PL. Moreover, the exciton lifetime is not significantly impacted by the side-chain nature (C8 or EH) on the TPD unit. One possible reason is that the molecular self-assembly is mainly controlled by the side-chains on the TAT moieties (see chapter 4), while the structural disorder in as-deposited films might be too high to allow the side-chain on the TPD unit to have an observable influence.

To compare the lifetimes more quantitatively, the TR-PL transients were fitted with a bi-exponential function. The possible origin of the bi-exponential PL decay will be discussed in section 5.3.3. The results of the fit are presented in table 5.3 and confirm the qualitatively observed trend. The lifetime values show that the exciton lifetimes of the four as-deposited derivatives are roughly the same: a short lifetime of about 0.10-0.20 ns and a longer one around 0.45-0.60 ns. Interestingly, the weight of these components depends on the nature of the side- chains on the TAT units. For both TPD-TAT$_{C8}$ derivatives, the higher lifetime is preponderant, but for both TPD-TAT$_{EH}$ derivatives, the shorter one is leading the decay, resulting in a longer global PL decay for the TPD-TAT$_{C8}$ derivatives, as observed on the TR-PL graphs.

Figure 5.1e and 5.1f show the CW-PL and the TR-PL transients measured in thin-films after the following annealing treatments: TPD$_{C8}$-TAT$_{C8}$ were annealed at 145°C during 2h; TPD$_{EH}$-TAT$_{C8}$ at 135°C during 2h; both TPD-TAT$_{EH}$ at 145°C during 2h (The

temperatures were chosen according to the DSC results). The positions of the Gaussian peaks deconvoluted from the CW-PL spectra (**Figure A5.3**) are presented in **Table 5.1** and **Table 5.2**. Here again, for the TPD-TAT$_{EH}$ annealed films, the energy gap between the transitions 0-1 and 0-0 is almost the same as between the transitions 0-2 and 0-1, and is in line with the previously obtained results. However, for TPD-TAT$_{C8}$ annealed thin-films, the energy gap between the transitions 0-1 and 0-0 transitions is larger than that between the transitions 0-2 and 0-1. Moreover, CW-PL spectra of TPD$_{C8}$-TAT$_{C8}$ shows a large red-shift than TPD$_{EH}$-TAT$_{C8}$ in their annealed thin-films. O. V. Mikhnenko, et al. [17] observed a similar phenomenon in diketopyrrolopyrrole (DPP) derivatives for which the PL spectrum undergoes a gradual red-shift going from solution to as-deposited films and a further red-shift after annealing treatment. Such red-shifts could occur due to stronger intermolecular interactions in solid-states, which are enhanced upon annealing-induced crystallization[17], which confirming the results observed from SAXS patterns (**Figure A5.10**) that TPD$_{C8}$-TAT$_{C8}$ show more strong crystalline than TPD$_{EH}$-TAT$_{C8}$ thin films.

The measured TR-PL transients show that the exciton lifetime decreases in TPD$_{EH}$-TAT$_{C8}$ annealed thin-film, but increases in TPD$_{C8}$-TAT$_{C8}$ after annealing. On the other hand, the exciton lifetime in TPD-TAT$_{EH}$ annealed thin-films does not differ significantly from those of as-deposited films. Several reasons may a priori contribute to the shorter decay in the annealed TPD$_{EH}$-TAT$_{C8}$ thin-film. Thermal annealing TPD$_{EH}$-TAT$_{C8}$ thin-film results in crystalline domains (as shown in **Figure A5.10**) that may lead to PL quenching at grain boundaries. O. V. Mikhnenko, et al.[17] show similar results on small molecules with a faster PL decay in annealed films compared to as-deposited films that they attribute to PL quenching at boundaries of grain domains. On the other hand, as we discussed before, a strong π-stacking interaction in annealed thin-films induces non-radiative recombination pathways which can decrease the exciton lifetime. Yet, the TR-PL transients of TPD$_{C8}$-TAT$_{C8}$ annealed thin-films (**Figure 5.1f**)

show significantly longer exciton lifetimes (**Table 5.3**) which even exceed the lifetime measured in solution (possible explanations of this uncommon phenomenon will be given below). As shown in **Figure 4.2**, the derivative with both linear side-chains (C_8) on TAT and TPD units gives rise to self-assembled micrometric-sized crystalline needles after thermal treatment, which are likely at the origin of the longer exciton lifetimes. Several previous reports have shown an increase in lifetime with increasing crystallinity in organic semiconductors which they attributed to a reduction in intra-grain defects acting as non-radiative recombination centers[18-20].

As shown in chapter 4, depending on the annealing treatment of the TPD$_{C8}$-TAT$_{C8}$ thin-films, it is possible to vary the size of the formed crystals. We therefore could investigate the impact of crystal size on the exciton lifetime. The results are summarized in the next section.

5.3.2 CW-PL and TR-PL on different sizes of crystal (TPD$_{C8}$-TAT$_{C8}$)

We studied four samples with different annealing conditions leading to either a film in frozen nematic state or crystalline films with different crystal sizes. The annealing steps are described below (**Figure 5.2a**), To obtain nematic films, the as-deposited thin-film was heated at 180 °C for 5s and cooled down to room temperature. Crystalline film composed of small (around 2.5μm) crystals (**Figure 5.2b**) were obtained by gradually increasing (to avoid de-wetting) the temperature of the as-deposited thin-film up to 145°C, stay at this temperature for 2h and then directly cool down to room temperature. To achieve crystals with bigger sizes (8.0μm and 20.0μm, respectively) **(Figure 5.2c and Figure 5.2d),** a preliminary annealing into the isotropic phase was necessary. Annealing at 180°C reduces the density of nucleation centers, and therefore, the longer the annealing at 180°C the larger (but fewer) crystals are formed during the subsequent annealing at 145°C. (**Figure 5.2c, Figure 5.2d**).

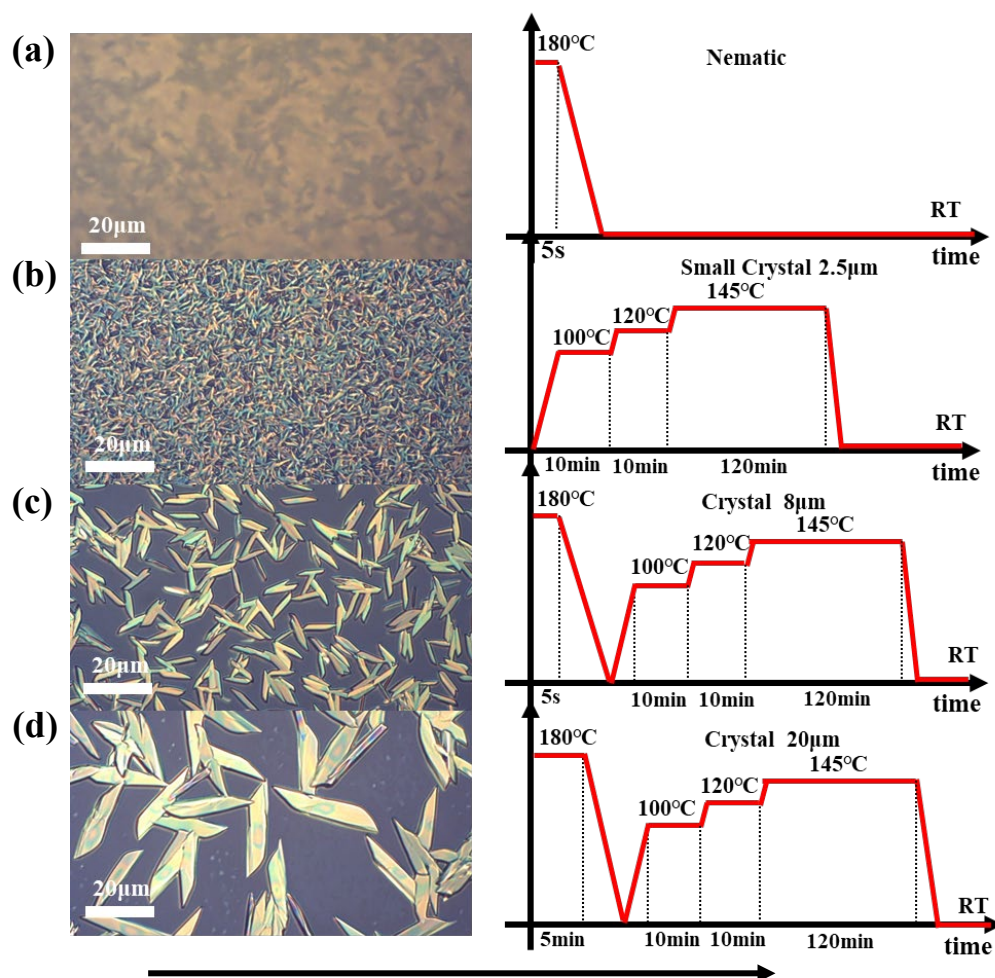***Figure 5.2*** *Left side: The microscopy pictures of a film in nematic state and three crystalline films with different crystal sizes. Right side: Corresponding annealing process.*

The CW-PL spectra of TPD$_{C8}$-TAT$_{C8}$ in solution and for as-deposited, nematic and crystalline thin-films are shown in **Figure 5.3a**. The spectra of as-deposited and nematic states present the same vibronic transitions and almost perfectly overlap, suggesting that the molecules in both thin-films have similar local environments and intermolecular coupling. This result is in line with the TR-PL transients (**Figure 5.3b**) showing almost identical lifetimes and amplitude values (**Tables 5.3 and 5.4**) in both films. It is also consistent with the DSC and XRD results: as-deposited and nematic thin-films solid-states present a high disorder in the long-rang, but have similar organization on the molecular scale or short-range (see chapter 4).

98

The CW-PL spectra of the crystalline samples (no matter the crystal size) (**Figure 5.3a**) show the same vibronic transitions, with a significant redshift compared to the as-deposited and nematic states. The TR-PL transients reveal that the exciton lifetime is also independent of crystal size. Considering that non-radiative recombination is enhanced near the crystal boundaries, the constant exciton lifetime as a function of crystal size indicates that the exciton diffusion length is much smaller than the average crystal size. Surprisingly, the exciton lifetime exceeds that measured in solution (red dash line in **Figure 5.3b**). A possible reason could be that the molecular environment in the crystals has a lower polarity than the solvent (in this case chloroform) and that intermolecular interactions do not favor non-radiative recombination. However, additional TRPL measurements carried out in low polar solvents (such as toluene) (not shown here) did not reveal any influence on the lifetime. The mechanism underlying the larger lifetime in crystals is thus not yet fully understood.
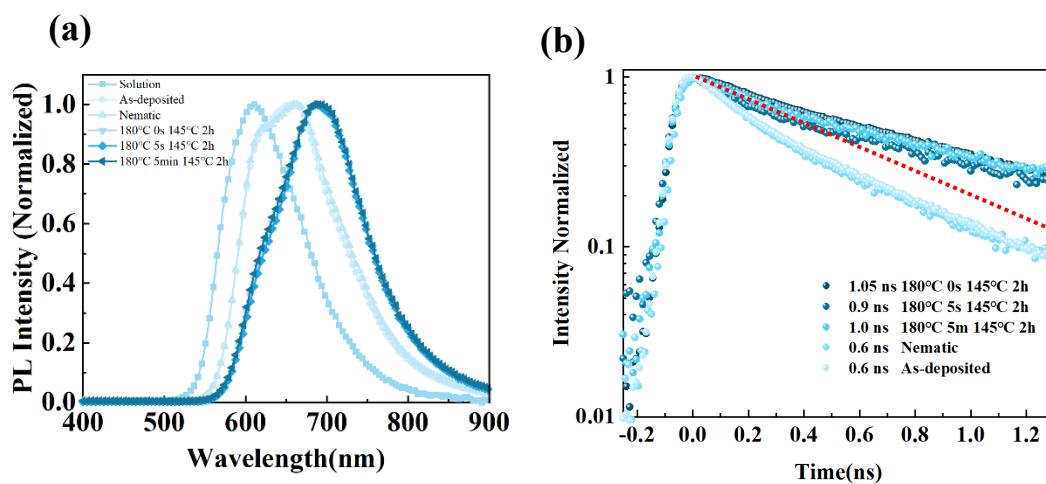

Figure 5.3 *(a) CW- PL and (b) TR-PL of TPDc8-TATc8 in the nematic and crystalline. For easier comparison, results in solution, and for as-deposited thin films have been added. The red dash line corresponds to the PL decay in solution.*

Table 5.4 *Lifetime of TPD$_{C8}$-TAT$_{C8}$ in thin films (nematic and crystalline states). The lifetime in thin film is obtained by the deconvolution of TR-PL transients with IRF and the fit with a bi-exponential function. For bi-exponential decay, the lifetime values are accompanied by that of their weight in normalized spectra (A$_1$+A$_2$=1). The values are given in ns and the error is around ±0.05 ns.*

TPD$_{C8}$-TAT$_{C8}$	Thin film $(A_1\ e^{-t/\tau_1} + A_2\ e^{-t/\tau_2})$	
180℃ 5s	$\tau_1 = 0.15$	$A_1 = 0.4$
Nematic	$\tau_2 = 0.60$	$A_2 = 0.6$
180℃ 5s 145℃ 2hours	$\tau_1 = 0.10$	$A_1 = 0.4$
$L_{crystal} \approx 8\ \mu m$	$\tau_2 = 0.90$	$A_2 = 0.6$
180℃ 5min 145℃ 2hours $L_{crystal} \approx 20\ \mu m$	$\tau_1 = 0.10$ $\tau_2 = 1.00$	$A_1 = 0.3$ $A_2 = 0.7$

The TR-PL transients (**Figure 5.3b**) performed on TPD$_{C8}$-TAT$_{C8}$ for different states (as-deposited, nematic and crystals with different sizes) clearly point out that the molecular organization in thin-films has a huge impact on the exciton lifetime. The TR-PL transients could only be fitted by bi-exponential function, as was the case for as-deposited and nematic states. The possible origin of the bi-exponential decay will be discussed in section 5.3.3. The increase in the longer lifetime (τ_2) by a factor of almost two between the nematic and crystal states (**Table 5.4**) is opposite to the trend generally observed for other small molecules, where strong intermolecular coupling (as revealed by XRD or charge transport measurements, see chapter 6) generally leads to short lifetimes[15, 21].

5.3.3 Spatially resolved TR-PL on TPD$_{C8}$-TAT$_{C8}$

As mentioned previously, the TR-PL decays in the solid-state are not mono-exponential, as is often seen in OSC thin films. The origin of this behavior is often unclear and leads people to report only the weighted average value of the exciton lifetimes[17, 22]. In order

to better understand the origin of the bi-exponential decay in our case, focused TR-PL experiments using two photon absorption under microscope were carried out (collaboration with P. Didier from the Bioimaging and Pathology Laboratory (LBP) at Illkirch - experimental details are shown in annex A5). **Figures 5.4a and 5.4b** show the PL intensity map as well as the lifetime map (both measured in a wavelength range from 600 to 700 nm) for a TPD$_{C8}$-TAT$_{C8}$ thin-film containing crystalline needles (as shown in **Figure 5.2c**). The lifetime map is obtained by fitting the TR-PL transients (measured under a microscope on each point of the map) with a mono-exponential function. **Figure 5.4c** presents the mono-exponential fits of the TR-PL decays for two typical points of the map: one point on the needle and the other close to the needle. The PL intensity map is obtained by integrating the area under the TR-PL transient of each point of the map. The PL intensity map clearly shows the very intense luminescence emitted by a crystalline needle, but also the presence of low luminescent phase around the needle. Interestingly, **Figures 5.4b and 5.4c** show the existence of two very distinct lifetime values: the crystalline phase (needle - point A) has a long lifetime (greater than 1.0 ns) while the phase around the needle (point B) has a shorter lifetime around 0.40 ns. Indeed, the PL decays obtained for thin films under a microscope are mono-exponential, unlike those obtained under excitation with a macroscopic laser beam (a few mm²). The value of the short lifetime (0.40 ns) obtained in the phase around the needle is close to the lifetime measured under microscope on a nematic film (0.45 ns, see **Figure A5.5**), suggesting that the low luminescent phase is constituted of a non-crystalline phase, probably a nematic state. We may therefore conclude that the TR-PL measurements carried out with a wide laser spot (radius around 1.0 mm) gives rise to double-exponential decays with the two distinct lifetimes corresponding to two different states of the thin-films. Moreover, in the nematic (or as-deposited) thin-films, the bi-exponential decay may be attributed the existence of residual small crystal germs visible under polarized optical microscope (small black dots in **Figure 4.2b**).
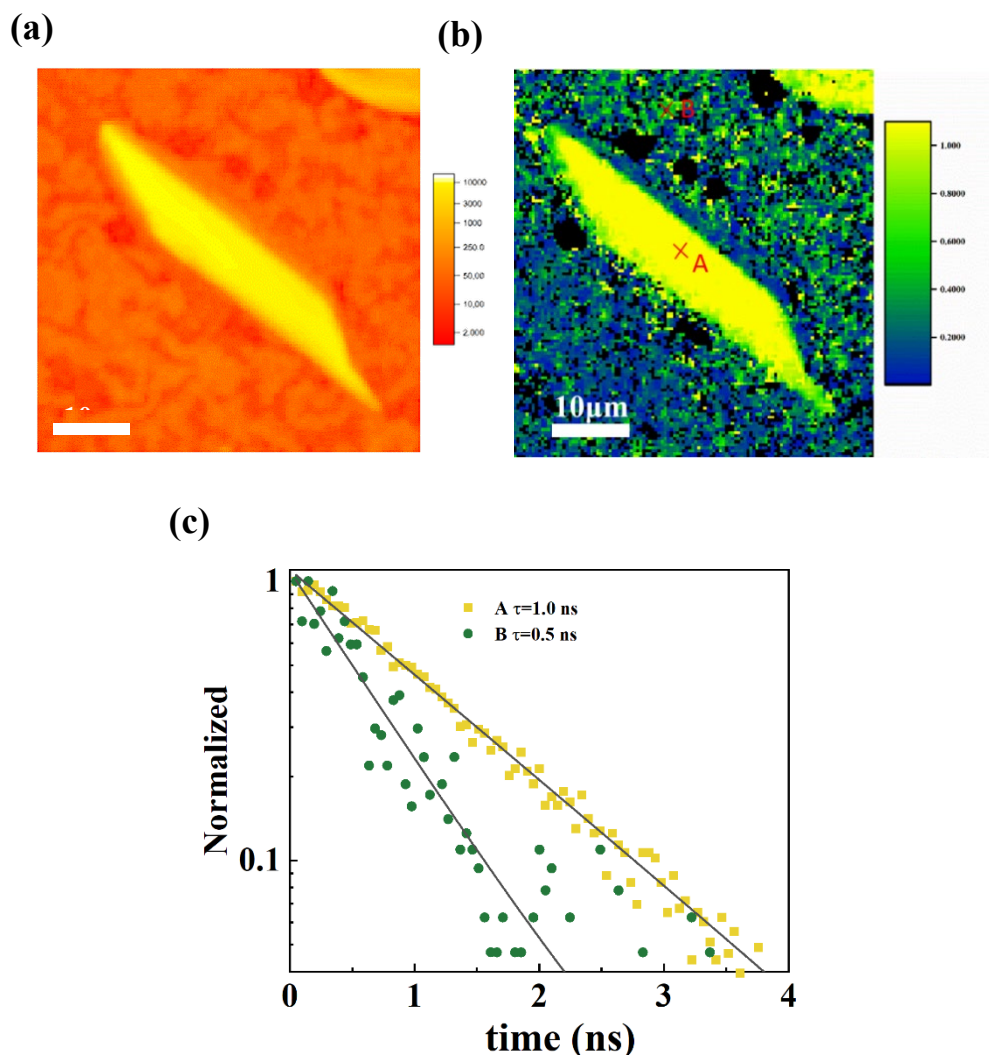
Figure 5.4 *(a) CW-PL intensity map and (b) exciton lifetime map obtained by fitting the TR-PL spectra of a thin film of TPD$_{C8}$-TAT$_{C8}$ containing crystalline needles with a decreasing mono-exponential function. Both CW-PL and TR-PL measurements were obtained through a microscope under laser excitation at 950 nm (two photons absorption) with an excitation power of 70 µw. (c) Fits by a mono-exponential function of TR-PL decays at points A and B in Figure 5.4 (b), and the data point was calculated by Ph.D. Antoine Mattern using MATLAB.*

5.3.4 Exciton diffusion length in TPD$_{C8}$-TAT$_{C8}$

As already written, a long exciton diffusion length in OSCs is a key factor to get high performances of OPV devices[3, 23-25]. Since TPD$_{C8}$-TAT$_{C8}$ is the derivative presenting the longest lifetime, it is a promising molecule for obtaining a long exciton diffusion length. We thus studied the exciton diffusion length in TPD$_{C8}$-TAT$_{C8}$ molecular thin-films only. In particular, we sought to answer the following question: how does the

molecular self-assembly (from as-deposited state to the crystalline state) impact the exciton diffusion length?

In this section, the evolution of the exciton diffusion length measured by PLQY and EEA theory techniques for different solid-states will be discussed.

Generally, the characteristic exciton diffusion length L_D is defined as[1]:

$$L_D = \sqrt{ZD\tau} \quad (5.1)$$

Where Z is equal to 1, 2 and 3 for exciton diffusion in one, two, and three dimensions and D is the exciton diffusion coefficient. As discussed by A. Köhler and H. Bässler[26], it is common in the organic semiconductor community to use $Z=1$ to define L_D even though the transport is 3D. Thus, we assume $Z=1$ in this thesis. τ is the exciton lifetime.

5.3.4.1 Exciton diffusion length from PLQY theory

Exciton diffusion in molecular OSCs occurs via a hopping mechanism mediated by FRET. In this theoretical framework, the exciton diffusion coefficient D can be estimated from the overlap of absorption and emission spectra of the chromophores (acceptor and donor, respectively), and can be expressed as[27]:

$$D = \frac{a^2}{6\tau_{hop}} \quad (5.2)$$

Where a is the inter-chromophore distance, assumed to be the shortest intermolecular distance obtained from X-ray diffraction (i.e., π-π distance equal to 0.38 nm) shown in **Figure 4.4**. τ_{hop} is the exciton hopping time. $1/\tau_{hop}$ is the Förster rate, also named k_F, which is given from the FRET theory[5]:

$$\frac{1}{\tau_{hop}} = k_F = \tau \left[\frac{a}{R_0}\right]^6 \quad (5.3).$$

Where R_0 is the Förster radius (distance between chromophores for 50% FRET efficiency). τ is the fluorescence lifetime in film. From Equation (5.1), (5.2) and (5.3), the diffusion length can thus be written as[27]:

$$L_D = \frac{1}{\sqrt{6}} \frac{R_0^3}{a^2} \quad (5.4)$$

Where the Förster radius R_0 can be calculated from the spectral overlap of the molar extinction coefficient (as shown in **chapter A5**) and the normalized PL spectrum (**Figure 5.5**) [28]:

$$R_0^6 = \frac{9\phi_{PL}\kappa^2}{128\pi^5 n^4} J \quad (5.5)$$

Where κ^2 is the relative orientation of dipoles (for rigid and randomly oriented dipoles, $\kappa^2 = 0.476$)[2], ϕ_{PL} is the PLQY of the film (experimental details are shown in chapter A5 and the corresponding data are presented in **Table 5.5**), n is the average refractive index in the wavelength range at which spectral overlap is significant; n was obtained using spectral ellipsometry (as shown in **Figure A5.7** – the corresponding data are shown in **Table 5.5**). Finally, J is the overlap integral between the normalized emission spectrum of the donor chromophore and the absorption spectrum of the acceptor chromophore (J has been computed by the software DecayFit-ae, the data are shown in **Table 5.3**). Here J (in M^{-1}cm^{-1}nm^4) is defined by[1]:

$$J(\lambda) = \int_0^\infty \varepsilon_A(\lambda)\lambda^4 F_D(\lambda)d\lambda \quad (5.6)$$

$\varepsilon_A(\lambda)$ is the molar extinction coefficient of the acceptor chromophore in thin film (represented in black solid lines in **Figure 5.5**), the corresponding calculations are shown in the **chapter A5**. $F_D(\lambda)$ is the emission spectrum of the donor chromophore (corresponding to the normalized CW-PL spectrum, represented in blue dotted lines in **Figure 5.5**). Finally, from Equation (5.4), and (5.5) the diffusion length (**Table 5.4**) can thus be written as[5, 27]:

$$L_D = \frac{1}{\sqrt{6}} \sqrt{\frac{9\kappa^2 \phi_F}{128\pi n^4 a^4} J} \quad (5.7)$$

(a)

(b)

(c)

(d)
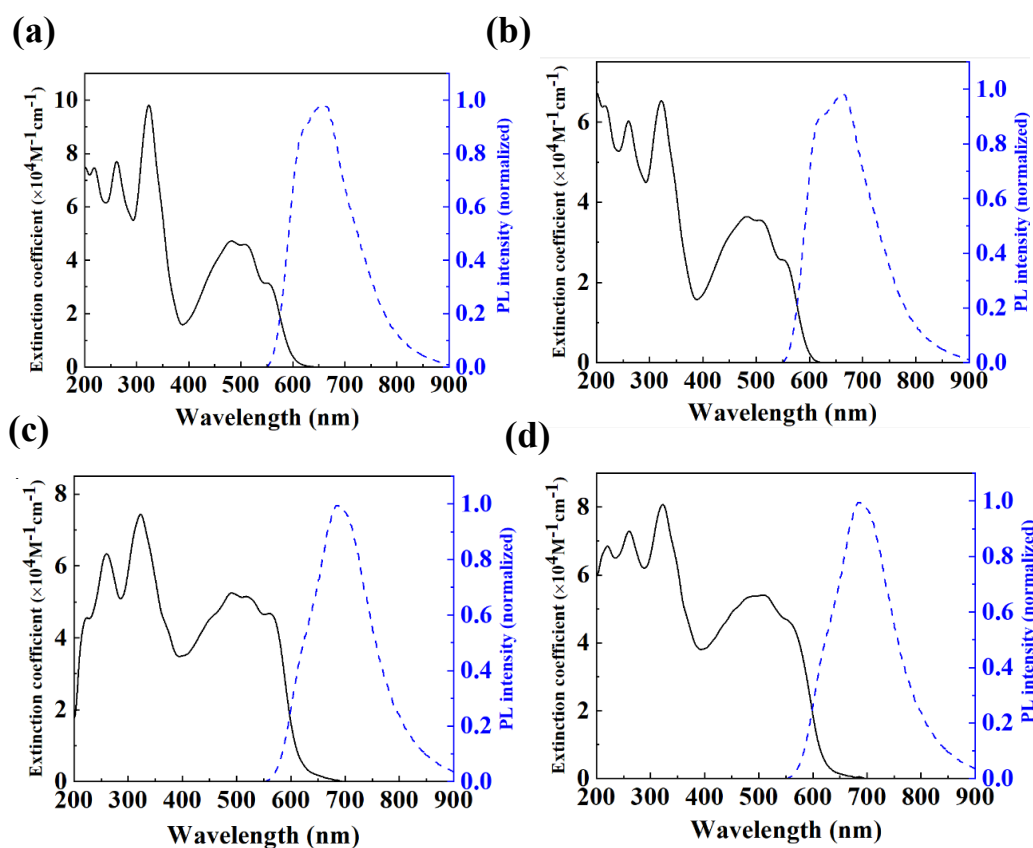
Figure 5.5. Molar extinction coefficient (black lines) obtained using spectral ellipsometry and normalized PL spectra (blue dotted lines) of films spin-coated on quartz substrates for (a) as deposited, (b) nematic, (c) small crystalline needles, (d) big crystalline needles. The absorption (abs), and thus the molar extinction coefficient, of the crystalline state is underestimated because the crystalline state has a low fill factor (F) on the surface of the quartz. We use ImageJ to estimate the proportion of crystal occupied area on the surface of the quartz. The fill factor is around 0.50 for the small crystals, and 0.30 for big crystals. The absorption of crystalline states is estimated to be equal to abs/F.

Table 5.5: *Exciton diffusion length obtained from the PLQY theory technique.*

TPD$_{C8}$-TAT$_{C8}$	k^2	n^1	J (nm^4/(M*cm))	Φ_{PL}	R_0 (nm)	a (nm)	L_D (nm)
As-deposited	0.476	1.88±0.05	1.43×10^{14}	0.023±0.01	3.3	0.38	10.5±1.0
Nematic	0.476	1.54±0.05	9.11×10^{13}	0.024±0.01	3.5	0.38	12.7±1.0
Small crystal	0.476	1.79±0.10	2.60×10^{14}	0.044±0.03	4.2	0.38	21.5±1.5
Big crystal	0.476	1.79±0.10	2.60×10^{14}	0.052±0.05	4.3	0.38	23.5±1.5

[1]*The measurement of n by ellipsometry is not suitable for small crystals due to strong light scattering caused by a high surface roughness. In contrast, n could be measured for large crystals by focusing on a crystal. We assume that n is the same for both crystal sizes.*

Applying the PLQY theory (**Equation 5.7**) to TPD$_{C8}$-TAT$_{C8}$ thin-films in different states: as-deposited, nematic and crystalline (big or small needles) states, allowed us to estimate the exciton diffusion length as a function of the solid state (**Table 5.5**). The value found in the as-deposited state (10.5±1.0nm) is close to that of the nematic state (12.7±1.0nm), while the one in small crystals (21.5±1.5nm) is close to those big crystals (23.5±1.5nm). These results are in agreement with the CW-PL and TR-PL measurements: CW-PL spectra and TR-PL transients perfectly overlap for as-deposited and nematic states, and the same is observed for different crystal sizes, revealing that the exciton is localized in a similar environment in as-deposited and nematic states on the one hand, and in crystalline state no matter the crystal size on the other hand. Importantly, exciton diffusion length is doubled from the as-deposited (or nematic) state to the crystalline state indicating that more ordered molecular stacking organization favor exciton diffusion. To confirm the diffusion lengths estimated by PLQY, a second method to estimate L_D has been applied.

5.3.4.2 Exciton diffusion length from EEA theory

As previously explained, in the case of high density of excitons, the exciton may encounter each other and annihilate, causing a faster decay of fluorescence. This phenomenon can be used to determine a statistical average exciton diffusion length. To

do this, the initial population of excitons and the evolution of the exciton population as a function of time must be determined as a function of light intensity. The initial population of excitons *N(0)* is determined by a number of absorbed photons per illuminated volume of the thin-films, using[11]:

$$N(0) = \frac{E_P}{V}\frac{\lambda}{hc}(1 - 10^{-A}) \quad (5.8)$$

Where, E_p is the excitation pulse energy, V is the volume of the film illuminated by the excitation beam (V is determined by the laser spot area and thin-films thickness), λ is the excitation wavelength, h is Planck's constant, c is the light speed in air, and A is the absorbance of the film at the excitation wavelength. The fluorescence intensity at time *t* is proportional to the exciton population *N(t)* which can be described by the rate equation[29]:

$$\frac{dN(t)}{dt} = G - kN(t) - \gamma N(t)^2 \quad (5.9)$$

Where *G* is the exciton generation rate, $k = 1/\tau$ is the exciton decay rate measured at low initial exciton population ($< 10^{16}$ cm^{-3}, assuming no EEA, as shown in **Figure 5.6**), and γ is the annihilation rate. For instantaneous exciton generation and time-independent γ, the reciprocal of the analytical solution to **Equation 5.9** can be written as[30]:

$$\frac{1}{N(t)} = \left(\frac{1}{N(0)} + \frac{\gamma}{k}\right)\exp(kt) - \frac{\gamma}{k} \quad (5.10)$$

The global linear fits (fit multiple datasets into a single curve) to this dependence for different excitation densities (**Figure 5.7**) give a single value of the annihilation rate γ for each film. For systems with an exciton diffusion in one-dimension, the annihilation rate is limited by diffusion and can be described by the solution of the equation[29, 31]:

$$\gamma = 4\pi R_a D (1 + \frac{R_a}{\sqrt{2\pi Dt}}) \quad (5.11)$$

where R_a is the annihilation radius and D is the exciton diffusion coefficient. Here, it is assumed that only one exciton is lost per encounter. A typical value of R_a in OSCs is around 1 nm [6, 30]. Since the exciton diffusion and the annihilation rate are time-independent on a long-time scale,[1, 30] the time-dependent component becomes negligible for $t > 0.35$ ns (as shown in **Figure A5.9**) and **Equation 5.11** can be simplified to the time-independent part[31]:

$$\gamma = 4\pi R_a D \quad (5.12)$$

We determined the exciton diffusion length of TPD$_{C8}$-TAT$_{C8}$ thin-films in different states: as-deposited, nematic, crystalline (big or small needles) states (**Figure A5.8**). following to the EEA method. The experimental and computational procedures are explained below. Firstly, as shown in **Figure 5.6**, different excitation densities were carried out on each thin-film. With increasing excitation density, the decay becomes faster due to the occurrence of EEA. As a reminder, the measurements were carried out in such a way as to ensure the absence of photobleaching, which could also be the cause of a reduction in the measured lifetime (see experimental section of chapter 5). Secondly, we plotted the graph $1/N(t)$ as a function of $Exp(kt)$ (**Figure 5.7)** and then we get γ (**Table 5.6**) through global linear fits by using Equation (5.10). Thirdly, D (**Table 5.6**) was obtained by using Equation (5.12). Finally, the average one-dimension exciton diffusion length (**Table 5.5**) can be computed with Equation 5.1 and Equation 5.12. The exciton diffusion length (**Table 5.5**) in as-deposited state (16.0±1.0nm) is close to that of the nematic state (18.0±1.0nm), and the one in small crystals (25.0±2.0nm) close to that of big crystals (30.0±2.0nm). Importantly, the tendency of EEA and PLQY results are in agreement despite different working hypotheses. In both cases the exciton diffusion length is doubled from the as-deposited (or nematic) state to the crystalline state (**Figure. 5.8**).
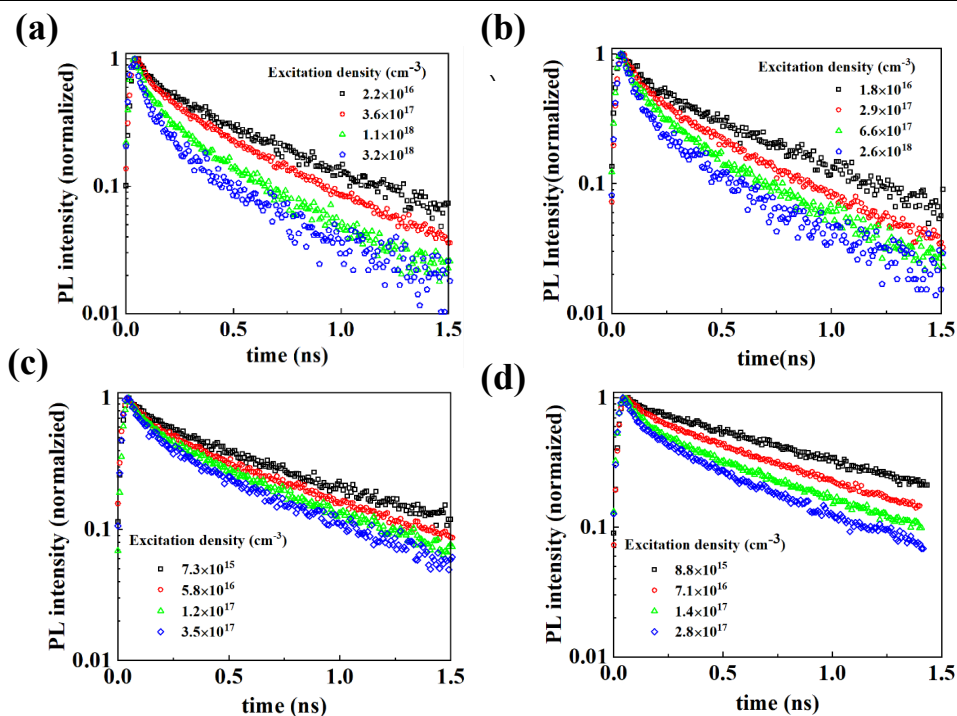
Figure 5.6: *TRPL transients measured in a wavelength range of 580-680 nm for different molecular states: (a) as-deposited, (b) nematic, (c) small crystals, (d) big crystals and for different initial excitation densities.*
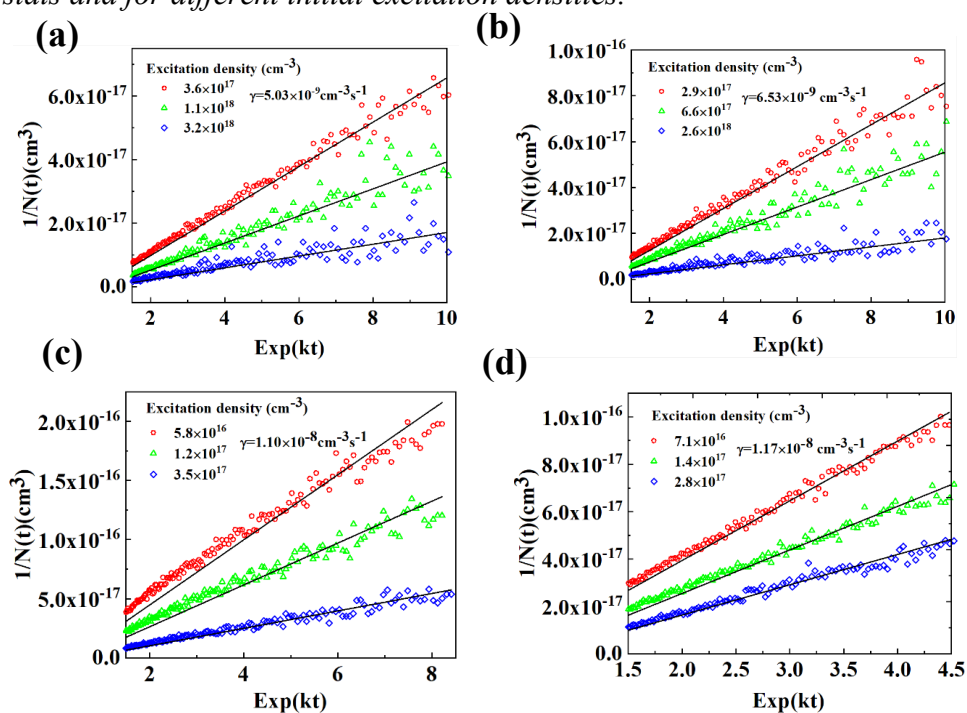

Figure 5.7: *The reciprocal of exciton density vs exp (kt)(dots) in different molecule states: (a) as-deposited, (b) nematic, (c) small crystals, (d) big crystals and global linear fits to equation (5.10) (lines) with γ values given in the insets.*

Table 5.6: *Exciton diffusion length determined from the EEA theory.*

States	γ(cm³s⁻¹)	R_a(nm)	D(cm²s⁻¹)	τ(ns)	L(nm)
As-deposited	5.03×10^{-9}	1.0	4.00×10^{-3}	0.6	16.0 ± 1.0
Nematic	6.53×10^{-9}	1.0	5.20×10^{-3}	0.6	18.0 ± 1.0
Small crystal	1.10×10^{-9}	1.0	8.76×10^{-3}	0.8	25.0 ± 2.0
Big crystal	1.17×10^{-9}	1.0	9.87×10^{-3}	0.9	30.0 ± 2.0

To sum up, we used two techniques (EEA and PLQY) to study the relationship between exciton diffusion length and different TPD$_{C8}$-TAT$_{C8}$ thin-film states. The results show that an increasing order in the molecular self-assembly has a notable beneficial effect on the exciton diffusion. Exciton diffusion length and diffusion coefficients increase after the annealing of as-deposited thin-films, but do not change significantly with the growth of the crystals. The PLQY results show the exciton diffusion length to increase from L_D=10.5±1.0 nm to L_D=23.5±1.5 nm and the diffusion coefficient from $(1.8\pm0.5)\times10^{-3}$ cm²s⁻¹ to $(5.5\pm1.3)\times10^{-3}$ cm²s⁻¹ ·from as-deposited to crystalline states. When measured using the EEA theory technique, the exciton diffusion length and diffusion coefficient increase from L_D=16.0±1.0 nm and D= $(4.0\pm1.0)\times10^{-3}$ cm²s⁻¹ in the as-deposited, to L_D=30.0±2.0 nm and D=$(9.87\pm1.0)\times10^{-3}$ cm²s⁻¹ for big crystals. Furthermore, the exciton diffusion coefficient and length are roughly independent on the crystal size. Our results differ from several reports on other OSCs, which found the exciton diffusion length to increase with increasing crystal size, a behavior that was attributed to the reduction of non-radiative losses at grain boundaries[1, 2, 5]. For instance, Y. Zhang et al.[31] demonstrated that increasing the crystal size of PffBT4T-2OD from 12 nm to 29 nm upon thermal annealing, leads to an increase of the exciton diffusion length from 14 to 24 nm. Lunt et al.[5] showed that the exciton diffusion length of PTCDA increased from 6 to 20 nm as the crystal size is enhanced from 100 to 400 nm. We note that in our case the crystal sizes are at the micron-level, which is much larger than the maximum singlet exciton diffusion length (at a few tens of nanometer-level), and possible the reason why the diffusion length is independent of the crystal size.
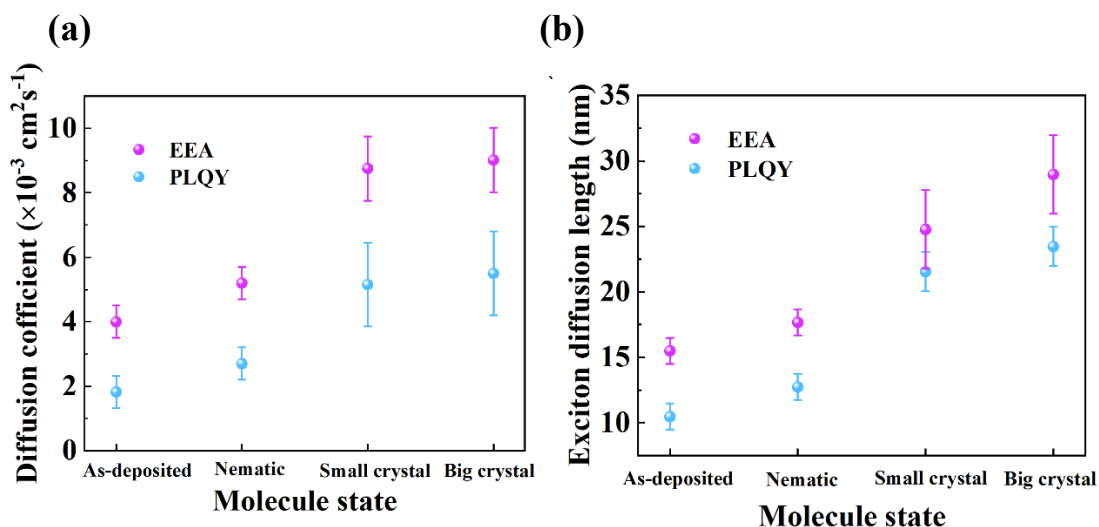
Figure 5.8 *(a) Diffusion coefficient and (b) Exciton diffusion length for different solid-states. The small crystal size is around 8.0 μm and the big crystal size is around 25.0 μm.*

Comparing both techniques (EEA and PLQY), the exciton diffusion length measured by EEA is slightly longer than that determined by PLQY. This difference may arise from the fact that both methods rely on different assumptions. In the PLQY theory, the dipole orientation factor κ^2 was assumed to be equal to 0.476, corresponding to rigid and randomly oriented dipoles. This dipole orientation factor can be maximized when all the transition dipoles are aligned, which may occur in single crystals and thus achieve in this condition a maximum value of $\kappa^2 = 4$[2, 8]. Therefore, the exciton diffusion length can be theoretically increased by almost a factor of 3 (according to Equation 5.7) for crystals compared to amorphous films. In our work, we assume that the value of κ^2 is 0.476 for all thin-films no matter their state; thus, the exciton diffusion length has been underestimated in the crystalline state (or LC) by PLQY. For the EEA technique, the annihilation radius R_a is assumed to be equal to 1.0 nm. However, in some reports, the d_{100}-spacing distance is used for the value of R_a[32], which is certainly different from 1.0 nm. Thus, our exciton diffusion length determined from the EEA theory could be different because of the value of R_a. Nevertheless, the relative variation for the exciton

diffusion length and coefficient in the different self-assembly organization is similar for both techniques (EEA and PLQY).

5.4 Conclusion

In summary, through the investigation of the exciton lifetime for different chemical and self-assembly structures in TPD-TAT derivatives, we showed that the side-chain nature on TPD and TAT units and the solid-states have a strong impact on their exciton lifetime. In particular, the exciton lifetime significantly increased from the as-deposited to the crystalline states, exceeding the lifetime measured in solution. These results may possibly be due to a decrease in the defect density in crystalline films (in comparison to as-deposited states) and to a non-polar environment in the crystalline state resulting in lower non-radiative recombination rates (although first measurements of the influence of polarity on the molecules did not allow us to confirm the latter proposition). Moreover, we revealed that non-exponential PL decay in OSCs is likely due to the co-existence of different molecular solid-states in a same thin-film. Finally, we have successfully computed the exciton diffusion length in TPD$_{C8}$-TAT$_{C8}$ thin-films for different states by using EEA and PLQY techniques. A significant increase in the diffusion length from the as-deposited to the crystalline states has been observed and is the outcome of both, a higher lifetime and a higher diffusion coefficient. Generally, a high intermolecular coupling leads to an increase in the exciton diffusion coefficient but to a decrease in the exciton lifetime. In our work, we have shown that both parameters increase, making the TPD-TAT derivatives excellent candidates for applications where long exciton diffusion lengths are required.

References:

[1]   J. D. A. Lin, O. V. Mikhnenko, J. Chen, Z. Masri, A. Ruseckas, A. Mikhailovsky, R. P. Raab, J. Liu, P. W. M. Blom, M. A. Loi, C. J. García-Cervera, I. D. W.

Samuel and T.-Q. Nguyen, *Materials Horizons*, 2014, **1**, 280-285.

[2]   O. V. Mikhnenko, P. W. M. Blom and T.-Q. Nguyen, *Energy & Environmental Science*, 2015, **8**, 1867-1888.

[3]   M. T. Sajjad, A. Ruseckas and I. D. W. Samuel, *Matter*, 2020, **3**, 341-354.

[4]   D. Yeboah and J. Singh, *Journal of Electronic Materials*, 2017, **46**, 6451-6460.

[5]   R. R. Lunt, J. B. Benziger and S. R. Forrest, *Advanced Materials*, 2010, **22**, 1233-1236.

[6]   A. J. Lewis, A. Ruseckas, O. P. M. Gaudin, G. R. Webster, P. L. Burn and I. D. W. Samuel, *Organic Electronics*, 2006, **7**, 452-456.

[7]   S. Cook, A. Furube, R. Katoh and L. Han, *Chemical Physics Letters*, 2009, **478**, 33-36.

[8]   S. M. Menke and R. J. Holmes, *Energy Environ. Sci.*, 2014, **7**, 499-512.

[9]   T. Han, I. Bulut, S. Méry, B. Heinrich, P. Lévêque, N. Leclerc and T. Heiser, *Journal of Materials Chemistry C*, 2017, **5**, 10794-10800.

[10]   F. C. Spano, J. Clark, C. Silva and R. H. Friend, *The Journal of Chemical Physics*, 2009, **130**, 074904.

[11]   Y. Long, G. J. Hedley, A. Ruseckas, M. Chowdhury, T. Roland, L. A. Serrano, G. Cooke and I. D. W. Samuel, *ACS Applied Materials & Interfaces*, 2017, **9**, 14945-14952.

[12]   P. Ehrenreich, S. T. Birkhold, E. Zimmermann, H. Hu, K.-D. Kim, J. Weickert, T. Pfadler and L. Schmidt-Mende, *Scientific Reports*, 2016, **6**, 32434.

[13]   A. Oleson, T. Zhu, I. S. Dunn, D. Bialas, Y. Bai, W. Zhang, M. Dai, D. R. Reichman, R. Tempelaar, L. Huang and F. C. Spano, *The Journal of Physical Chemistry C*, 2019, **123**, 20567-20578.

[14]   S. R. Marques, J. A. Labastide and M. D. Barnes, *The Journal of Physical Chemistry C*, 2018, **122**, 15723-15728.

[15]   S. M. Menke and R. J. Holmes, *Energy & Environmental Science*, 2014, **7**, 499-512.

[16]   M. Ban, Y. Zou, J. P. Rivett, Y. Yang, T. H. Thomas, Y. Tan, T. Song, X. Gao, D. Credgington and F. Deschler, *Nature communications*, 2018, **9**, 1-10.

[17]   O. V. Mikhnenko, J. Lin, Y. Shu, J. E. Anthony, P. W. M. Blom, T.-Q. Nguyen and M. A. Loi, *Physical Chemistry Chemical Physics*, 2012, **14**, 14196-14201.

[18]   B. Lin, X. Zhou, H. Zhao, J. Yuan, K. Zhou, K. Chen, H. Wu, R. Guo, M. A. Scheel and A. Chumakov, *Energy & Environmental Science*, 2020, **13**, 2467-2479.

[19]   S. R. Forrest, *Philosophical Transactions of the Royal Society A: Mathematical, Physical and Engineering Sciences*, 2015, **373**, 20140320.

[20]   M. Gerhard, B. Louis, R. Camacho, A. Merdasa, J. Li, A. Kiligaridis, A. Dobrovolsky, J. Hofkens and I. G. Scheblykin, *Nature communications*, 2019, **10**, 1-12.

[21]   A. M. Müller, Y. S. Avlasevich, K. Müllen and C. J. Bardeen, *Chemical physics letters*, 2006, **421**, 518-522.

[22]   A. Classen, C. L. Chochos, L. Lüer, V. G. Gregoriou, J. Wortmann, A. Osvet, K. Forberich, I. McCulloch, T. Heumüller and C. J. Brabec, *Nature Energy*, 2020, **5**, 711-719.

[23]   S. M. Menke, W. A. Luhman and R. J. Holmes, *nature materials*, 2013, **12**, 152-157.

[24]   T. K. Mullenbach, I. J. Curtin, T. Zhang and R. J. Holmes, *Nature Communications*, 2017, **8**, 14215.

[25]   R. C. Powell, *Journal of Luminescence*, 1975, **11**, 1-45.

[26]   A. Köhler and H. Bässler, *Electronic processes in organic semiconductors: An introduction*, John Wiley & Sons, 2015.

[27]   R. R. Lunt, N. C. Giebink, A. A. Belak, J. B. Benziger and S. R. Forrest, *Journal of Applied Physics*, 2009, **105**, 053711.

[28]   Y. Firdaus, V. M. Le Corre, S. Karuthedath, W. Liu, A. Markina, W. Huang, S. Chattopadhyay, M. M. Nahid, M. I. Nugraha, Y. Lin, A. Seitkhan, A. Basu, W.

Zhang, I. McCulloch, H. Ade, J. Labram, F. Laquai, D. Andrienko, L. J. A. Koster and T. D. Anthopoulos, *Nature Communications*, 2020, **11**, 5220.

[29]   P. E. Shaw, A. Ruseckas, J. Peet, G. C. Bazan and I. D. W. Samuel, *Advanced Functional Materials*, 2010, **20**, 155-161.

[30]   P. E. Shaw, A. Ruseckas and I. D. W. Samuel, *Advanced Materials*, 2008, **20**, 3516-3520.

[31]   Y. Zhang, M. T. Sajjad, O. Blaszczyk, A. J. Parnell, A. Ruseckas, L. A. Serrano, G. Cooke and I. D. W. Samuel, *Chemistry of Materials*, 2019.

[32]   M. T. Sajjad, O. Blaszczyk, L. K. Jagadamma, T. J. Roland, M. Chowdhury, A. Ruseckas and I. D. W. Samuel, *Journal of Materials Chemistry A*, 2018, **6**, 9445-9450.

Chapter 6
Charge carrier transport

Space-Charge-Limited Current (SCLC) devices, Organic field-effect transistors (OFET)

Planar conjugated molecular backbones are essential for achieving high charge carrier mobilities along molecular π-stacking directions but are often concomitant with poor charge transport in other directions. This is particularly the case for molecules that are functionalized with alkyl chains, which ensure good processability in solution but introduce detrimental insulating regions. In chapter 4, we have already shown that the TAT derivatives form a columnar-nematic mesophase in which columns of stacked TAT units spaced by molten chains are interconnected by TPD bridges. Upon annealing, a crystalline phase, stemming from the parent hexagonal mesophase, is obtained with the molecular π-stacking direction lying in-plane. This particular stacking network (as illustrated in **Figure 4.3c**) in both columnar-nematic mesophase and crystalline phase might be able to break through the limitations of insulating aliphatic periphery of the columns and facilitate efficient 3-dimensional charge carrier transport.

This chapter is dedicated to charge transport investigations in TPD$_{C8}$-TAT$_{C8}$. Firstly, the motivation for investigating charge transport in planar soluble molecules will be given in part 6.1. In part 6.2, the working principle of SCLC (space-charge-limited-current) and OFET (organic field-effect transistor) devices, which are used to probe charge transport, are described. The out-of-plane (measured by SCLC) and in-plane (measured by OFET) mobilities measured in TPD$_{C8}$-TAT$_{C8}$ thin films will be presented and discussed in part 6.3. Please note that the results presented in this chapter have been published in the article: "Efficient 3D charge transport in planar triazatruxene-based dumbbell-shaped molecules forming a bridged columnar phase, *J. Jing et al., J. Mater. Chem. A, 2021, 9.*"

6.1 Introduction

Charge transport is known to be a limiting factor in the performance of organic electronic and photovoltaic devices. Much efforts have therefore been devoted to better

understand the relationships between molecular structure, self-assembling and charge transport and to develop materials with high charge carrier mobilities[1-6]. As strong intermolecular coupling and high structural order are recognized prerequisites for efficient charge transport[7, 8], many planar conjugated units such as triphenylene[9], dinaphtho-thieno-thiophene (DNTT)[10, 11], [1]benzothieno[3,2-*b*]benzothiophene (BTBT) derivatives[12], polycyclic aromatic hydrocarbons (PAHs)[13], or triazatruxene (TAT)[14, 15] have been used as molecular building blocks[16-18] and led to some of the highest mobilities reported so far for molecular semiconductors[15]. However, beyond molecular planarity, charge transport anisotropy is another critical parameter that must be taken into account when seeking to improve charge transport. Indeed, S. Fratini et al. have recently shown that the degree of charge transport anisotropy determines the impact of dynamic disorder on charge carrier mobility[1, 19]. Their results imply that molecular packings leading to isotropic transfer integrals are more tolerant against disorder-induced carrier localization and are therefore more prompt to achieve high mobilities. In addition, isotropic charge transport also simplifies the elaboration of efficient organic devices by avoiding the requirement to align the high mobility axes with the charge flow direction (i.e., in-plane for field-effect transistors or out-of-plane for light emitting diodes or solar cells). Yet, with the exceptions of herringbone-type assemblies, common ordered molecular solid-state packings lead to intermolecular transfer integrals that are highly anisotropic[1]. In the particular case of planar molecules that can be processed from solution, strong molecular π-π stacking interactions often result in efficient charge transport along the molecular stacking, while the solubilizing alkyl chains hinder charge transfer in perpendicular directions[20-23]. For instance, discotic molecules based on soluble TAT derivatives generally self-assemble into columnar structures that allow efficient carrier transport along the columnar direction only, giving rise essentially to one-dimensional transport[22]. Designing soluble planar molecular semiconductors that lead to strong π-stacking interactions while allowing efficient 3D charge transport is thus still a challenging and important target for organic

electronics. In this context, the recent synthesis of a new family of donor (D)-acceptor (A)-donor (D) type molecules based on two TAT electron donor units and a central thiophene-thienopyrroledione-bithiophene (TPD) unit, reported by Han et al.,[23] is of particular interest. Indeed, one of these D-A-D compounds was found to support 3D charge transport despite the self-assembling into a columnar mesophase similar to those of other discotic TAT derivatives[15]. First evidence for efficient 3D transport was provided by the promising out-of-plane and in-plane hole mobilities, of the order of $10^{-3} cm^2 V^{-1}s^{-1}$, measured in as-deposited films[23]. The presence of two planar TAT units as molecular end-groups may possibly be at the origin of this astonishing property, since these two TAT units belong to two neighboring columns. However, a full investigation and optimization of the molecular self-assembly of this compound and their consequences on charge transport is still lacking.

In this chapter, we explored the charge transport properties of this TAT-based dumbbell-shaped derivative in greater depth in order to elucidate and take advantage of the unique structural properties of this molecule for achieving efficient 3D charge transport. The out-of-plane hole mobility was measured in space-charge limited current (SCLC) devices and reached a maximum SCLC mobility of 0.17 $cm^2 V^{-1}s^{-1}$ for the crystalline state. This value is close to the highest mobility reported to date for soluble small molecules[24], which was measured along the columns of a discotic TAT derivative. A lower limit of 0.05 $cm^2V^{-1}s^{-1}$ was found for the in-plane hole mobility in field-effect transistors. Importantly, the structural investigations (as shown in chapter 4) demonstrate that the efficient out-of-plane carrier transport occurs along a direction perpendicular to the molecular stacking, in strong contrast with the properties of other TAT-based discotic molecular semiconductors. Overall, our results show that this remarkable behavior can be linked to the self-assembly of this TAT-based dumbbell-shaped derivative into an unusual and distinctive molecular network that comprises efficient transport pathways along three dimensions. Finally, although performances

are still low compared to best liquid-crystalline 2D semiconductors[25], the bridged columnar architecture represents a versatile alternative to other promising liquid-crystalline 3D structures such as bi-continuous cubic phases[26].

6.2 Charge transport measurement

6.2.1 SCLC measurement

In this part, the working principle of SCLC devices will be described. The fabrication process detail of "standard SCLC devices" and "thick SCLC devices" will be presented in the annex of chapter A6. The annealing steps, that were employed to put the molecules in a given solid phase, have been described in chapter 4.

In SCLC measurements, an OSC materials of thickness L is sandwiched between two contacts (**Figure 6.1a**). The evolution of the current with the applied voltage is recorded and the two regimes can be distinguished, as shown in **Figure 6.1b**. For electrically conducting materials, the dielectric relaxation time (τ_{relax}) is defined as the time necessary for the charges to restore the local electric neutrality after charge injection (**Figure 6.1c**). It is given by[27]:

$$\tau_{relax} = \frac{\varepsilon_0 \cdot \varepsilon_r}{\sigma} \quad (6.1)$$

Where ε_0 is the dielectric constant in vacuum, ε_r is the relative dielectric constant and σ is the electrical conductivity. On the other hand, the time-of-flight (τ_{flight}) describes the time it takes for the injected charges to cross the OSCs under an applied voltage. It is given by[27]:

$$\tau_{flight} = \frac{L^2}{\mu \cdot V} \quad (6.2)$$

121

Where L is the thickness of the active layer, μ is the out-of-plane mobility and V is the applied voltage. If τ_{flight} is far higher than τ_{relax} ($\tau_{flight} \gg \tau_{relax}$), (Ohmic part in **Figure 6.1b**), the current follows the Ohm's law[27]:

$$J_{ohmic} = \mu \cdot q \cdot p_0 \cdot \frac{V}{L} \quad (6.3)$$

Where p_0 is the background charge carrier density. However, the conductivity of OSCs is low, and τ_{relax} is often much higher than τ_{flight} ($\tau_{relax} \gg \tau_{flight}$). As a consequences, Ohm's law is no valid anymore, while Mott-Gurney's law would apply (SCLC part in **Figure 6.1b**)[27]:

$$J = \frac{9\varepsilon_0\varepsilon_r}{8} \cdot \mu \cdot \frac{V^2}{L^3} \quad (6.4)$$
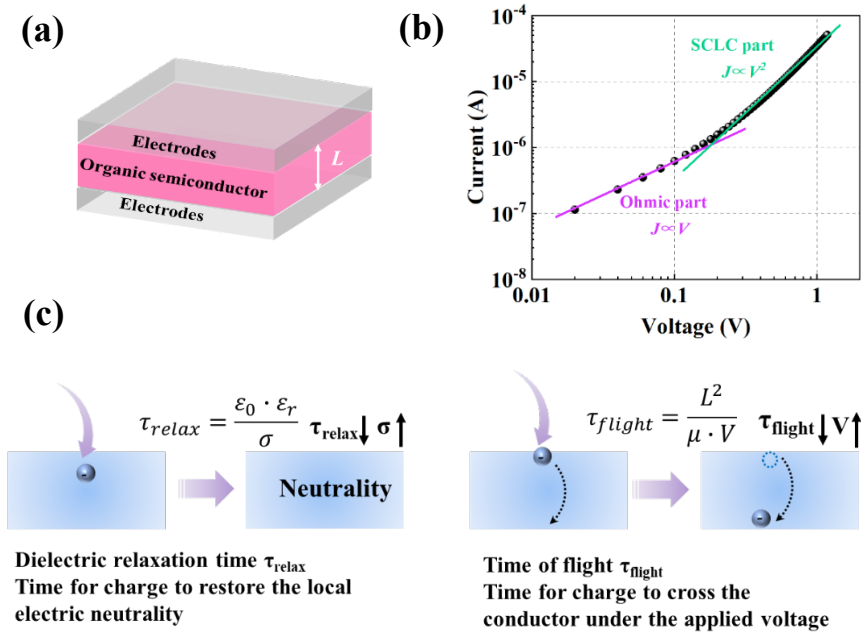
Figure 6.1 *(a) SCLC device. (b) J-V cure of SCLC measurement. (d) Schematic diagram of time-of-flight.*

6.2.2 OFET measurement

In this thesis, the in-plane hole mobility has been characterized by both bottom-contact-bottom-gate and top-contact-bottom-gate transistors as described above. Details of the working principle of the OFET devices are described in this part. The fabrication process for both kinds of transistors will be presented in the annex of chapter A6. The annealing steps, that were employed to put the molecules in a given solid phase, have been described in chapter 4.

In the OFET devices, on the one hand, applying a voltage between the gate and the source electrodes (V_{gs}), an electric-field is induced that charge carriers accumulated at the OSCs/insulator interface. On the other hand, applying a voltage between source and drain electrodes (V_{ds}), the electric-field drive the charge carrier pass through the channel length and a source-drain current (I_{ds}) will generate[28, 29].

When V_{gs} larger than threshold voltage (V_{th}) is applied and with a small V_{ds}, $V_{ds} \ll V_{gs}$-V_{th}, charge carriers will uniform distribution in the channel and the device is operating in the linear regime (as shown in **Figure 6.2a** and **6.3a-b**). In the liner regime, the $I_{ds,lin}$ increases with the applied V_{ds}, following below equation[30]:

$$I_{ds,lin} = \frac{W}{L}\mu_{lin}C_i(V_{gs} - V_{th})V_{ds} \quad (6.5)$$

Where C_i is capacitance of the dielectric, μ_{lin} is the linear regime field-effect mobility. μ_{lin} can thus be given from equation.[30]

$$\mu_{lin} = \frac{L}{C_iW}\frac{\partial I_{ds}}{\partial V_{gs}} \quad (6.6)$$

For larger V_{ds}, $V_{ds} \gg V_{gs}$-V_{th}, as a result, pinch-off phenomenon will occur because the free charge carrier density is zero at drain terminal (as shown in **Figure 6.2b**). The drain

current becomes independent of the drain voltage, this regime is named as saturation regime (as shown in **Figure 6.2c** and **6.3c**). In the saturation regime, $I_{ds,sat}$ following the equation[30]:

$$I_{ds,sat} = \frac{W}{2L} \mu_{sat} C_i \left(V_{gs} - V_{th}\right)^2 \quad (6.7)$$

Where μ_{sat} is the saturation regime field-effect mobility and can be given by the following equation[30]:

$$\mu_{sat} = \frac{2L}{C_i W} \left(\frac{\partial \sqrt{I_{ds}}}{\partial V_{gs}}\right)^2 \quad (6.8)$$

Notably, in field-effect mobilities of OSCs usually increase with charge carrier density, for example, with increasing gate voltage. As a result, the mobilities obtain from the saturation regime are higher than in the linear regime[31].
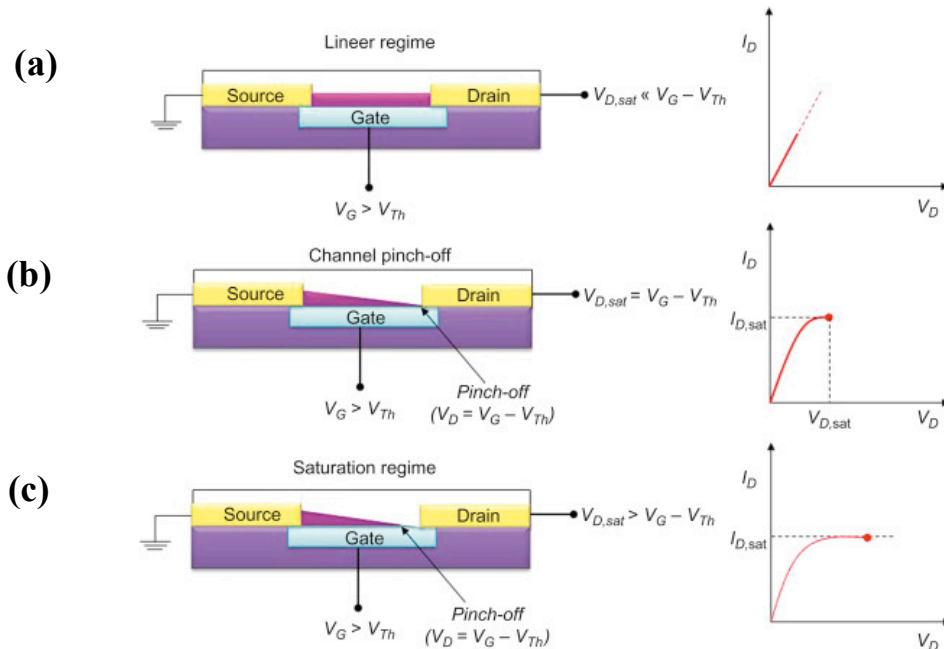
Figure 6.2 *OFET working conditions and corresponding current-voltage characteristics: (a) linear regime condition; (b) start of saturation regime at pinch-off; (c) saturation regime condition. (d) output characteristics indicating the linear and saturation regimes (copyright from Mahmut Kus,et al[28]).*
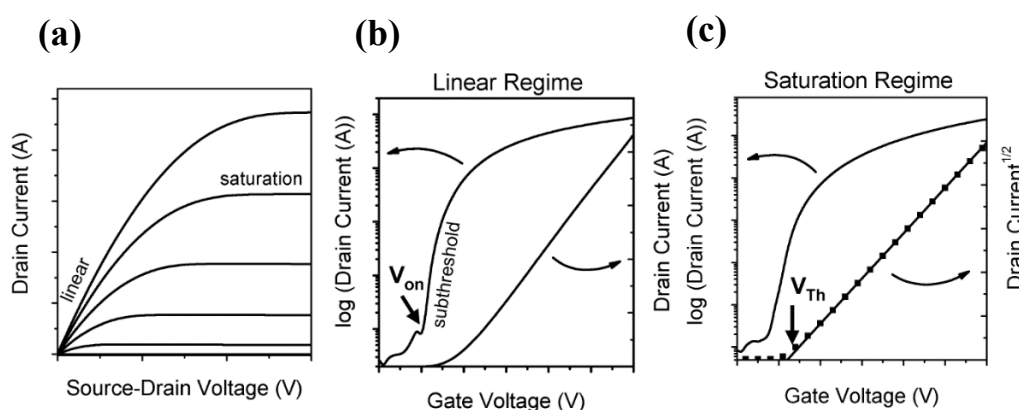
Figure 6.3 *(a) output characteristics indicating the linear and saturation regimes; (b) transfer characteristics in the linear regime, indicating the onset voltage (V_{on}) when the drain current increases abruptly; (c) transfer characteristics in the saturation regime, indicating the threshold voltage V_{th}, where the linear fit to the square root of the drain current intersects with the x-axis. Reproduced from reference Zaumseil, J. et a, Chem. Rev. 2007, 107,1269-1323.*

6.3 Results and discussion

6.3.1 SCLC

Space-charge limited current devices provide a convenient and well-established way to study charge transport in semiconducting thin films perpendicular to the substrate and is also the method we have chosen to investigate out-of-plane charge transport in TPD$_{C8}$-TAT$_{C8}$ thin films[24, 32-34]. As part of this work, two distinct hole-only SCLC device structures have been developed, referred to as "standard" and "thick" devices, respectively (**Scheme A6.1** and **A6.2.** See also annex chapter A6 for experimental details). Standard devices were fabricated by sequential deposition of the hole injection and transporting layers and the organic semiconducting layer, the thickness L of the latter being of the order of a few hundreds of nanometers.

Controlling the semiconductor thickness is crucially important for SCLC measurements, since the current density scales as L^{-3}. Surface roughness can lead to a significant

overestimation of the hole mobility, as shown by numerical simulations in the annex chapter A6 (**Figure A6.1** and **A6.2**). Since crystalline TPD$_{C8}$-TAT$_{C8}$ thin films exhibit a pronounced surface roughness (**Figure A6.3**), we developed the "thick" device structure to minimize the error margin on L. Thick devices consist of an assembly of two ITO-glass substrates coated with thin hole transporting layers and separated by micrometer-sized spacers (**Scheme 6.2b**). The interspace between both substrates is filled by a layer of TPD$_{C8}$-TAT$_{C8}$ powder. The sample is then annealed under mechanical pressure (applied to both substrates) to form either the crystalline or the nematic phase (See annex chapter A6 for experimental details). In contrast to standard devices, the molecular layer thickness is in this case of the order of tens of micrometers and is well-defined even in the crystalline state. For both structures, the annealing conditions and device fabrication are described in more details in chapter 4 and annex chapter A6.

The measurements were performed at room temperature in either the glassy nematic state or the crystalline state. Representative room-temperature current density-voltage curves measured in both solid states and both device architectures are plotted in **Figure 6.4 and 6.5**. Additional experimental results are given in the annex chapterA6. For each device structure, measurements on different film thicknesses have been performed to verify the absence of current-limiting injection barriers (**Figure 6.4 and 6.5**). In accordance with Mott-Gurney's law (see equation 6.1 below), the current density-voltage (J-V) curves measured for different L overlap in the high voltage range when $J \times L$ is plotted versus V/L (**Figure 6.4a and 6.5a**)[4, 35]. Interestingly, for thick devices, the curves coincide as well in the lower voltage range, when $J \times L$ is traced versus V (**Figure 6.4b**), as predicted by Ohm's law, in contrast to standard devices (**Figure 6.5b**). This can be understood by considering that in thick devices the background carrier concentration (p_o) is fixed by residual non-intentional dopants and is independent of L, while in standard devices the average p_o is determined by carrier in-diffusion from

contacts and decreases with increasing L[4]. Moreover, the ohmic resistance of thick devices (determined from the slope of the $J(V)$ curves at low voltages) varies linearly with L, as expected, and scales down to zero at zero layer thickness (**Figure 6.4c**). The charge carrier injection barrier can therefore be considered to be negligible in these devices.
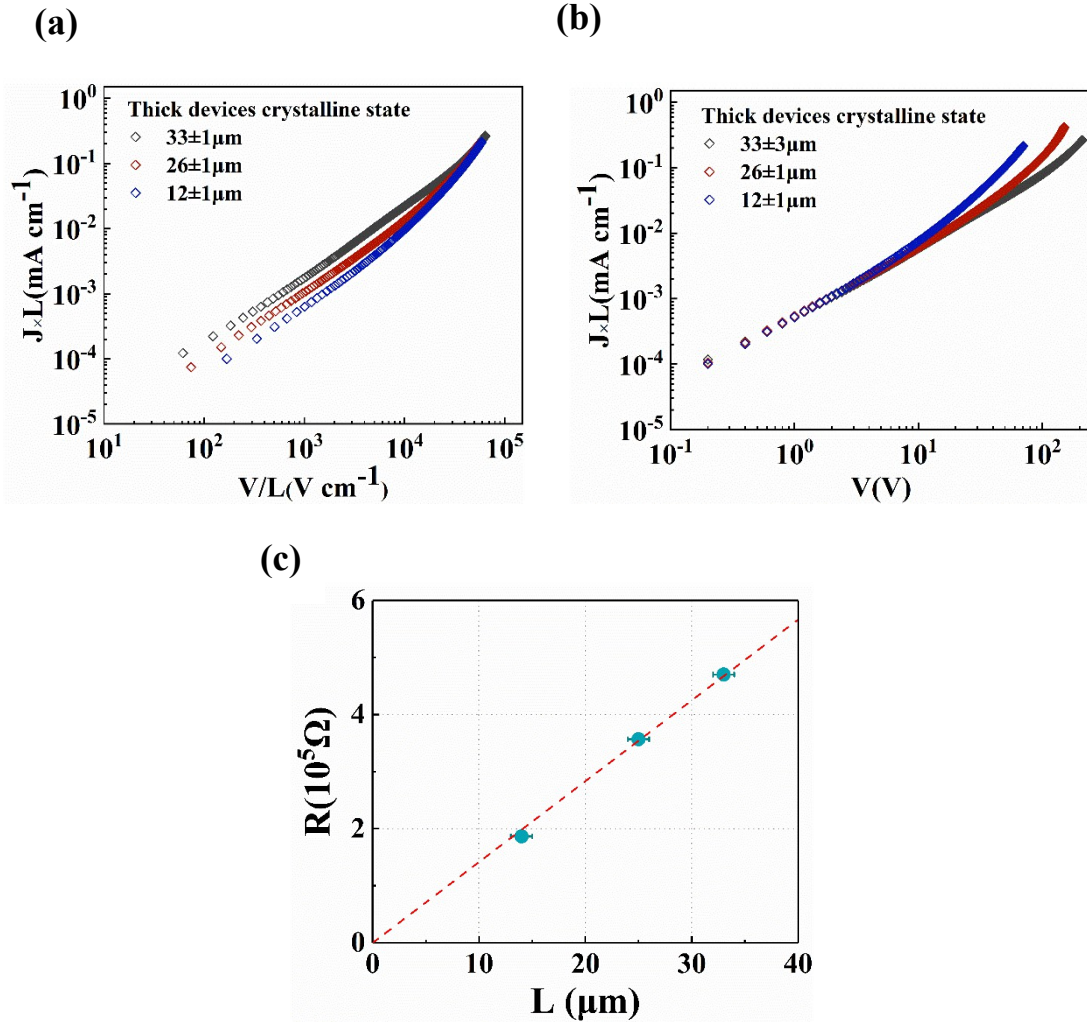

Figure 6.4 *J-V characteristics of thick SCLC devices at 296 K with different film thicknesses. (a) J×L as a function of V/L: the curves overlap in the SCLC part, as predicted by equation 1 (Mott-Gurney term). (b) J×L as a function of V: the curves overlap in the ohmic part, as predicted by equation 1 in case of a constant background carrier concentration. (c) Ohmic resistances estimated from the ohmic part of the J(V) curves of thick crystalline devices as a function of the layer thickness.*

(a)

(b)
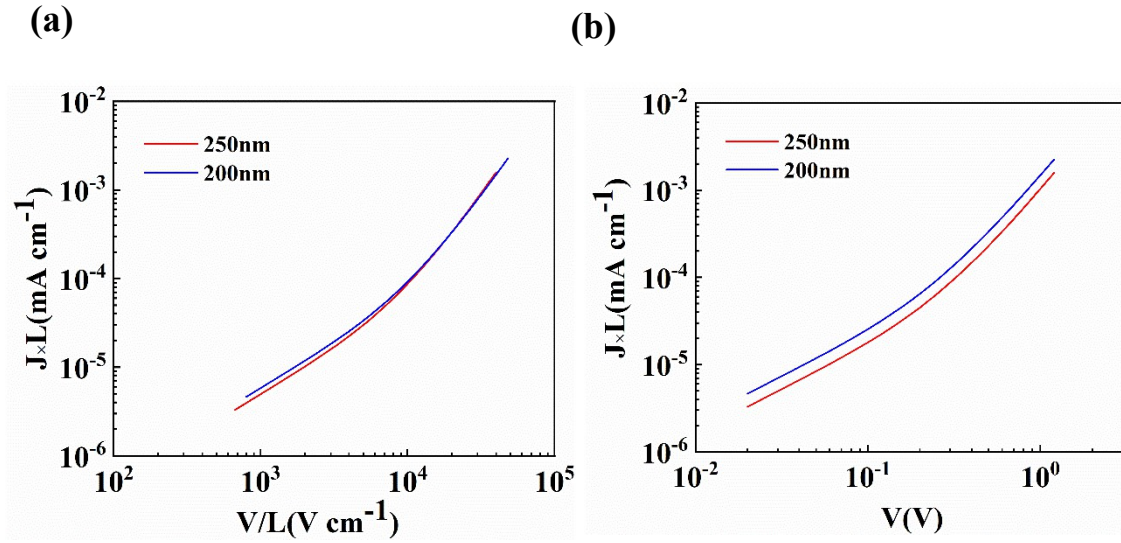
Figure 6.5 *J-V characteristics of standard SCLC devices in the columnar-nematic state. (a) J×L as function of V/L: the curves overlap in the SCLC part, as predicted by equation 1. (b) J×L as a function of V: the curves do not overlap in the ohmic part, suggesting that the average background carrier concentration depends on the applied voltage.*

To estimate the hole mobility, we fitted the *J(V)* curves to the following equation:[36]

$$J = q\mu_h p_o \frac{V}{L} + \frac{9}{8}\varepsilon_o\varepsilon_r\mu_h\frac{V^2}{L^3} \qquad (6.9)$$

where the first term corresponds to Ohm's law and the second to Mott-Gurney's law. A field independent mobility (μ_h) and p_o are used as fitting parameters. The dielectric constant (ε_r) was estimated to 3.0 from the geometric capacitance of a standard SCLC device. The relevance to compare SCLC data to a sum of both laws has been recently discussed by Jason A. Röhr[36] and was confirmed by our numerical simulations (**Figure A6.1**).

The results obtained on standard devices agree well with equation (6.1) (**Figure 6.6a and 6.6b**), suggesting that carrier transport in thin layers can be described by a field-independent hole mobility. The corresponding room temperature mobility data and p_o

128

values are summarized in **Table 6.1**. The error margins are based on the histograms shown in **Figure 6.7** and correspond to the interval that includes 68% of the number of counts. In the columnar nematic phase, the SCLC mobility equals $(5.0\pm0.8)\times10^{-3}$ cm^{2}V^{-1}s^{-1}, which is a factor of two above the previously reported value measured in as-deposited films.[23] This difference is likely due to the larger columnar nematic domains and higher structural order after annealing. For the crystalline films, a remarkably high mobility of 0.34 ± 0.20 cm^{2}V^{-1}s^{-1} is found when using the average thickness $<L>$. However, this value is likely to be overestimated due to the high surface roughness, as shown by the simulated current-voltage characteristics for a rough surface profile (**Figure A6.5**).

The results obtained on thick devices, for both solid states, follow closely, but not fully, **equation (6.9)** (**Figure 6.6c and 6.6d**). The slight deviation may be the consequence of an electric field dependent hole mobility.[37] Although the origin and amplitude of the latter remain uncertain, we tentatively attribute its existence to the larger number of disordered domains in thick devices (i.e., crystal or domain boundaries). In the following, this rather minor effect will be neglected. The corresponding effective field independent mobility values are summarized in **Table 6.1**. In the nematic state, the mobility is found to be $(2.7\pm0.5)\times10^{-3}$ cm^{2}V^{-1}s^{-1}, a value slightly below the mobility measured in standard devices. Since p_o is also lower by roughly one order of magnitude, it is possible that the lower mobility is the outcome of a reduced occupancy rate of deep electronic states, which may be acting as hole traps[38]. It is worth to note that the comparable mobility values observed in the standard and thick SCLC devices suggest that the TAT columns are similarly oriented (i.e., in-plane) in both cases. The bright Schlieren textures observed by POM on thick SCLC devices confirm this assertion (**Figure A6.3d**).

In the case of crystalline films, the field independent mobility value is estimated to 0.17±0.05 $cm^2V^{-1}s^{-1}$. Although lower than the value measured in standard devices, this value is close to the highest SCLC mobility reported so far for solution-processed molecular semiconductors[13, 22, 39, 40]. The factor of two difference in mobility between both kinds of devices may be the consequence of both, the higher p_o and the higher surface roughness in standard devices.
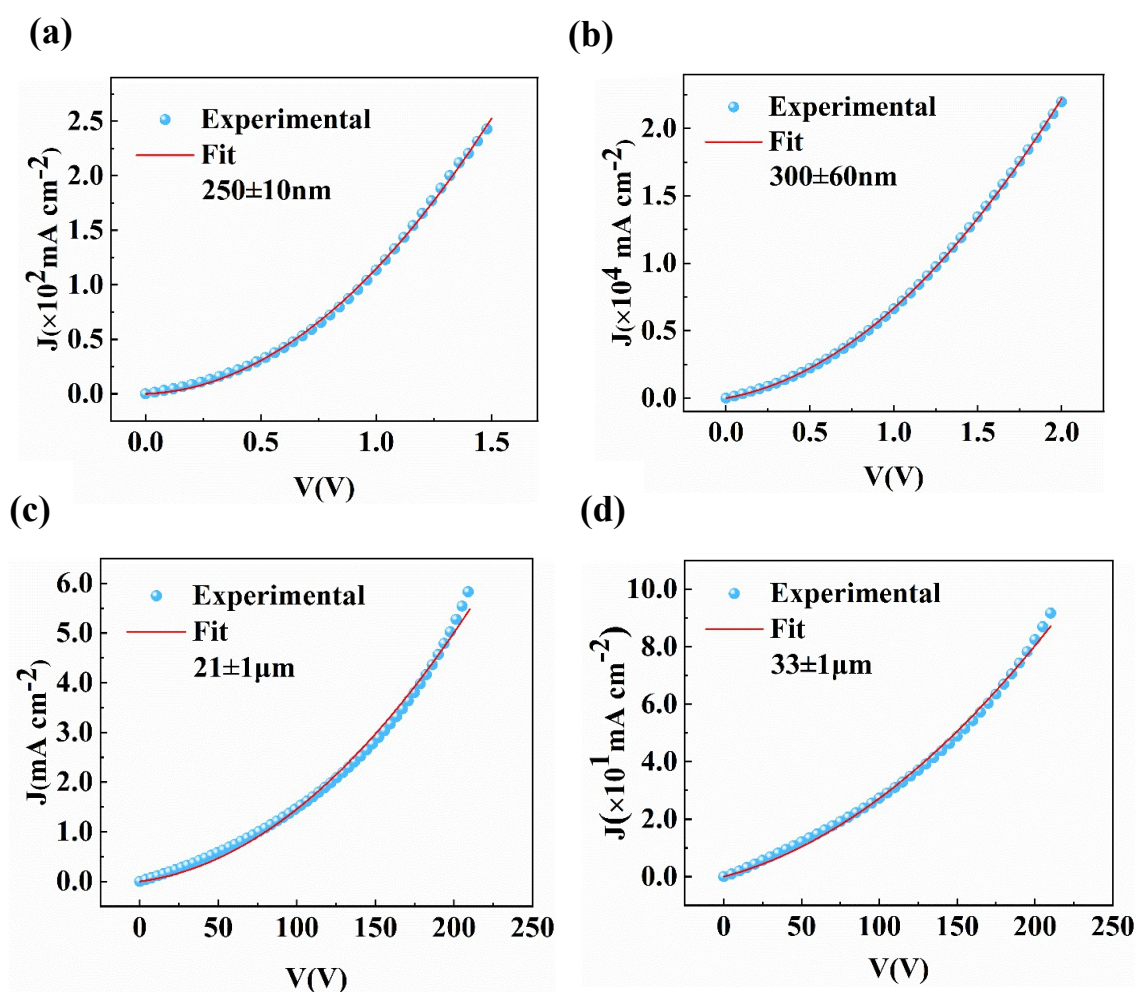
(a)

(b)

(c)

(d)

Figure 6.6 *Room temperature current-voltage characteristics of SCLC devices for different device structures and solid states. (a) Standard device in the columnar-nematic state (250±10 nm film thickness). (b) Standard device in the crystalline state (300 nm average film thickness with a surface roughness of 60 nm). (c) Thick device in the columnar-nematic state (21±1 μm layer thickness). (d) Thick device in the crystalline state (33±1 μm layer thickness). The red solid lines represent fits to equation (1) (corresponding χ2 statistics: (a) 0.9993, (b) 0.9999, (c) 0.9949, (d) 0.9969)*
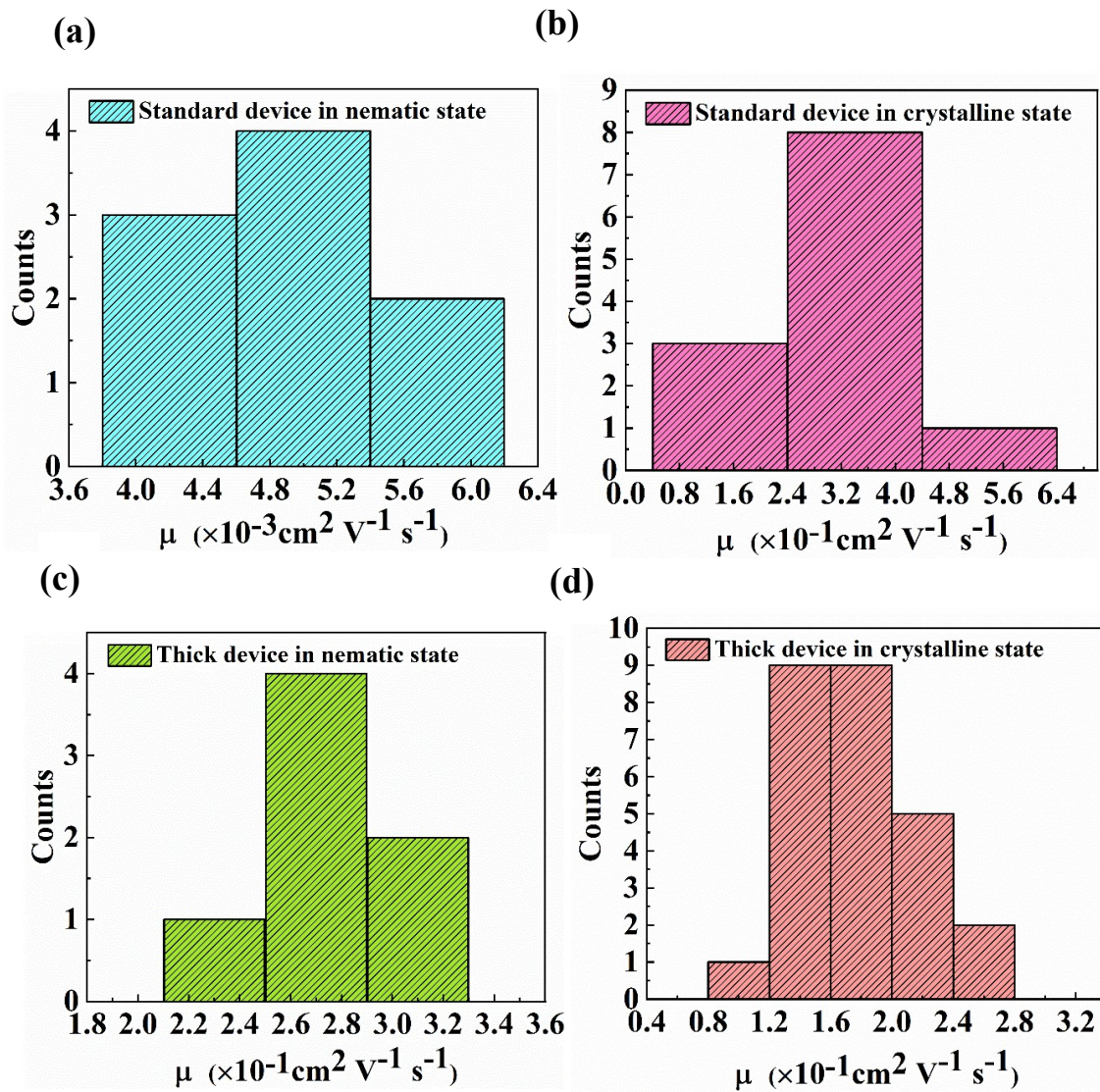
Figure 6.7 *Histograms of SCLC measurements. (a) Standard SCLC devices in columnar-nematic state, thickness is 250±10nm. (b) Standard SCLC devices in crystalline state, thickness is 300±60 nm. (c) Thick SCLC devices in columnar-nematic state, thickness is 21±1μm. (d) Thick SCLC devices in crystalline state, three different thickness is 33±1μm, 26±1μm, 12±1μm, respectively. The width of the columns represents the error margin on film thickness and mobility measurements.*

Table 6.1 *Charge transport properties of TPD$_{C8}$-TAT$_{C8}$ in SCLC and OFET devices*

Solid state	Devices	μ_h at RT [cm^{2}V^{-1}s^{-1}]	p_0 at RT [cm^{-3}]	E_a [meV]
Glassy nematic	Standard SCLC	$(5.0\pm0.8)\times10^{-3}$	$(1.7\pm0.3)\times10^{14}$	120 ± 10
	Thick SCLC	$(2.7\pm0.5)\times10^{-3}$	$(3.3\pm0.7)\times10^{13}$	-
	Top contact OFET	$(2.3\pm0.7)\times10^{-4}$	-	-
Crystalline	Standard SCLC	*0.34 ± 0.20	$(1.6\pm1.2)\times10^{15}$	30 ± 8
	Thick SCLC	0.17 ± 0.05	$(2.6\pm2.0)\times10^{13}$	-
	Top contact OFET	$(3.0\pm1.0)\times10^{-3}$	-	-
	Bottom contact OFET	$(>5.0\pm1.0)\times10^{-2}$	-	-

*The asterisk (*) indicates an overestimated value. Room temperature (RT) is 296 K. Histograms of SCLC and OFET mobility data are shown in **Figure 6.4** and **Figure 6.8**.*

Temperature dependent SCLC

We further evaluated the quality of charge transport in both solid states by measuring the SCLC mobility as a function of temperature (**Figure 6.8**). Only the temperature dependent response of standard devices is reported, since charge transport should be less impacted by crystal boundaries in these devices and since the surface roughness should not interfere with the temperature dependency of the current. Given the rather narrow temperature range accessible to our equipment, we fitted our data to a simple Arrhenius law defined by:

$$\mu_h = \mu_\infty \cdot exp\left(-\frac{E_a}{kT}\right) \qquad (6.10)$$

where E_a is the activation energy for charge carrier hopping, k the Boltzmann constant, T the absolute temperature and μ_∞ a pre-factor (**Figure 6.8b**). In the nematic state, E_a is estimated to 0.12 ± 0.01eV, which is near the lower limit of the range generally reported for organic semiconductors $(0.1\sim0.6)$ eV[41, 42]. For crystalline films on the other hand, the activation energy drops down to 0.030 ± 0.008 eV, which is exceptionally

low and corroborates the existence of highly efficient pathways for charge transport perpendicular to the molecular stacking direction.
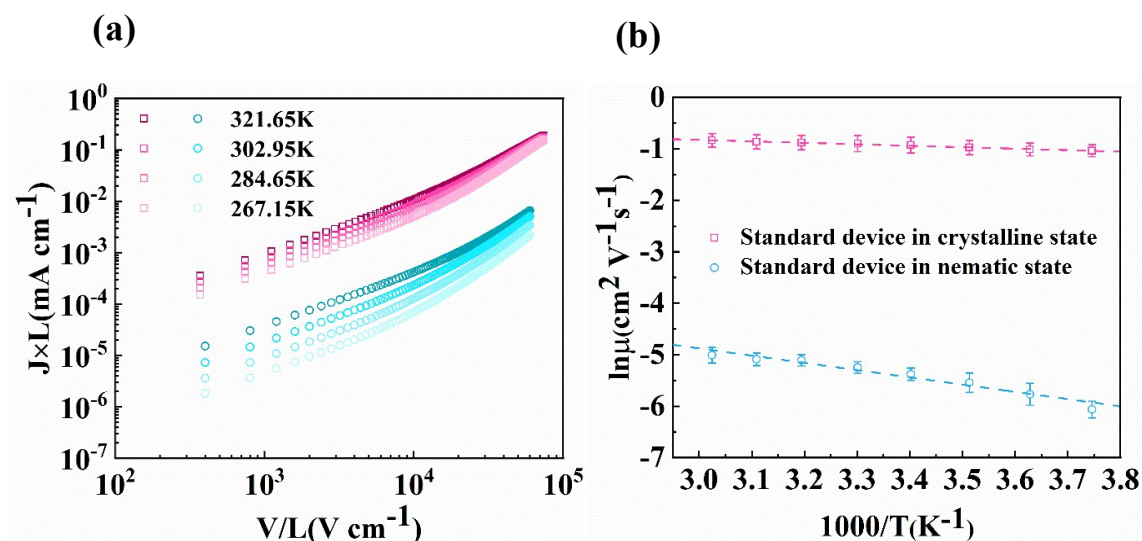

Figure 6.8 *(a) J-V characteristics as a function of temperature on standard SCLC devices, in the crystalline state (open red squares) and columnar-nematic state (open blue dots). (b) Arrhenius plots of the hole mobility. Error bars are estimated from the measurements on four individual diodes.*

6.3.2 OFET

We finally assessed in-plane charge transport in both, nematic and crystalline states, by measuring the hole mobility in top-contact-bottom-gate organic field-effect transistors (OFET) with channel widths varying between 60 and 90 μm. For the nematic state, the as-deposited film was annealed for 5 seconds into the isotropic phase (180 °C) followed by natural cooling to room temperature, while for the crystalline state, the film was annealed at 145 °C for 40 minutes to obtain a uniform distribution of relatively small crystalline needles (**Figure 6.9a**). Top-contact-bottom-gate OFET transfer characteristics are displayed in the **Figure 6.9**. For the nematic state, the field-effect mobility was estimated from the saturation regime to 2×10^{-4} cm^{2}V^{-1}s^{-1}. This value is about one order of magnitude lower than that of the SCLC mobility, despite the fact that charge transport should occur preferentially along the molecular stacking direction,

133

which lies in-plane in OFET and SCLC devices. Possible reasons for this rather moderate value could be the small columnar correlation length, but also, and most importantly, the fact that since nematic domains are distributed randomly in-plane, not all of them are best oriented for an efficient conduction through the channel length. On the other hand, random in-plane orientation should not affect charge transport in SCLC devices.

For the crystalline state, high contact resistances led unfortunately to strongly non-linear transfer characteristics and allowed only a rough estimation of the field-effect mobility in the saturation regime. The latter was found to be approximately 3×10^{-3} $cm^2V^{-1}s^{-1}$ (**Table 6.1**). As this value is likely to be impacted by non-negligible charge carrier trapping, inter-crystal charge transport (the average crystal size being smaller than the channel length) and contact resistance, they represent a lower limit for the hole mobility. To minimize the impact of inter-crystal charge carrier hopping on the mobility value, we investigated additional bottom-contact-bottom-gate transistors elaborated with large crystals and using a channel length (2.5 μm) that was smaller than the average crystal size (**Figure 6.10 and A6.6**). In these devices, a majority of molecular crystals bridged the gap between source and drain electrodes, covering a significant fraction of the channel width (*W*). By considering an effective channel width that was determined optically to 0.17±0.02 cm, (**Figure A6.4**), we estimated the field-effect mobility in the saturation regime to 0.050±0.010 $cm^2V^{-1}s^{-1}$ (**Table 6.1**). Although this value remains underestimated due to the pronounced contact resistance (**Figure 6.10c and 6.10d**), it is more than one order of magnitude above the value measured in large-channel top-contact OFETs, pointing out that charge transport may occur very efficiently also along the long axis of the crystalline needles, i.e., along the direction of molecular stacking. More advanced device structures and further optimization of the crystal growth, which are required to assess the in-plane mobility more accurately, lies beyond the scope of the present work.
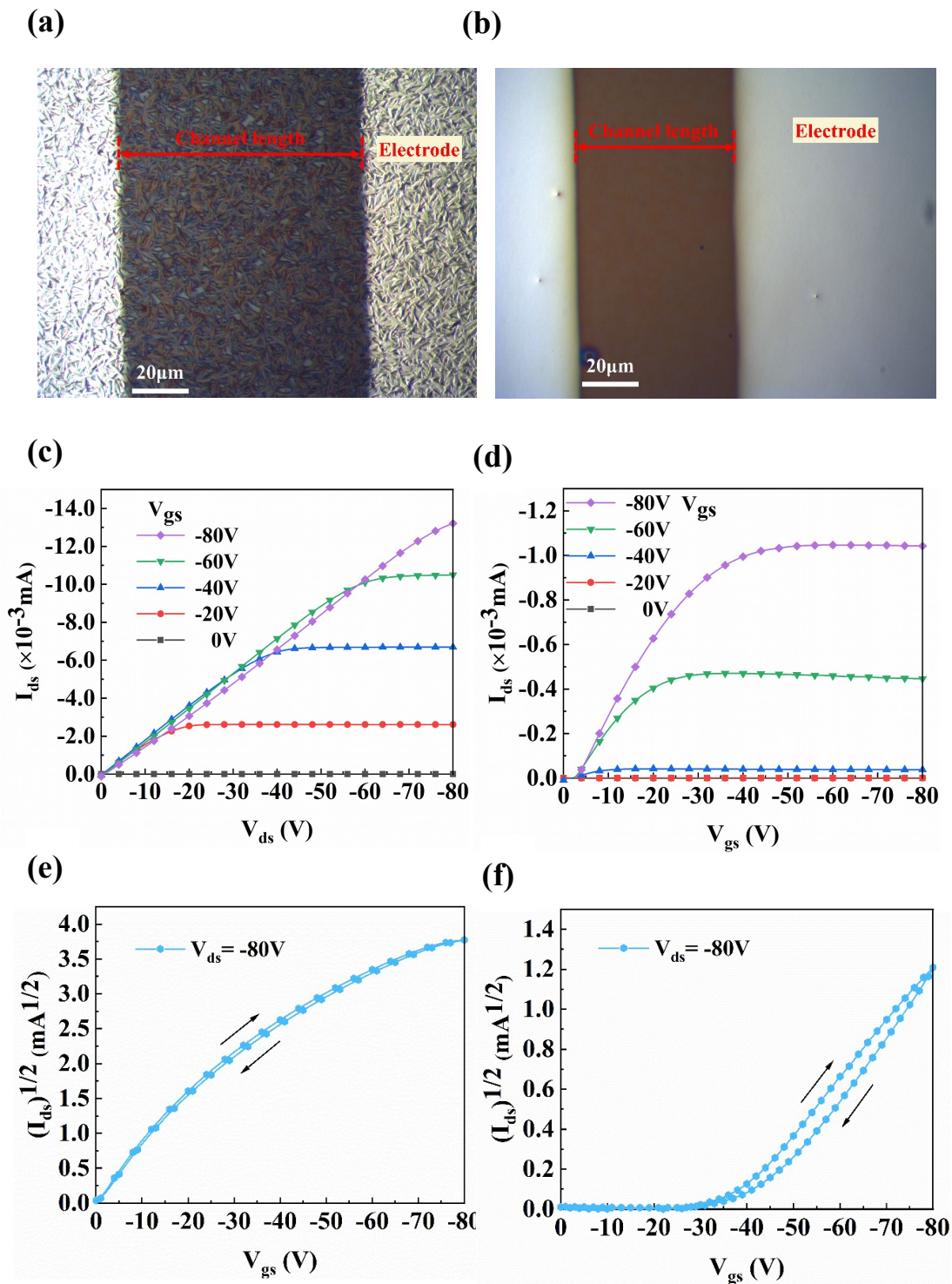
(a)

(b)

(c)

(d)

(e)

(f)

Figure 6.9 *Top-contact-bottom-gate transistor device. Optical micrographs of a transistor in (a) the crystalline state and (b) the columnar-nematic state. Output characteristics for (c) the crystalline state and (d) the columnar-nematic state. Transfer characteristics in the saturation regime for (e) the crystalline state and (f) the columnar-nematic state.*
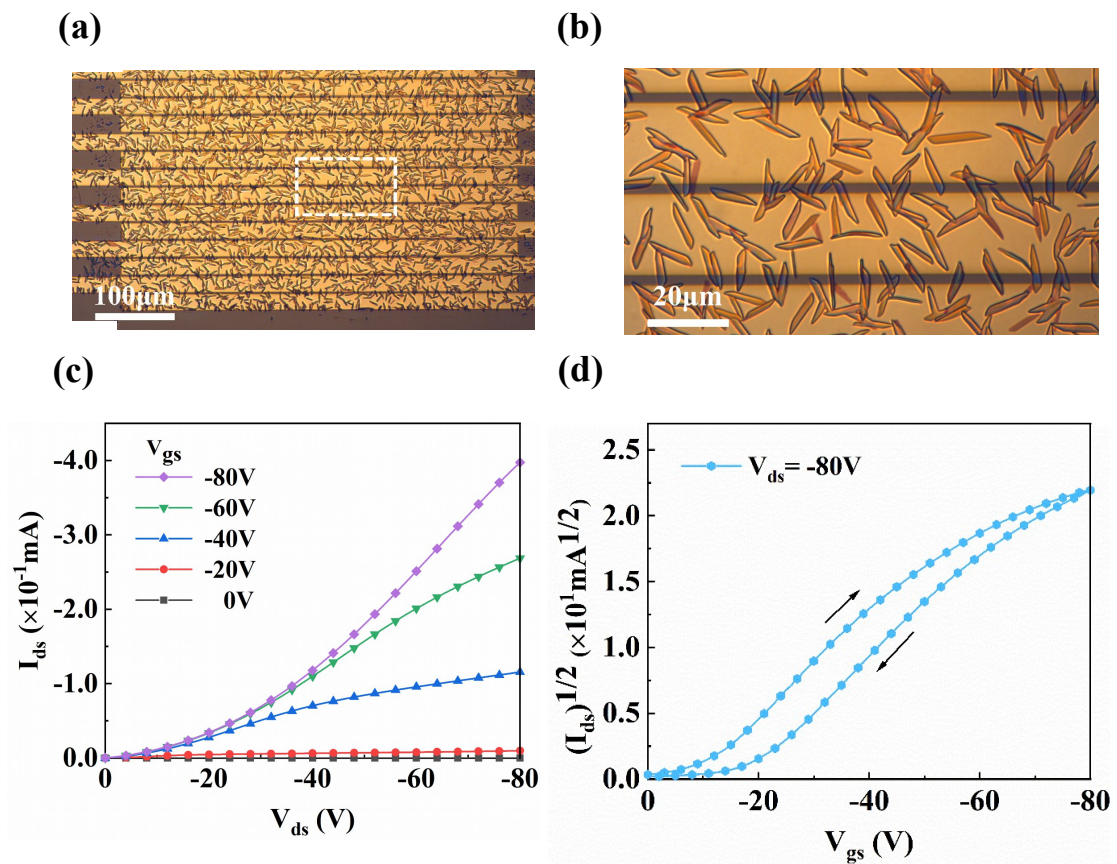
Figure 6.10 *(a) Optical micrograph of source and drain contacts of a bottom-contact-bottom gate transistor with TPD$_{C8}$-TAT$_{C8}$ layer of large crystalline needles (channel length = 2.5 µm, channel width = 1.0 cm). (b) Zoom of dashed area in (a). (c) Output characteristics of the bottom-gate-bottom-contact OFET. (d) Transfer characteristics in the saturation regime.*

(a)

(b)

(c)
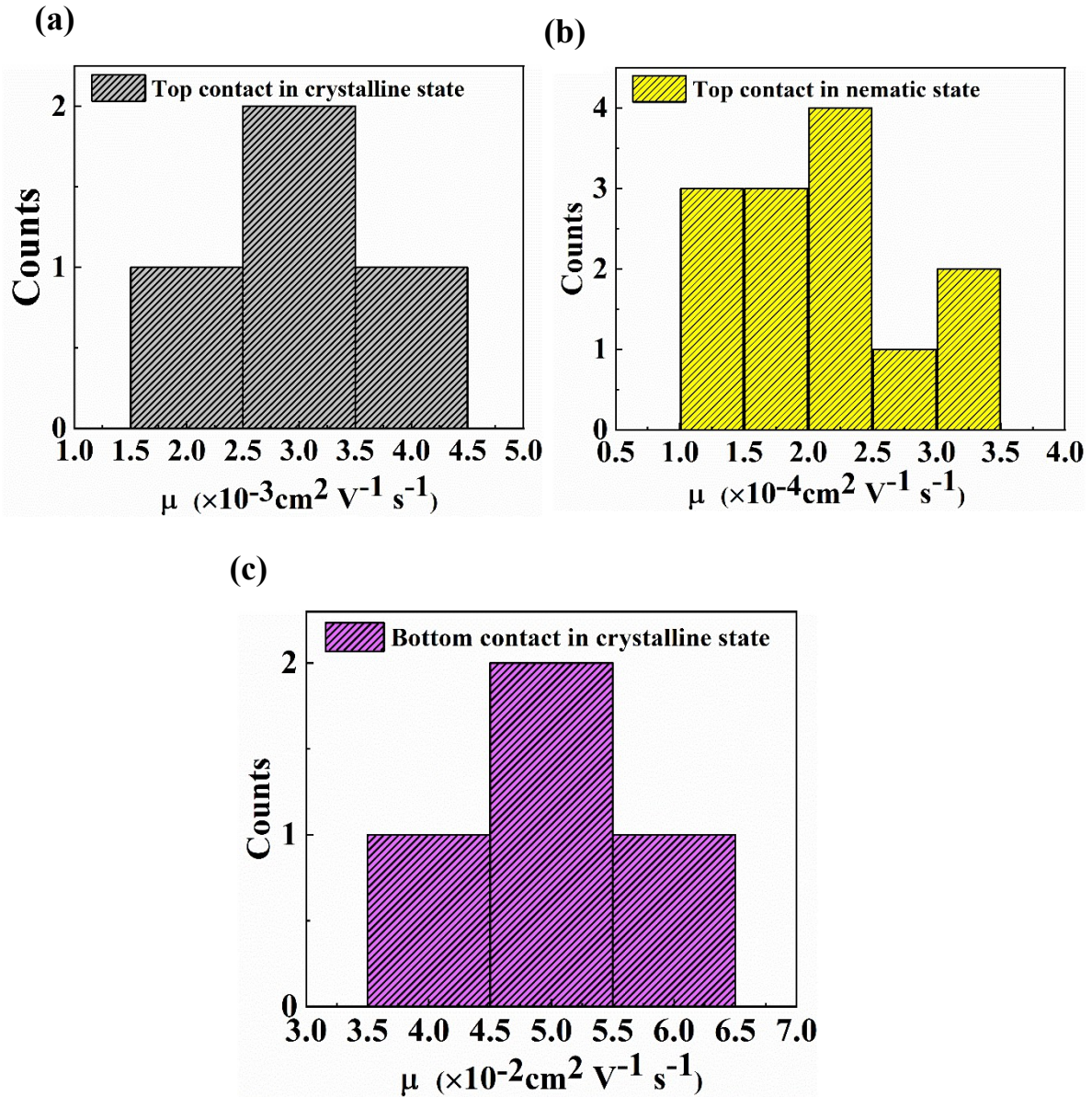
Figure 6.11 *Histograms for field-effect mobility data. (a) Top-contact-bottom-gate transistors in the crystalline state (average crystal size ≈ 2.5 μm, channel length = 90 μm, channel width= 3.646 cm). (b) Top-contact-bottom-gate transistors in the nematic state (channel length= 60 μm, channel width = 2.917 cm). (c) Bottom-contact-bottom-gate transistors in the crystalline state (average crystal size ≈ 10 μm, channel length= 2.5 μm, channel width= 0.17±0.02 cm as estimated from Figure S11). The width of the columns represents the error margin on the channel width estimation and hole mobility extraction.*

Overall, the mobility data extracted from SCLC and OFET measurements, summarized in **Table 6.1**, point out a one order of magnitude difference between out-of-plane and

in-plane mobilities for both solid states. Interestingly, the SCLC mobility values are systematically larger than field-effect mobilities, which is rather uncommon, in particular when the molecular stacking directions are oriented parallel to the substrate. However, considering the significant impact that measurement devices generally have on the mobility data (due for instance to different contact resistances, lengths scales, electrostatic environments, carrier densities…), our results indicate that charge transport in TPD$_{C8}$-TAT$_{C8}$ thin films, in both the mesophase and the crystalline state, is almost isotropic.

6.4 Conclusion

In summary, we have explored hole transport in a donor-acceptor-donor type planar dumbbell-shaped molecular semiconductor comprising two triazatruxene (TAT) end units and a central thiophene-thienopyrroledione-thiophene (TPD) unit. Taking into account the molecular packing structure properties described in chapter 4, the charge transport results support the assertion that the conjugated segments connecting two TAT units act as intercolumnar conjugated bridges. Charge transfer is then no longer limited to intermolecular hopping along one-dimensional columnar stacks, as usually observed in other single TAT-derivatives or discotic molecules, but becomes effective in 3D.

In the mesophase, the out-of-plane hole transport was estimated by SCLC to be about 10^{-3} cm^{2}V^{-1}s^{-1}, slightly above the field-effect in-plane mobility. On the other hand, an outstandingly high out-of-plane SCLC mobility of 0.17 cm^{2}V^{-1}s^{-1}, in combination with a low activation energy of 30 meV, was measured in the crystalline phase. Although only a lower limit of 0.05 cm^{2}V^{-1}s^{-1} could be obtained so far for the in-plane field-effect mobility, the results support the conclusion that the molecular assembly allows for efficient charge transport perpendicular as well as parallel to the molecular stacking

direction. Overall, our observations suggest that the two highly planar TAT end-groups are effectively driving the molecules into a unique 3D conducting bridged columnar phase, wherein the molecules are bridging adjacent columns or molecular stacks through the insulating aliphatic domains. As a consequence, 3D charge-transport with a low degree of anisotropy, a feature rarely observed in solution processable crystalline small molecules, has been demonstrated.

References:

[1]   S. Fratini, M. Nikolka, A. Salleo, G. Schweicher and H. Sirringhaus, *Nature Materials*, 2020, **19**, 491-502.

[2]   S. K. Park, J. H. Kim and S. Y. Park, *Advanced Materials*, 2018, **30**, 1704759.

[3]   H. Kleemann, K. Krechan, A. Fischer and K. Leo, *Advanced Functional Materials*, 2020, **30**, 1907113.

[4]   G. A. H. Wetzelaer and P. W. M. Blom, *Physical Review B*, 2014, **89**, 241201.

[5]   O. P. Lee, A. T. Yiu, P. M. Beaujuge, C. H. Woo, T. W. Holcombe, J. E. Millstone, J. D. Douglas, M. S. Chen and J. M. J. Fréchet, *Advanced Materials*, 2011, **23**, 5359-5363.

[6]   X. Liu, T. Usui and J. Hanna, *Chemistry of Materials*, 2014, **26**, 5437-5440.

[7]   M. C. Scharber and N. S. Sariciftci, *Progress in Polymer Science*, 2013, **38**, 1929-1940.

[8]   O. Ostroverkhova, *Chemical Reviews*, 2016, **116**, 13279-13412.

[9]   S. K. Pal, S. Setia, B. S. Avinash and S. Kumar, *Liquid Crystals*, 2013, **40**, 1769-1816.

[10]   K. Takimiya, I. Osaka, T. Mori and M. Nakano, *Accounts of Chemical Research*, 2014, **47**, 1493-1502.

[11]   M. Sawamoto, M. J. Kang, E. Miyazaki, H. Sugino, I. Osaka and K. Takimiya, *ACS Applied Materials & Interfaces*, 2016, **8**, 3810-3824.

[12]   Y. Dong, H. Li, J. Liu, J. Zhang, X. Shi, Y. Shi, C. Li, Z. Liu, T. Li and L. Jiang, *Organic Electronics*, 2020, **77**, 105537.

[13]   Y. Li, R. G. Clevenger, L. Jin, K. V. Kilway and Z. Peng, *Journal of Materials Chemistry C*, 2014, **2**, 7180-7183.

[14]   A. Punzi, E. Maiorano, F. Nicoletta, D. Blasi, A. Ardizzone, N. Ventosa, I. Ratera, J. Veciana and G. M. Farinola, *European Journal of Organic Chemistry*, 2016, **2016**, 2617-2627.

[15]   X.-C. Li, C.-Y. Wang, W.-Y. Lai and W. Huang, *Journal of Materials Chemistry C*, 2016, **4**, 10574-10587.

[16]   H. Zhang, Y. Liu, Y. Sun, M. Li, B. Kan, X. Ke, Q. Zhang, X. Wan and Y. Chen, *Chemical Communications*, 2017, **53**, 451-454.

[17]   K. Sun, Z. Xiao, S. Lu, W. Zajaczkowski, W. Pisula, E. Hanssen, J. M. White, R. M. Williamson, J. Subbiah, J. Ouyang, A. B. Holmes, W. W. H. Wong and D. J. Jones, *Nature Communications*, 2015, **6**, 6013.

[18]   B. Kan, M. Li, Q. Zhang, F. Liu, X. Wan, Y. Wang, W. Ni, G. Long, X. Yang, H. Feng, Y. Zuo, M. Zhang, F. Huang, Y. Cao, T. P. Russell and Y. Chen, *Journal of the American Chemical Society*, 2015, **137**, 3886-3893.

[19]   S. Fratini, S. Ciuchi, D. Mayou, G. T. de Laissardière and A. Troisi, *Nature Materials*, 2017, **16**, 998-1002.

[20]   I. Bulut, P. Chávez, A. Mirloup, Q. Huaulmé, A. Hébraud, B. Heinrich, S. Fall, S. Méry, R. Ziessel, T. Heiser, P. Lévêque and N. Leclerc, *Journal of Materials Chemistry C*, 2016, **4**, 4296-4303.

[21]   Z.-F. Yao, J.-Y. Wang and J. Pei, *Crystal Growth & Design*, 2018, **18**, 7-15.

[22]   E. M. García-Frutos, U. K. Pandey, R. Termine, A. Omenat, J. Barberá, J. L. Serrano, A. Golemme and B. Gómez-Lor, *Angewandte Chemie International Edition*, 2011, **50**, 7399-7402.

[23]   T. Han, I. Bulut, S. Méry, B. Heinrich, P. Lévêque, N. Leclerc and T. Heiser, *Journal of Materials Chemistry C*, 2017, **5**, 10794-10800.

[24]   G. Schweicher, Y. Olivier, V. Lemaur and Y. H. Geerts, *Israel Journal of Chemistry*, 2014, **54**, 595-620.

[25] H. Iino, T. Usui and J.-i. Hanna, *Nature Communications*, 2015, **6**, 6828.

[26] O. Kwon, X. Cai, W. Qu, F. Liu, J. Szydłowska, E. Gorecka, M. J. Han, D. K. Yoon, S. Poppe and C. Tschierske, *Advanced Functional Materials*, 2021, **31**, 2102271.

[27] A. Köhler and H. Bässler, in *Electronic Processes in Organic Semiconductors*, 2015, pp. 1-86.

[28] M. Kus, T. Y. Alic, C. Kirbiyik, C. Baslak, K. Kara and D. A. Kara, in *Handbook of Nanomaterials for Industrial Applications*, ed. C. Mustansar Hussain, Elsevier, 2018, pp. 392-429.

[29] N. Zehra, L. R. Adil, A. S. Tanwar, S. Mondal and P. Krishnan Iyer, in *Chemical Solution Synthesis for Materials Design and Thin Film Device Applications*, eds. S. Das and S. Dhara, Elsevier, 2021, pp. 369-405.

[30] J. Zaumseil and H. Sirringhaus, *Chemical Reviews*, 2007, **107**, 1296-1323.

[31] S. Fall, L. Biniek, Y. Odarchenko, D. V. Anokhin, G. de Tournadre, P. Lévêque, N. Leclerc, D. A. Ivanov, O. Simonetti, L. Giraudet and T. Heiser, *Journal of Materials Chemistry C*, 2016, **4**, 286-294.

[32] T. He, X. Zhang, J. Jia, Y. Li and X. Tao, *Advanced Materials*, 2012, **24**, 2171-2175.

[33] R. W. I. d. Boer, M. Jochemsen, T. M. Klapwijk, A. F. Morpurgo, J. Niemax, A. K. Tripathi and J. Pflaum, *Journal of Applied Physics*, 2004, **95**, 1196-1202.

[34] J. A. Röhr, X. Shi, S. A. Haque, T. Kirchartz and J. Nelson, *Physical Review Applied*, 2018, **9**, 044017.

[35] J.-I. Hanna, in *Liquid Crystalline Semiconductors: Materials, properties and applications*, eds. R. J. Bushby, S. M. Kelly and M. O'Neill, Springer Netherlands, Dordrecht, 2013, pp. 39-64.

[36] J. A. Röhr and R. C. I. MacKenzie, 2020.

[37] !!! INVALID CITATION !!! [4, 34, 35].

[38] J. M. Montero and J. Bisquert, *Journal of Applied Physics*, 2011, **110**, 043705.

[39]   X. Bai, K. Zong, J. Ly, J. S. Mehta, M. Hand, K. Molnar, S. Lee, B. Kahr, J. M. Mativetsky, A. Briseno and S. S. Lee, *Chemistry of Materials*, 2017, **29**, 7571-7578.

[40]   A. Benito-Hernández, U. K. Pandey, E. Cavero, R. Termine, E. M. García-Frutos, J. L. Serrano, A. Golemme and B. Gómez-Lor, *Chemistry of Materials*, 2013, **25**, 117-121.

[41]   V. Coropceanu, J. Cornil, D. A. da Silva Filho, Y. Olivier, R. Silbey and J.-L. Brédas, *Chemical Reviews*, 2007, **107**, 926-952.

[42]   S. Züfle, S. Altazin, A. Hofmann, L. Jäger, M. T. Neukom, W. Brütting and B. Ruhstaller, *Journal of Applied Physics*, 2017, **122**, 115502.

Chapter 7
Organic solar cells

TPD-TAT /Polymer acceptor bulk heterojunctions

Depending on the nature of the materials, solution-processed organic solar cells can be divided into all-polymer, all-small-molecule (molecular), polymer/molecular blends solar cells. Blends of electron-donor polymers with electron-acceptor molecules have so far led to the highest OPV performances (above 18%), following the introduction of non-fullerene acceptors (NFAs)[1-3]. NFAs were introduced to improve photon harvesting, but did finally also allow, rather unexpectedly, to reduce losses due to charge carrier recombination (for reasons that are still under investigations)[4, 5]. On the other hand, only few examples of blends of electron-acceptor polymers with electron-donor molecules have been reported up to now, with a maximum PCE of 10%. As the TPD-TAT molecules have good photon harvesting, charge transport and exciton properties, it is interesting to investigate molecular donor/polymer acceptor blends using TPD-TAT as donor.

In this chapter, a first trial to use blends of TPD$_{C8}$-TAT$_{C8}$ molecular donor (M$_D$) / Polynaphtalene-bithiophene P(NDI2OD-T2) polymer acceptor (P$_A$) in BHJ solar cells will be described. The first section gives an overlook of the state-of-the-art of M$_D$/P$_A$ devices. In the second section, the experimental details for device fabrication and characterization will be presented, while first results will be discussed in the last section.

7.1 Introduction

The development of organic solar cells based on molecular donor/polymer acceptor (M$_D$/P$_A$) still lags behind the other three types of BHJ devices. A major difficulty in designing efficient new polymer/molecular solar cells has been the control of the thin film morphology at the nanoscale. In the case of planar small molecules, strong intermolecular interactions favor crystallization and may trigger the formation of excessively large domains[6, 7], that are unfavorable for efficient exciton dissociation. A possible strategy suggested to obtain nanoscale phase separation (on the order of

exciton diffusion length) in the blends of polymer/molecular. Another reason for delay in the development of efficient M_D/P_A type solar cells is the lack of available high-performance polymer acceptors[8-10].

Polymer acceptors can be roughly classified as perylene diimide (PDI)-based[11], naphthalene diimide (NDI)-based[12], diketopyrrolopyrrole (DPP)-based[13] and bipyridyl (BNBP)-based[14] [15]. Notably, NDI is considered a promising polymer acceptor since it has a high electron affinity and good chemical and photochemical stability[14]. In 2009, Facchetti's group[16] synthesized an n-type NDI-based polymer, named P(NDI2OD-T2) (also named as PNDI-2T or N2200) (**Figure 7.1**), in which naphthalene (NDI) is the electron-withdrawing unit and 2, 2′-bithiophene is the electron-donating unit. P(NDI2OD-T2) exhibits field-effect electron mobilities around 0.85 $cm^2\,V^{-1}s^{-1}$ (measured by top-gate bottom-contact transistors). Since then, it has become a widely used acceptor material in M_D/P_A-type solar cells. Several studies have focused on molecular donors blended with P(NDI2OD-T2), and evaluated how the planarity of the molecular donor impacts the photovoltaic performance. The major results of these studies are summarized in the **Table 7.1**.

Table 7.1 *Summary of the photovoltaic properties of the combinations of different molecular donor with PNDI2OD-T2 polymer acceptor. (Copyright from W. Xu at al.* [17])

Donor	V_{oc} (V)	J_{sc} (mA/cm²)	FF (%)	PCE_{max} (%)	Ref
BDT2TR	0.86	7.26	71.0	4.43	[18]
DPP-B	0.63	0.69	43.4	0.20	[8]
DPP-N	0.83	1.14	53.2	0.50	[8]
DPP-P	0.78	4.45	58.5	2.05	[8]
C-DPP	0.87	8.59	62.0	4.64	[19]
Si-DPP	0.86	8.14	54.0	4.02	[19]
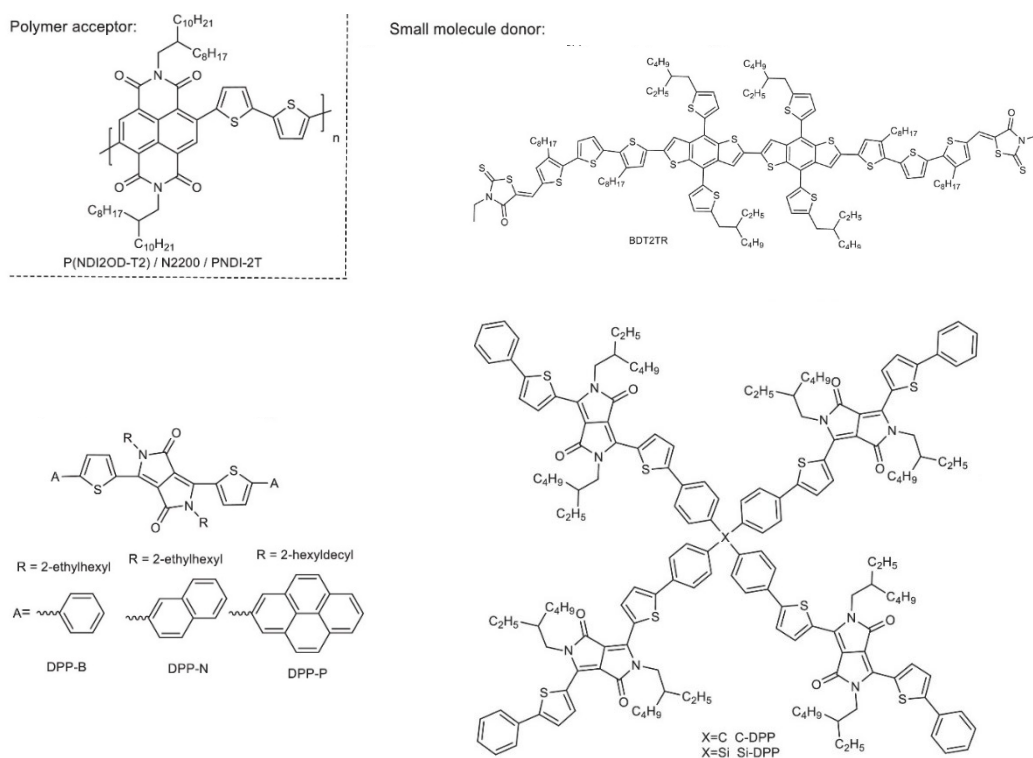
Figure 7.1 *Chemical structures of different molecular donor and P(NDI2OD-T2) polymer acceptor. (Copyright from W. Xu at al.* [17]*).*

Oh et al.[18] introduced a highly planar benzo[1,2-b:4,5-b']dithiophene (BDT) unit into the BDT2TR molecule (**Figure 7.1**), and used it as donor in blends with P(NDI2OD-T2). A PCE of 4.43% could be reached (**Table 7.1**). In the BDT2TR/ P(NDI2OD-T2) blends, the hole and electron SCLC mobilities were measured to be 1.13×10^{-4} cm^{2}V^{-1}s^{-1} and 1.42×10^{-5} cm^{2}V^{-1}s^{-1}, respectively. The high FF of 71% (**Table 7.1**) for M$_D$/P$_A$-type system is mainly benefiting from the highly crystalline and balanced charge carrier mobilities. Besides the BDT unit, the 1,4-diketo-pyrrolo[3,4-c]pyrrole (DPP)-based D-A-D type molecule is also a donor material with strong electron-withdrawing ability and high planarity. Yuan et al.[8] reported three DPP-based molecular D-A-D donors, named as DPP-B, DPP-N and DPP-P derivatives with different end groups benzene, naphthalene and pyrene, respectively (**Figure 7.1**). The SCLC hole mobilities in the DPP-B(-N, -P)/P(NDI2OD-T2) blends increased with increasing planarity of the end-groups. The SCLC hole mobilities of DPP-B(-N, -P)/N2200 blends are 1.7×10^{-6} cm^{2}V^{-1}s^{-1}, 1.6×10^{-5} cm^{2}V^{-1}s^{-1} and 3.2×10^{-4} cm^{2}V^{-1}s^{-1}, respectively. DPP-P with the largest π-

conjugated end-group showed the highest planarity and hole mobility resulting in a PCE of 2.05% (**Table 7.1**). In addition to the above mentioned two-dimensional (2D) DPP-based molecules, three-dimensional (3D) DPP derivatives (C-DPP and Si-DPP in **Figure 7.1**), which are expected to support 3D hole transport, were designed by Liu et al. and used as electron donor in M_D/P_A blends,[19]. The SCLC hole mobilities of (C-DPP or Si-DPP)/P(NDI2OD-T2) blends, are $3.58 \times 10^{-4} cm^2 V^{-1} s^{-1}$, $2.12 \times 10^{-4} cm^2 V^{-1} s^{-1}$, respectively, and the corresponding electron mobility in the blends are $2.87 \times 10^{-4} cm^2 V^{-1} s^{-1}$, $0.89 \times 10^{-4} cm^2 V^{-1} s^{-1}$, respectively. Finally, (C-DPP or Si-DPP)/P(NDI2OD-T2)-based devices with PCE of 4.64% or 4.02% (**Table 7.1**), respectively, could be demonstrated. The higher performances in comparison to 2D molecules, suggest that 3D charge transport in OSC is a promising strategy to improve the performance of the organic solar cell.

In this context, the particular packing structure of TPD_{C8}-TAT_{C8} molecules, which support 3D charge transport (see chapter 6), appears as a promising material for M_D/P_A based solar cells. Also, the rather long exciton diffusion length in the crystalline phase is of interest and makes TPD_{C8}-TAT_{C8} appear as a potentially efficient molecular donor for organic solar cell devices. We therefore investigated the photovoltaic properties of TPD_{C8}-TAT_{C8} /P(NDI2OD-T2) blends.

7.2 Experimental details

7.2.1 Organic solar cells fabrication

BHJ organic solar cells were elaborated using TPD_{C8}-TAT_{C8} as electron donor and PNDI2OD-T2 as electron acceptor. The device structure was the following: glass/ITO/ZnO (7-10 nm)/ TPD_{C8}-TAT_{C8}: PNDI2OD-T2/MoO$_3$ (7 nm)/Ag (120 nm), where the ITO/ZnO bilayer behaves as electron collecting / hole blocking bottom electrode, and the MoO$_3$/Ag bilayer as hole collecting / electron blocking top electrode.

The device fabrication process was as follows:

1.) Cleaning substrates: Glass/ITO substrates were cleaned sequentially by ultrasonic treatments in acetone, isopropyl alcohol, and deionized water at 45°C for 15 minutes.

2.) UV-ozone treatment: an additional cleaning was conducted under ultra-violet generated ozone for 30 minutes.

3.) Deposition of ZnO: Filtering the ZnO suspension by nylon filter with pore diameter of 0.45μm; 7-10 nm thick layer of ZnO was obtained by spin-coating (5000 rpm, 60s); cleaning the ZnO with ethanol from part of the substrate; thermal annealing for 10 minutes at 110°C to remove the residual solvent.

After this step, the samples were transferred into the glove-box (nitrogen-filled).

4.) Deposition of active layer: The chloroform solutions of TPD$_{C8}$-TAT$_{C8}$: PNDI2OD-T2 were stirred for at least 12 hours at room temperature before spin-coating. The acceptor solution concentrations were 10 mg. mL^{-1}. The relative TPD$_{C8}$-TAT$_{C8}$: PNDI2OD-T2 weight ratio was varied from 1:1 to 3:1. The active layer spin-coating parameters were: speed of 2000 rpm, duration of 90s, acceleration of 1000 rpm s^{-1}; in order to improve the thin-films self-assembly organization, thermal annealing treatment can be performed at different temperatures (80°C or 145°C) and keep different durations before the electrode evaporation.

5.) Evaporation of top electrode: Thin layers of MoO$_3$ (7 nm) and Ag (120 nm) were sequentially thermally evaporated under vacuum (pressure<1×10^{-6} mbar). Each organic solar cell device has four diodes (**Figure 7.2**), and the effective working area (12 mm^2) of each diode has been carefully defined by a shadow mask.
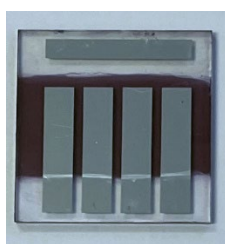
Figure 7.2 *Example of an organic solar cell device.*

7.3 Results and discussion

7.3.1 Optical properties

UV-visible absorption and photoluminescence of thin-films of pure TPD$_{C8}$-TAT$_{C8}$, pure P(NDI2OD-T2) and blends of TPD$_{C8}$-TAT$_{C8}$: P(NDI2OD-T2) are shown in **Figure 7.3**. In pure TPD$_{C8}$-TAT$_{C8}$ thin-films, a strong absorption peak centered around 320 nm is observed and may be attributed to π-π* transitions of TAT units, while a broader absorption band around 500 nm is likely due to an intramolecular charge transfer. For pure P(NDI2OD-T2) thin-films, the absorption spectrum includes a π-π* transition peak centered around 395 nm and an intramolecular charge transfer around 700nm. For TPD$_{C8}$-TAT$_{C8}$: P(NDI2OD-T2) blends, the weak overlap between the absorption spectra of both components leads to a broad absorption range (200-900 nm) which covers a significant fraction of the solar spectrum and should lead to high short-circuit currents. The photoluminescence spectra (**Figure 7.3b**) show that TPD$_{C8}$-TAT$_{C8}$ have a stronger photoluminescence yield than P(NDI2OD-T2). In blends, the photoluminescence of P(NDI2OD-T2) is almost suppressed, while the TPD$_{C8}$-TAT$_{C8}$ luminescence is attenuated by a factor of 5 (ratio of integral area). These results suggest that exciton dissociation at the D/A interface is almost complete for excitons generated on the polymer, while roughly 20% of the excitons generated in the TPD-TAT domains recombine before dissociation.
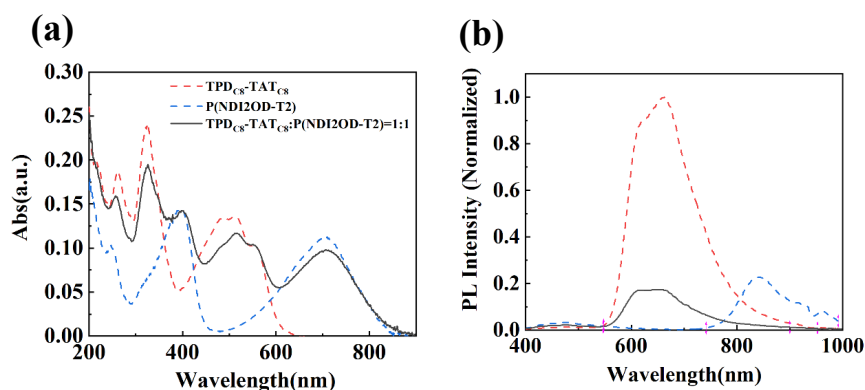
Figure 7.3 *(a) Absorption and (b) photoluminescence of pure TPD$_{C8}$-TAT$_{C8}$ (red dash line), pure P(NDI2OD-T2) (blue dash line) and blends (TPD$_{C8}$-TAT$_{C8}$: P(NDI2OD-T2) =1: 1) (black solid line) thin-films. PL intensity normalized to the maximum value of TPD$_{C8}$-TAT$_{C8}$.*

7.3.2 Photovoltaic properties

In order to find appropriate conditions for efficient M_D/P_A type BHJ organic solar cells, the D/A weight ratio along with different annealing conditions have been explored, as described below. The average values of PCE (%), V_{oc} (V), J_{sc} (mA cm^{-2}), FF (%) obtained under these conditions are summarized in **Table 7.2**, and *J-V* characteristics are shown in **Figure 7.4**.

Table 7.2 *Summary of the photovoltaic properties of the TPD$_{C8}$-TAT$_{C8}$/P(NDI2OD-T2). (a-h) corresponding to the different conditions. (Two samples per condition)*

| | Ratio | Annealing Time (min) | | Device Performances | | | |
	D: A	80°C	145°C	V_{oc} (V)	J_{sc} (mA cm^{-2})	FF (%)	PCE (%)
a	1:1	-	-	0.73	0.14	32	0.03
b	1:1	10	-	0.60	0.61	55	0.17
c	1:1	-	10	0.64	1.91	48	0.58
d	1.5:1	-	10	0.84	2.15	52	0.94
e	3:1	-	10	0.83	2.40	51	1.02
f	3:1	-	15	0.85	2.63	50	1.11
g	3:1	-	20	0.85	2.73	49	1.15
h	3:1	-	40	0.71	3.92	43	1.20

We initially fixed the M_D/P_A weight ratio to 1:1 and change the thermal treatment conditions. A first annealing step at 80°C (10min) is applied to remove residual solvents (chloroform) and has a dramatic effect on the device performance. The annealing at 145°C (near the cold-crystallization transition, **Figure 4.2a**) aims to change the thin-film morphology (domain size). Annealing at 145°C for 10 min results in an increase in PCE, from 0.17% to 0.58% which correlates well with the increase in J_{sc} from 0.61 mA cm^{-2} to 1.9 mA cm^{-2}. The strong increase in performance is likely due to partial crystallization of TPD-TAT facilitating exciton diffusion and charge carrier transport (as shown in chapter 5 and 6). At the same time, V_{oc} decreased from 0.73V to 0.64V

indicating either a more pronounced recombination or less efficient charge generation. The decrease in *FF,* from 55% to 48%, suggest inefficient charge collection [20-22]. In addition, for the blends in the condition *c* (**Table 7.2**), the SCLC hole mobility was estimated to $1.2\pm0.2\times10^{-4}$cm^{2}v^{-1}s^{-1}, and the corresponding SCLC electron mobility to $1.0\pm0.5\times10^{-3}$cm^{2}v^{-1}s^{-1} (**Figure A7.3**). The one order of magnitude difference in mobility may be at least partly responsible for the low FF [23, 24].
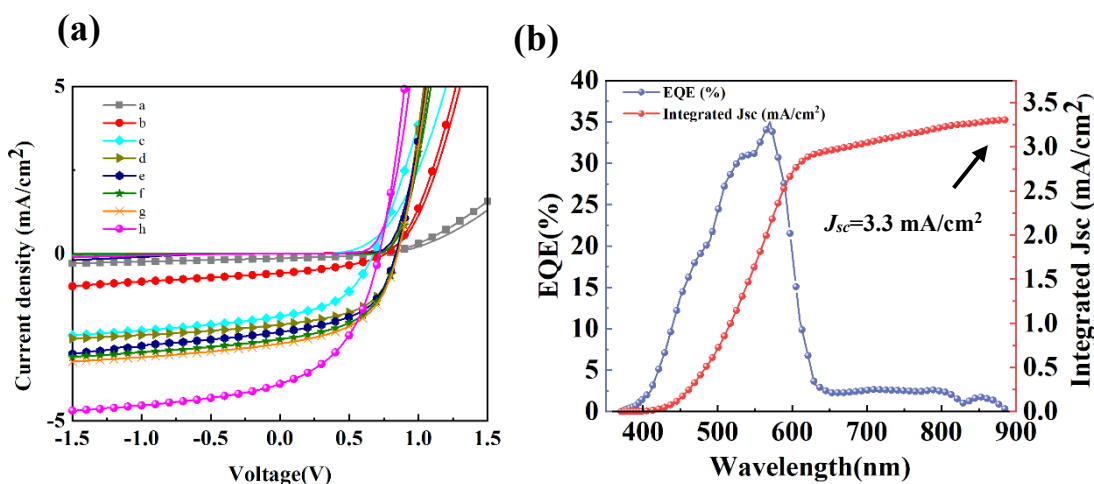
Figure 7.4 *(a) J-V characteristics of BHJ solar cells based on TPD$_{C8}$-TAT$_{C8}$ / P(NDI2OD-T2). (a-h) corresponding to the different conditions in the **Table 7.2**. Solid lines without and with symbols correspond to measurement under dark and under illumination, respectively. (b) External quantum efficiency (EQE) and integrated photocurrent density measured for condition **h** in Table 7.2. J$_{sc}$ was calculated from http://jsc-from-eqe.herokuapp.com/.*

Increasing the proportion of M$_D$ in the blend may increase the SCLC hole mobility and improve the PCE. We therefore kept the annealing temperature at 145°C constant and increased the weight ratio of M$_D$/P$_A$ from 1:1 to 3:1 in a second series of experiments (*c-e*, **Table 7.2**). As a result, the *V$_{oc}$, J$_{sc}$, FF* and PCE increased to 0.83V, 2.40 mA cm^{-2}, 51%, and 1.02%, respectively.

Since the crystal size is expected to increase with annealing time (as seen for pure materials in **chapter 4**) and enhance the hole mobility, we further increased the

annealing time at 145°C from 10 min to 40 min. As shown in the **Figure 7.5**, the crystalline domains did indeed grow, causing the PCE to further increase from 1.02% to 1.20%. Surprisingly, the better performances are due to a higher J_{sc} (which increased by a factor of 1.5) rather than FF, which, although linked to the mobility, decreased to 43%. Also, since larger crystals reduce the D/A interfacial area, they should be unfavorable for charge generation (and thus J_{sc}). The origin of the observed behavior is still unclear and requires further investigations. It is possible that the pronounced film roughness, which accompanies crystallization of TPD-TAT, hinders proper device operation. The film thickness may locally be too large to enable efficient charge collection, or the interface with the HTL layer may be of insufficient quality. In addition, as shown in **Figure 7.4b**, the EQE reveals that the contribution of the polymer to the charge generation is very low. This is at least partly due to the small polymer content in the blend and contributes to the low performances of the OPV devices.
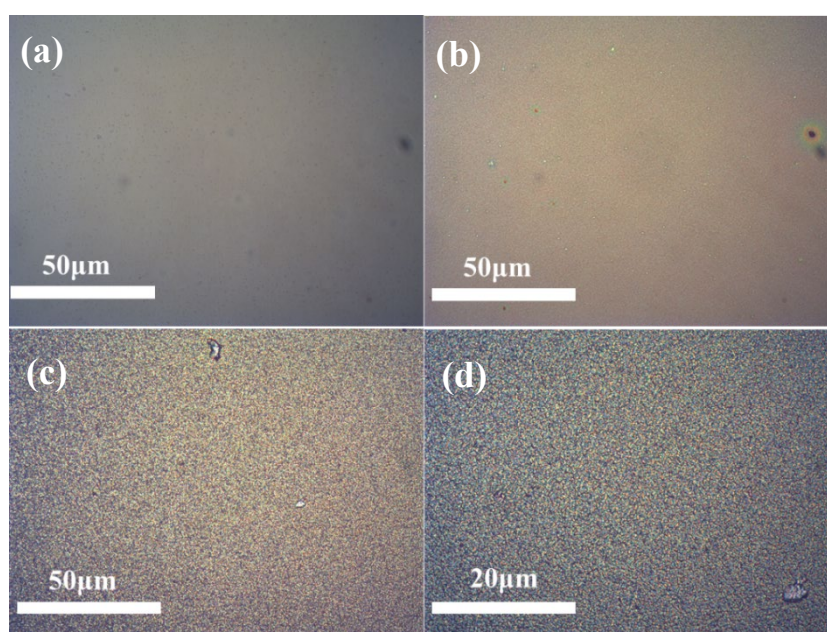
Figure 7.5 *Optical picture of BHJ solar cells based on TPD$_{C8}$-TAT$_{C8}$ /P(NDI2OD-T2) under different annealing conditions: (a) as-deposited, (b) annealed at 145°C, 10min, (c) annealed at 145°C, 40min. (d) picture magnification 2.5 times (c).*

Unfortunately, due to time constraints (the OPV devices were elaborated towards the end of my PhD), a more extensive exploration of other conditions to improve the performance of OPV devices, such as for instance using different processing solvents, annealing conditions or interfacial layers, has not yet been done.

7.4 Conclusion

In summary, we have explored the performance of the TPD_{C8}-TAT_{C8} / P(NDI2OD-T2) blends OPV device varying a range of conditions. The results show that TPD_{C8}-TAT_{C8} crystallization process enhance J_{sc} despite growing D domains. On the other hand, the significant loss in V_{oc} points towards either more pronounced recombination or less charge generation. Yet, the EQE results show that charge generation is most effective in the donor domains. Further studies of the absorption spectra of the solar devices, of their thin film morphology and ambipolar charge carrier transport are necessary to elucidate these apparently contradictory results and figure out the maximum performances that could be reached with this M_D/P_A system.

References:

[1]   J. Hou, O. Inganäs, R. H. Friend and F. Gao, *Nature materials*, 2018, **17**, 119-128.

[2]   C. Yan, S. Barlow, Z. Wang, H. Yan, A. K.-Y. Jen, S. R. Marder and X. Zhan, *Nature Reviews Materials*, 2018, **3**, 1-19.

[3]   P. Cheng, G. Li, X. Zhan and Y. Yang, *Nature Photonics*, 2018, **12**, 131-142.

[4]   P. Sonar, J. P. F. Lim and K. L. Chan, *Energy & Environmental Science*, 2011, **4**, 1558-1574.

[5]   S. Li, W. Liu, C. Z. Li, M. Shi and H. Chen, *Small*, 2017, **13**, 1701120.

[6]   Z. Zhang, T. Wang, Z. Ding, J. Miao, J. Wang, C. Dou, B. Meng, J. Liu and L. Wang, *Macromolecules*, 2019, **52**, 8682-8689.

[7]   Y. Yang, B. Qiu, S. Chen, Q. Zhou, Y. Peng, Z.-G. Zhang, J. Yao, Z. Luo, X. Chen, L. Xue, L. Feng, C. Yang and Y. Li, *Journal of Materials Chemistry A*, 2018, **6**, 9613-9622.

[8]   J. Yuan and W. Ma, *Organic Electronics*, 2016, **39**, 279-287.

[9]   Z. Zhang, Z. Ding, D. J. Jones, W. W. Wong, B. Kan, Z. Bi, X. Wan, W. Ma, Y. Chen and X. Long, *Science China Chemistry*, 2018, **61**, 1025-1033.

[10]   Z. Zhang, Z. Ding, J. Miao, J. Xin, W. Ma, C. Dou, J. Liu and L. Wang, *Journal of Materials Chemistry C*, 2019, **7**, 10521-10529.

[11]   M. Liu, J. Yang, C. Lang, Y. Zhang, E. Zhou, Z. Liu, F. Guo and L. Zhao, *Macromolecules*, 2017, **50**, 7559-7566.

[12]   J. Choi, K.-H. Kim, H. Yu, C. Lee, H. Kang, I. Song, Y. Kim, J. H. Oh and B. J. Kim, *Chemistry of Materials*, 2015, **27**, 5230-5237.

[13]   P. Sonar, G.-M. Ng, T. T. Lin, A. Dodabalapur and Z.-K. Chen, *Journal of Materials Chemistry*, 2010, **20**, 3626-3636.

[14]   X. Long, Z. Ding, C. Dou, J. Zhang, J. Liu and L. Wang, *Advanced materials*, 2016, **28**, 6504-6508.

[15]   C. Zhao, J. Wang, J. Jiao, L. Huang and J. Tang, *Journal of Materials Chemistry C*, 2020, **8**, 28-43.

[16]   H. Yan, Z. Chen, Y. Zheng, C. Newman, J. R. Quinn, F. Dötz, M. Kastler and A. Facchetti, *Nature*, 2009, **457**, 679-686.

[17]   W. Xu, Y. Chang, X. Zhu, Z. Wei, X. Zhang, X. Sun, K. Lu and Z. Wei, *Chinese Chemical Letters*, 2021.

[18]   S. Oh, S. Badgujar, D. H. Kim, W.-E. Lee, N. Khan, M. Jahandar, S. Rasool, C. E. Song, H. K. Lee, W. S. Shin, J.-C. Lee, S.-J. Moon and S. K. Lee, *Journal of Materials Chemistry A*, 2017, **5**, 15923-15931.

[19]   S.-Y. Liu, J. W. Jung, C.-Z. Li, J. Huang, J. Zhang, H. Chen and A. K. Y. Jen, *Journal of Materials Chemistry A*, 2015, **3**, 22162-22169.

[20]   A. Cabas Vidani, ETH Zurich, 2020.

[21]   M. Hiramoto, in *Organic Solar Cells*, Springer, 2021, pp. 255-267.

[22]   K. D. Rosenthal, M. P. Hughes, B. R. Luginbuhl, N. A. Ran, A. Karki, S. J. Ko, H. Hu, M. Wang, H. Ade and T. Q. Nguyen, *Advanced Energy Materials*, 2019, **9**, 1901077.

[23]   N. Liu, S. Mei, D. Sun, W. Shi, J. Feng, Y. Zhou, F. Mei, J. Xu, Y. Jiang and X. Cao, *Micromachines*, 2019, **10**, 344.

[24]   V. D. Mihailetchi, H. Xie, B. de Boer, L. A. Koster and P. W. Blom, *Advanced Functional Materials*, 2006, **16**, 699-708.

Chapter 8
Conclusion and perspectives

As already established by the organic electronics community, exciton dynamics and charge carrier transport are important factors that influence the performances of optoelectronic devices and have been shown to be highly dependent on molecular and solid state structures. In this context, my PhD work, in the field of organic photovoltaics, aimed to study the exciton dynamics and charge carrier transport in TAT based D-A-D molecular thin-films. The investigated molecular semiconductors are composed of a central TPD unit and two peripheral TAT units, where TAT is highly planar, soluble, and functionalized electron donor moieties that act as π-stacking platforms. TPD is an electron acceptor unit that determines the optical bandgap. "TPD-TAT" derivatives functionalized with either linear side chains or branched side chains on the central TPD unit and on both TAT units have been investigated.

We first focused on the molecular self-assembly structure of TPD-TAT derivatives. The DSC and POM results demonstrated that the molecular packing order can be tuned by side-chain engineering and thermal treatments. Strong intermolecular stacking interactions are induced by the discotic-planar TAT units, which dominate the molecular self-assembly. Therefore, the side-chains on the TAT units play a key role in the process of self-assembling of the molecules. We found indeed that only TPD_{C8}-TAT_{C8} (with linear side-chains on both units) and TPD_{EH}-TAT_{C8} (with linear side-chains on TAT units) can form a hexagonal columnar-nematic liquid crystalline and crystalline solid-states. Moreover, GIWAXS and Microfocus X-ray diffraction results on TPD_{C8}-TAT_{C8} thin-films revealed that, in both bridged hexagonal columnar-nematic phase and crystalline solid-states, the molecular π-stacking direction is oriented parallel to the substrate.

Having the above information about the molecular self-assembly structure, we investigated exciton dynamics as a function of chemical and self-assembly structure in TDP-TAT derivatives. In particular, we showed that the exciton lifetime significantly increased from the as-deposited to the crystalline states, the lifetime value in the

crystalline state having been determined to be longer than that in solution. This latter unusual phenomenon may be attributed to a low non-radiative recombination rate in the crystalline state due to a low defect density. Moreover, we established that the non-exponential PL decay in our molecular OSCs originates from the co-existence of different molecular solid-states in a single thin-film, each having its own lifetime. Thanks to two techniques (EEA and PLQY theories) presenting different working hypothesis, we were able to determine the exciton diffusion length in TPD$_{C8}$-TAT$_{C8}$ thin films with different solid-states, and ensured the consistency of these values. We showed that the exciton diffusion length is doubled from the as-deposited to the crystalline states, this result being associated with an increase in both the exciton lifetime and diffusion coefficient. Since, generally, a higher intermolecular coupling leads to an increase in the exciton diffusion coefficient but simultaneously a decrease in the exciton lifetime, this uncommon behavior makes TPD-TAT molecules promising for OPV applications, for which a long diffusion length is of particular interest.

To probe the (an)isotropic character of the studied planar molecules, we explored out-of-plane (by SCLC) and in-plane (by OFET) hole transport in TPD$_{C8}$-TAT$_{C8}$ thin-films as a function of the molecular packing structure. Our observations suggest that the two highly planar TAT units are effectively driving the molecules into a unique 3D conducting bridged columnar phase, wherein the molecules are bridging adjacent columns or molecular stacks through the insulating aliphatic domains. As a consequence, 3D charge-transport with a low degree of anisotropy was observed in solution processable crystalline small molecules.

In order to exploit the interesting properties of the TPD$_{C8}$-TAT$_{C8}$ molecule, both in terms of exciton diffusion and charge transport, we studied the performance of TPD$_{C8}$-TAT$_{C8}$/P(NDI2OD-T2) blends in OPV devices by optimizing the deposition and the post-treatment conditions. The results demonstrated that the thin-films crystallization process favors the increase of the short circuit current, thanks to the good exciton

diffusion and charge transport properties obtained in the crystalline phase. However, the crystallization process can lead to a decrease in the open circuit voltage of OPV devices, due to an increase in non-radiative recombination at the crystalline domain boundaries. A maximum PCE value of 1.2% was obtained during this work. This value is below the values of the state of the art but in-depth investigations and optimizations should allow it to be improved.

In conclusion, the above studies elucidate how the molecular structure and self-assembly of a particular class of planar dumbbell-shaped molecular semiconductors impact exciton dynamics and charge transport, and thereby the optoelectronic properties of thin films and devices. Yet, some open questions and issues are worth to be further addressed. In particular, the crystallographic structure of the crystalline needles is not fully resolved yet. Also, the origin of the remarkably long exciton lifetime in the crystals, which exceeds that observed in solution, is still unclear. On the device part, the elaboration of optimized OFET devices with reduced contact resistance would allow a better estimate of the charge mobility along the stacking direction and achieve better transistor performance. Finally, the major bottlenecks that currently limit the performances OPV devices based molecules blended with N-type polymers donor, are still be clarified in order to enable us to take fully advantage of the optoelectronic properties of this material for OPV applications.

Annex

Chapter A4 Materials

Grazing Incidence Wide-Angle X-ray Scattering (GIWAXS): The relative locations of scattering peaks are directly correlated to the molecular packing orientation with respect to the substrate. As shown in **Figure A4.1**, when the lamellar stacking is perpendicular to the substrate and the π-π stacking orientation is parallel to the substrate, the lamellar peak (100) will appear in the q_z direction and the π-π peak (010) in the q_r direction. Such kinds of molecules packing style are namely "edge-on" oriented in the film (**Figure A4.1a**). On the contrary, when the π-π stacking orientation is perpendicular to the substrate and the lamellar stacking is parallel to the substrate, the π-π peak (010) will appear in the q_z direction and the lamellar peak (100) in the q_r direction. Such kinds of molecules packing style are namely "face-on" oriented (**Figure A4.1b**). In some cases, the crystallites could be randomly oriented with respect to the substrate, giving rise to a ring-like scattering feature (**Figure A4.1c**)[1, 2].

GIWAXS measurements were conducted by Dr. Benoit Heinrich at PLS-II 9A U-SAXS beamline of Pohang Accelerator Laboratory (PAL) in Korea. The X-rays coming from the vacuum undulator (IVU) were monochromated using Si (111) double crystals and focused on the detector using K-B type mirrors. Patterns were recorded with a 2D CCD detector (Rayonix SX165). The sample-to-detector distance was about 222 mm for energy of 11.07 keV (1.120 Å).
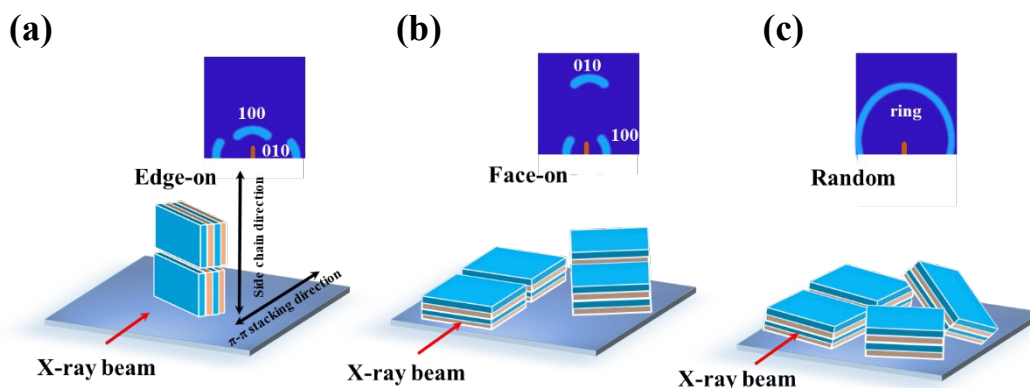
Figure A4.1 *Schematic of the packing orientations and the resultant 2D GIWAXS patterns. (a) "edge-on" oriented. (b) "face-on" oriented. (c) random oriented.*

Microfocus X-ray diffraction: Microfocus X-ray diffraction experiments were carried out at the ID13 beamline of the European Synchrotron Radiation Facility (ESRF) in Grenoble (France). For the measurements spin-coated films of TPD$_{C8}$-TAT$_{C8}$ were crystallized on a 1 μm thick suspended Si3N4 window from Silson Ltd. (UK). The region of interest on a membrane was identified with an on-axis optical microscope. The X-ray diffraction measurements were performed with a photon energy of 13 keV (0.9537 Å) at a sample-to-detector distance of (155.96±0.02) mm. The footprint of the X-ray beam was 2.5×2.5 μm^2. The sample was fixed on a piezo translation stage, which in turn was placed on a hexapod stage for coarse movements. The sample was 2D scanned with a step of 1 μm along both coordinates. The resulting 2D diffractograms were centered, geometrically corrected and calibrated using a corundum standard.

Polarizing microscope (POM): The characteristic of a polarizing microscope is to change the ordinary light into polarized light for microscopic examination, in order to identify whether a matter is isotropic or anisotropic. When light passes through a matter, if the nature and approach of the light does not change due to the direction of illumination, the matter is optically 'isotropic', also known as single refraction, such as ordinary gases, liquids, and amorphous solid. On contrary, if light passes through

another matter, the speed, refractive index, absorbency, and vibration of the light are different depending on the direction of illumination. This matter is optically 'anisotropic', also known as birefringent. It occurs for crystals, fibers, liquid crystals.

Differential scanning calorimetry (DSC): Differential scanning calorimetry (DSC) were performed with a TA Instruments Q1000 instrument by Dr. Benoit Heinhrich (Institut de physique et de chimie des Matériaux de Strasbourg), operated at a scanning rate of 5 °C min^{-1} on heating and on cooling.

Film thickness measurements: The nematic state thin film thickness was measured using a Bruker Dektak profilometer with a scan speed of 10 µm s^{-1}, lateral resolution of 0.6 µm, and stylus force 1.0 mg. The crystalline state thin film thickness and roughness was measured using atomic force microscopy (AFM).
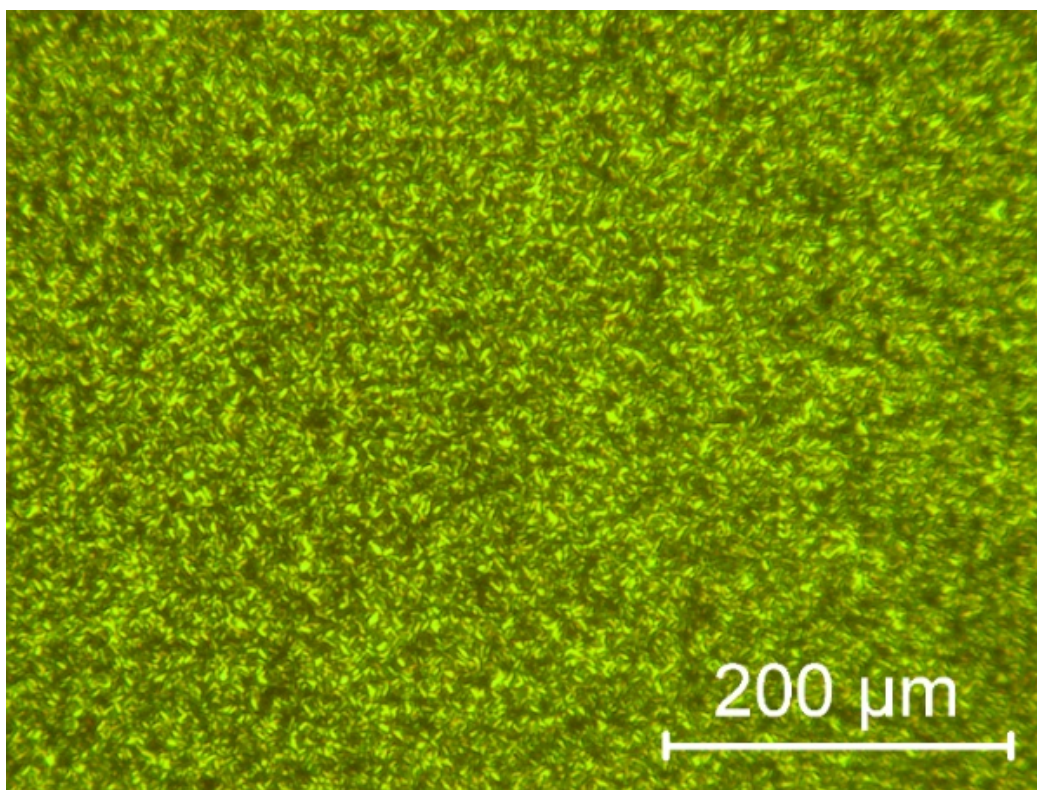
***Figure A4.2** POM of a TPD$_{C8}$-TAT$_{C8}$ thin film on small crystals.*

Chapter A5 Exciton dynamics

UV-visible spectroscopy

UV-visible absorption spectrum is necessary for measuring exciton diffusion length of TDP$_{C8}$-TAT$_{C8}$ thin films function of molecular self-assembly by PLQY theory techniques. In this thesis, since the TDP$_{C8}$-TAT$_{C8}$ thin films form crystals after follow annealing steps (as shown in chapter 4), it has a large surface roughness which leads to strong light diffusion, so it is necessary to apply an integrating sphere attachment for UV-vis spectroscopy, as shown in the **Scheme A5.1**. Correct measurement can be performed when an integrating sphere is applied, because all of measurement lights are irradiated on the light-sensitive surface of the detector after light being diffused inside the integrating sphere.
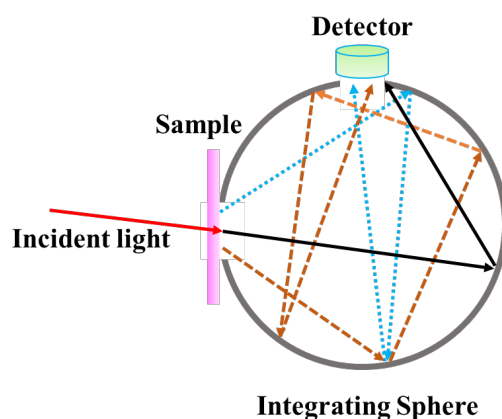
Scheme A5.1 *Schematic of an Integrating Sphere.*

Extinction coefficient (*k*) is determined by the absorption properties of light in the materials. In case of Molar extinction coefficient (ε), is represented as how strongly a substance absorbs light at a given wavelength, per molar concentration. Molar extinction coefficient (in M^{-1}cm^{-1}) is given by[2]:

$$\varepsilon = \frac{A}{cl} \quad (A5.1)$$

Where (A) is absorbance, (*l*) is the optical path length and (*c*) is the molar concentration. In this thesis, for thin films measurements assumed the optical path length is equal to the film thickness. (*c*) is the molar density, which is[3]

$$c = 1000 \frac{\rho}{M_n} \quad (A5.1)$$

Where ρ is the density of thin films and M_n is the molecular weight of a chromophore. In this thesis, ρ is 1.11 g/cm^3, M_n is 1789.65 g/mol for TDP$_{C8}$-TAT$_{C8}$ bulks materials.

Refractive index (n)

Refractive index (*n*) was obtained by using spectral ellipsometry TN01, HORIBA. The principle of ellipsometry is shown in **Scheme A5.2**. Ellipsometry is an optical technique that measurement the change in the polarization state of light, reflected from the surface of a sample. When a light wave interacts with a material, its state of polarization is modified. The measurement of the variation of polarization between the incident and the reflected wave makes it possible to deduce physical and optical information related to the thin film stack. In this thesis, for organic thin films fitting data by using Generalized Oscillator model[4, 5]. This measurement was carried out at ICube (guide by Dr. Jeremy Bartringer).
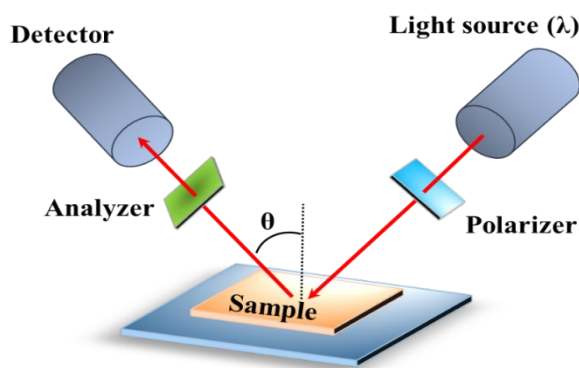
Scheme A5.2 *Schematic of spectroscopic ellipsometry.*

Continuous-wave photoluminescence (CW-PL)

The samples (thin-films or solutions) were excited at 315nm by a Nd-YAG laser, laser power is 88mW, frequency is 15000Hz, FWHM is 12.5ns. Spectrometer by using BRC112E CCD. This measurement was carried out at ICube (guide by Dr. Jeremy Bartringer).

Time-resolved micro-PL measurements

The spot diameter is 300 nm, this is the spatial resolution. Temporal resolution is around 0.05 ns. The laser power is 250 microW (50microW for big amount of small crystals-75 microW for big crystals) and laser wavelength 950 nm (2 photons absorption). This measurement was carried out at LBP, Illkirch, the thin-films samples were prepared at ICube.

Quantum yield (QY)

Quantum yield measurement by FluoroMax®-4 - Spectrofluorometer by HORIBA Scientific. The thin-films obtain by spin coating on the top of round glass slice (Diameter=13mm, thickness =0.17mm). Principle of quantum yield measurement as shown in **Scheme A5.3**. This measurement was carried out at ICPEES (guide by Dr. Gilles Ulrich), and the thin-films samples were prepared at ICube.
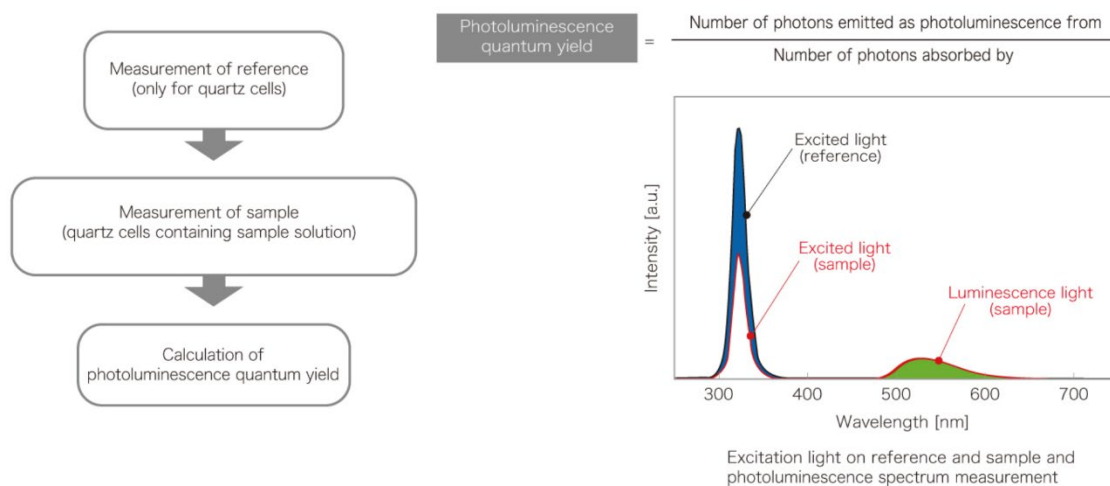
Scheme A5.3 *Principle of quantum yield measurement (copyright from https://www.hamamatsu.com/eu/en/product/photometry-systems/luminescence-efficiency-measurement-system/quantaurus-qy/measurement-principle/index.html).*
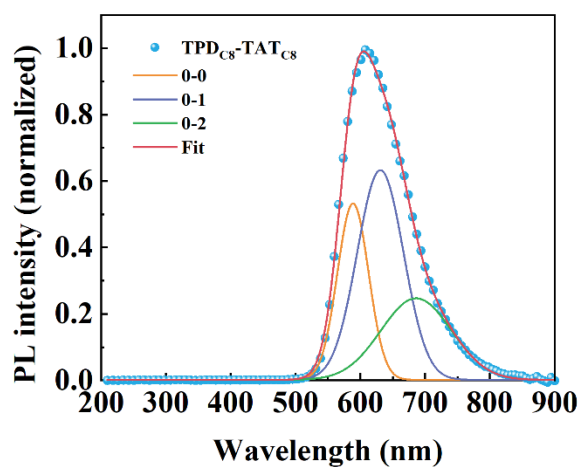
Figure A5.1 *PL spectrum and Gaussian peak fit for molecule in the solution. Both of four molecules have the same PL spectrum and Gaussian peak fit.*

(a)

(b)

(c)

(d)
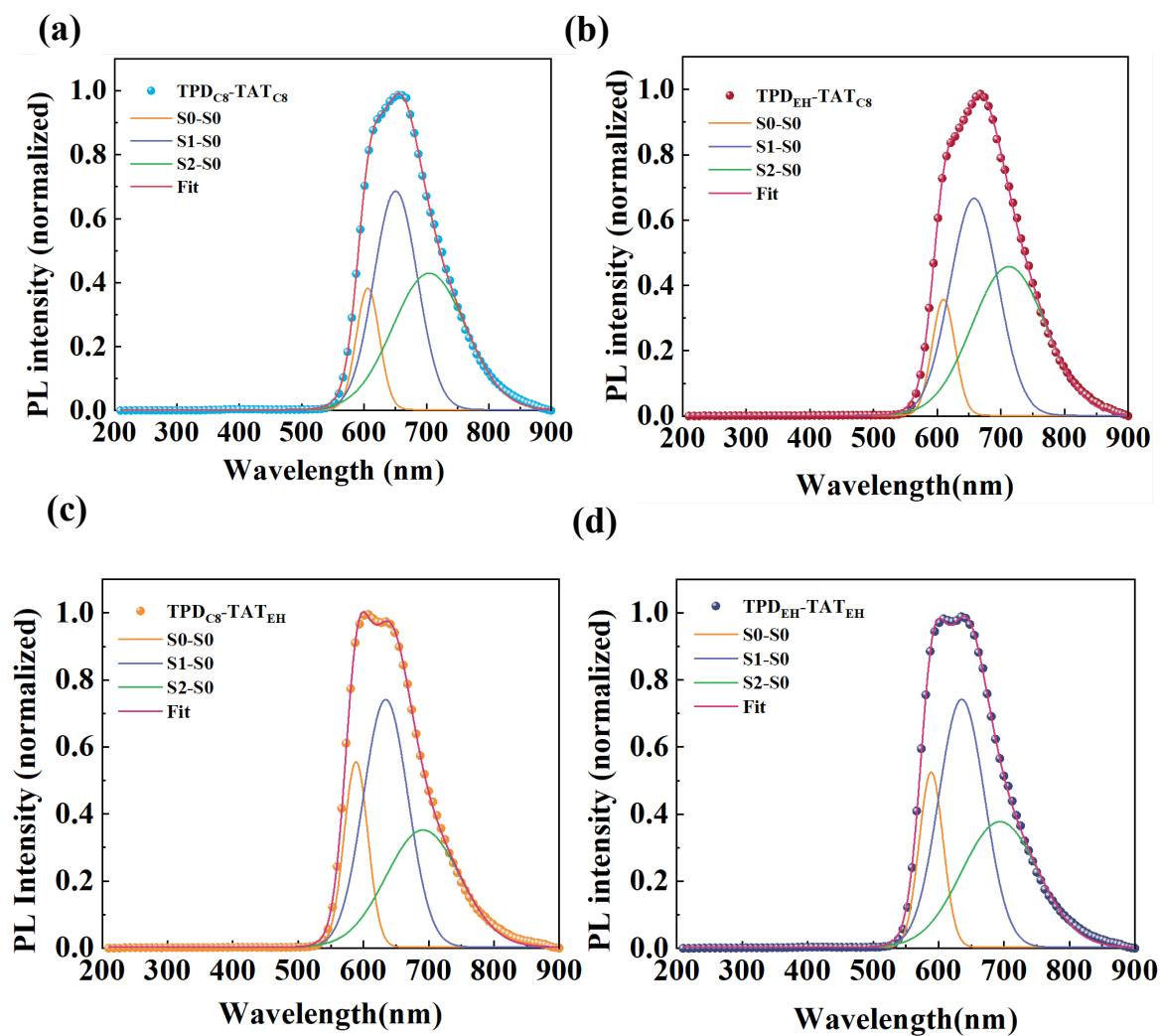
Figure A5.2 *PL spectrum and Gaussian peak fit for four molecules in the as deposited state.*
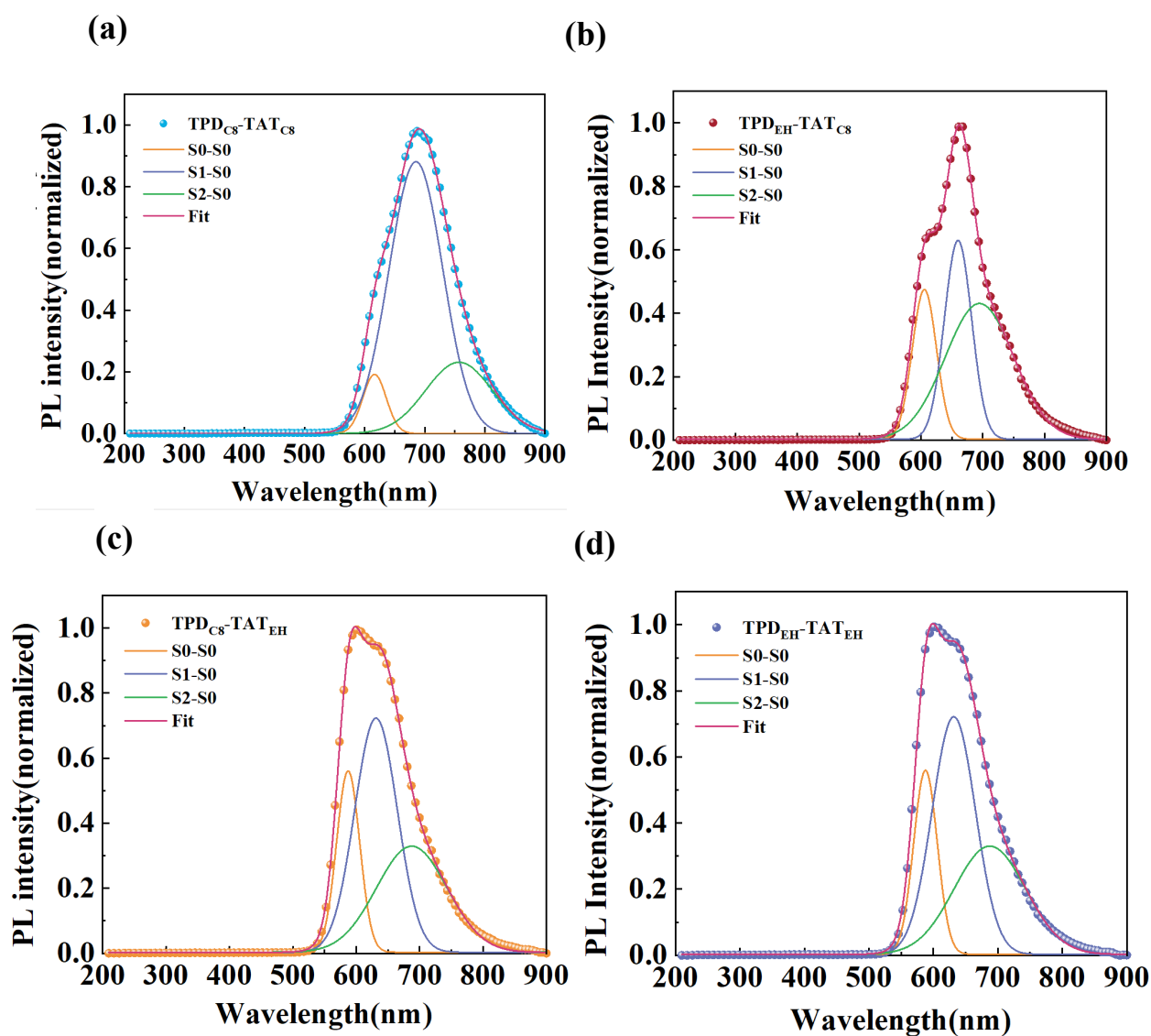
Figure A5.3 *PL spectrum and Gaussian peak fit for four molecules after thermal treatment.*
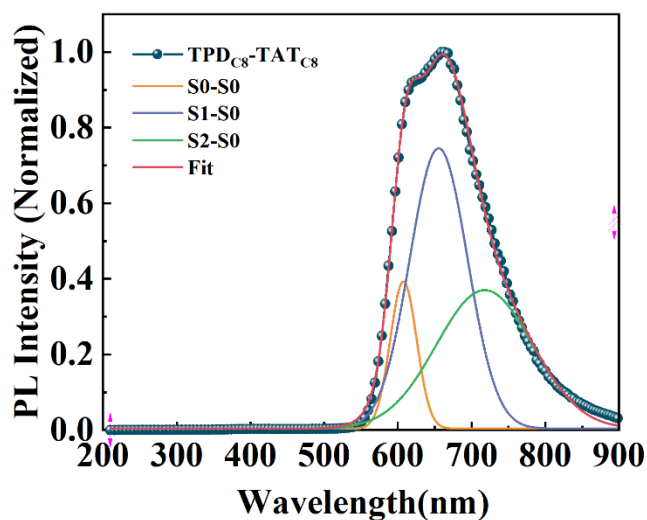
Figure A5.4 *PL spectrum and Gaussian peak fit for molecules in the nematic state.*
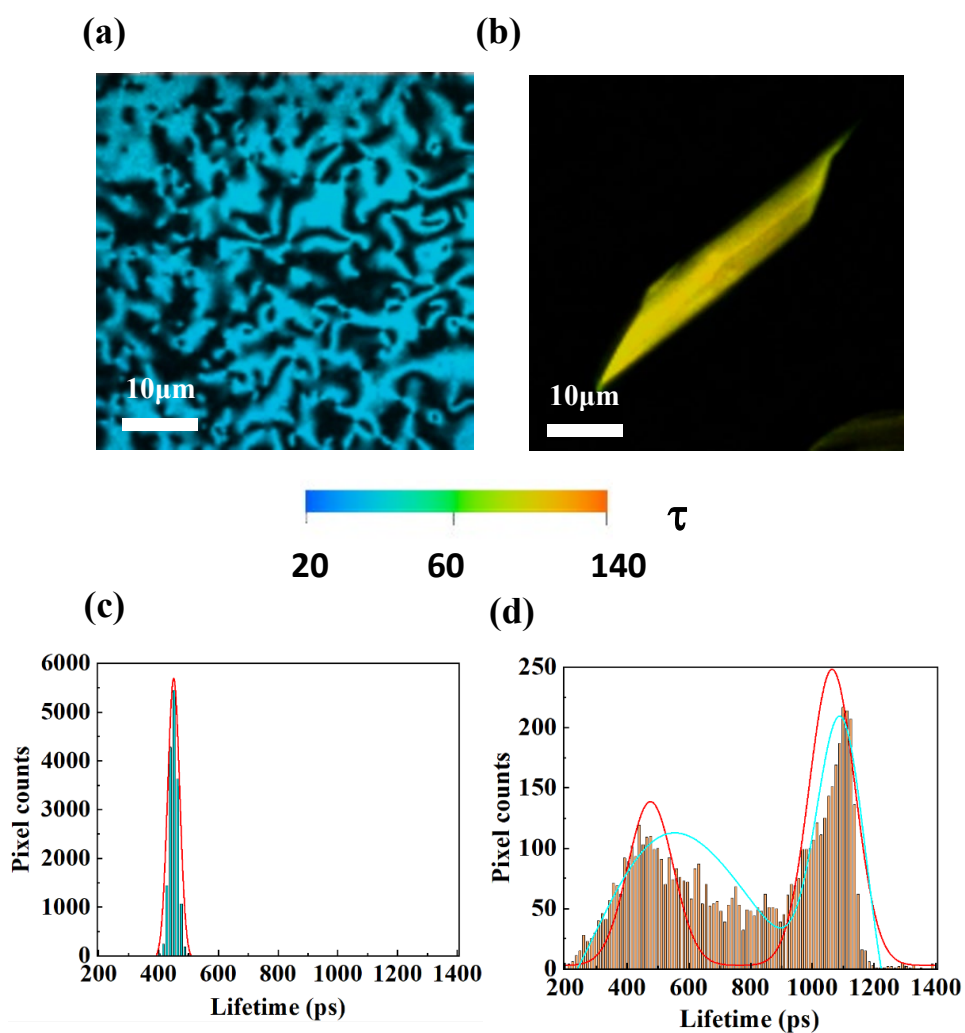
Figure A5.5 *Mic-PL of TPD$_{C8}$-TAT$_{C8}$ molecule in (a) nematic state, (b) crystalline state. Distribution of lifetime in (c) nematic state, in (d) crystalline state. The color scale represents the PL decay lifetime.*
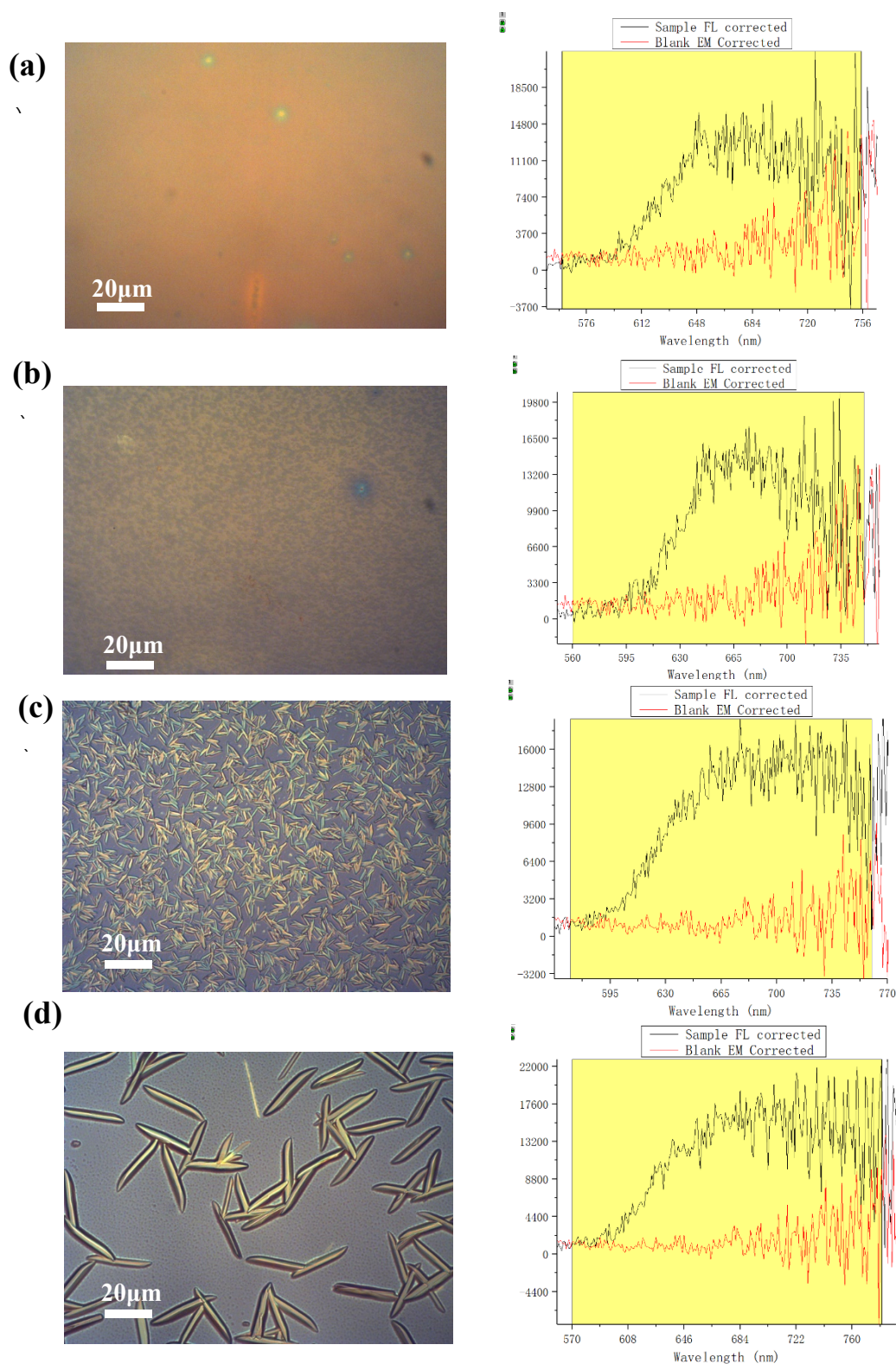
Figure A5.6. *Picture of thin films and the corresponding Quantum yield in (a) as-deposited state 2.3±0.1%, (b) nematic state 2.4±0.1%, (c) small crystal around (8.0μm) 4.4±0.3%, (d) big crystal around (25.0μm) 5.2 ±0.5%. Quantum yield calculate by software HORIBA, integrate the area between the black line (sample) and the red line (blank).*

(a)

(b)

(c)

(d)
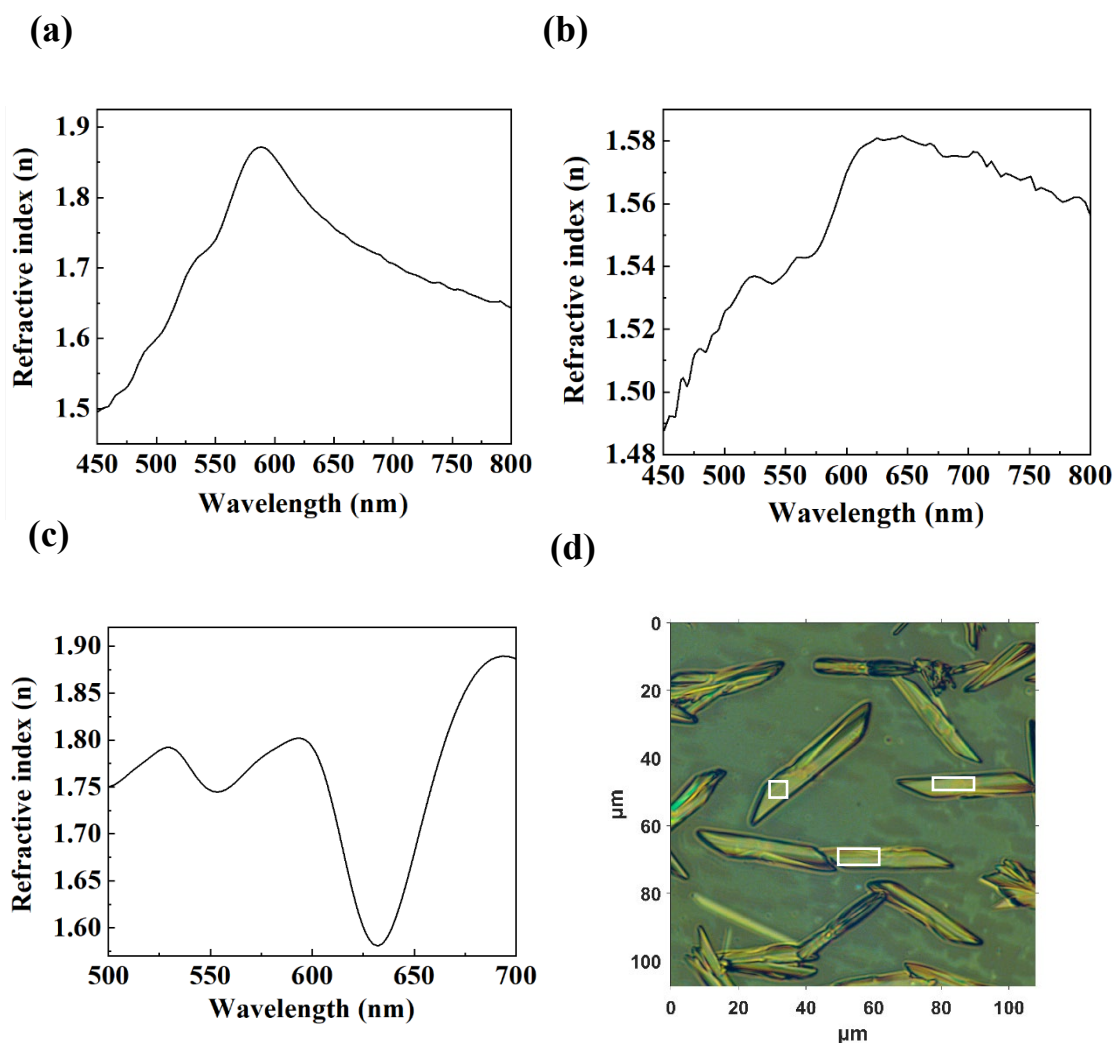
Figure A5.7: *Refractive index (n) obtain from ellipsometry at wavelength 575nm for TPD$_{C8}$-TAT$_{C8}$ in (a) as-deposited and (b) nematic state. The refractive index (n) obtained from wight-light interference microscopy, at wavelength 600nm for TPD$_{C8}$-TAT$_{C8}$ in (c) crystalline state. Because the crystalline state has a low fill factor on the surface of the quartz, it was no longer appropriate to use ellipsometry to measure the n. On the contrary, wight-light interference microscopy technique allow us to focus on the surface of isolated crystals. According to the equation $R = \left[\dfrac{n-1}{n+1}\right]^2$, we measurement the reflectance (R) of isolated crystals and assumed there is no absorption effect. We analyzed three different places (white rectangle in **Figure A5.7 (d)**) on top of isolated crystals and also in three different area of whole samples.*
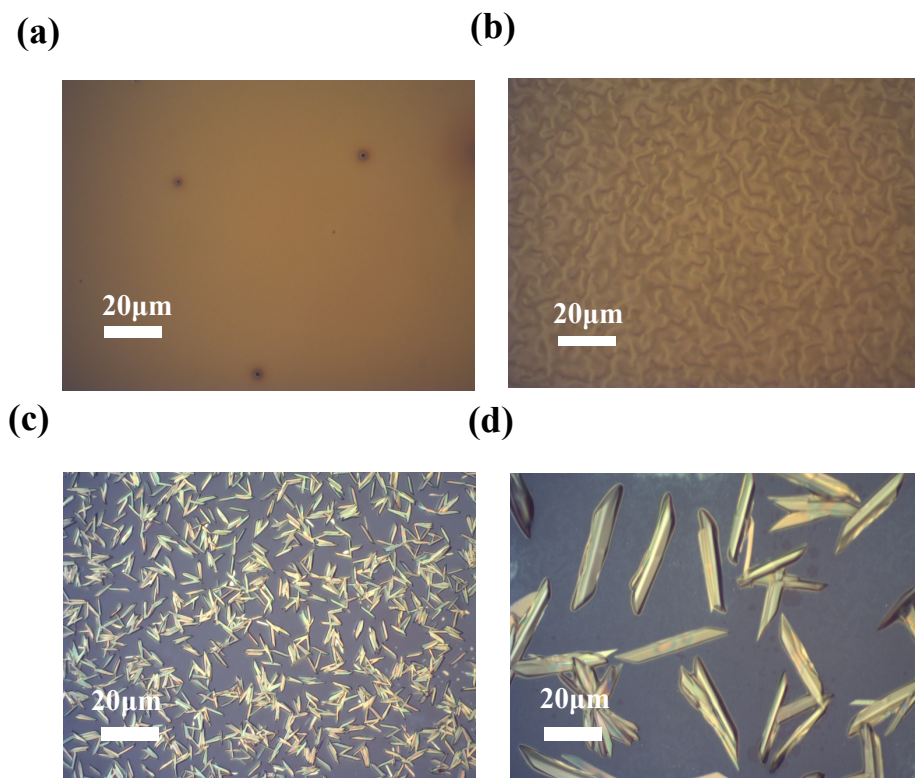
Figure A5.8: *Microscope of TPDc8-TATc8 in different molecule state (a) as-deposited, (b) nematic, (c) small crystal around 8.0μm, (d) big crystal around 25.0μm for EEA measurement. Radius of laser spot size is 9 μm.*
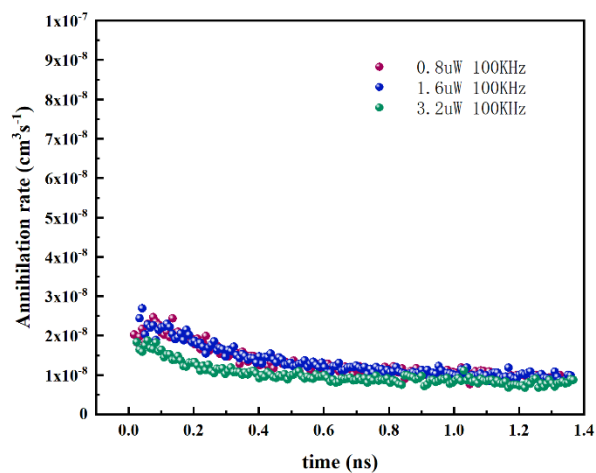
Figure A5.9: *Rate constant γ of singlet–singlet exciton annihilation function of decay time for TPDc8-TATc8 in crystalline thin-films.*
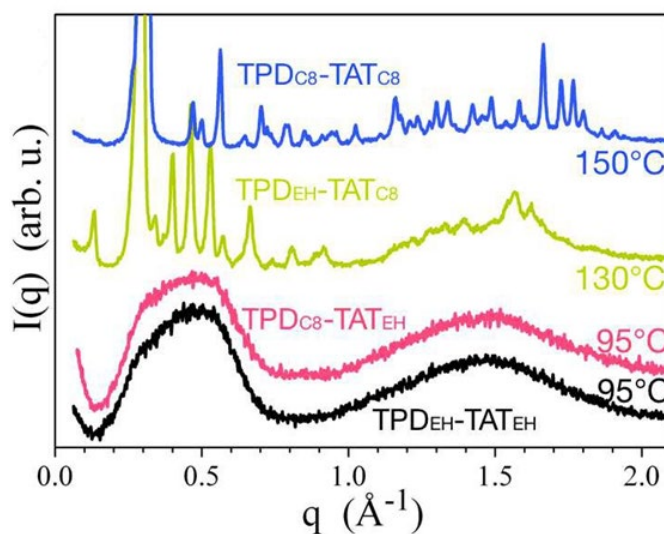
Figure A5.10: *SAXS patterns measured a) on pure TPD-TAT materials at room-temperature; b) on TPD$_{C8}$-TAT$_{C8}$ at 150°C and TPD$_{EH}$-TAT$_{C8}$ at 130°C, after their cold crystallization; TPD$_{C8}$- TAT$_{EH}$ and TPD$_{EH}$-TAT$_{EH}$ in the isotropic liquid at 95°C. (Copyright from Tianyan Han[6])*

Chapter A6 Charge carrier transport

A6.1 Space-charge-limited-current (SCLC)

Standard SCLC devices

The standard device structure used for hole mobility measurements is shown in **Scheme A6.1**. The Indium Tin Oxide (ITO) coated glass substrates were first cleaned in soapsuds, deionized water, acetone, isopropyl alcohol at 45 °C for 15 minutes and treated by UV-ozone for 30 minutes. Poly (3,4- ethylenedioxythiophene): polystyrene sulfonate (PEDOT: PSS) was spin-coated on top of the ITO (5000 rpm for 60 s), dried at 140 °C for 30 minutes in N_2 atmosphere and used as hole injection electrode. A 20 mg·mL^{-1} chloroform solution of TPD$_{C8}$-TAT$_{C8}$ was spin-coated on top of the PEDOT: PSS layer under nitrogen ambient. Different thicknesses were achieved using different spin speeds (typically, 1500 rpm for 60 s leads to a 250 nm thick layer). Lastly, 7 nm thick MoO$_3$ and 120 nm thick Ag layers were deposited by physical vapor deposition on top of the active layer under vacuum ($< 10^{-6}$ mbar). The electrode surface area varied

between 1.0 mm^2, and 2.5×10^{-2} mm^2. The small device areas were necessary to avoid the compliance of the measurement equipment for high mobility samples.
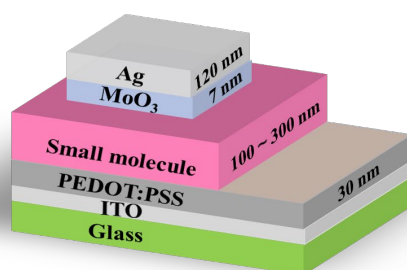

Scheme A6.1 *Structure of a standard SCLC device.*

Thick SCLC devices

Thick devices were manufactured by first structuring the ITO layers with acid etching into an array of parallel, 1 mm wide, ITO stripes. Both glass/ITO substrates were coated by PEDOT: PSS and used as building block for the final device (**Scheme A6.2**). A suitable amount of molecular powder (0.5~3 mg) was accurately weighted (to the nearest one-hundredth of a mg) and was deposited on the center of one structured glass/ITO substrate. Several spacers (8, 20, 28 µm thick) were added on the four corners in order to define the approximate final active layer thickness. The second ITO-glass substrate was put on top of the molecular powder with the electrodes being perpendicularly oriented with respect to the ITO strips of the bottom substrate. The sample was then heated above the isotropic transition temperature (180 °C) for several minutes under mechanical compression. Being in the liquid state, the molecules were able to spread over the device area, while a mechanical pressure was constantly and evenly applied over the entire surface of the cell. After cooling to room temperature, some of the samples were annealed at 145 °C for 40 minutes to form the crystalline phase. The final device thickness L of the active layer was estimated by taking into account the mass m of the organic materials deposited on the first substrate and the area S occupied by the organic materials as evaluated from the micrograph (red area of **Scheme A6.2d**), according to $L = m/(\rho \cdot S)$ and assuming a volume density ρ of 1.0 mg

cm^{-3}. The individual diode area was fixed to 1 mm². For each sample, approximately 4 individual diodes could be characterized.
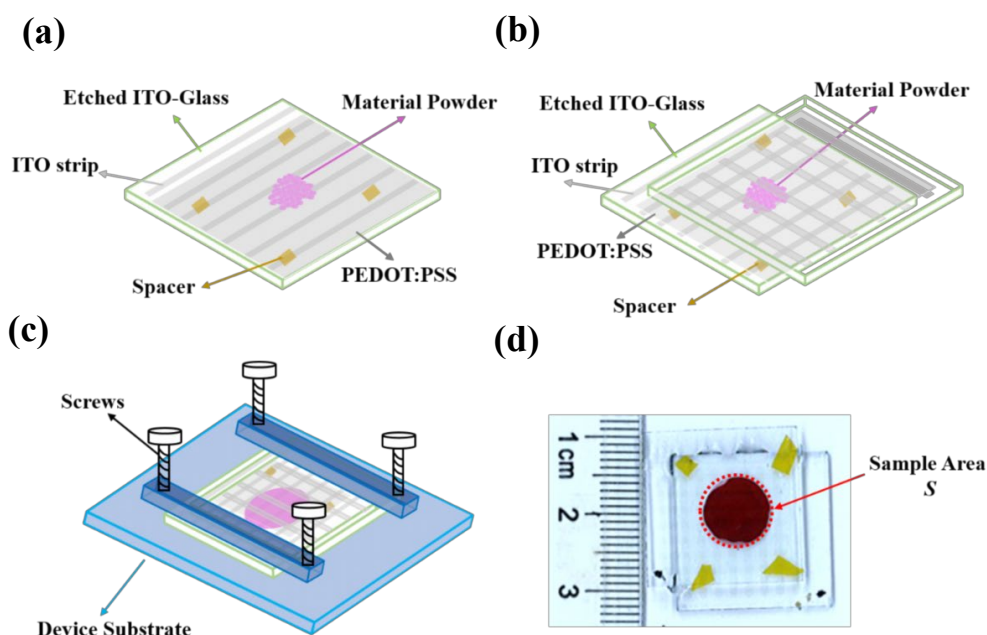
Scheme A6.2 *Thick SCLC devices. (a)-(c) Fabrication procedure of thick SCLC devices. (d) Image of thick SCLC device. For each sample, four efficient diodes were obtained with 1.0 mm² individual active area (crossing of ITO stripes).*

A6.2 Organic field-effect transistors

Bottom-contact-bottom gate transistors

Bottom-contact-bottom gate transistors were fabricated using commercially available Si/SiO₂ substrates with lithographically defined source and drain contacts (**Scheme A6.3a**). The latter were composed of ITO (10 nm)/Au (30 nm) bilayers defining a channel length of 2.5 μm and channel width of 1.0 cm. The 230 nm thick SiO₂ layer was used as a gate dielectric. The substrates were cleaned in soapsuds, acetone and isopropyl alcohol and subsequently for 30 minutes in an UV-ozone system. A 5 mg ml⁻¹ concentrated anhydrous chloroform solutions of TPD$_{C8}$-TAT$_{C8}$ were spin-coated (1500 rpm for 60 s) in N₂ ambient.

Top-contact-bottom gate transistors

Top-contact-bottom gate transistors were fabricated using a silicon substrate with a 200 nm thermal silicon oxide (SiO$_2$) layer as gate dielectric (**Scheme A6.3 b**). The substrates were cleaned in soapsuds, acetone and isopropyl alcohol and subsequently for 30 minutes in an UV-ozone system. A 5 mg ml^{-1} concentrated anhydrous chloroform solutions of TPD$_{C8}$-TAT$_{C8}$ were spin-coated (1500 rpm for 60 s) in nitrogen ambient. The top electrodes (7 nm MoO$_3$ and 120 nm Ag) were thermal evaporated on top of the active layer under secondary vacuum (<10^{-6} mbar).
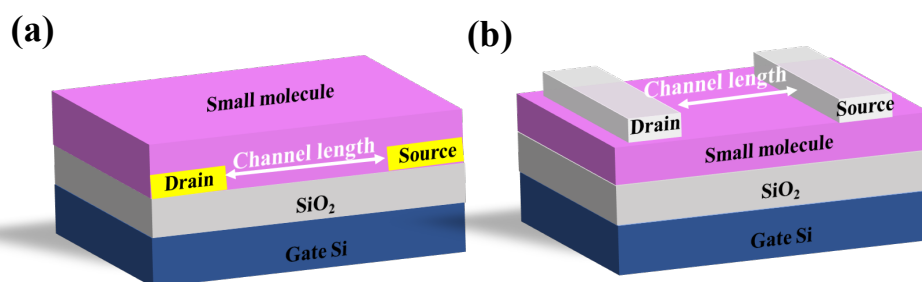
Scheme A6.3 *OFET device structures. (a) Bottom-contact-bottom-gate transistors, with ITO/Au bilayers used as drain and source electrode. (b) Top-contact-bottom-gate transistors, with MoO$_3$/Ag layers used as drain and source electrode.*

Electrical characterization

SCLC and OFET devices were characterized in nitrogen ambient using a probe station and a Keithley 4200 semiconductor analyzer. A Peltier thermo-module was used for temperature dependent SCLC measurements. The SCLC devices were placed directly on top of the Peltier module. The temperature was measured by a RTD Pt100 sensor and varied between 263 K to 323 K. The field-effect hole mobility was calculated by fitting the measured transfer curves in the saturation regime to the standard transistor model.[44]

A6.3 Device modellig

Least-square fitting $J=J_{(ohmic)}+J_{(SCLC)}$

The least-square fitting method takes advantage of the fact that the *I-V* characteristics can be approximated by equation 6.1 $J = q\mu_h p_o \frac{V}{L} + \frac{9}{8}\varepsilon_o\varepsilon_r\mu_h\frac{V^2}{L^3}$, as shown by Röhr and MacKenzie[7]. This makes the procedure more robust when the SCLC region is narrow, because the entire voltage range is contributing.

Figure A6.1 demonstrates the fitting approach for a standard SCLC device in the crystalline state. First, the *I-V* characteristics are fitted to equation 6.1, yielding an estimate for the hole mobility μ_h and the background concentration p_0 (black curve). These parameters are then fed into a 1D drift-diffusion model solved using the COMSOL Multiphysics software® (red curve). The good accordance between both curves confirms a posteriori the validity of summing the ohmic and Mott-Gurney's contributions.
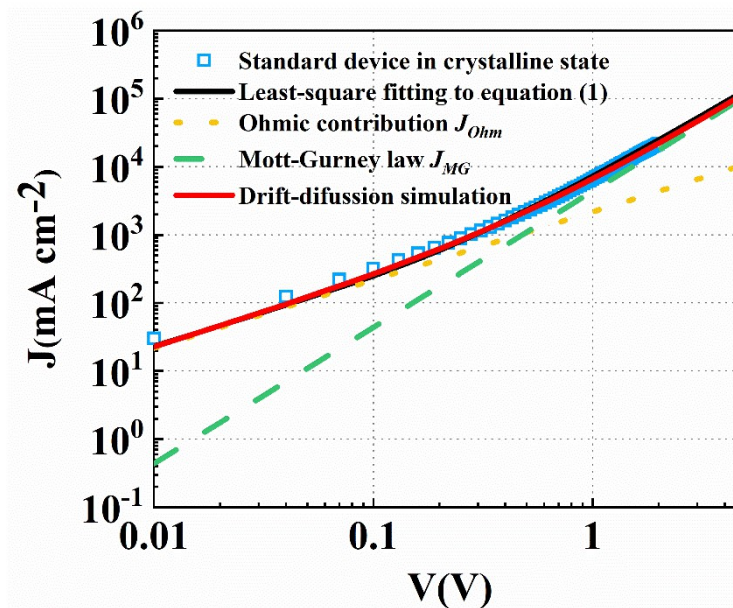

Figure A6.1 Least-square fitting method for the determination of μh.

Simulated *J-V* characteristics with rough surface profile.

In the case of standard SCLC devices, the surface roughness can lead to an overestimation of the mobility. This is because, strictly speaking, Mott-Gurney's law

only applies to flat device. Due to the L^{-3} dependence of equation (6.1), thinner sections will contribute disproportionately to the current, such that applying Mott-Gurney with the average thickness is no longer appropriate. This is illustrated on **Figure A6.2**. **Figure A6.2a** shows a thickness profile obtained by AFM measurement on the standard device. This profile was used to set up a 2D drift-diffusion simulation using the COMSOL Multiphysics software®, resulting in the *J-V* characteristics shown in **Figure A6.2b** (black curve). Clearly, equation (6.1) (green curve) using the average thickness fails to describe the SCLC regime in that case. As a result, the parameter fitting method will tend to overestimate the mobility. In the presented case for instance, a correction factor of 1.65 needs to be applied to Mott-Gurney's law to recover the *J-V* characteristics (shown as a red dotted line on **Figure A6.2**). As a result, μ_h would be overestimated by 65%.
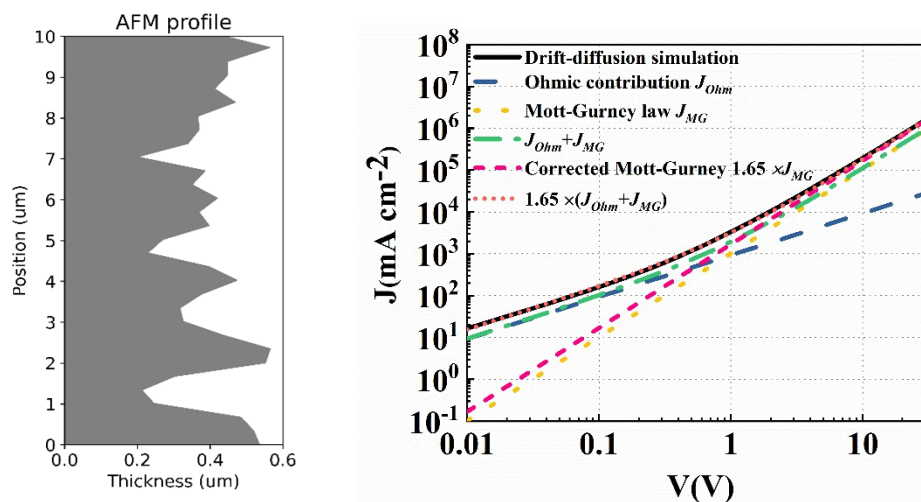

Figure A6.2 *Consequence of surface roughness on Mott-Gurney's law applicability. (a) AFM profile across a 10 μm wide representative region. (b) Simulated J-V characteristics resulting from the rough profile.*
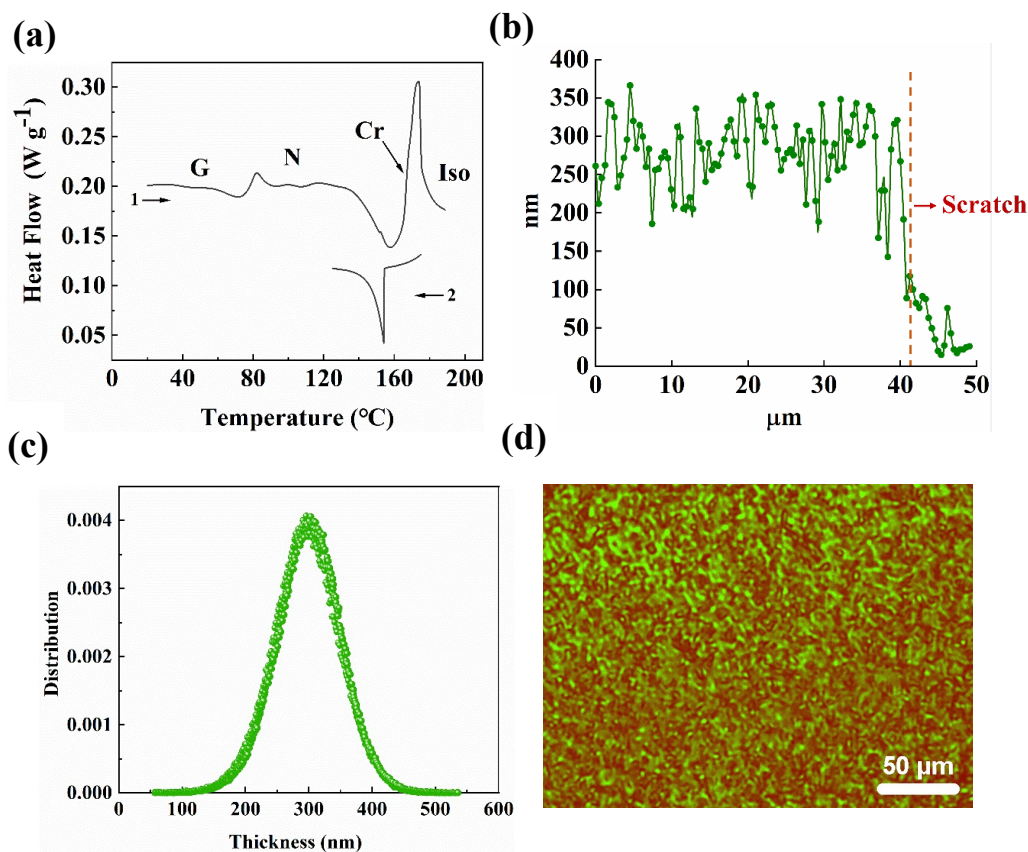
(a)

(b)

(c)

(d)

Figure A6.3 *(a) Differential scanning calorimetry heating scan for TPD$_{C8}$-TAT$_{C8}$. First heating run from glassy nematic state (G) to isotropic liquid phase (Iso), through fluid nematic phase (N) and crystalline phase (Cr), obtained through cold crystallization and followed by melting. 2nd cooling run from Iso to N. (b) Surface profile of a TPD$_{C8}$-TAT$_{C8}$ thin film in the crystalline state as measured using atomic force microscopy (AFM) (small crystals). (c) Thickness distribution of a crystalline thin film. (d) Polarized optical micrograph of a thick SCLC device in the nematic state prepared following the procedure described in Scheme 6.2 (note that the thickness was reduced with respect to SCLC devices in order to increase transparency). The bright Schlieren texture is similar to the one observed in spin-coated films and points out in-plane orientation of the nematic director.*
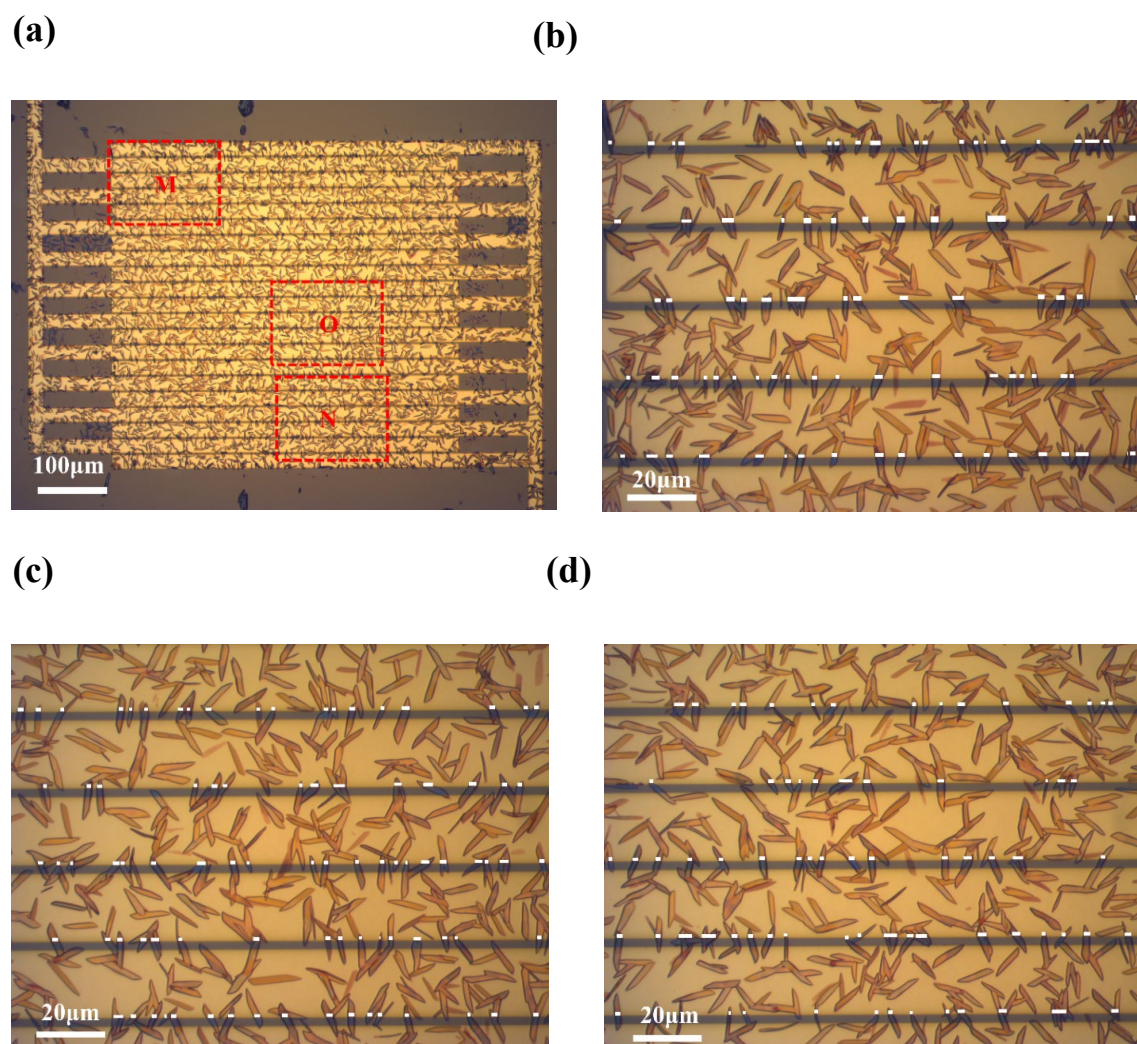
Figure A6.4 Optical micrographs of bottom-contact-bottom-gate transistor with a 2.5 µm channel length and 1.0 cm channel width. (a) Full device. (b), (c) and (d) zoom ×5 of three regions used to estimate the fraction of channel width covered by the crystalline needles. The corresponding effective channel width is 0.17±0.02 cm.

Chapter A7 Organic photovoltaic

A7.1 OPV device structure

Based on the OPV device structure, OPV devices can be divided into standard structure and the inverted structure as shown in **Figure A7.1**. In the standard OPV structure, transparent ITO/glass substrate as bottom electrode collect holes and top electrode

collect electrons. PEDOT: PSS is commonly used as hole transport layer (HTL) to blocks electrons between ITO and active layer, which also increase the work function of ITO. HTL has a high ionization potential and high hole mobility, it allows holes to flow across the layer, avoid electrons pass through go wrong way. Metals with low work function such as Zinc oxide (ZnO), Aluminum (Al) or Calcium (Ca) /Al, are used as top electrodes. However, Metals Al and Ca are easily oxidized in air resulting in poor device performance and stability.

In an inverted OPV structure, transparent ITO/glass substrate as bottom electrode collect electron and top electrode collect holes. For inverted structure devices, PEIE or ZnO is commonly used as electron transport layer (ETL) to blocks hole between ITO and active layer. ETL has a high electron affinity and high electron mobility, it allows electrons to pass through the layer, while holes cannot. So, metals with a high work function like Ag and Au are used as top electrodes, at the same time, use MoO_3 as the HTL to block electrons.
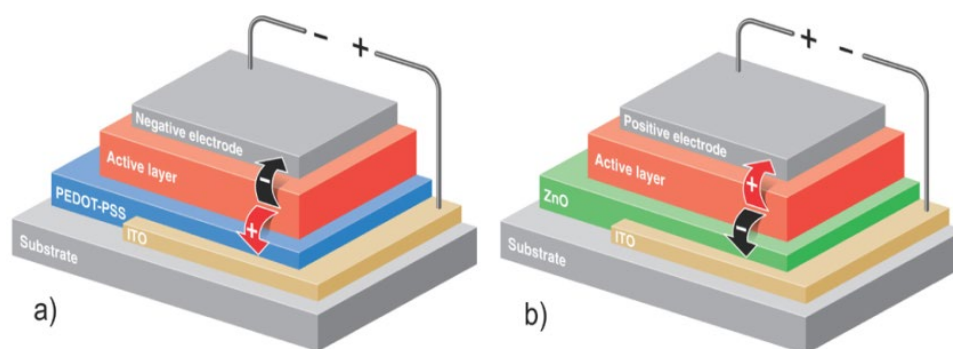

Figure A7.1 *Solar cell with (a) standard structure and (b) inverted structure. (Copyright from https://www.newcastle.edu.au/research/centre/coe/research/organic-solar-cells/coralie)*

A7.2 OPV active layer configuration

Based on the active layer, OPV can be divided into three types: single layer, multilayer and bulk-heterojunction, as shown in **Figure A7.2**.

Single layer configuration

Single layer organic solar cell (**Figure A7.2a**) is the simplest form of organic solar cells. This kind of OPV device is consisted of a single active layer between two electrodes with different work function. In fact, single layer organic solar cells work poorly and photovoltaic efficiency is quite low at around 0.1%. This is because that the charge dissociation only occurs at the interfaces between the active layer and the electrodes. Electric field between the two electrodes is not enough to make the charge reach the electrode before the electrons recombine with the hole.

Multilayer configuration

With the continuity of the research organic solar cells, multilayer organic solar cells have been developed. The multilayer architecture OPV consists of an electron donor (D) layer and an electron acceptor (A) layer between the electrodes (as shown in **Figure A7.2b**). The D layer and A layer have different ionization energy and electron affinity, so the energy offset is generated between the D/A interface, and exciton dissociation could occur at the D/A interface. At the same time, electrons and holes diffuse to their respective electrodes in separated layer so that could reduce the photo-excited charges recombination. Multilayer solar cells more effective than single-layer, however, the photo-generation of charges is still low because of the limited D/A interface area.

Bulk heterojunction configuration

In bulk heterojunction (BHJ) solar cells, electron donors and acceptors OSC are blend to form a thin film via solution processed. In this case, blend film eventually forms an interlocking, continuous network-like of D and A domains structure. Therefore, the D/A interface area is increased and results more excitons can be dissociated at interface (as shown in **Figure A7.2c**). Ideally, donor and acceptor domains should be less size of the exciton diffusion length (around 10nm), which allows excitons to diffuse to the D/A interface and thus achieves efficient exciton dissociation and charge generation. Finally,

the power conversion efficiency would increases significantly compare to the multilayer solar cells. However, the BHJ solar cells are highly depends on morphology of the active layer, which huge influence on the charge separation, recombination and transport.
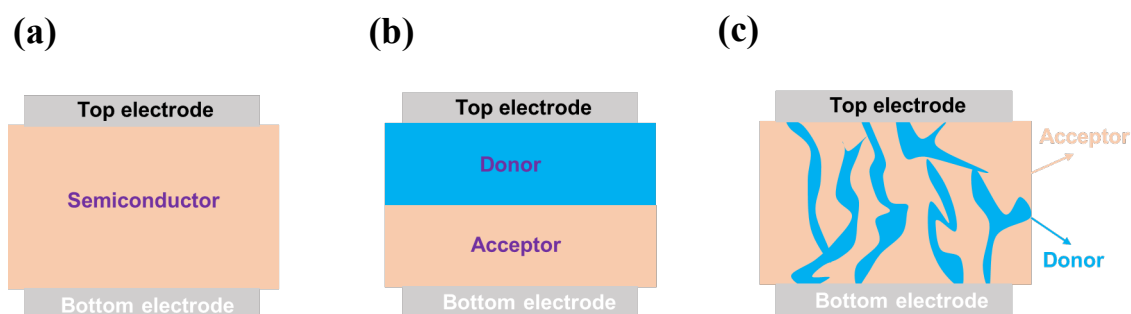

Figure A7.2 *Schematic of (a) single layer, (b) multilayer and (c) bulk heterojunction architecture OPV.*
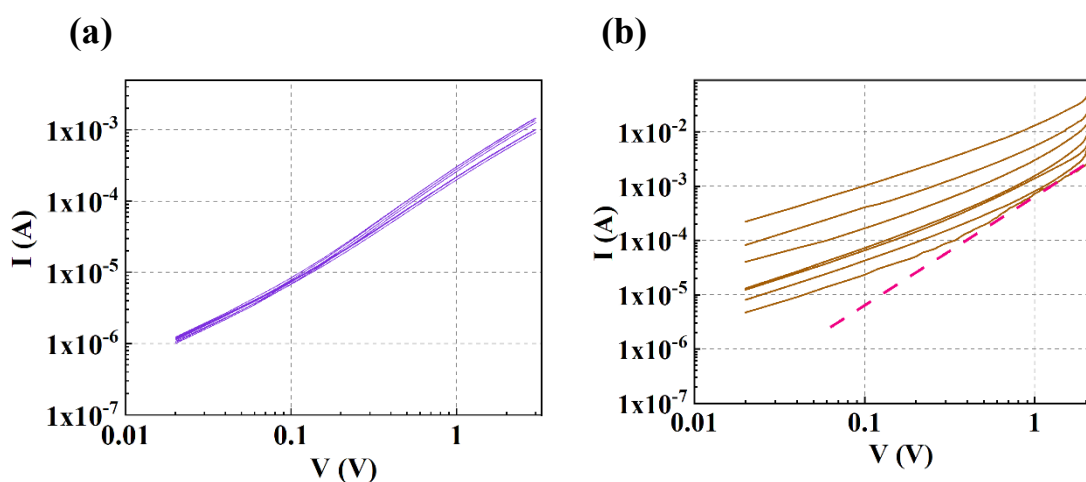

Figure A7.3 *I-V curve of (a) hole, (b) electron mobilities in the blends thin-films (condition **c**, **Table 7.2**).*

References:

[1]   A. Hexemer and P. Müller-Buschbaum, *IUCrJ*, 2015, **2**, 106-125.

[2]   A. Mahmood and J. L. Wang, *Solar RRL*, 2020, **4**, 2000337.

[3]   J. D. A. Lin, O. V. Mikhnenko, J. Chen, Z. Masri, A. Ruseckas, A. Mikhailovsky,

R. P. Raab, J. Liu, P. W. M. Blom, M. A. Loi, C. J. García-Cervera, I. D. W. Samuel and T.-Q. Nguyen, *Materials Horizons*, 2014, **1**, 280-285.

[4]   D. Yokoyama, K. i. Nakayama, T. Otani and J. Kido, *Advanced Materials*, 2012, **24**, 6368-6373.

[5]   A. Big-Alabo, E. O. Ekpruke, C. V. Ossia, D. O. Jonah and C. O. Ogbodo, *International Journal of Mechanical Engineering Education*, 2020, 0306419019896586.

[6]   T. Han, I. Bulut, S. Méry, B. Heinrich, P. Lévêque, N. Leclerc and T. Heiser, *Journal of Materials Chemistry C*, 2017, **5**, 10794-10800.

[7]   J. A. Röhr and R. C. I. MacKenzie, *Journal of Applied Physics*, 2020, **128**, 165701.

Acknowledgements

Time flies. My PhD thesis work was proceeded under the supervision of Prof. Dr. Thomas Heiser, and Dr. Emilie Steveler in ICube, Strasbourg. I would like to express sincere gratitude to them for their mentoring, trust, inspiration, and patience during last three years. We work together, they are more like my friends and I have enjoyed the most valuable friendships during my PhD training.

I would like to thank the laboratory collaborators: Dr. Nicolas Leclerc from ICPEES, and Dr. Stéphane Méry from IPCMS for providing and improving the quality of the molecules. Dr. Benoît Heinrich from IPCMS, Prof. D.A. Ivanov from IS2M for measuring and analyzing the molecular crystalline structure. They helped me achieve a milestone result.

I would like to thank the laboratory collaborators: Prof. Jérémie Léonard and PhD student Amira Gharbi from IPCMS for ultrafast spectroscopy measurement. They kind and patient give me a lot of help with the measurement at any time when I needed.

I would like to thank the laboratory collaborators: Dr. Gilles Ulrich from ICPEES, for quantum yield measurement and Dr. Anthony D'Aléo from IPCMS for analyzing the continuous-wave photoluminescence results. They kind give me a lot of useful information and clear out a lot of my doubt.

I would like to thank the laboratory collaborators: Prof. Leroy Yann and PhD student Alexis Prel for numerical simulation of space-charge-limit-current. Their constructive suggestions have been very helpful in improving my work.

Jiang JING

Strasbourg, France

1th February 2022

188

Résumé

Dynamique des excitons et transport de charge dans des films minces ordonnés à base de dérivés de triazatruxène

Dans les années 1970, les scientifiques ont découvert pour la première fois que les polymères conjugués dopés de polyacétylène ($[C_2H_2]n$) pouvaient être électriquement conducteurs[1]. Depuis lors, la recherche sur les matériaux semi-conducteurs organiques a connu un véritable essor dans les instituts de recherche ainsi que dans l'industrie[2, 3]. Par rapport aux matériaux semi-conducteurs inorganiques classiques, les semi-conducteurs organiques présentent de nombreux avantages tels que la facilité de fabrication de dispositifs en couches minces par évaporation sous vide ou par voie humide, la compatibilité du processus avec les substrats flexibles, etc. Les matériaux semi-conducteurs organiques peuvent être divisés en deux catégories: les « petites » molécules mono-disperses et les polymères. Le génie chimique des molécules organiques permet virtuellement de concevoir un nombre infini de molécules pouvant être utilisées comme matériau semi-conducteur avec des propriétés opto-électroniques diverses. Les propriétés semi-conductrices de petites molécules organiques conjuguées sont généralement dues à des électrons π délocalisés[4-7]. Contrairement aux polymères, les petites molécules semi-conductrices sont mono-disperses, plus faciles à purifier et conduisent souvent à des films minces cristallins présentant un désordre structurel réduit et des performances électroniques améliorées [8, 9].

Les propriétés remarquables des semi-conducteurs organiques ont conduit à leur utilisation dans trois principaux domaines d'application : les diodes électroluminescentes organiques (OLED), les transistors à effet de champ organiques (OFET) et les cellules photovoltaïques organiques (OPV)[4, 10-12]. La dynamique des

189

exciton et le transport des porteurs de charge sont des propriétés centrales qui déterminent les performances des dispositifs semi-conducteurs organiques. Celles-ci dépendent fortement de la structure moléculaire et de l'assemblage moléculaire à l'état solide[13-15]. La longueur de diffusion L_D des excitons est d'une importance cruciale pour les cellules solaires à hétérojonction donneur (D) / accepteur (A), puisqu'elle détermine la probabilité que les excitons atteignent l'interface D/A, où ils sont dissociés en porteurs de charge libres. L_D doit être supérieure ou égale à la largeur moyenne des domaines accepteur et donneur pour permettre une conversion photovoltaïque efficace. Cependant, les films minces semi-conducteurs organiques donnant lieu à un transport efficace des excitons sur des distances supérieures à 10 nm sont encore rares[13, 16].

Dans cette thèse, le transport de charges et la dynamique des excitons dans des films minces constitués de molécules semi-conductrices originales de type donneuses d'électrons ont été étudiés. Ces dernières sont composées d'une structure TPD-TAT, où TAT représente un groupement triazatruxène et TPD un groupement thiophène-thiénopyrroledione-thiophène. Le TAT est une unité particulièrement plane, qui favorise l'empilement des cœurs aromatiques moléculaires à l'état solide. Le TPD joue le rôle de chromophore. Les dérivés moléculaires TPD-TAT possèdent des chaînes latérales sur l'unité centrale TPD et sur les deux unités TAT, qui sont soit linéaires (chaîne octyle : C8) ou soit ramifiées (chaîne éthylhexyl : EH). Comme exemple, TPD_{EH}-TAT_{C8} correspond au dérivé portant une chaîne latérale ramifiée sur l'unité TPD et des chaînes latérales linéaires sur les deux unités TAT.

Des études antérieures ont montré que les dérivés TPD-TAT peuvent s'organiser en diverses phases à l'état solide (mésophases cristal liquide, cristallines ou amorphes), en fonction de la nature des chaînes latérales et des traitements post-dépôt[17]. Mon travail de thèse a porté essentiellement sur ces molécules et est composé de trois parties qui

sont (1) l'étude de la dynamique des excitons, (2) la caractérisation du transport de charge et (3) l'élaboration de dispositifs photovoltaïques.

Pour l'étude des excitons, des expériences de photoluminescence résolue en temps (TR-PL) et de photoluminescence continue (CW-PL) ont été réalisées en solution et à l'état solide, sur des molécules portant différentes chaînes latérales et ayant subi divers traitements thermiques. L'objectif de cette étude a été d'établir les corrélations entre durée de vie et longueur de diffusion des excitons d'une part, et structure moléculaire et assemblage moléculaire d'autre part. Les durées de vie des excitons ont été obtenues par ajustement des courbes TR-PL avec des modèles d'exponentielles décroissantes des premier et second ordres. Les longueurs de diffusion ont été estimées pour différentes phases solides de la molécule TPD_{C8}-TAT_{C8} à partir de mesures d'annihilation d'exciton-exciton (EEA) et de rendement quantique de photoluminescence (QY). En solution, tous les dérivés TPD-TAT ont présenté une durée de vie des excitons identique (≈0,7ns), considérée comme valeur de référence en absence d'interactions intermoléculaires. Les résultats de TR-PL sur les films minces ont révélé une augmentation significative de la durée de vie des excitons avec l'augmentation du degré d'ordre structurel. Les durées de vie relativement élevées (jusqu'à 1,0 ns), observées pour le TPD_{C8}-TAT_{C8}, sont en accord avec les bonnes performances photovoltaïques obtenues précédemment en cellules solaires [8]. Par ailleurs, les mesures de EEA et QY ont montré que la longueur de diffusion des excitons augmente significativement en passant de la mésophase à la phase cristalline. Ainsi, L_D a été estimée à 10.5 ± 1.0 nm par QY et à 15.5±1.0 nm par EEA dans les films sans recuit, et atteint respectivement 23.5±1.5 nm (mesurée par QY) et L_D=29.0±2.0 nm (mesurée par EEA) dans les films les plus cristallins (après un recuit de 2h à 145°C). Les différences entre les deux mesures peuvent être attribuées au degré d'incertitude des modèles utilisés. Néanmoins, la variation relative de L_D en fonction de la structure est similaire pour les deux

méthodes et confirme le fort impact que peut avoir l'organisation moléculaire sur la mobilité des excitons.

La deuxième partie de mon travail a porté sur le transport de charges dans les films TPD$_{C8}$-TAT$_{C8}$ pour différentes phases solides. Il est attendu des molécules planaires qu'elles améliorent les interactions intermoléculaires et facilitent le transport de charge le long des directions d'empilement π. En revanche, la conduction le long des autres directions est souvent réduite[18, 19]. C'est particulièrement le cas pour les molécules fonctionnalisées par des chaînes alkyles, qui assurent une bonne solubilité mais introduisent des régions isolantes. Les résultats obtenus dans cette thèse montrent que les molécules TPD$_{C8}$-TAT$_{C8}$ s'auto-assemblent en une structure originale qui permet un transport de charge efficace en 3D. Des études de diffraction de rayons X révèlent que les TPD$_{C8}$-TAT$_{C8}$ forment une mésophase colonnaire-nématique dans laquelle les TAT sont empilés en colonnes, orientées parallèlement au substrat. Les colonnes sont espacées par les chaînes alkyles et sont interconnectées par des ponts de TPD. Après recuit thermique, une phase cristalline, issue de la mésophase mère, est obtenue. Des mesures de diffraction X en incidence rasante ainsi que des expériences aux rayons X focalisées sur des monocristaux ont montré que la direction d'empilement des unités TAT est également orientée parallèlement au substrat dans la phase cristalline.

Des mesures de transport de charge ont été réalisées à l'aide de diodes à courant limité par la charge d'espace (SCLC) (pour la mesure des mobilités perpendiculaire au substrat, $\mu_\perp$) et de transistors à effet de champ organiques (OFET) (pour la mobilité parallèle au substrat, $\mu_{//}$) pour différentes phases solides. En raison de la forte rugosité de surface des films cristallins les mesures de $\mu_\perp$ avec des dispositifs SCLC standards conduisent à une surestimation significative de la mobilité liée à l'erreur sur l'épaisseur du film. Cela nous a conduit à développer une nouvelle architecture de dispositif SCLC "épais", afin de permettre un meilleur contrôle de l'épaisseur de la couche semi-conductrice et

de réduire ainsi la marge d'erreur sur les valeurs de mobilité. Les résultats sur les dispositifs SCLC épais montrent que $\mu_\perp$ augmente de $(2,7\pm0,5)\times10^{-3}$ cm^{2}V^{-1}s^{-1} à une mobilité de 0,17 cm^{2}V^{-1}s^{-1}, lorsque les films minces passent de la phase nématique colonnaire à la phase cristalline. Cette dernière valeur de mobilité est parmi les valeurs les plus élevées mesurées par SCLC pour des semiconducteurs moléculaires. De plus, l'étude en fonction de la température montre que l'énergie d'activation (E_a) diminue de $0,12\pm0,01$ eV, dans l'état nématique, à $0,030\pm0,008$ eV dans l'état cristallin. Cette dernière valeur est exceptionnellement basse pour les semi-conducteurs organiques et corrobore l'existence de voies très efficaces pour le transport de charges perpendiculairement à la direction d'empilement moléculaire.

Le transport de charges parallèle au substrat, en phase nématique et cristalline, a été étudié à l'aide de transistors à effet de champ organiques (OFET). En phase nématique, la mobilité $\mu_{//}$ a été estimée à 2×10^{-4} cm^{2}V^{-1}s^{-1}. Cette valeur est inférieure d'environ un ordre de grandeur à $\mu_\perp$.

Pour la phase cristalline, des caractéristiques de transfert fortement non linéaires ont été obtenues. Nous attribuons ce comportement à l'existence d'un piégeage efficace des porteurs de charge aux niveaux des joints de grains cristallins (la taille moyenne des cristaux étant significativement plus petite que la longueur du canal) et d'une résistance de contact élevée. Pour minimiser l'impact des joints de grains, des transistors supplémentaires avec des cristaux de taille comparable à la longueur de canal (2,5 μm) ont été élaborés. Dans ces dispositifs, les cristaux moléculaires étaient en contact direct avec les deux électrodes et couvraient une fraction significative de la largeur du canal (W). Dans ces conditions, la mobilité $\mu_{//}$ a pu être estimée à une valeur minimale de $0,050\pm0,015$ cm^{2}V^{-1}s^{-1}. L'ensemble des résultats SCLC et OFET soulignent l'existence d'un transport de trous efficace en trois dimensions, c'est-à-dire le long et perpendiculairement à la direction d'empilement moléculaire. Nous attribuons ce

comportement remarquable aux segments conjugués TPD qui pontent les colonnes TAT voisines et permettent un transport intercolonnes efficace.

La dernière partie de mon travail porte sur l'application des molécules TPD$_{C8}$-TAT$_{C8}$ dans les OPV à base de mélange polymères/petites molécules. En effet, les propriétés de ces molécules (longueur de diffusion des excitons et mobilité des porteurs de charge élevées) en font de bons candidats pour le photovoltaïque. Jusqu'à présent, la majorité des travaux de la littérature sur les cellules solaires organiques ont été consacrées soit à des mélanges polymères/polymères, soit à des mélanges polymères(donneurs d'électrons)/ molécules (acceptrices d'électrons). Seules quelques publications ont porté sur les mélanges molécules donneuses/ polymères accepteurs[20-23]. Les performances de ces systèmes étaient principalement limitées par une séparation de phase prononcée entre le donneur et l'accepteur[20, 22]. Les premiers résultats sur les cellules solaires BHJ basées sur le TPD$_{C8}$-TAT$_{C8}$ comme donneur et PNDIT2 comme polymère accepteur montrent que la performance dépend fortement de l'ordre d'empilement de la petite molécule. En effet, le rendement de conversion photovoltaïque augmente de 0,2% à 1,5% lorsque le film mince passe de l'état non-recuit à l'état cristallin. Cependant, l'origine du faible rendement obtenu jusqu'à présent reste encore à clarifier.

Références:

[1]   H. Shirakawa, *Angewandte Chemie International Edition*, 2001, **40**, 2574-2580.

[2]   F.-C. Chen, in *Encyclopedia of Modern Optics (Second Edition)*, eds. B. D. Guenther and D. G. Steel, Elsevier, Oxford, 2018, pp. 220-231.

[3]   T. Hasegawa, in *Handbook of Organic Materials for Electronic and Photonic Devices (Second Edition)*, ed. O. Ostroverkhova, Woodhead Publishing, 2019, pp. 579-597.

[4]   J. E. Anthony, A. Facchetti, M. Heeney, S. R. Marder and X. Zhan, *Advanced*

Materials, 2010, **22**, 3876-3892.

[5]   M. Graetzel, R. A. J. Janssen, D. B. Mitzi and E. H. Sargent, *Nature*, 2012, **488**, 304-312.

[6]   A. Köhler and H. Bässler, in *Electronic Processes in Organic Semiconductors*, 2015, pp. 1-86.

[7]   Y. Liu, X. Duan, H.-J. Shin, S. Park, Y. Huang and X. Duan, *Nature*, 2021, **591**, 43-53.

[8]   G. Giri, D. M. DeLongchamp, J. Reinspach, D. A. Fischer, L. J. Richter, J. Xu, S. Benight, A. Ayzner, M. He, L. Fang, G. Xue, M. F. Toney and Z. Bao, *Chemistry of Materials*, 2015, **27**, 2350-2359.

[9]   T. Han, I. Bulut, S. Méry, B. Heinrich, P. Lévêque, N. Leclerc and T. Heiser, *Journal of Materials Chemistry C*, 2017, **5**, 10794-10800.

[10]   D. Wöhrle and D. Meissner, *Advanced Materials*, 1991, **3**, 129-138.

[11]   S. Haque, M. S. A. Sher Shah, M. Rahman and M. Mohiuddin, in *Biopolymer Composites in Electronics*, eds. K. K. Sadasivuni, D. Ponnamma, J. Kim, J. J. Cabibihan and M. A. AlMaadeed, Elsevier, 2017, pp. 277-310.

[12]   Q. Burlingame, X. Huang, X. Liu, C. Jeong, C. Coburn and S. R. Forrest, *Nature*, 2019, **573**, 394-397.

[13]   S. M. Menke and R. J. Holmes, *Energy & Environmental Science*, 2014, **7**, 499-512.

[14]   A. Köhler and H. Bässler, in *Electronic Processes in Organic Semiconductors*, 2015, pp. 1-86.

[15]   O. V. Mikhnenko, P. W. Blom and T.-Q. Nguyen, *Energy & Environmental Science*, 2015, **8**, 1867-1888.

[16]   A. Köhler and H. Bässler, *Electronic processes in organic semiconductors: An introduction*, John Wiley & Sons, 2015.

[17]   I. Bulut, P. Lévêque, B. Heinrich, T. Heiser, R. Bechara, N. Zimmermann, S. Méry, R. Ziessel and N. Leclerc, *Journal of Materials Chemistry A*, 2015, **3**,

6620-6628.

[18]   Z.-F. Yao, J.-Y. Wang and J. Pei, *Crystal Growth & Design*, 2018, **18**, 7-15.

[19]   S. Fratini, M. Nikolka, A. Salleo, G. Schweicher and H. Sirringhaus, *Nature Materials*, 2020, **19**, 491-502.

[20]   B. H. Wunsch, K. Kim, Y. Rho, B. Ahn, S. Jung, L. E. Polander, D. G. Bucknall, S. R. Marder and M. Ree, *Journal of Materials Chemistry C*, 2013, **1**, 778-785.

[21]   S. Holliday, R. S. Ashraf, A. Wadsworth, D. Baran, S. A. Yousaf, C. B. Nielsen, C.-H. Tan, S. D. Dimitrov, Z. Shang, N. Gasparini, M. Alamoudi, F. Laquai, C. J. Brabec, A. Salleo, J. R. Durrant and I. McCulloch, *Nature Communications*, 2016, **7**, 11585.

[22]   Z. Zhang, T. Wang, Z. Ding, J. Miao, J. Wang, C. Dou, B. Meng, J. Liu and L. Wang, *Macromolecules*, 2019, **52**, 8682-8689.

[23]   D. Hu, Q. Yang, H. Chen, F. Wobben, V. M. Le Corre, R. Singh, T. Liu, R. Ma, H. Tang, L. J. A. Koster, T. Duan, H. Yan, Z. Kan, Z. Xiao and S. Lu, *Energy & Environmental Science*, 2020, **13**, 2134-2141.

Jiang JING

Exciton dynamics and charge transport in ordered thin films based on triazatruxene derivatives

Résumé

La dynamique des excitons et le transport des porteurs de charge dans les semi-conducteurs organiques sont des propriétés essentielles qui déterminent les performances des dispositifs opto-électroniques (comme par exemple les cellules solaires organiques) et dépendent fortement de la structure moléculaire et de l'état solide associé des molécules semi-conductrices. Dans cette thèse, nous nous sommes concentrés sur une famille de semi-conducteurs moléculaires de type donneur-accepteur-donneur (D-A-D) en forme d'haltère. La partie donneuse d'électrons était composée d'une unité planaire fonctionnalisée de triazatruxène (TAT), qui est très soluble et agit comme une plateforme d'empilement π, tandis qu'une unité de thiophène-thiénopyrroledione-thiophène (TPD) a été utilisée comme unité acceptrice d'électrons. Les structures auto-assemblées à l'état solide des molécules TPD-TAT dépendent fortement des chaînes latérales alkyles greffées sur les deux unités et des traitements thermiques post-dépôt. La durée de vie et la longueur de diffusion des excitons ont été étudiées en détail en fonction de la structure chimique moléculaire et de la structure de l'état solide. De même, les mobilités des porteurs de charge dans le plan et hors du plan ont été étudiées en fonction de la structure de l'empilement moléculaire. Enfin, les premières cellules solaires organiques utilisant le TPD-TAT comme donneur d'électrons mélangé à un polymère accepteur d'électrons ont également été développées.

Mots clés : semi-conducteurs organiques à petites molécules, durée de vie des excitons, longueur de diffusion des excitons, transport de charge, transistors à effet de champ organiques, courant limité par la charge d'espace.

Résumé en anglais

Exciton dynamics and charge carrier transport in organic semiconductors are essential properties that determine the performances of opto-electronic devices (such as for instance organic solar cells) and are highly dependent on the molecular structure and associated solid-state packing of the semiconducting molecules. In this thesis, we focused on a family of "dumbbell-shaped" donor-acceptor-donor (D-A-D) type molecular semiconductors. The electron donor moiety was composed of a functionalized planar triazatruxene (TAT) unit, which is highly soluble and acts as a π-stacking platform, while a thiophene-thienopyrroledione-thiophene (TPD) unit was used as the electron acceptor unit. The self-assembled solid-state structures of the TPD-TAT molecules are highly dependent on the alkyl side-chains grafted on both units and on post-deposition thermal treatments. The exciton lifetime and diffusion length were investigated in detail as a function of molecular chemical structure and solid-state structure. Also, the in-plane and out-of-plane charge carrier mobilities were studied as a function of molecular packing structure. Finally, first organic solar cells using TPD-TAT as electron donor blended with an electron-acceptor polymer were also developed.

Keywords: small-molecule organic semiconductors, exciton lifetime, exciton diffusion length, charge transport, organic field-effect transistors, space-charge-limited-current